2022

Use of complex environmental data for realistic wave tank testing of Wave Energy Converters

Wang, Daming

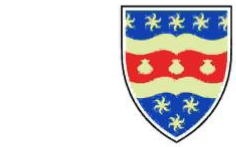

UNIVERSITY OF
PLYMOUTH

Use of complex environmental data for realistic wave tank testing of Wave Energy Converters

By

Daming Wang

A thesis submitted to the University of Plymouth
in partial fulfilment for the degree of

DOCTOR OF PHILOSOPHY

School of Engineering, Computing and Mathematics

August 2022

Acknowledgements

First and foremost, I would like to thank my supervisory team, Prof. Deborah Greaves, Prof. Daniel Conley, Dr. Martyn Hann, and Dr. Keri Collins who have supported me from the beginning to the end of my study at the University of Plymouth. Their expertise helped me overcome many obstacles and difficulties. I could not remember how many times they spent their time and efforts answering my questions, checking my MATLAB scripts, and reviewing my papers, even out of their working hours. I would also thank the technical staff Dr. Kieran Monk and Dr. Federica Buriani in the COAST laboratory for the timely support and assistance during the experiments I did. I would also thank my colleagues Prof. Min Yu and Dr. Siya Jin, Nanting Yu, Qi Ye, Siming Zheng, Qinwei Ding, Lei Liu, and Jie Ji who supported me a lot when I had questions during my study. I would like to thank my parents and other relatives as well for their constant support of my study.

Author's declaration

At no time during the registration for the degree of Doctor of Philosophy has the author been registered for any other University award. Work submitted for this research degree at the University of Plymouth has not formed part of any other degree either at Plymouth University or at another establishment.

Relevant scientific seminars and conferences were regularly attended at which work was often presented.

Word count for the main body of this thesis: **47888**

Signed: Daming Wang

Date: August 13, 2022

Presentations and conferences attended:

D. Wang, D. Conley, M. Hann, K. M. Collins, and D. Greaves, "Use of HF Radar for Replicating Complex Wave Condition for Testing of Wave Energy Converters." PRIMARE Bristol University, UK, 2018

D. Wang, D. Conley, M. Hann, K. M. Collins, and D. Greaves, "Using AI technique to obtain representative sea conditions for Wave Energy Converters (WECs) testing." 3min thesis competition, University of Plymouth, UK, 2019

D. Wang, D. Conley, M. Hann, K. M. Collins, and D. Greaves, "Use of HF radar for replicating wave conditions for testing of wave energy converters with different regrouping methods." PRIMARE Cardiff University, UK, 2019

D. Wang, D. Conley, M. Hann, K. M. Collins, and D. Greaves, "Use of HF radar for replicating wave conditions for testing of wave energy converters with different regrouping methods." INORE Nocera Umbra, Italy, 2019

D. Wang, D. Conley, M. Hann, K. M. Collins, and D. Greaves, "Use of HF radar for replicating wave-current combined wave conditions for testing of wave energy converters." EWTEC Naples, Italy, 2019

D. Wang, D. Conley, M. Hann, K. M. Collins, and D. Greaves, "Tank testing of hinged-raft wave energy converter with representative sea states." PRIMARE Bangor University, UK, 2021

D. Wang, D. Conley, M. Hann, K. M. Collins, and D. Greaves, "Power output estimation of WEC with HF radar measured complex representative sea states." EWTEC Plymouth, UK, 2021

Journal and conference papers accepted:

D. Wang, D. Conley, M. Hann, K. Collins, S. Jin, and D. Greaves, "Power output estimation of WEC with HF radar measured complex representative sea states," *International Marine Energy Journal,* 2022.

J. Ohana *et al.*, 'Round robin tests on a hinged raft wave energy converter', *EWTEC* 2021.

T. Davey *et al.*, "Round Robin Testing: Exploring Experimental Uncertainties through a Multifacility Comparison of a Hinged Raft Wave Energy Converter," *Journal of Marine Science and Engineering*, vol. 9, no. 9, p. 946, 2021.

D. Wang, D. Conley, M. Hann, K. M. Collins, and D. Greaves, "Use of HF radar for replciating wave-current combined wave conditions for testing of wave energy converters," *EWTEC* 2019.

Use of complex environmental data for realistic wave tank testing of Wave Energy Converters

Daming Wang

Abstract

Wave tank model testing is a commonly used method to assess the performance of Wave Energy Converters (WECs). Wave data collected for testing can be obtained by different instruments (e.g. buoys, ADCP, and HF radar). Currently, the widely accepted way to re-create the wave conditions for WEC model testing is to obtain wave parameters from the wave data collected and apply them to a suitable generic wave spectrum, such as the JONSWAP spectrum or Pierson-Moskowitz spectrum, then reproduce it in the wave tank. By using this method, each wave condition is simplified to several wave parameters such as the significant wave height, wave peak period, etc. However, the parametric wave spectrum obtained by this method is just a simplified mathematical model that omits much useful wave information, such as the details of the wave spectrum and the wave directional information. At later development stages, there is a need to use site-specific complex wave conditions representative of the potential prototype deployment sites for model testing of the WECs. Today, with the development of advanced wave measurement instruments, such as the high-frequency radar system, the site-specific hourly/ half-hourly wave spectra can be obtained to provide the information to recreate the wave conditions in the wave tank in a much more accurate way.

After obtaining numerous hourly/ half-hourly wave spectra, it is necessary to determine a certain number of sea states that can best represent the ocean environment of interest for WEC model testing.

This thesis compared ten regrouping methods to obtain a small number of representative sea states from a large data set. It was found that the method based on the non-directional wave spectrum *K*-means clustering technique obtained the sea states with the highest representativeness regardless of the total data set used. The representative sea states were tested both numerically and physically using two different WEC designs, a point absorber and a 1:25 hinged-raft device for their power output performance. The results have shown that the representative sea states obtained from the method not only represented well the ocean environments but also represented the annual power output conditions of the WECs well regardless of the non-linearity. The error in the annual energy output predicted using representative sea states from different regrouping methods was within 1%. The error in the annual energy output predicted using the same regrouping method with a different number of groups was less than 5%.

Contents

List of Figures

List of Tables

Nomenclature

1D	one dimensional
2D	two dimensional
3D	three dimensional
a	average response amplitude
b	distance from the hanging axis to the centre of gravity of model
d	relative difference of two members
d_h	distance between two hanging points
f	wave frequency
f_p	peak frequency
f_r	radiation impulse function
f_{step}	frequency step
g	gravitational parameter
h	water depth
i	imaginary unit
k	group label
k_{DoF}	gyradius in a certain DoF
k_p	wave number at spectral peak
k_R	rotational PTO damping parameter
k_{spring}	stiffness of the tension spring
k_T	translational PTO damping parameter
k_w	wave number
k_{xx}	gyradius in roll
k_{yy}	gyradius in pitch
k_{zz}	gyradius in yaw
l	length of the suspension line.

m_k	k - th order spectral moment
p	power output
t	time
v	spectral band width
x	displacement
$\dot{x}$	velocity
$\ddot{x}$	acceleration
A	added mass matrix
A_{mean}	mean peak value
A_{target}	target regular wave amplitude
B	damping matrix
C	restoring matrix
C_g	group velocity
C_k	k - th subgroup
C_p	phase speed of the wave in limited water depth
C_R	reflection coefficient
D	model width
$D(f,\theta)$	directional spreading function
$D_{PSD}(f)$	difference between the wave spectrum
$E_{full\ scale}$	annual energy output in full scale
$E_{full\ accurate}$	accurate annual energy output in full scale
E_k	energy in k - th group
E_{model}	annual energy output predicted in model scale
$E_{model\ actual}$	actual annual energy output in model scale
E_P	relative error between the accurate energy output and the estimated value
E_{total}	total energy from all groups
$\overline{E_w}$	average total wave energy over a wave period
F_0	amplitude of the excitation force
F_e	excitation force
$F_{initial}$	minimum force for the spring to start extension
F_{moor}	mooring force

F_r	Froude number
F_{rad}	radiation force
$F_{restoring}$	restoring force of the spring
F_{PTO}	PTO force
H	regular wave height
$H_{1/3}$	mean of 1/3 largest wave height
H_{m0}	significant wave height calculated by the zeroth moment of the spectrum
H_s	significant wave height
$H_T(f)$	transfer function
K	total number of groups
L	model length
M	mass matrix
N_k	number of members in cluster k
P	wave power
$P_{average}$	average power output value
$\overline{Pw}$	average power of a regular wave
P_{PTO}	PTO power output
$P_{physical}$	average power output from physical model testing
$P_{WEC-SIM}$	average power output from WEC-SIM numerical model
R_e	Reynolds numbers
S	total data set
$S(f)$	non-directional wave spectrum
$S(f,\theta)$	directional wave spectrum
S_η	incoming wave spectrum
S_B	in-between-group scatter matrix
S_{DoF}	spectrum in a DoF
S_p	wave peak steepness
$S_{PTO}(f)$	power output spectrum
S_{peak}	spectrum peak value
S_{rep-k}	representative directional sea state of the group k
$S_{rep-k-2D}$	representative non-directional sea state of the group k

S_W within-cluster group matrix

T wave period/free oscillation period

T_1 lower boundary of time window

T_2 upper boundary of time window

T_e energy period

T_p peak period

T_{repeat} repeat time

V fluid velocity

γ weighting parameter

Γ wave shape parameter gamma

δ wave parameters used for metric one

δ_P relative error between the numerical average power output and physical testing result

ϵ phase angle

ζ_a wave amplitude

η surface elevation

θ wave direction

θ_m mean wave direction

λ scaling parameter

λ_p wave length at spectral peak

μ dynamic viscosity

μ_k vector mean of the members in cluster k

ξ kinematic viscosity

ρ fluid density

σ_θ wave directional spreading parameter

φ gain value for wave calibration

φ_S the relative error between the area of the measured wave spectrum and the target JONSWAP spectrum

ψ_K relative error between the accurate annual energy output for K groups

ω wave angular frequency

ω_p peak wave frequency

Abbreviations

ADCP	Acoustic Doppler Current Profiler
BEM	Boundary Element Method
CFD	Computational Fluid Dynamics
CLARA	Clustering LARge Applications
COAST	Costal, Ocean and Sediment Transport
CoG	Centre of Gravity
CWR	Capture Width Ratio
DFT	Discrete Fourier Transform
DoF	Degree of Freedom
ECN	Ecole Centrale de Nantes
EMEC	European Marine Energy Centre
FFT	Fast Fourier Transformation
FLS	Fatigue Limit State
GEOS	Geosynchronous Earth Orbit Satellite
HF	High Frequency
JONSWAP	Joint North Sea Wave Observation Project
MaRINET 2	Marine Renewable Infrastructure Network for Enhancing Technologies 2
MEP	Maximum Entropy Method
MLM	Maximum Likelihood Method
MOI	Moment of Inertia
MRE	Marine Renewable Energy
MWP	McCabe Wave Pump
NASA	National Aeronautics and Space Administration
NDBC	National Data Buoy Centre
NREL	National Renewable Energy Laboratory
OSWEC	Oscillating Surge Wave Energy Converter
OTEC	Ocean Thermal Energy Converter
OWC	Oscillating Water Column

PM	Pierson-Moskowitz
PTO	Power Take Off
R&D	Research and Development
RA	Radar Altimeter
RAO	Response Amplitude Operator
RM	Reference Model
RMSE	Root Mean Square Error
SAR	Synthetic Aperture Radar
SNL	Sandia National Laboratories
SNR	Signal to Noise Ratio
SSE	Sum of Squared Error
STD	Standard Deviation
SWL	Still Water Level
TRL	Technology Readiness Level
UoP	University of Plymouth
UoE	University of Edinburgh
UCC	University College Cork
ULS	Ultimate Limit State
WEC	Wave Energy Converter
WERA	WavE RAdar
WG	Wave Gauge

1. Introduction

In order to mitigate climate change and achieve zero net greenhouse gas emissions by 2050 [1], research in renewable energy has gained more and more attention in recent years. Among different types of renewable energy sources, Marine Renewable Energy (MRE) is considered with high potential [2]. MRE mainly consists of six types, which are wave energy, ocean current energy, tidal energy (tidal range and tidal currents energy [3]), ocean thermal energy (OTE), offshore wind energy, and osmotic energy (derived from the difference in the salt concentration between different water layers). Wave energy has a relatively high power density compared to other types of MRE. According to estimations, the global potential of wave energy is about 26,000 TW.h/yr [2]. However, due to the complexity of wave environments, the utilization of wave energy is still under-developed.

1.1 Background

Wave energy converters (WECs) are devices that are able to convert the energy within waves into electricity [4]. Various types of WECs are being investigated and tested by companies and universities around the world, but just a few of the concepts have the opportunity for full-scale open water testing, not to mention commercial deployment. It

is expected that the cost of WEC devices can be decreased in the future to be competitive with the conventional power plants ([5], [6]). The potential of WECs is high, especially in the UK, which has the strongest waves in the north of Scotland. It has been reported that in the UK alone, WECs have the potential to provide more than 50 TW.h/yr [7]. As the demand for electricity in the UK increases every year [8], WECs are considered a promising green energy resource.

In the process of developing a successful WEC, model testing in the wave tank is important to design and improve the performance and finally commercialize a WEC. For a specific WEC, after it is tested in regular waves, it is necessary to test the model in a realistic wave condition to better understand the performance of the device in real life. This can be achieved by using the site-specific sea states. Due to the limit of tank testing resources, there comes a question about how to select a suitable number of sea states from the measured ocean area to best represent the wave environment. To generate realistic waves in the laboratory environment, a good measure of waves in the field is needed. First of all, it is very important to select an ocean area with suitable wave conditions to deploy a WEC. Secondly, it is important to have a suitable instrument to measure the long-term wave conditions of the area.

In this thesis, there was a suitable ocean area selected, which was the Wave Hub WEC testing site located outside the coastline of Cornwall. To measure the wave conditions of the testing site, different kinds of instruments can be used. However, there was a relatively new technology chosen for this study, which was a shore-based high-frequency radar system deployed and maintained by the University of Plymouth (UoP). The effectiveness of wave measurement of the device has been validated by previous research [9]. It

provided thousands of site-specific hourly/half hourly wave spectra of the ocean area annually, which was suitable for this research.

In addition to the selection of sea states, it is necessary to test them on WECs for the performance evaluation. This was achieved by testing the sea states on both numerical and physical WEC models. The physical testing part was supported by the Marine Renewable Infrastructure Network for Enhancing Technologies 2 (MaRINET 2), which was an EU-sponsored project that ensured the enhancement of all leading European research infrastructure and facilities specializing in research, development, and testing of offshore renewable energy devices [10]. As part of the project, a 1:25 hinged-raft WEC model was manufactured and tested in four different Universities in October 2020. This physical model was used for this study.

1.2 Originality and objectives of the Ph.D. project.

The thesis aims to use the HF radar measured sea states from an ocean area (Wave Hub) as a total data set and obtain a small number of hourly sea states that can accurately represent the characteristics of the ocean area, thus can be used to assess the performance of WECs in this ocean area during model testing.

The objectives are:

1. To select a small number of representative sea states from HF radar measured hourly sea states in a certain period of time (e.g. one year) by using different data regrouping methods.

2. To assess the quality of the representative sea states from different regrouping methods and determine the most suitable method for wave classification. The preferred regrouping method that can best represent the characteristics of the sea states will be decided.

3. To test the representative sea states from different regrouping methods on a simple numerical WEC model (RM3 point absorber) to assess the power output performance of the WEC using representative sea states. The annual energy output using representative sea states from different regrouping methods will be compared.

4. To test the representative sea states obtained on a realistic physical model. This will be achieved by testing a 1:25 hinged-raft WEC model in the Coastal, Ocean, and Sediment Transport (COAST) laboratory of UoP. Additionally, the numerical WEC model will be built and validated based on the physical testing results. The quality of the power output performance using representative sea states from different regrouping methods will be compared both physically and numerically. The most suitable regrouping method will be determined.

5. To give the recommendations for selecting suitable seas states for the model testing of WEC. The benefit of using the regrouping method with the highest representativeness will be explained.

The thesis consists of seven chapters. Chapter 1 is the introduction to the research background. Chapter 2 is the literature review that gives a brief introduction to the development of modern WECs and steps to commercialize a WEC, the importance of physical model testing, and the commonly used method to select sea states for model testing from a large data set, also an introduction for the numerical analysis software that will be used in the thesis. Chapter 3 is to introduce ten sea state regrouping techniques based on binning method and *K*-means clustering method to obtain representative sea states from a total data set, and to use two metrics to assess the regrouping quality of different regrouping methods. In this chapter, two types of data sets are used to show the applicability of the regrouping methods. The preferred method for sea state regrouping will be determined. Chapter 4 is to test the representative sea states from Chapter 3 on a WEC-SIM numerical model (RM3 point absorber). The annual energy output estimation using representative sea states and the linearity of the model will be discussed. Chapter 5 is to test the sea states on a more realistic WEC model (1:25 hinged raft) both experimentally and numerically. The non-linearity of the model and the influence on the results will be discussed. Chapter 6 is the discussion chapter that explains the position of this research, the limitations and contributions of this research, and future work. Chapter 7 is the conclusion chapter.

2. Literature review

This chapter consists of the following sections:

Section 2.1 is a brief introduction to the development of WECs, which includes the main categories of different devices and the procedures to commercialize a WEC. Section 2.2 is to introduce the model testing procedures of WECs, including the scaling criterion and different wave conditions used for model testing. Section 2.3 is to introduce different instruments that can be used to measure the wave conditions from a certain ocean area for model testing. Section 2.4 is to introduce the numerical analysis software, which will be used in this research.

2.1 A brief introduction to WEC design and research history

2.1.1 Early development of modern WECs

Humans started to explore the use of power from waves a long time ago. The earliest WEC can be tracked back to 1799 [11]. However, the modern WEC was firstly developed in the 1960s, when a Japanese former navy officer Yoshio Masuda invented a buoy equipped with an air turbine that uses wave energy as the power supply, see Figure 2.1.

This device was later named an Oscillating water column (OWC). In the 1970s, Masuda developed a floating device named Kaimei [12], which was a barge (80 m by 12 m) equipped with several different OWCs using different air turbines to test the performance of different designs, see Figure 2.2.

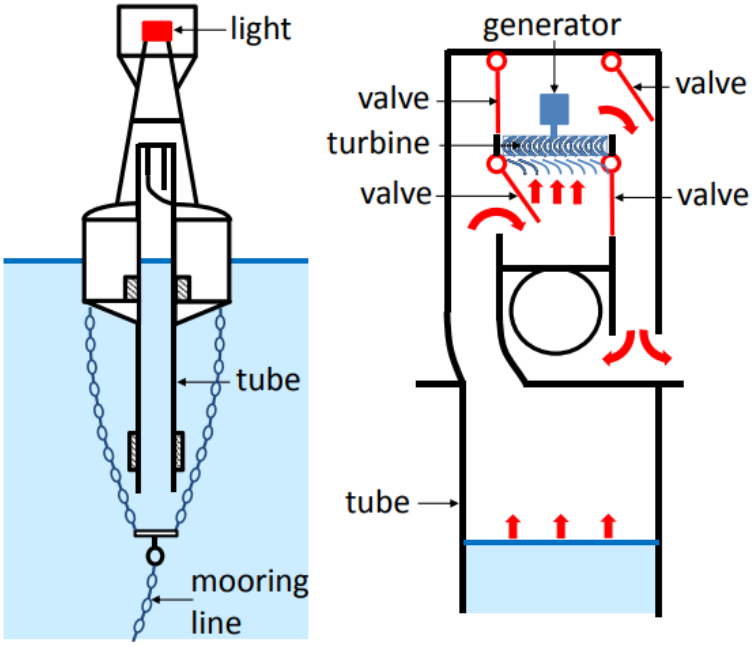

Figure 2.1: The design of a navigation buoy equipped with an air turbine for power supply [13].

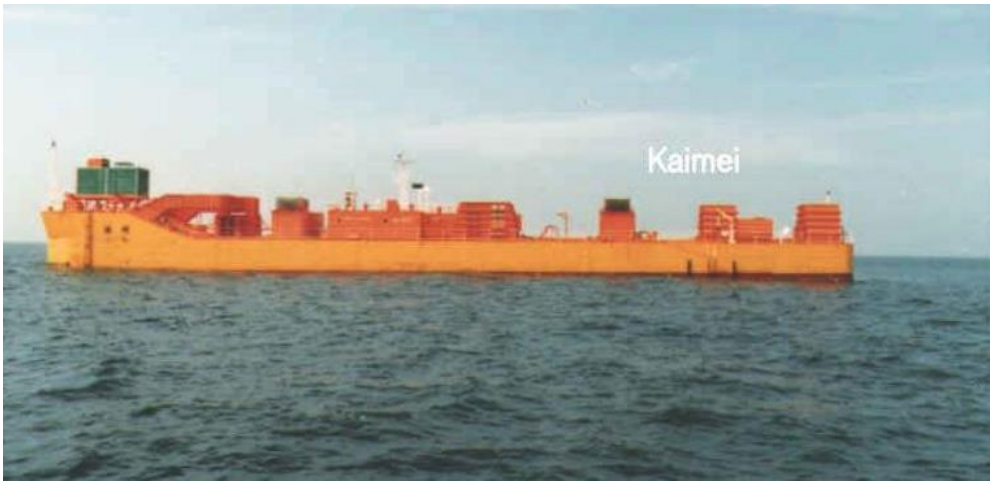

Figure 2.2: A WEC developed by Masuda with multiple OWCs mounted, named Kaimei [12].

Stephen Salter from the University of Edinburgh published his research in the journal *Nature* in 1974 and attracted attention to wave energy conversion from the scientific community [14]. From then on, more than 1000 patented WECs have been designed globally and the number is still growing rapidly ([13], [15], [16]).

2.1.2 Main WEC categories by operating functions

A. Oscillating water column (OWC)

The OWC is a semi-submerged structure with the bottom open below the water surface. It harnesses wave energy from the oscillation of the seawater inside a hollow space due to the movements of waves. It keeps a trapped air pocket above the water column and the movement of the waves forces the water column to act as a piston. The air goes in and out of the chamber through a turbine repeatedly. Due to the continuous movement of

high-velocity airflow, by using an axial-flow self-rectifying turbine [17], it converts the mechanical energy of airflow into electricity. The OWC can be either fixed or floating.

An example is the OWC located in Sakata Port in Japan [18], the design of the power extraction caisson is shown in Figure 2.3. The caisson has an air chamber with an area of 7 m by 20 m. Two self-rectifying turbines were installed to get a one-way airflow for power generation.

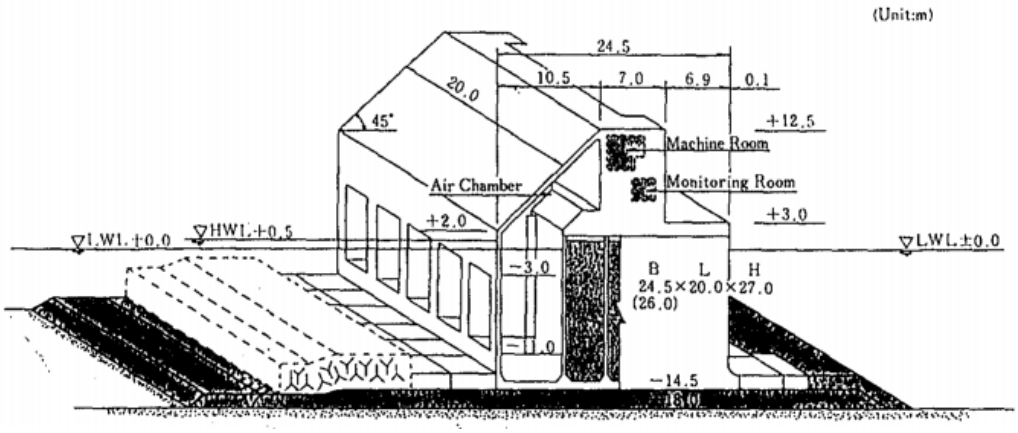

Figure 2.3: The design of wave power extracting caisson of Sakata Port. [18]

Another device is the LIMPET plant located in the UK [19], see Figure 2.4. Different from a typical OWC with a vertical water column, it features an inclined water column. The model testing results have shown a significant advantage in power output efficiency for this design [19]. It is because the inclination of the water column increases the water plane area for a given chamber cross-section [20].

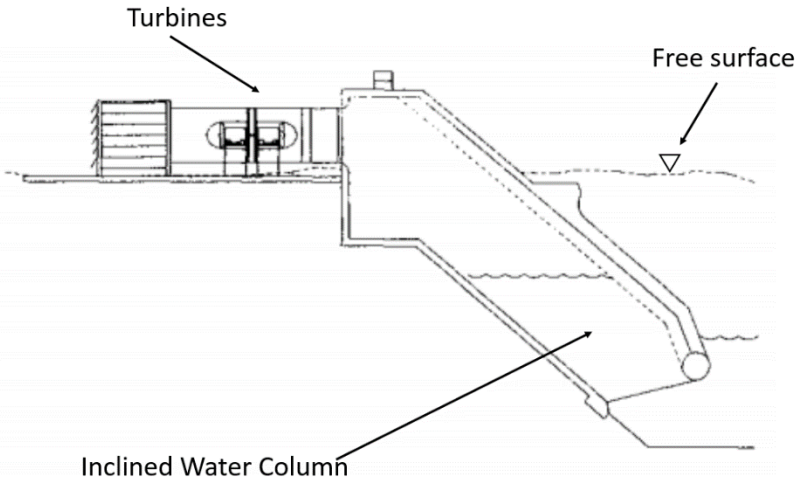

Figure 2.4: The concept design of the LIMPET OWC device. [19]

Another design is the shoreline OWC plant in Portugal [21], see Figure 2.5. It was built on a rocky bottom with 8 m water depth and spans along a natural harbour in the Azores. It was equipped with a horizontal axis power generator just like the LIMPET OWC.

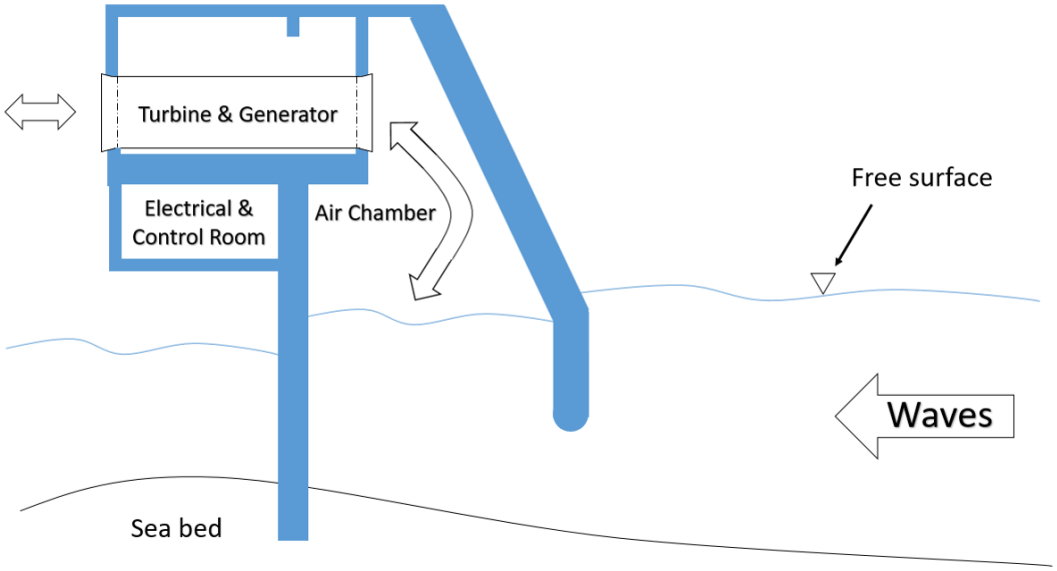

Figure 2.5: The longitudinal section of the shoreline OWC in the Azores, redrawn from [21]

Another example is a floating OWC device, which is the 1:40 spar buoy built and tested in UoP [22], see Figure 2.6 below. The model was tested with two types of mooring systems, a traditional catenary mooring system and a hybrid mooring system consisting of clump weights and floats. The increased heave motion of the OWC using the hybrid mooring system led to a power output performance enhancement compared to the catenary mooring design [22].

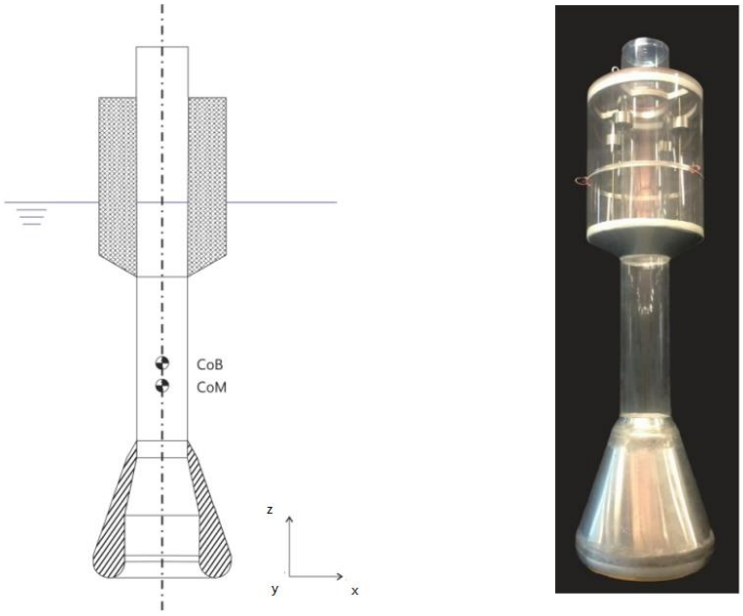

Figure 2.6: Side view of the spar buoy geometry (left) and the 1:40 physical model built for tank testing (right) [22].

B. Oscillating surge wave energy converter (OSWEC)

The oscillating surge wave energy converters harness wave energy by using a buoyant flap hinged on the sea bed or relative to a floating reference frame. The movement of the flap activates a set of hydraulic rams mounted on the sea bed and pumps high-pressure fluid to shore through a pipe. The hydraulic fluid can be either seawater (Oyster [23]) or oil (WaveRoller [24]). This kind of WEC is usually deployed in shallow water due to the increased cost of building large flaps for deep water.

The Oyster system has a buoyant flap, which is 18 m wide by 10 m high and hinged to a sub-structure that is fixed to the sea bed by anchors [23], see Figure 2.7 below. There are two hydraulic rams installed between the flap and the sub-structure that transfers seawater

through a pipeline to the beach. The seawater drives a power generator through a Pelton wheel turbine to generate electricity.

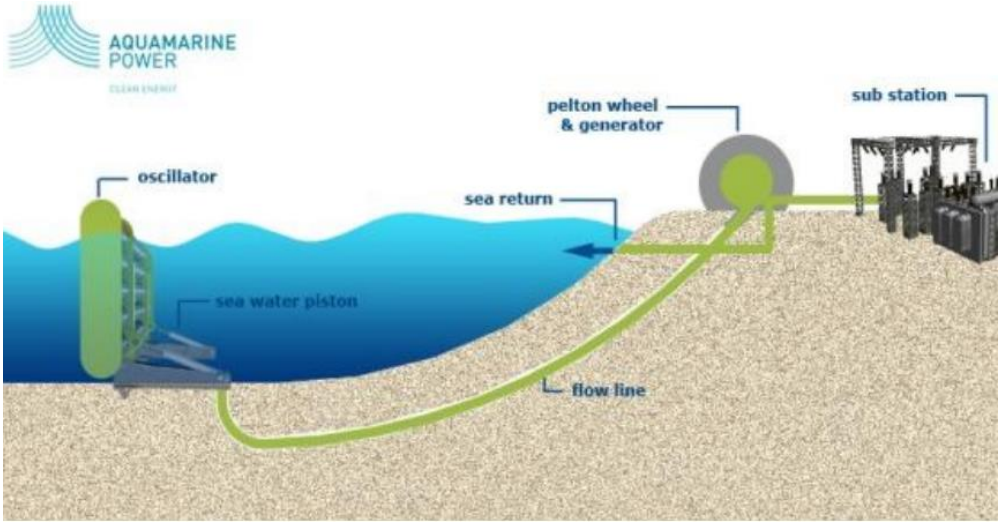

Figure 2.7: The general arrangement of the Oyster WEC system [23].

C. Point absorber

The point absorber is a kind of WEC with working components much smaller than the incident wavelength and can harness wave energy from any direction due to the symmetric design of the device. The working component produces energy by reacting against the sea bottom or a fixed structure or another working component. The relative movement between the working component and the other component can generate electricity via a power take-off (PTO) system. According to the statistics, point absorbers are the most popular types of WECs and take up about 50% of all WEC designs [4].

The first example is Powerbuoy [25], see Figure 2.8. This point absorber consists of a float and a spar. There is relative motion between the spar and the plate due to the interaction with waves. In order to increase the relative heave movement, the movement of the spar is suppressed by a heave plate which is mounted at the lower end of the spar. The relative movement between two bodies drives a PTO system that converts the relative linear movement of the float and the spar into rotational action and drives a power generator to produce electricity.

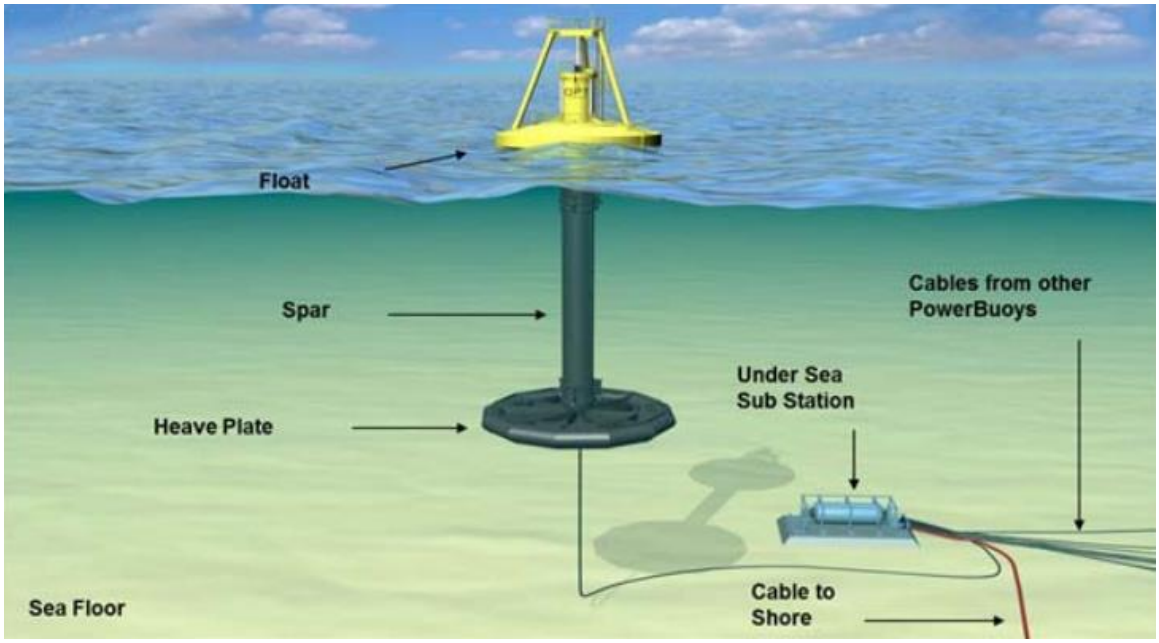

Figure 2.8: The Powerbuoy point absorber [25].

Another design is the Wavestar [26], see Figure 2.9. It is a multiple point absorber system. Each of the point absorbers is a float driven by waves. There is a beam connected to the float and the heave motion of the float is transferred to a hydraulic axial piston via the beam with the other end of the beam hinged on the main body of the device. The hydraulic piston works as a pump and drives a power generator to generate electricity. One advantage of this system is the increased power output smoothness compared to the single

point absorber system. It is because with multiple point absorbers working at the same time, even if the power output is low for some of the floats due to small responses, others can still compensate for the power gap.

Figure 2.9: The Wavestar point absorber system [26].

D. Overtopping device

Overtopping devices collect and store water into a reservoir that is held at a higher altitude than the free water surface. The stored potential energy in the water can be converted into electricity by traditional power generators such as low-head turbines.

A typical overtopping device is Tapchan from Norway [27], see Figure 2.10. The design is simple without any moving components except the turbines. It consists of a collector, a reservoir, an energy converter, and a power plant. The collector concentrates the water

and leads the water to the reservoir. The water in the reservoir then comes through the energy converter, in which the potential energy is transformed into mechanical power by a water turbine. The turbine drives the power generator mounted in the power plant nearby to produce electricity.

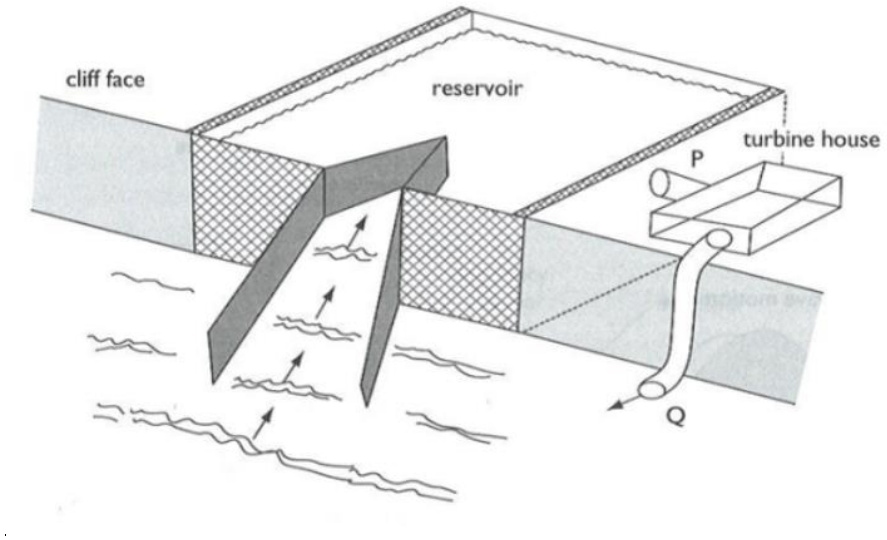

Figure 2.10: Tapchan overtopping device [28].

Another example is the Wave Dragon from Denmark [29], which is shown in Figure 2.11. The main structure of the device consists of a ramp and a water reservoir. There are two reflectors leading the waves towards the ramp. It has been verified that the ramp can increase the power efficiency by 70% [29]. Multiple propeller turbines are used to convert the potential energy of water into electricity.

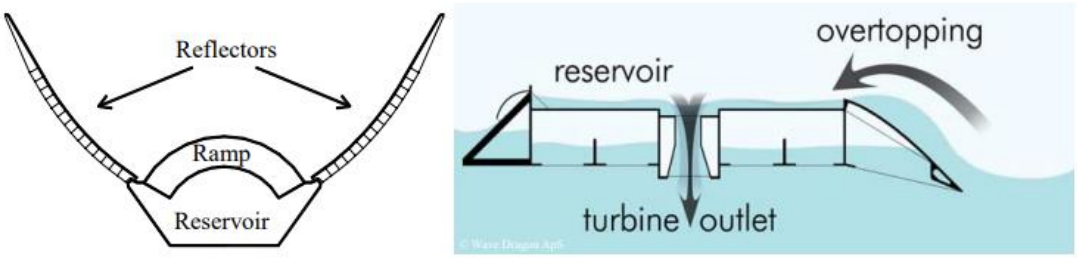

Figure 2.11: Wave Dragon overtopping device [29].

E. Attenuator

An attenuator is a floating device with multiple parts connected and floats following the wave direction. This kind of device harnesses energy from the relative movement of the adjacent working components when the wave passes them. The wave-induced motion of the working components is resisted by a PTO to produce electricity. A typical device is Pelamis [30], see Figure 2.12 below. It features a series of cylindrical floating bodies and hydraulic PTOs hinged together. It was designed and tested at model scale and full scale respectively. It was the first WEC that was connected to the UK power grid in 2004. There were two designs of Pelamis, which were the first generation machine P1 and the second generation P2. Three P1 machines were tested in a WEC farm off the coast of Portugal in 2009 and two P2 machines were tested in Orkney, UK, between 2010 and 2014.

Figure 2.12: The 1:7 scaled model of Pelamis during the open water testing (left) and the model in the wave tank (right) [30].

In 1996, a three-body full-scale attenuator named the McCabe Wave Pump (MWP) was tested in Ireland. It consists of three floating bodies, which are a central body, and two floating pontoons hinged on both sides [17]. A plate structure was connected beneath the central body to decrease the heave movement of the central body and to increase the relative pitch motion of the floating pontoons relative to the central body. Both of the floating pontoons were connected to the central body with a hydraulic PTO, see Figure 2.13 below:

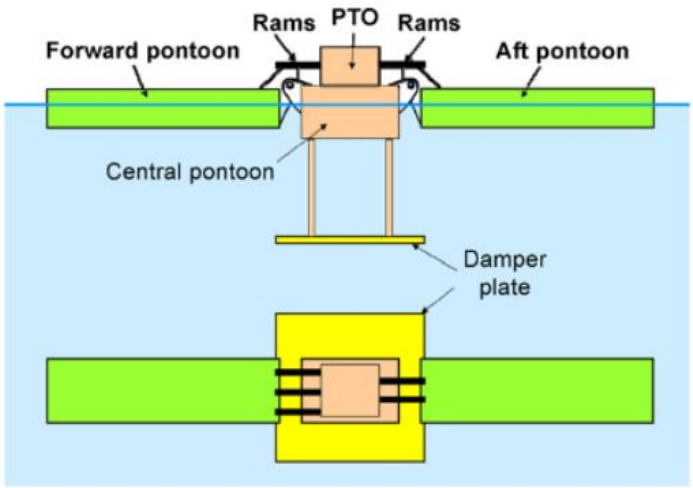

Figure 2.13: The McCabe wave pump [17].

Another device is the Mocean WEC which was designed and tested in the UK, it features a two-body hinged raft structure with a rotational PTO [31]. The main difference between Mocean WEC and traditional hinged-raft is that the two bodies are very different in size and configurations, see Figure 2.14. The larger body's water plane area and smaller body's submerged volume can be adjusted to change the hydrostatic restoring force and the added mass respectively, in order to get a balance in the water and maximize the response of the device and the power generation efficiency.

Figure 2.14: The Mocean device [31].

In 2016, A two-body hinged raft named the Sea Power WEC was designed and a model with scaling parameter 1:4 was tested in Ireland [32]. It consists of three floats, a central larger float, and two smaller symmetrical floats on both sides. The central float is connected to a smaller one to make body 1 and the other smaller float is body 2. Both bodies are hinged together. The relative movement of two bodies is transformed into

electricity via a PTO system. Two types of PTO systems, which are a rotational PTO and a translational PTO were tested and compared. The design is shown in Figure 2.15 below:

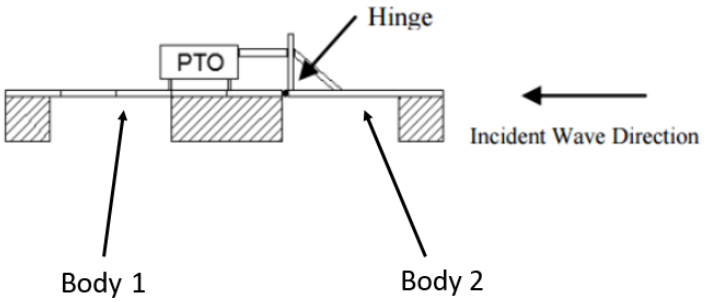

Figure 2.15: Design of Sea Power WEC. [32]

Another device, the M4 WEC was designed in the UK and a 1:8 model has been tested [33]. It has three cylindrical floats. These 3 floats make 2 floating bodies, which is similar to the Sea Power WEC. However, for M4, the 3 floats all have different sizes, which are small, medium, and large. The small float and medium float (central float) make body 1 and the large float makes body 2. The hinge point of the two bodies is located above the central float. Rather than using a rotational PTO, the rotational movement of bodies was transformed into translational movement and a hydraulic translational PTO was used to generate electricity. The design of M4 is shown in Figure 2.16 below:

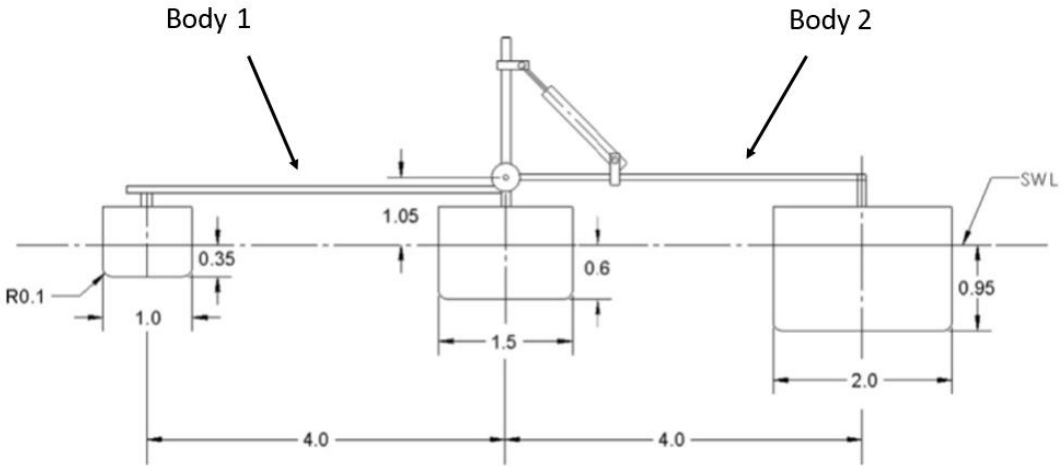

Figure 2.16: The M4 device [33].

Another device DEXA was designed and several 1:60 models were tested simultaneously to simulate a WEC farm [34]. The DEXA device consists of two floating pontoons that are hinged together. Each floating pontoon consists of two horizontally floating cylinders. It features a special PTO with low-pressure power transmission technology, see Figure 2.17 below:

Figure 2.17: Concept design of DEXA device. [34]

2.1.3 Stages to commercialize a WEC

Technology Readiness Level (TRL) [35] is an approach created by the US Space Agency (NASA) to describe the state of a technology programme. It is accepted to milestone the state of the WEC development due to the high financial and technical risk during the development of WECs. Starting from the TRL concept, many guidelines have been published to guide the wave resource assessment, design, manufacture, and maintenance of WECs [36]. After years of development, a five-staged approach is now recommended as the standard approach for the development of WECs worldwide [37], which is:

(1) Proof of concept: Design validation of the WEC in regular waves with a basic model PTO and design optimization in irregular waves with a scale of 1:25 to 1:100.

(2) Validation and design model: Performance verification in realistic sea states with detailed laboratory tests with a scale of 1:10 to 1:25.

(3) Process model: Open water tests at a relatively benign test site to verify all the systems with a fully operational PTO to evaluate the energy production with a scale of 1:2 to 1:10.

(4) Prototype model: Deploy a full-size prototype device. The grid connection should be taken into account with a scale of 1:1 to 1:2.

(5) Demonstration: Small array trails with 3 to 5 devices in full scale.

It can be found that the tank testing of a WEC plays an important role throughout different TRLs. The research and development (R&D) activity of WECs is a complex and expensive process. Although certain progress can be achieved in theoretical and numerical modelling analysis, model testing in wave basins is still necessary [17]. The high cost of manufacturing and testing the WEC models and prototypes in harsh environments is a big challenge. In the late stages, due to the large size of the WEC in full scale, the testing is usually conducted in open water areas.

2.2 Model testing procedures for WECs

As mentioned in Section 2.1.3, tank testing is very important for WECs in order to minimize the risk and to improve the engineering and scientific knowledge from the initial

verification of the concept to the final full-scale prototype. Assuming the potential deployment site has been decided for the WEC, it is important to test the WEC model with a suitable scaling parameter λ.

2.2.1 Scaling parameter selection for WEC model testing

The scaling factor λ is identified as the ratio between the side length of the full-scale prototype and the model. As explained in Section 2.1.3, in stage 1, a small scale (1:25 to 1:100) model is used [38]. In stage 2, medium scale (1:10 to 1:25) is used [30]. In addition to the TRL stages, other parameters need to be considered to decide the scaling parameter such as the size of the wave basin, the highest and lowest wave frequency generation ability of the wave paddles, and the maximum basin water depth. The cost of building a WEC model should also be taken into consideration. Usually, the cost of building a WEC model increases with the increase of the size of the model.

After the scaling parameter λ is decided, the physical properties of WECs have to be correctly scaled by using the scaling criterion. There are two commonly used scaling criteria for WEC model testing, which are the Froude scaling criterion and the Reynolds scaling criterion. The definition of Froude number *Fr* and Reynolds *Re* numbers are shown in Equations 2.1 and 2.2 below:

$$Fr = \sqrt{\frac{inertia\ force}{gravity\ force}} = \sqrt{\frac{\frac{mV^2}{L}}{mg}} = \frac{V}{\sqrt{gL}} \tag{2.1}$$

and

$$Re = \frac{inertia\ force}{viscosity\ force} = \frac{\frac{\rho V^2}{L}}{\frac{\mu V}{L^2}} = \frac{VL}{\xi} \quad (2.2)$$

in which V is the wave characteristic velocity; g is the gravity acceleration parameter; L is the characteristic length of the model, μ is the dynamic viscosity parameter of the fluid, and ξ is the kinematic viscosity parameter. It can be seen from the equations that both *Re* and *Fr* are dimensionless parameters. The Froude number is the ratio between inertia force and gravity force while the Reynolds number is the ratio between inertia force and viscosity force. Froude scaling is used in the situation where gravity forces are dominant and the effect of remaining forces such as kinematic viscous force is small. Reynolds scaling is used when viscous and inertial forces are dominant and remaining forces such as gravity forces are small. Froude scaling is when the Froude number is conserved between model and prototype, and the same for Reynolds. Froude scaling and Reynolds scaling are shown in Table 2.1 below.

Table 2.1: Comparison of scaling factors for Froude and Reynolds scaling criteria [39]

Parameter	Dimension	Froude	Reynolds
Geometric similarity			
Length	$[L]$	λ	λ
Area	$[L^2]$	λ^2	λ^2
Volume	$[L^3]$	λ^3	λ^3
Rotation	[-]	1	1
Kinematic similarity			
Time	$[T]$	$\lambda^{1/2}$	λ^2
Velocity	$[LT^{-1}]$	$\lambda^{1/2}$	λ^{-1}
Acceleration	$[LT^{-2}]$	1	λ^{-3}
Discharge	$[L^3T^{-1}]$	$\lambda^{5/2}$	λ
Dynamic similarity			
Mass	$[M]$	λ^3	λ^3
Force	$[MLT^{-2}]$	λ^3	1
Pressure and stress	$[ML^{-1}T^{-2}]]$	λ	λ^{-2}
Energy and work	$[ML^2T^{-2}]$	λ^4	λ
Power	$[ML^2T^{-3}]$	$\lambda^{7/2}$	λ^{-1}

From Equations 2.1 and 2.2 it can be seen that both the two scaling criteria cannot be satisfied at the same time. For example, for a WEC model with a scaling factor of 25, according to the Froude scaling law, the velocity of the model should be 1/5 of that of the full-scale prototype. While by using the Reynolds scaling law, if the scaled model and full-scale prototype are tested in the same fluid, the velocity of the WEC model should be 25 times the velocity of the full-scale prototype, and it is impossible to satisfy both at the same time.

For WECs model testing, since most of the interactions between the model and waves are gravity dominated and the influence from viscosity force is considered small (with a high Reynolds number in the turbulent regime), Froude scaling is usually chosen as the scaling criterion.

2.2.2 Model testing in regular waves

Regular (single frequency) wave testing plays an important role in the early stage of WEC development. It can be used to provide a direct indication of how the WEC works in simple wave conditions. There are three main purposes of regular wave model testing, which are described below:

A. Theoretical and numerical model performance verification

Numerical analysis plays an important role in the development of WECs. In order to achieve a reliable numerical model, calibration and validation using the physical testing results are important. It is necessary to test the physical model in a series of regular waves with different wave heights *H* and wave periods *T* to obtain the response amplitudes in a certain degree of freedom (DoF). For a floating rigid object, based on the linear wave theory when the viscous force is neglected, the following Equation 2.3 [40] is satisfied:

$$[M + A(\omega)]\ddot{x} + B(\omega)\dot{x} + Cx = F(\omega) \tag{2.3}$$

in which *x* is the displacement in a certain DoF; $\dot{x}$ is the velocity; $\ddot{x}$ is the acceleration; *M* is the mass of the floating body; ω is the angular frequency of wave; $A(\omega)$ is the added mass; $B(\omega)$ is the linear damping term; *C* is the restoring force coefficient and $F(\omega)$ is the excitation force. For a linear wave, the input wave can be expressed as:

$$\zeta = \zeta_a e^{i\omega t} \tag{2.4}$$

in which ζ_a is the regular wave amplitude; *i* is the imaginary unit; *t* is time; ζ is the input wave elevation signal. The response of the floating body in a certain DoF *x* in Equation 2.3 can be solved as:

$$x = a e^{i\omega t} \tag{2.5}$$

in which a is the amplitude of the response in *x*. The response amplitude operator (RAO) can be expressed as:

$$\mathrm{RAO}(\omega) = \frac{a}{\zeta_a} = \frac{F_0}{C-\left(M+A(\omega)\right)\omega^2+iB(\omega)\omega} \quad (2.6)$$

in which F_0 is the amplitude of the wave excitation force.

By testing a series of regular waves on the physical model, the RAO in a certain DoF can be obtained [41], which can be used to calibrate the numerical WEC model. Additionally, the responses of the regular wave testing can also help better understand the power output performance of the WECs in different sea states [42]. Usually, the power Capture Width Ratio (CWR) is used to estimate the power generation efficiency, see Equation 2.7 below:

$$CWR = \frac{P_{WEC}}{P_{Wave*D}} \quad (2.7)$$

in which P_{WEC} is the average power output from the WEC [W]; P_{wave} is the incoming wave power per unit length [W/m]; *D* is the width of the WEC [m]. The equation for the wave power of a regular wave in infinite water depth is shown in Equation 2.8 [40]:

$$P_{wave} = \frac{\rho g^2 H^2 T}{32} \quad (2.8)$$

in which *H* is the wave height; *T* is the wave period; the unit of P_{wave} is W/m.

B. Non-linear effect study

According to the linear wave theory [40], the propagation of waves on the water surface above a horizontal bottom is shown in Equation 2.9 below:

$$\eta(x,t) = \zeta_a cos(k_w x - \omega t) \tag{2.9}$$

where ζ_a is wave amplitude; k_w is wave number; ω is the angular frequency. However, if the wave height of the regular wave is increased to a certain value, the wave cannot be considered regular anymore and Equation 2.9 cannot be used. The non-linear effect can be studied through the RAO by testing the WEC model in regular waves [43]. Usually, a fully linear WEC model has a frequency-dependent RAO which is not affected by the wave amplitude ζ_a. However, for a non-linear WEC model, the RAO is not only frequency-dependent but is also dependent on the wave amplitude.

2.2.3 Model testing in irregular waves

After the fundamental studies of WECs in regular waves, it is necessary to test the model in more complex wave conditions. Based on linear wave theory, irregular waves can be obtained as the sum of a large number of regular wave components. Similar to Equation 2.9, the wave elevation signal of an irregular wave is shown in Equation 2.10 below [40]:

$$\eta(x,t) = \sum_{j=1}^{N} \zeta_{aj} cos(k_{wj} x - \omega_j t + \epsilon_j) \tag{2.10}$$

in which ζ_{aj}, k_{wj}, ω_j and ϵ_j mean respectively the wave amplitude, wave number, angular frequency, and random phase angle evenly ranging from 0 to 2π of wave component j. The wave amplitude ζ_{aj} can be expressed as Equation 2.11:

$$\frac{1}{2}{\zeta_{aj}}^2 = S(f_j)df \tag{2.11}$$

in which

$$\frac{1}{f_j} = T_j = \frac{2\pi}{\omega_j} \tag{2.12}$$

where T_j and f_j are the wave period and wave frequency of wave component j, $S(f)$ is the non-directional wave spectrum. It can be noticed that the irregular wave shown in Equation 2.10 is irrelevant to the wave direction, which is named the long-crested wave. $S(f)$ is used as the wave spectrum for long-crested waves. However, for the wave that is influenced by wave directions (shorted-crested waves), the directional wave spectrum $S(f,\theta)$ is used, θ is wave direction. The relationship between $S(f)$ and $S(f,\theta)$ is shown in Equation 2.13 below [44]:

$$S(f,\theta) = S(f) * D(f,\theta) \tag{2.13}$$

in which $D(f,\theta)$ is the directional spreading function (DSF), and it satisfies:

$$\int D(f,\theta) = 1 \tag{2.14}$$

Two kinds of wave spectrum can be used at this stage for WEC model testing. The first is the generic/parametric wave spectrum obtained from the mathematical wave model. The second is the site-specific complex wave spectrum, which is directly obtained from the sea state measuring devices, which will be shown in Section 2.3.

A. Model testing in generic/parametric irregular waves

There are 3 kinds of commonly used generic/parametric single peak spectrum for WEC model testing, which are:

1. The Pierson-Moskowitz (PM) spectrum

The PM spectrum [45] is the simplest wave spectrum that is used for a fully developed sea state. It is an empirical equation based on the assumption that the input wind is in equilibrium with the waves, see Equation 2.15:

$$S(f) = \frac{{H_{m0}}^2}{4}(1.057f_p)^4 f^{-5} exp[-\frac{5}{4}\left(\frac{f_p}{f}\right)^4] \tag{2.15}$$

in which f is wave frequency. H_{m0} is significant wave height. f_p is the peak wave frequency.

2. The Bretschneider wave spectrum

The Bretschneider spectrum[46] is an expansion of the PM spectrum due to the fact that the prerequisite to using the PM spectrum (in a fully developed sea condition) is usually hard to satisfy because the wave is always developing. The Bretschneider spectrum is used to describe sea states that are not fully developed and the equation is shown below:

$$S(f) = \frac{5}{16}\frac{H_{m0}^2}{f}\left(\frac{f_p}{f}\right)^4 exp\left[-\frac{5}{4}\left(\frac{f_p}{f}\right)^4\right] \quad (2.16)$$

3. The Joint North Sea Wave Observation Project (JONSWAP) wave spectrum

Hasselmann discovered that the wave spectrum is never fully developed [47]. Therefore a peak enhancement factor Γ is introduced to the PM spectrum to correct it, see Equations 2.17 to 2.19 [48]:

$$S(f) = [1 - 0.287ln(\Gamma)]S_{PM}\Gamma^{\alpha} \quad (2.17)$$

and

$$\alpha = exp[-(\frac{\frac{f}{f_p}-1}{\sqrt{2}\sigma})^2] \quad (2.18)$$

in which

$$\sigma = \begin{cases} 0.07 \; f \leq f_p \\ 0.09 \; f > f_p \end{cases} \tag{2.19}$$

S_{PM} is the PM spectrum from Equation 2.15; f_p is the peak frequency. The peak enhancement factor Γ is used to increase the peak of the PM spectrum, which is usually regarded to have an upper limit of about 7 [49]. A commonly used approximation of Γ is 3.3 [50].

Among the three wave spectra mentioned above, the JONSWAP spectrum can be used to represent the PM and the Bretschneider spectrum. Therefore, it is the most widely used wave spectrum. The peak of the JONSWAP spectrum is more pronounced compared to the PM spectrum except from Γ = 1, when Equation 2.17 is equal to Equation 2.15.

When the final deployment site for the WEC has not been decided or the WEC is under consideration for several different potential deployment sites, the usage of a generic/parametric wave spectrum is preferred, which can provide a suitable approximation and representation of possible sea states (standard from EMEC [51]).

B. Model testing in site-specific complex irregular waves

It is suggested that in the latter part of TRL stage 1 and certainly by stage 2, the site-specific spectrum should be used to evaluate the performance and seaworthiness of the

WECs [52]. At this stage, the design of the WEC should have been finalized and the deployment site should also have been decided. It is necessary to test the WEC model in the site-specific complex wave conditions since the waves can be quite different from the waves created using the generic/parametric wave spectrum.

Usually, there are thousands of hourly sea states measured from a certain ocean area annually. It is important to find a method to obtain a small number of suitable sea states for model testing among a large number of measured wave spectra.

Traditionally, each hourly sea state is transformed into H_s and T_e bi-variate data points. All of the H_s - T_e points are plotted into H_s - T_e space. A table with multiple bins is created based on the range of H_s and T_e. The bins with sea states inside are selected as the preferred bins, from which the average H_s and T_e of the bin can be used as the input of the parametric wave spectra in Section 2.2.3. These parametric spectra are then used for WEC model testing. A typical example is shown in Figure 2.18.

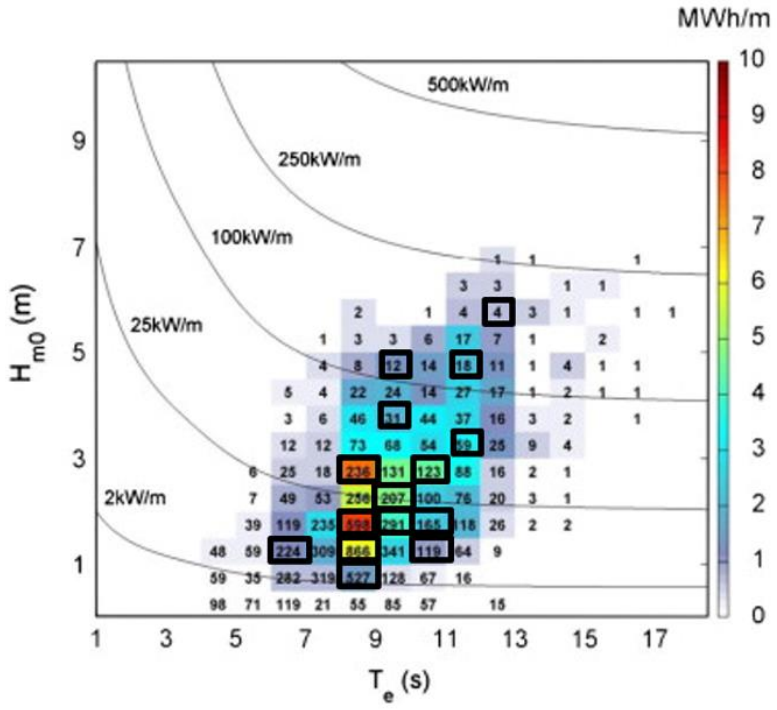

Figure 2.18: Traditional binning method of annual average scatter diagram of the wave resources at the site considered for a breakwater OWC. All of the 15 bins selected are circled in black.[53]

In addition to the traditional binning method that only considers wave height and wave period, other methods based on spectrum similarity have been used. Hamilton used the Clustering LARge Applications (CLARA) statistical sampling algorithm (*K*-means clustering technique) on the site-specific complex non-directional wave spectra taken from a buoy on the northwest shelf of Australia ([54],[55]). Hamilton found that the statistical algorithm can effectively and automatically create a number of *K* wave spectra groups. This approach needs no prior curve-fitting or parametrization of the wave spectra and no wave information was lost during the regrouping process. These kinds of sea states are named site-specific complex representative sea states. Hamilton showed that wave spectra from clustering presented site characterization well, which can be used for WEC testing both physically and numerically [55]. However, Hamilton didn't quantify the difference between the regrouping results from the traditional binning methods and the

novel *K*-means clustering method. Based on his work, Draycott extended the algorithm and created and compared different binning and clustering methods by obtaining the representative sea states from different methods on the buoy measured directional wave spectra from European Marine Energy Centre (EMEC) ([56],[57]). In his work, the algorithm was not only applied for the non-directional/directional wave spectra directly as Hamilton did but also for several wave parameters derived from the wave spectra. Draycott tested eight regrouping methods in his early research and used a metric that calculates the average difference between the group mean and each group member to evaluate the regrouping quality. He found the regrouping methods based on the non-directional/directional wave spectrum *K*-means clustering method showed a clear advantage over other methods [56]. In his later work [58], he used a different metric that includes the relative difference between each group's mean value and found that no regrouping method showed a clear advantage over others. Draycott found that the regrouping quality was influenced by the number of groups (*K*) created and a large number of sea states with low energy were grouped into a single group. He also discovered that the significant wave height and energy period of the representative sea states of the groups from the *K*-means clustering method distributed un-evenly in *H* - *T* space.

2.2.4 Time duration and number of cases for model testing

The total time duration of a WEC model testing in the laboratory is usually a few days, which means it is important to decide the time duration for each wave case carefully. For regular waves, it's enough to run 50 to 100 full wave periods, while for irregular non-directional waves, the industrial standard length of a wave condition is usually 20 min to

30 min at full scale [51]. According to Froude scaling law in Section 2.2.1, the time length for model testing in model scale $T_{model-scale}$ and full scale $T_{full-scale}$ satisfies the following Equation 2.20:

$$T_{full-scale} = \sqrt{\lambda} * T_{model-scale} \tag{2.20}$$

in which λ is the scaling parameter.

The number of total cases for model testing achievable is related not only to the time duration for each wave case but also to the calm-down period between two adjacent wave cases.

The number of test cases for regular waves can be large due to the fact that the wave period *T* for regular cases is short on the model scale. Even if each case is run with 100 full wave periods, each case can be finished in a couple of minutes and the calm-down period for regular wave testing is usually short. It means the average time spent on each regular wave case is short and many regular wave cases can be tested each day. In order to guarantee a smooth RAO curve and CWR curve for different wave heights and wave periods, the number of regular wave cases can be large.

For testing irregular waves, as explained above, the time duration is much longer than regular waves. As a result, the number of irregular wave cases is much fewer than that of regular wave cases. If the time duration for an irregular wave tested is 12 min (1-hour

time duration for full scale with scaling factor 1:25). Assuming the calm down period between each case is 10 min, there are only about 3 irregular wave tests that can be finished in each hour, which means about 20 cases per day.

2.3 Wave measuring instruments

As stated in Section 2.1.3, from stage 2 of TRL, site-specific complex wave conditions need to be determined for the model testing. There exist several instruments that can be used to measure the sea states from a specific wave environment, which are introduced below:

A. Surface buoy

Surface buoys have been used for the measurement of wave conditions at a fixed location for many years ([59], [60]). There exist mainly two types of buoys for wave measurement. The first type is the pitch-roll-heave surface following buoy. This kind of buoy measures the slope and vertical elevation of the wave surface ([61], [62]). They are usually discus-shaped in order to easily follow water surface movements. A typical design of a pitch-roll-heave buoy is shown in Figure 2.19. The second type is the particle following buoys [63]. This kind of buoy follows the orbits of water particles at the water surface. The particle following buoys work by measuring the surge, sway and heave acceleration signals of the buoy. After obtaining the heave-roll-pitch or tri-axis acceleration signals, numerous numerical algorithms can be used to obtain the directional wave spectra, including the Maximum Likelihood Method (MLM) [64], Maximum Entropy Principle

(MEP) [65], Iterative MLM, Eigen-vector MLM, Direct Fourier Transform method [66], etc.

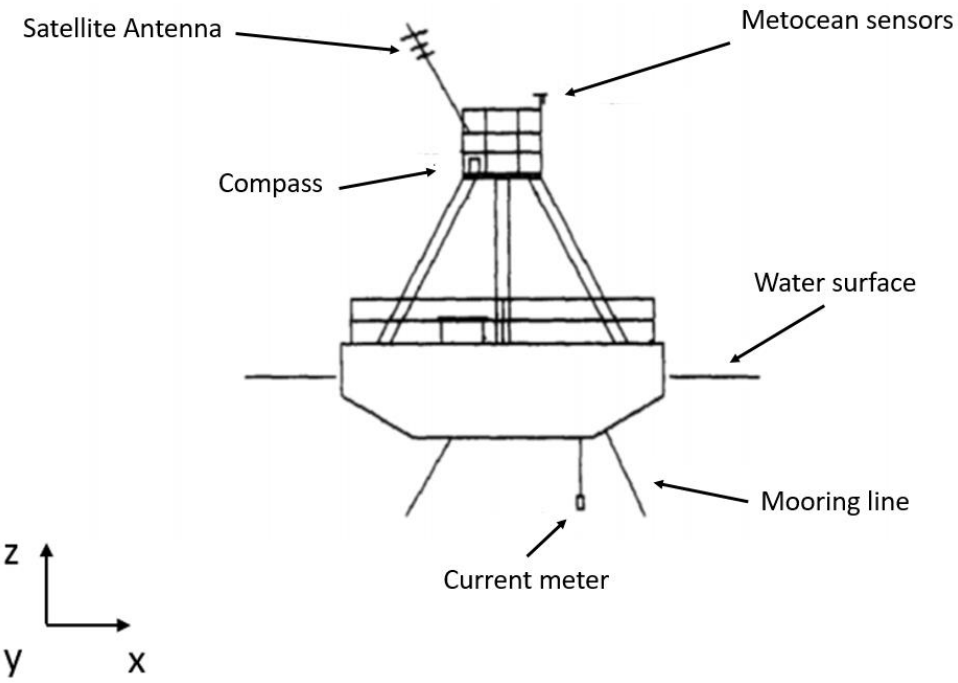

Figure 2.19: The U.K. roll-pitch-heave buoy DB2 with a diameter of 6 m and a draft of 1.25 m. It is moored in the English Channel with 3-point catenary moorings. Redrawn from [61]

Wave buoys need to be moored to remain at a certain location to be free to oscillate in the waves. When the water is deep or the current velocity is too high, it needs a sub-surface float system to help the buoy hold position. During the measurement, the data can be either stored in the buoy by using an internal hard drive waiting to be recovered manually or transmitted on shore in real-time. The transmitted signal can be either time history measurements or processed spectral data. Surface buoys are suitable for wave measurement at only one fixed location.

B. Acoustic Doppler Current Profiler (ADCP)

The ADCP is a hydroacoustic current meter to measure the water current speed and direction through the water column. It works by transmitting pulses of acoustic waves along multiple beams towards the water surface. There are mainly two types of designs, the ‘Janus’ and the ‘3+1’, see Figure 2.20 below:

Figure 2.20: Standard ‘Janus’ ADCP (left) and vertical beam ‘3+1’ ADCP [67].

There are two types of ADCPs shown in Figure 2.20. The ‘Janus’ type is the most used design for ADCP [68].

When measuring the water current velocity, the sonar of each beam transmits the acoustic signals, and the acoustic energy in the inclined beams is scattered by particles in the water (e.g. plankton or sediment particles). Some of the return signals are received by the device. The travelling time of sound waves gives an estimation of the travelling distance from the

Doppler effect and the sonar measures the instantaneous current velocity component projected along each beam [68]. Since the averaged current velocity is horizontally uniform over the beams, the current velocity and direction can be obtained by a linear combination of the measured along-beam acoustic velocities.

The measurement of waves using ADCP is more complicated than the measurement of water current because the wave velocities vary spatially across the beams at any time. When analysing the return acoustic signals of four beams, a range-gating technology has to be used on each of the beams, which allows the calculation of the wave velocities along each beam. The range-gating algorithm can determine the velocity's vertical variation by dividing the water column into multiple horizontal layers [69]. Each layer has four beams passing through it and each of them results in a time series of velocity that can be used in the inversion algorithm to obtain the wave properties such as the wave direction [70]. There are several methods that can be used such as a truncated Fourier series expansion method [71], MLM, and MEP. The ADCP has been used for wave measurement since the 1980s ([72], [73], [74]).

The ADCP is usually sea bed deployed and recovered every couple of months or uses data telemetry via a floating buoy. Data can be transmitted to an onshore station or a satellite. The disadvantage of an ADCP is that it usually cannot measure current and waves simultaneously. When the water depth increases, due to the low signal-to-noise ratio, the high-frequency energy can be overestimated [69].

C. X-band radar

X-band radar is a remote sensing instrument that measures the wave field from a long distance away. The wave field is measured from X-band marine radar with working frequency ranging from 8 to 12 GHz with a wavelength of 3.75 cm to 25 cm. The use of X-band radar for measuring directional wave spectra is quite recent [75]. In working conditions, it scans the water surface at grazing incidence angle (the angle between the transmitted wave and the water surface is close to zero degrees) by transmitting microwaves and recording the reflections. Due to the reflection of the electromagnetic waves from the sea surface elevations caused by the wind ([76], [77], [78]), it produces a backscattered electromagnetic field and a resulting image pattern in the radar display monitor, see Figure 2.21. This image is commonly known as sea clutter and considered as undesirable for navigation purposes and usually suppressed by some filtering algorithms [79]. However, by using the temporal sequences of consecutive sea clutter images, the spatial and temporal variability of the sea surface can be analysed by some inversion algorithms (e.g. MLM, MEP) to extract an estimation of the directional wave spectrum ([80], [75]).

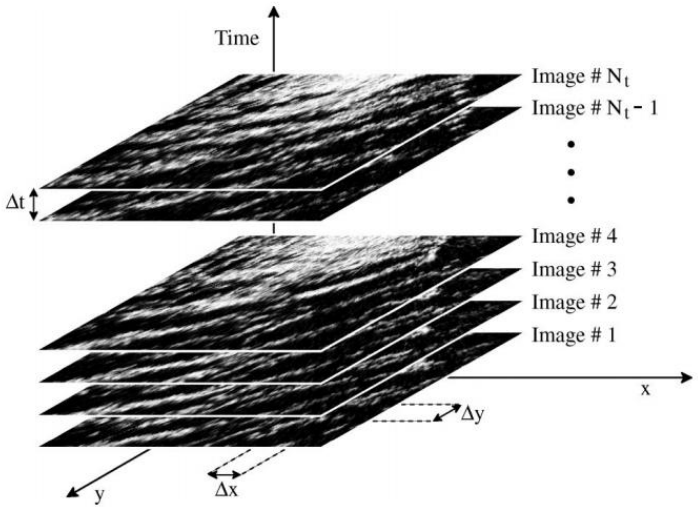

Figure 2.21: The temporal sequences of sea cluster images, the greyscale corresponds to the radar backscatter strength. Δt is the temporal resolution decided by the antenna rotation period, and Δx and Δy are the spatial resolutions in x and y respectively [79].

Since the sea clutter values are decided by the electromagnetic backscatter signals of the sea surface other than the wave elevation itself, the directional wave spectrum derived from the X band radar analysis is hard to be correctly scaled and therefore the wave height of the sea surface cannot be directly obtained. To obtain the correct wave height, several methods are introduced. The most commonly used method is by assuming that the significant wave height of the sea is linearly dependent on the square root of the signal-to-noise ratio (SNR), in which the energy of the signal is the total energy of the wave energy derived by the sea clutter analysis and the noise is computed as the energy due to the speckle (the white dots in the sea clutter images) caused by the sea surface roughness [81]. Alternatively, the wave height can be corrected by deploying a buoy within the analysis area of the X-band radar that provides the significant wave height accurately.

X-band radar can monitor the sea surface for several square kilometres and output a high-quality directional wave spectrum [75]. However, as explained above, X-band radar cannot provide correctly scaled directional spectra [81]. Additionally, the detection range

of X-band radar is much smaller than that of HF radar, which is because the X-band waves can be more easily interrupted by fog and other objects compared with HF radar waves.

D. HF radar

1. Surface current measurement by using HF radar

High-frequency radar is a shore-based radar system, which can measure both the wave and current data of an ocean area. The wavelength of high-frequency waves ranges from 10 to 100 m, which is close to the water wavelength. Due to the high detection range (up to hundreds of kilometres), HF radar can be a supplement between satellite and X-band radar measuring instruments [9].

The working principle of HF radar is based on the transmission of consistent vertically polarized electromagnetic waves, which will be scattered by the water surface current. The scattered high-frequency waves can go in any direction and the waves travelling back are named backscattered waves and can be received by the radar [82]. By analysing the backscattered wave spectra (Doppler spectrum) by using Discrete Fourier Transform (DFT), two nearly symmetric dominant peaks from the spectrum can be found. Crombie was the first to notice this effect and deduced it is due to the scattering of the electromagnetic waves off the water surface current [83]. The two peaks represent two different travelling directions moving towards the radar and away from the radar respectively. This phenomenon is called Bragg scatter [84]. An example is shown in Figure 2.22 [85].

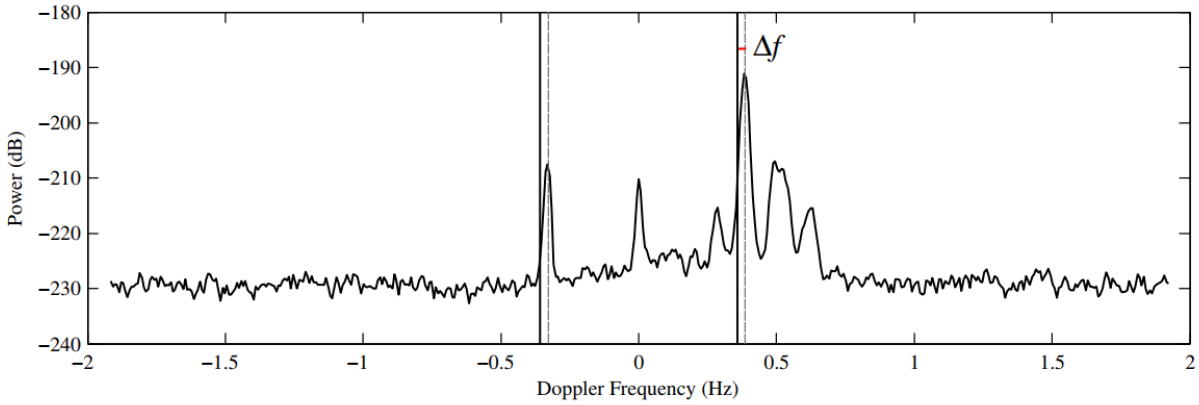

Figure 2.22: Doppler spectrum measured by an HF radar transmitting at 12 MHz. The vertical black lines are the theoretical values of the negative and positive Bragg wave frequencies. Δf is the frequency shift (Doppler frequency) generated by the water surface current [85].

Crombie also noticed that those two frequency peaks are symmetrical around the carrier frequency (radar frequency) of the electromagnetic wave and the positions of the peaks change with the group velocity of the moving Bragg waves [86]. The frequency shift of the two peaks and the transmitted frequency is called the Doppler frequency. The Doppler frequency is determined from the phase velocity of the scattering water waves and the surface current [87]. Because the phase velocity of the water waves can be derived by the dispersion relationship, the surface current velocity can be obtained. It constitutes the foundation for surface current measurement. Nowadays HF radar is widely used for the surface current measurements ([88], [89], [90]).

2. Non-directional wave spectrum measurement by HF radar

By analysing the remaining part of the Doppler spectrum (second-order part) with certain wave inversion algorithms [91], the non-directional wave spectrum can be obtained.

However, compared with the first-order Bragg wave signal, the second-order signal is relatively weak and can be buried in noise. The second-order Bragg wave is generated from the nonlinear wave interactions and can be very difficult to interpret, which means measuring the non-directional wave spectrum is more difficult than measuring surface current. Much research on the inversion algorithm has been published ([92], [93], [94]).

3. Directional wave spectrum measurement by using multiple HF radar system

Using only one HF radar station to measure an ocean area is not possible to obtain directional wave information due to the lack of directional wave information [95].

After years of development, it has been discovered that by using inversion algorithms (e.g. MLM, MEP [96]) on the power spectrum of the backscattered radar signal from multiple HF radars, the directional wave spectrum of the ocean area can be obtained ([97], [98]). The directional wave spectrum is calculated on a grid defined by the intersection of multiple radar beams. The spatial resolution is between 1 km to 5 km and the working radius ranges from hundreds of kilometres to tens of kilometres depending on the radar operating frequency and radar geometry [9]. It can provide nearly real-time sea states.

Wellen Radar (WERA) was developed specifically for wave measurements and was mainly used in pairs to obtain directional information. Compared to traditional HF radar, which only focuses on current measurement, WERA consists of a high number of receive antennas and allows for high resolution of wave spectra measurement from second-order spectral bands. The large array also guarantees a greater range and a higher spatial

resolution than the traditional HF radar systems [99]. Gurgel developed an empirical method (WERA algorithm), which assumes a linear relationship between the ratio of second- to first-order Doppler energy and the wave spectrum weighted by a directional spreading function [96]. This algorithm was validated by real field experiments by using two WERA HF radars in Fedje and Lyngoy, Norway respectively covering the same ocean area with an operating frequency of 27.65 MHz and 40 km by 40 km covering range [96]. The obtained directional wave spectra were compared with the record from a directional wave buoy. It was found that there was a good agreement between the radar and buoy results.

Toro [100] analysed the data obtained from the Gulf of Tehuantepec, Mexico by using a modified WERA algorithm. It included a wind speed-dependent relation between the Doppler spectra and wave frequencies to scale the Doppler spectra [9]. After analysis, linear correlations of 73% and 0.39 m Root Mean Square Error (RMSE) of the radar and buoy measured data were found.

Lopez [9] analysed a two WERA covered area off the coast of Cornwall, the UK in 2011. A modified WERA algorithm was used by introducing calibration from in situ measurements [9]. The radar-obtained directional wave spectra were compared with three in situ devices (2 ADCPs and a buoy). It was found that the modified method increased the quality of the results significantly. The significant wave height obtained had nearly zero bias with a linear correlation higher than 90% and RMSE ranged between 0.29 m (buoy) to 0.44 m (ADCP). Additionally, the relative error of the energy period was within 10%.

Although the HF radar has been proven valid for measuring directional wave spectra, the utilization of HF radar for wave spectrum measurement is still under scrutiny. Quality control has to be applied for certain operational applications and some of the quality control is only available in a post-processing mode and is not part of operational real-time products [100]. Sometimes the measured directional wave spectrum has a low SNR and cannot be used.

E. Satellite

Many satellites have been launched to monitor the sea environments [101]. There are mainly two types of measuring devices mounted on satellites for this purpose. The first is the satellite Radar Altimeter (RA) and the second is the Synthetic Aperture Radar (SAR). The RA is a vertically pointing pulsed radar that can measure the elevation of the ocean surface with a few centimetres' accuracies. The backscatter of the pulse is influenced by the waves and the return signal can be analysed to estimate the wave height. The SAR system provides images with high resolution by analysing the phase and amplitude of the return signal. SAR can be used to measure the directional waves as well. Due to the high orbit position, the global grid resolution of the RA and SAR is low, which is about 7 km to 10 km [101].

In addition to the Geosynchronous Earth Orbit Satellite (GEOS), most SAR satellites rotate around the earth and cannot overlook a certain ocean area consistently. It means it is not possible to provide the temporal sequences of consecutive images like the X-band radar does. The SAR image needs an inverse algorithm to calculate the correct directional

wave spectrum. Several numerical tools have been developed to solve the problem ([102], [103], [104]). However, the accuracy of the significant wave height obtained from the SAR directional wave spectrum is still not as high as the result measured from the RA. RA has reached the accuracy of floating buoys while SAR turns out to be far from the actual wave spectrum [101]. The advantages and disadvantages of each measuring instrument are listed in Table 2.2 below:

Table 2.2: Comparison of different instruments

Type	Scope of application	Pros and Cons	Description
Surface buoys	Fixed location	Advantages	High accuracy. (nearly zero bias in H_s)
		Disadvantages	Needs a sub-float system (mooring) in deep water and can only measure at a fixed point
ADCP	Fixed location	Advantages	Can measure both the surface current and wave spectrum with high accuracy. (nearly zero bias in H_s)
		Disadvantages	Limited to shallow water without extra support.
X-band radar	Several kilometres	Advantages	High accuracy if correctly scaled using a buoy.
		Disadvantages	The microwave can be easily interrupted by fog and other objectives with a short detection range.
HF radar	Hundreds of kilometres	Advantages	Can measure both the surface current and wave spectrum at the same time with a medium detection range and accuracy. (nearly zero bias in H_s and 10% in T_e)
		Disadvantages	Needs multiple radars covering the same ocean area for directional waves.
Satellite	Thousands of kilometres	Advantages	Very large detection range. High accuracy in $H_s$using RA. (nearly zero bias in H_s)
		Disadvantages	Low global grid resolution. (7 to 10 km)

2.4 Numerical analysis software of WECs.

In addition to physical model testing of WECs in wave basins, numerical analysis also plays an important role in their development. Numerical simulation can provide significant insights and data that are either expensive or difficult to measure or test experimentally [105]. Compared to physical model testing in wave basins, numerical models are relatively less expensive and can be easily modified. It provides a third option

of the science of equal importance with theoretical and experimental sciences. Thanks to the fast development of computers since the 1960s, numerous numerical analysis tools have been developed.

One type of software that has been used widely is based on Computational Fluid Dynamics (CFD, which solves the Navier-Stokes (N-S) equations. However, the solution of the N-S equation can be extremely difficult and computationally expensive [105]. There are mainly four types of turbulence models. The first one is the Direct Numerical Simulation (DNS), which is the most accurate method but highly computationally expensive. The second model is the Large Eddy Simulation (LES) method [106], which is capable of capturing the dynamics of the large eddies and is relatively computationally economical. The third model is the Reynolds Averaged Navier Stokes (RANS) method [106], which is of modest computational cost and widely used for solving engineering problems, however, it is not possible to simulate 3D turbulence or flow details. The fourth model is the Detached Eddy Simulation (DES) method [107], which is to utilize the RANS method in the boundary layer close to the wall and LES outside the boundary layer. It is impossible to capture flow details in the near-wall region. Many commercial CFD software (Fluent, Autodesk CFD, SimScale) were developed in the past decades. However, the licence fee of these software ranges from 10,000 to 50,000 USD annually, which is beyond the budget of this study.

OpenFOAM is an open-source CFD software that is widely used in wave-structure interaction and other applications. OpenFOAM was developed by Imperial College, London, and was acquired by OpenCFD Ltd [105]. It is the first and the most widely used open-source CFD software (39% of the total [108]), it provides more than seventy N-S

equation standard solvers that were tailored to specific physical problems such as combustion, compressible flow, electromagnetics, heat transfer, incompressible flow, multiple phase flow, etc [105]. OpenFOAM has been widely used for the analysis of different kinds of WECs, such as overtopping devices [109], point absorbers [110], OWCs [111], and OSWECs [112], etc. However, this Ph.D. research requires the power output performance of WECs in thousands of sea states. It was not possible to support the high computational cost of OpenFOAM with the resources available for this study, thus OpenFOAM was excluded.

Another type of numerical analysis software is using Boundary Element Method (BEM), which is based on linear potential theory, assuming linear waves with low steepness, while also assuming small motion amplitude of the motions of the floating WEC bodies [113]. This method takes into consideration of wave diffraction, wave radiation, and inertia loads. However, it cannot account for the viscous effect [40].

Firstly, the hydrodynamic coefficients need to be solved in a BEM code such as NEMOH, WAMIT, AQWA, or OrcaWave. The results are used to solve the time-domain behaviour of the model in given wave conditions. Compared to the CFD method, the BEM method is less computationally demanding.

Several commercial software has been developed (e.g. OrcaFlex, WaveFarmer). Taking OrcaFlex for example, various kinds of WECs such as the point absorber [114], the attenuator [115], and the OWC [116] were analysed with high accuracy. The open-source

BEM software WEC-SIM is selected for use in this research because of its availability and suitability to the application considered.

2.4.1 WEC-SIM

In this thesis, an open-source BEM software WEC-SIM is used. The flow chart below shows the workflow of WEC-SIM, see Figure 2.23 below:

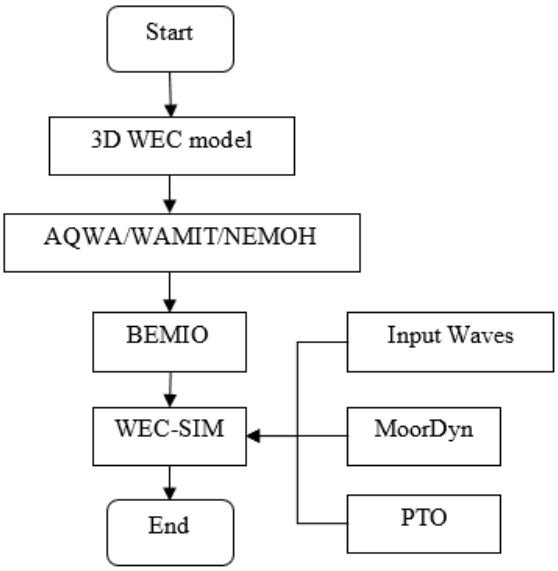

Figure 2.23: Workflow chart for WEC-SIM.

WEC-SIM is developed by National Renewable Energy Laboratory (NREL) and Sandia National Laboratories (SNL) [117]. It simulates the interaction between incoming waves and WECs [118]. It is a time-domain analysis software. The motion equation in a certain DoF x is shown in Equation 2.21 below:

$$(M + A)\ddot{x} + B\dot{x} + Cx = F_e(t) + F_{PTO}(t) + F_{moor}(t) + F_{rad}(t) \quad (2.21)$$

in which *M* is the mass matrix of the WEC. *A* is the added mass term; *B* is the damping term; *C* is the restoring term; F_e is the excitation force due to the incoming waves; F_{PTO} is the PTO force; F_{moor} is the mooring force; and F_{rad} is the radiation term. F_{rad} is the convolution integral that represents the resistive force on the body due to wave radiation [119], which is shown in Equation 2.22:

$$F_{rad}(t) = -\int_{-\infty}^{t} f_r\,(t-\tau)\dot{x}(\tau)d\tau \quad (2.22)$$

in which f_r(t) is the radiation impulse function calculated by potential flow models. Additionally, the added mass term *A*, the damping term *B*, and the restoring term *C* are also calculated by hydrodynamic analysis software (e.g. AQWA, NEMOH, WAMIT). All of the hydrodynamic coefficients are written into a .h5 file through a BEMIO module as part of the WEC-SIM input.

The interactions between different WEC bodies, the PTO system, the mooring system, and the boundary conditions are all defined using one single model based on MATLAB Simulink.

Much research has been done using WEC-SIM. It can simulate the responses of WECs of different types, from the point absorbers [120], and the attenuators [121] to the OWCs [122]. It has been used to analyse the responses of WECs with different mooring systems

such as the 3-point catenary mooring [123] and taut mooring system consisting of 4 mooring lines [124]. WEC-SIM is also used to simulate WECs with PTO (Power Take Off) systems, such as rotational hydraulic PTOs [125] and translational PTOs [126]. WEC-SIM can be also used for non-linear analysis of WECs such as non-linear buoyancy and non-linear excitation force[127].

As shown in Figure 2.23, to use WEC-SIM, hydrodynamic coefficients of the WEC need to be obtained first, which can be achieved by using one of the three BEM software, which is introduced in Section 2.4.2.

2.4.2 BEM software used in WEC-SIM

A. AQWA

AQWA is a frequency domain BEM module based on ANSYS. It is used to calculate the hydrodynamic coefficients for floating bodies. The model is based on potential flow theory, therefore assuming:

• Inviscid fluid, incompressible and irrotational flow (potential theory valid).

• Small wave steepness and small motion of the WEC about a mean position.

• Linearized free surface.

To use AQWA for hydrodynamic coefficients calculation of WECs, the 3D geometric model of the WEC has to be built or imported to AQWA first. Numerical software such as AutoCAD and Solidworks can be used to build the 3D models [128]. The outputs from AQWA are the frequency dependant hydrodynamic coefficients which are the added masses, radiation damping, excitation force, and the impulse response function as explained in Section 2.4.1 at each wave frequency component and incoming wave directions.

A lot of research has been done using AQWA. Qi analysed the mooring system coupled with the hull of an FPSO in the Gulf of Mexico and the sea conditions from Africa using AQWA, in which the forces and motions in each mooring line have been accurately simulated [129]. Majid analysed the influence of the non-linear effect of mooring lines on the power output performance of a point absorber. It has been found that the material's non-linearity has a significant impact on the tension and WEC responses [130]. Seyed compared the numerical analysis results of a floating pontoon breakwater with the physical model testing results in different waves, which has shown good consistency [131].

B. WAMIT

WAMIT is a BEM numerical tool for analysing wave interactions with offshore platforms and other structures and vessels. It was firstly established in 1987 at MIT [132]. It is also based on the same assumption as AQWA. WAMIT has been used to analyse complex

structures and has shown a high degree of accuracy and efficiency. However, WAMIT is not open-source.

Eng [134] calculated the added mass of the numerical model of a complex-shaped remotely operated vehicle (ROV) and compared the results with small-scale physical testing results, which showed good agreement [133]. Michael built the numerical model of the Pelamis attenuator using WAMIT and calculated the power output performance in different wave conditions. The results were combined into a power matrix to have an overall estimation of the power output ability [134]. Lee built the numerical model of an LNG tank and analysed the coupled interactions between the ship motion and the inner tank sloshing using WAMIT. The numerical results showed similar trends to the physical model testing results [135].

C. NEMOH

NEMOH is the world's first open-source BEM software based on the same assumption as AQWA. It has been developed by Nantes University (ECN) in the past 30 years [136]. Typical use of NEMOH is dynamic response calculation of floating structures and power output performance assessment of WECs [137].

Verao [139] analysed the impact of hydrodynamic interactions of a WEC on the surrounding wave field using NEMOH, they analysed a single WEC, five and nine WECs arrays respectively in irregular waves and calculated the impact of one WEC on the surrounding wave field [138]. Filippo calculated the RAO of an icebreaker from the

numerical model built by NEMOH and compared the results with the data recorded during the expedition across the Southern Ocean from 2016 to 2017 [139]. It has shown that the numerical results and the data recorded have good agreements.

2.4.3 MoorDyn

As shown in Figure 2.23, MoorDyn is one of the modules that is used to simulate the mooring system of WECs in WEC-SIM. It is an open-source dynamic mooring line simulation software, which can be used independently or in WEC-SIM as a mooring analysis module. It can freely define the axial elasticity, hydrodynamics, and seabed contact properties of the mooring lines [140].

The entire definition of the mooring system in MoorDyn is contained in one input file. It includes the diameter, weight per unit length, Young's modulus of the mooring line, the coordinates of the mooring points on the WEC and at the sea bed at the initial position, the length of the mooring lines, and the number of mooring lines, etc. During the analysis, the position and configuration of the mooring lines are calculated at each time step.

Srinivas built a 1:25 floating WEC connected to a traditional three-point catenary mooring system using Moordyn and compared the body response and tension force in the mooring lines with a commercial code (OrcaFlex), and the results showed a good agreement [123]. West modified MoorDyn to simulate the synthetic mooring ropes that have complex nonlinear tension-strain responses. The results were compared with a 1:52

scale floating offshore wind turbine model testing results, which showed a strong correlation [141].

3. Site-specific representative sea states

This chapter aims to use two data sets, which are the HF radar measured sea states from Wave Hub and buoy measured sea states from Long Island, south of Islip, New York, the USA for analysis to obtain a certain number of *K* representative sea states respectively, which are suitable for WEC model testing. Ten regrouping methods are used to obtain the representative sea states. Two metrics are introduced to assess the regrouping quality from different regrouping methods. The influence of the *K* value on the regrouping quality is also discussed.

Section 3.1 is to introduce the two data sets used in this thesis. Section 3.2 is the introduction of eight regrouping methods to obtain the representative sea states. Section 3.3 is to show the regrouping results of eight methods in H_s - T_e space and their limitations. In Section 3.4, two new regrouping methods are introduced to solve the limitations. Section 3.5 is to introduce two metrics that are used to assess the regrouping quality of different regrouping methods. Section 3.6 and Section 3.7 are the assessment of the regrouping quality using two metrics respectively. Section 3.8 is to discuss the influence of *K* (number of groups) on the regrouping quality. Section 3.9 is the discussion of the results and determines the preferred method to use, in order to obtain the representative sea states to test on WECs in Chapter 4 and Chapter 5.

3.1 HF radar and buoy measured wave spectra data sets

3.1.1. HF radar measured sea states from Wave hub

The Wave Hub testing site shown in Figure 3.1 was an ocean area specifically tailored for WEC testing in the UK. It was located 16 km offshore from Hayle on the north coast of Cornwall at the eastern edge of the Atlantic Ocean with an average water depth of 50m. Wave Hub was founded in September 2010 by the European Regional Development Fund Convergence Programme and the UK Government [142]. It was operated by Wave Hub Ltd and works as a 'socket' for different WECs to be plugged into. A cable from the hub to the mainland transferred electricity from the WECs to the electric grid. The total capacity of the hub was 30MW (upgradable to 48MW). There was a 3 by 1 kilometre rectangular area in the Wave Hub testing site which allowed multiple WECs to be deployed at the same time. In 2021, Wave hub was sold to Hexicon and renamed Celtic Sea Power for offshore wind demonstrations [143].

Two WERA were installed to look over the Wave Hub area in 2011. They aimed to measure the directional wave spectra from Wave Hub [144]. The two HF radars were adjusted to cover the same ocean area to obtain the directional information of waves. The first radar was located in Pendeen and the second radar was located in Perranporth at a 40 km distance apart as shown in Figure 3.1. Each radar consisted of a 16-element phased-array receiver and a rectangular 4-element transmitter located parallel to the coastline. The boresight of the station in Pendeen was 23° clockwise from true North and the boresight of the station in Perranporth was 305° clockwise from true North.

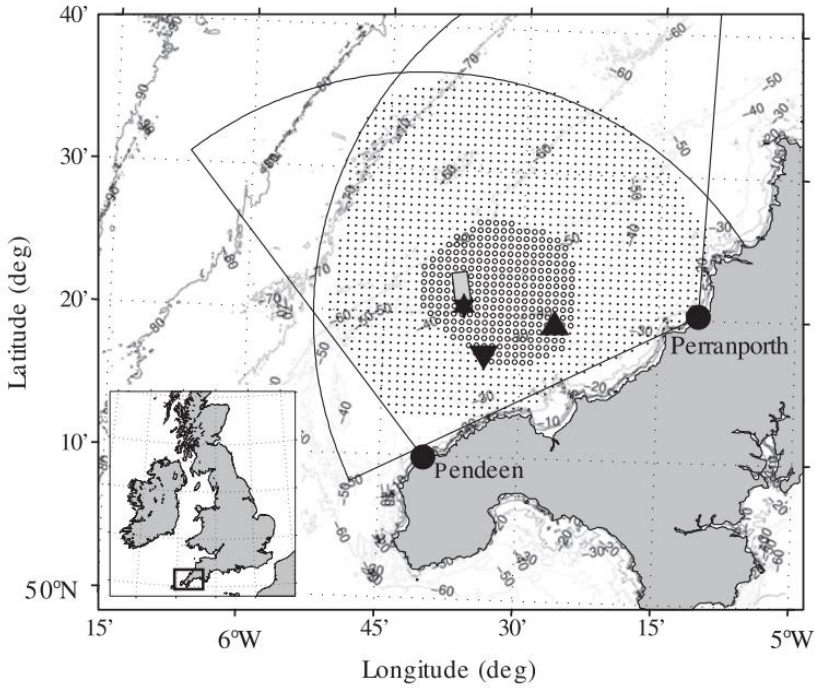

Figure 3.1: Two radar stations and their coverage area on Wave Hub [9], the black spots represent the HF radar stations and the fans represent the radar detection range, and the rectangle represents the area of Wave Hub. Only the surface current measurement is achievable over the full range of the radar footage (black dots area) due to the high SNR of the second-order return signal. The radius of wave spectrum measurement is only half of that of the current measurement (small black circle area).

With the help of the HF radar system, thousands of hourly wave spectra have been obtained annually by using a modified WERA algorithm [9] as introduced in Section 2.3. In this thesis, 3161 hourly directional wave spectra measured from April 2nd, 2012 to December 4th, 2012 from Wave Hub were used as the first data set. The reason why there were only 3161 usable hourly wave spectra in the year 2012 (8760 hours in total in one year) was because the measured wave data with low signal-to-noise ratio were considered low quality and have been removed from the data set.

Each measured hourly sea state was represented by an individual directional wave spectrum. The unit of the power spectrum density was $m^2/Hz/rad$. There were 30

angular directions ranging from 0 to $29\pi/15$ with an interval of $\pi/15$ and 92 frequency components with a minimum of 0.0342 Hz and a maximum of 0.2815 Hz. An example hourly directional wave spectrum measured by an HF radar system from Wave Hub is shown in Figure 3.2. 0° wave direction corresponds to true North and 90° corresponds to true East.

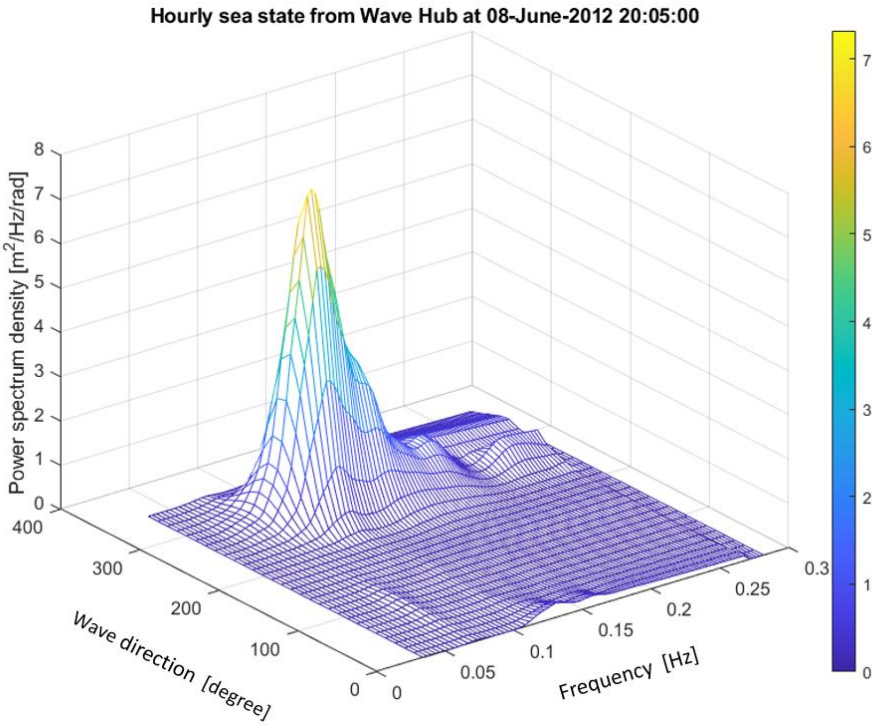

Figure 3.2: A typical example of an hourly directional wave spectrum measured by HF radar from Wave Hub at 20:05:00, June 08th, 2012. H_s = 2.78 m; T_e = 7.60 s; MDIR = 271.54°.

With the directional wave spectrum $S(f,\theta)$ obtained, the non-directional wave spectrum can be calculated from Equation 3.1:

$$S(f) = \int_0^{2\pi} S(f,\theta)\, d\theta \qquad (3.1)$$

in which f is the frequency component and θ is the wave direction. The k - th order spectral moment can be calculated by Equation 3.2:

$$m_k = \int_0^\infty f^k S(f) df \tag{3.2}$$

With the k - th order spectral moment obtained, wave parameters such as significant wave height H_{m0} and wave energy period T_e can be obtained. The significant wave height is calculated by Equation 3.3:

$$H_{m0} = 4\sqrt{m_0} \tag{3.3}$$

After calculation, H_{m0} of all the 3161 hourly HF radar measured sea states ranged from 0.43 m to 6.70 m. As introduced in Section 2.3, the significant wave height obtained from HF radar had nearly zero bias with linear correlations higher than 90% and RMSE ranged between 0.29 m to 0.44 m compared to the buoy and ADCP results. The relative error of the energy period was within 10% [9].

It can be noticed that H_{m0} below 0.43 m was not included in the total data set, it was because the sea states in the middle of the Atlantic never achieve zero wave height. Based on the buoy data taken from the Wave Hub (unpublished data measured by the University of Plymouth), during three years of measurement, the minimum wave height was 0.22 m and wave height between 0.22 m and 0.45 m took up only 1.3% of the time. Additionally,

the accuracy of the HF radar sea states was validated by the comparison with buoy and ADCP data taken from the same ocean area [85].

The energy period was calculated from Equation 3.4, which is:

$$T_e = \frac{m_{-1}}{m_o} \tag{3.4}$$

After calculation, T_e ranged from 4.93 s to 14.12 s in this data set.

The mean wave direction is calculated by Equation 3.5, which is:

$$\theta_m = \int_0^{2\pi} D(f,\theta)\theta d\theta \tag{3.5}$$

in which $D(f,\theta)$ is the DSF of the hourly directional wave spectrum, θ is the wave direction. After calculation, θ_m ranged from 59.5° to 283.8°.

The wave rose of HF radar sea states is shown in Figure 3.3 below. The wave direction is expressed as the direction from which the waves are propagating.

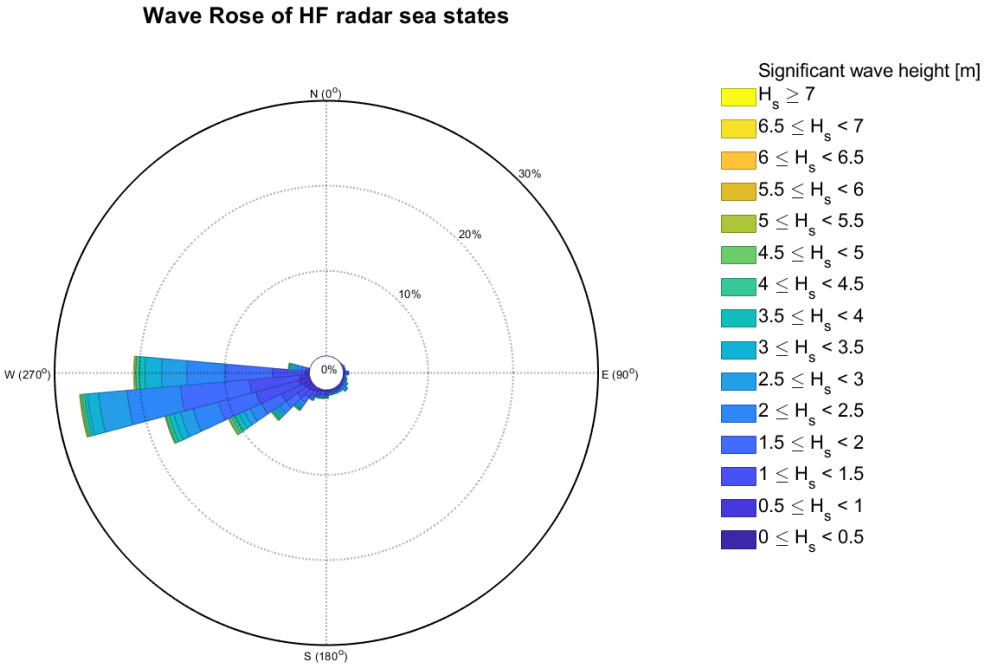

Figure 3.3: The Wave rose of HF radar sea states from Wave Hub [142].

It can be noticed that most of the incoming waves came from the range between 245° to 275°. It means the HF radar measured sea states from Wave Hub present low directionality.

3.1.2. Buoy measured sea states from Long Island

The buoy-measured sea states were used as a comparison group (2^{nd} data set) with the HF radar measured sea states to see if the results are device & location independent. They were collected from a roll-pitch-heave buoy No. 44025, which was deployed close to Long Island with an average water depth of 36.3 m, South of Islip, New York, the U.S. It was owned and maintained by National Data Buoy Centre (NDBC) [145], see Figure 3.4 below. The hourly sea states were recorded and shared with the public for free.

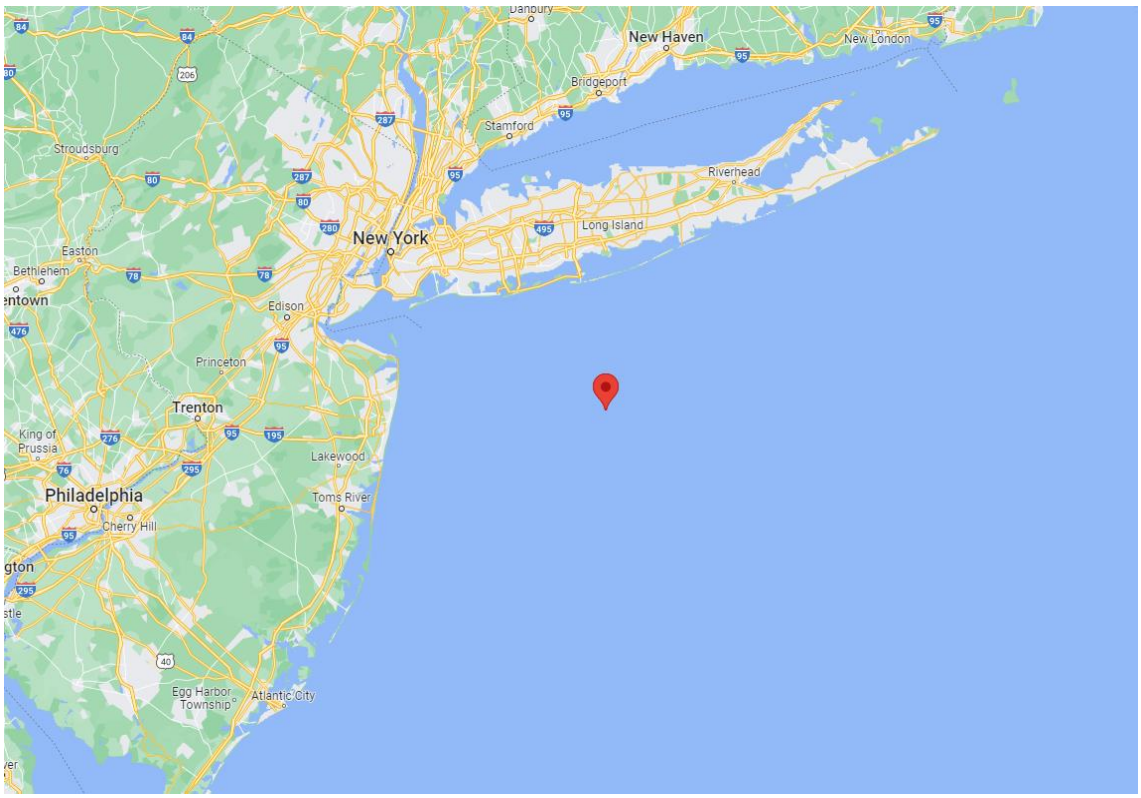

Figure 3.4: Long Island buoy No. 44025 deployed off the coast of New York, U.S. with coordinate 40˚15'3" N 73˚9'52" W.

There were historical wave data available from the year 1996 to 2017 for this buoy. However, after examination, only the data in 2008 and afterward can be used because the data earlier lacked directional information. The number of sea states available for each year is shown in Table 3.1 with the erroneous hourly data excluded. The number of useful sea states in different years varies. Each of the sea states is given in the form of a non-directional wave spectrum. In total there were 74,896 hourly non-directional wave spectra obtained for the analysis.

Table 3.1: Each year's number of useful sea states from 2008 to 2017.

Year	2008	2009	2010	2011	2012
Number of sea states	8298	7904	8714	6300	8756
Year	2013	2014	2015	2016	2017
Number of sea states	7036	2543	8205	8738	8402

According to the wave theory introduced in Section 2.2.3 [40], the non-directional wave spectrum can be transformed into a directional wave spectrum using Equation 3.6:

$$S(f,\theta) = S(f) \cdot D(f,\theta) \tag{3.6}$$

For this data set, the DSF can be calculated from Equation 3.7:

$$D(f,\theta) = \frac{\frac{1}{2}+\frac{2}{3}r_1\cos(\theta-\alpha_1)+\frac{1}{6}r_2\cos[2(\theta-\alpha_2)]}{180} \tag{3.7}$$

The parameters $\alpha_1, \alpha_2, r_1, r_2$ are Longuet-Higgins Fourier coefficients [59], which were provided on the NDBC website together with each hourly non-directional wave spectrum $S(f)$. All of these four parameters were frequency dependent.

Wave direction θ can be chosen with any step interval. In order to be consistent with the HF radar directional wave spectrum, $\pi/15$ was chosen as the directional interval. Then there were 30 angular directions, which was the same as HF radar data. After calculation, there were in total 74,896 directional wave spectra obtained. However, the total data set

of buoy data was very large and the computation time can be unacceptable. As a result, for the calculation from Section 3.2 to Section 3.7, only the year 2017 was used, which had 8402 sea states.

In the Long Island data set of 2017, H_s ranged from 0.16 m to 6.05 m; T_e ranged from 3.55 s to 13.08 s, and θ_m ranged from 106.1° to 243.2°. The wave rose plot is shown in Figure 3.5 below:

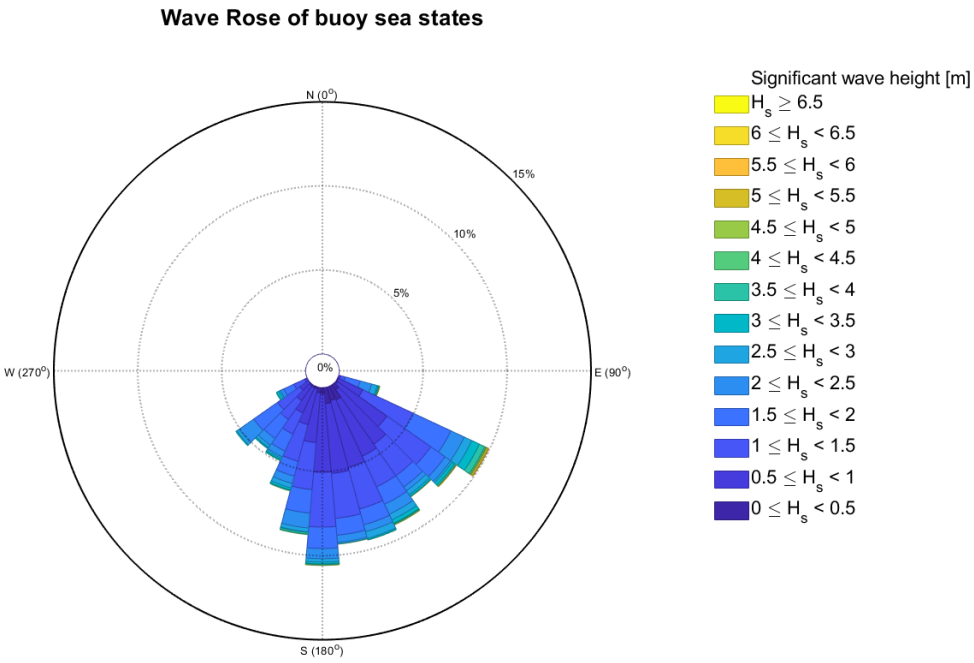

Figure 3.5: The wave rose of buoy sea states from Long Island 2017.

It can be seen that compared to the HF radar wave rose in Figure 3.3, the directionality of the Long Island data is much higher. The incoming wave mostly ranges from 115° to 195°, which is much wider than HF radar sea states. However, the buoy data set is still not fully directional (360°).

3.2 Methods to select site-specific complex representative sea states for WEC model testing.

From Section 3.1, there were thousands of site-specific complex wave spectra taken from the ocean area for each data set. However, for a WEC model testing, it was unrealistic to test all of the sea states due to the limit of the resources. As a result, how to use a large number of hourly sea states to obtain a few sea states suitable for WEC model tank testing was important. In this section, two types of regrouping methods will be explained. The first type is based on the widely used *H* - *T* bivariate scatter plot binning method ([146], [147]) and the second type is based on a novel *K*-means clustering method ([54], [57]). Based on them, in total eight regrouping methods are introduced.

3.2.1 Binning method and *K*-means clustering method

A. *H* - *T* bivariate binning method

The *H* - *T* bivariate binning method has been commonly used to determine the desired irregular wave cases for site-specific sea states for WEC model testing. It uses an H_s - T_e or H_s - T_p two-dimensional scatter diagram with bins plotted. By defining the size of the bins in *H* and T dimension respectively, a number of bins can be found. The widely used size of bins is 1 m by 1 s and 0.5 m by 0.5 s ([146], [147], [148], [149]). An example is shown in Figure 2.18. For convenience, the example scatter diagram has already been

transformed into the number of sea state points marked in each bin rather than data points. It can be seen the size of each bin is 0.5 m by 0.5 s.

Once the sea states are binned, site-specific sea states from a certain bin can be obtained by averaging the sea states inside the same bin. Usually, the sea state used to 'represent' a bin is calculated by averaging the directional or non-directional wave spectra in the same bin. Sometimes there are no wave spectra available from an ocean area but simplified wave parameters such as H_s and T_e (or T_p). Then the method to obtain the site-specific sea states is even simpler by averaging H_s and T_e (or T_p) of the data points in each bin respectively and using the average values as the input values for the generic/parametric wave spectrum (e.g. JONSWAP) shown in Section 2.2.3. In this thesis, the HF radar and the buoy-measured sea states are all in the form of directional wave spectra. Thus, the representative sea state in each bin is the average of all the sea state members' directional wave spectra in the same bin.

The binning method only uses two one-dimensional wave parameters to represent each hourly sea state, which means most of the detail of the sea states is neglected. Additionally, the size of bins is determined subjectively. Another problem with the binning method is that for the *H* - *T* bivariate scatter diagram, the binning method usually creates a large number of bins. Due to the limit for WEC tank testing resources, only a small portion of the bins are selected and tested, which means that most of the sea states measured are wasted.

To solve the problem, the size of bins is changed from the commonly used small bins (e.g. 1 m×1 s) to large bins to guarantee that the total number of non-empty bins is equal to the number of the sea states that will be tested on a WEC model. An example is shown in Figure 3.6, which creates 24 large-size bins (6 by 4) aiming to obtain 20 non-empty bins and corresponding 20 representative sea states by averaging all of the members inside the same bin. However, as shown in Figure 3.6, it introduces another problem that the total number of non-empty bins is different from the number of site-specific sea states desired to test. In Figure 3.6, there are 24 large bins created but only 19 of them are not empty, which results in only 19 sea states.

In this thesis, all of the sea states obtained from the binning method are obtained from large bins to guarantee that each hourly sea state is located in a certain bin without anyone left outside.

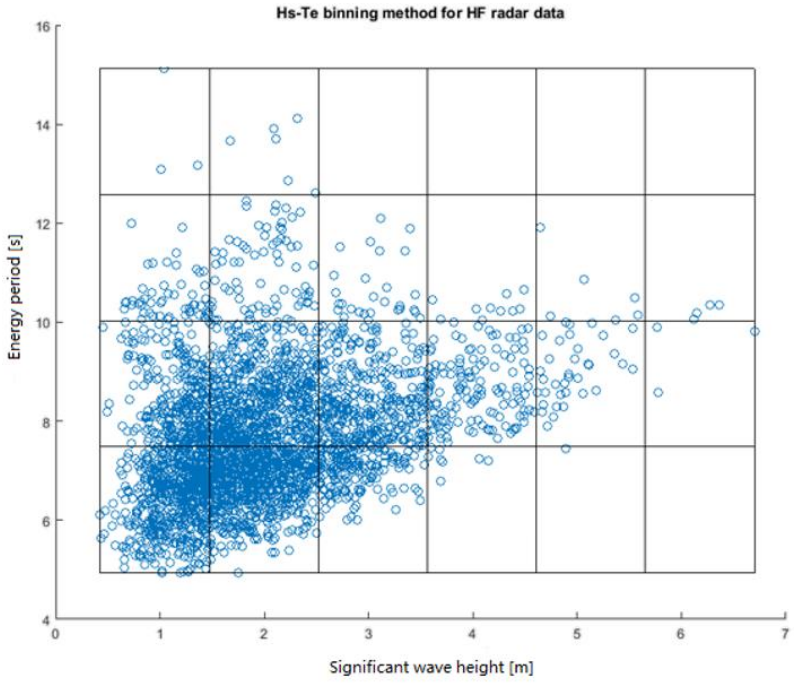

Figure 3.6: H_s - T_e binning method for 3161 HF radar hourly sea states and 24 large bins created, each blue circle represents an hourly sea state. There are in total 19 non-empty bins obtained.

B. *K*-means clustering method

Clustering is a method to group a large number of data members into a number of sub-groups and make sure that data members with similar characteristics are grouped together. The members are organized into an efficient representation that characterizes the group being sampled ([150], [151], [152], [153]).

Given a total data set S, the clustering method is defined as obtaining a set of *K* sub-groups $C = C_1, \dots, C_k$ of S to satisfy that: $S = \cup_{i=1}^{K} C_i$ and $C_i \cap C_j = 0$ for i ≠ j. It means any member in S belongs to exactly one and only one subset [154]. From the definition of the clustering method, we can find that the traditional binning method shown in Figure

2.18 is not a clustering method while the binning method using large bins introduced in Section 3.2.1 is actually a clustering method.

Since the clustering method assigns similar members to the same group, it requires a measure that can determine whether two members are similar or not. Given two *p*-dimensional data members $x_i = (x_{i1}, x_{i2}, \dots, x_{ip})$ and $x_j = (x_{j1}, x_{j2}, \dots, x_{jp})$, the distance between two members can be calculated by using the Minkowski metric [155], which is shown in Equation 3.8：

$$d(x_i, x_j) = (|x_{i1} - x_{j1}|^g + |x_{i2} - x_{j2}|^g + \dots + |x_{ip} - x_{jp}|^g)^{1/g} \quad (3.8)$$

When g = 2, the value *d* is equal to the Euclidean distance of two data points.

In order to obtain the preferred clustering results, it is necessary to make the sum of squared error (SSE) to a minimum. The definition of SSE is shown in Equation 3.9:

$$\text{SSE} = \sum_{k=1}^{K} \sum_{x_i \in C_k} ||x_i - \mu_k||^2 = \sum_{k=1}^{K} \sum_{x_i \in C_k} d(x_i, \mu_k)^2 \quad (3.9)$$

in which C_k is the set of members in cluster *k* ($k = 1,2,3 \dots K$); μ_k is the vector mean of the members in cluster *k*. μ_k is defined in Equation 3.10:

$$\mu_k = \frac{1}{M(k)} \sum_{x_i \in C_k} x_i \tag{3.10}$$

where $M(k) = |C_k|$ is the number of the members in cluster *k*.

There are many ways to minimize the SSE [154]. Among these, the *K*-means algorithm is the simplest and a commonly used method ([156], [157]). This algorithm divides the total data set into *K* clusters $(C_1, C_2, \ldots, C_k)$, each cluster is represented by its centre of it. The centre of each cluster is calculated as the cluster mean, which is μ_k.

Figure 3.7 shows the flow diagram of how the *K*-means clustering method is used in the iterations to reduce SSE to a minimum. This algorithm starts with an initial set of *K* cluster centres that are usually chosen randomly. It is important to select the initial *K*-centres from the total data set S. There are many methods that can be used. For example, by randomly selecting *K* members from S and assigning each of them as *K* centres; or by randomly dividing S into *K* grouping and using the mean of each group as the initial centres (most commonly used method); or by dividing S into *K* sub-groups according to the range of S and picking up one member from each sub-group randomly as the initial centres. The choice of the initial *K* group centres is the only factor that can affect the final clustering result.

During each iteration, each member is assigned to its nearest cluster centre by comparing the distances *d* between this member and all of the *K* cluster centres, which is calculated by using the Euclidean distance in Equation 3.8. After all of the members are assigned,

the cluster centres are re-calculated by averaging the members in each group and the next iteration starts.

A number of convergence principles are possible to use. The iterations can stop when the SSE is not reduced by the relocation of the centres, which indicates that the present partition is optimal. Other convergence principles can be used such as the excess of a pre-defined number of iterations or to calculate the SSE after each iteration and stop the iterations when the SSE is below a certain value.

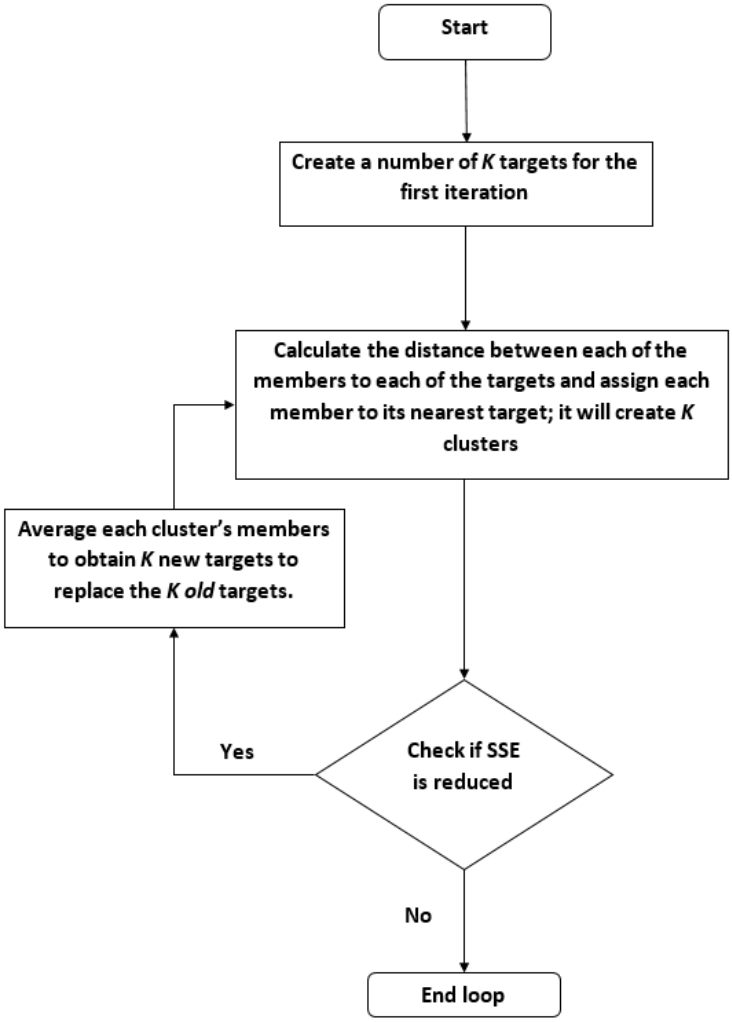

Figure 3.7: The flow diagram of the *K*-means clustering method and how it works to minimize the SSE after iterations.

The *K*-means clustering method is widely used for multi-dimensional data points clustering. It can also be used for 1D curves, 2D surfaces, and 3D objects clustering. 1D curves and 2D surfaces and 3D objects can all be transformed into data points with multiple dimensions and the *K*-means clustering can be applied. It makes the *K*-means clustering method an important tool for AI techniques such as human face recognition [158]. As a result, it has been used for the regrouping of non-directional wave spectra (1D curves) ([54], [55]) and directional wave spectra (2D surfaces) ([57], [56]).

The main disadvantage of the *K*-means clustering method is the number of groups *K* must be defined subjectively before the iteration starts. It is not a problem for WEC model tank testing because the total number of site-specific wave cases for model testing is usually determined prior to the testing starting based on the limited resources.

As explained, the choice of the initial *K* centres is the only factor that can affect the clustering results. In order to eliminate this uncertainty, a typical way is to repeat the whole *K*-means clustering method with random initial centres multiple times and choose the one that provides the result with the lowest SSE as the optimal regrouping result. It is preferable to repeat the *K*-means clustering process 10 to 100 times [159].

All of the regrouping processes in this thesis were carried out using MATLAB [160]. MATLAB allows data importation and analysis, plotting of functions results, and implementation of algorithms and metrics.

3.2.2 Eight regrouping methods A to H

In order to select site-specific complex sea states for WEC model testing, different regrouping methods are used in this section. Along with the commonly used *H* - *T* bivariate scatter diagram binning method introduced in Section 3.2.1, other regrouping methods are based on the *K*-means clustering technique.

It is necessary to review these regrouping methods using both the HF radar sea states and Long Island buoy sea states to see if the conclusion is affected by different ocean areas and measuring instruments. The following eight regrouping methods are from previous research [58].

A. H_s - T_e bivariate scattering diagram binning method

This method is actually the same method introduced in Section 3.2.1, which is the binning method with large bins in H_s - T_e space. The number of non-empty bins after binning is *K* [58]. As it was explained, it is difficult to guarantee *K* is equal to the target value due to the existence of empty bins. The directional wave spectra in the same non-empty bin are averaged and the result is considered the representative wave spectrum in each bin.

B. H_s - T_e - θ_m binning method

In this method, a third wave parameter, which is the mean wave direction θ_m, is taken into account. It is calculated from Equation 3.11 :

$$\theta_m = \int_0^{2\pi} D(f,\theta)\theta d\theta \tag{3.11}$$

Similar to the H_s - T_e two-dimensional binning method, the H_s - T_e - θ_m three-dimensional binning method uses the third variable θ_m to determine the height of the bins. Each bin is a cuboid of the same size [58]. This method is also subjective since the numbers of bins in H_s, T_e, and θ_m are determined subjectively. The same as method A, given a fixed data set, the creation of bins is the only factor that influences the final regrouping results. Additionally, it is very difficult to guarantee that the number of total non-empty bins is equal to the desired value of *K*. After creating the bins and averaging the members in the same non-empty bin, the representative wave spectrum in each non-empty bin can be obtained.

C. Non-directional wave spectrum clustering method

In order to apply the *K*-means clustering method on non-directional wave spectra to obtain *K* groups, the difference between two wave spectra have to be quantified. The difference between two non-directional wave spectra $S_i(f)$ and $S_j(f)$, $f = (f_1, f_2, \dots, f_p)$ can be calculated by Equation 3.12, in which each $S(f)$ is considered as a data point with p dimensions [55]. It is the summation of the difference of all of the frequency components between two non-directional wave spectra:

$$\mathrm{d}\big(S_i(f), S_j(f)\big) = (|S_i(f_1) - S_j(f_1)|^2 + \big|S_i(f_2) - S_j(f_2)\big|^2 + \ldots + |S_i\big(f_p\big) - S_j\big(f_p\big)|)^{1/2} \quad (3.12)$$

The same approach can be used to quantify the difference between the cluster mean and each group member. By using the *K*-means method, each member is allocated to its nearest centre for the next iteration as shown in Figure 3.7. After calculation, the directional wave spectra of each group's members are averaged to obtain the representative directional wave spectrum. In total there are *K* representative wave spectra obtained.

D. Directional wave spectrum clustering method

This method is to group hourly directional wave spectra directly without losing any information. The directional wave spectrum with p frequencies and q directions is considered a data point with $p \times q$ dimensions [58]. The difference between two directional wave spectra $S_i(f,\theta), S_j(f,\theta)$ in which $f = (f_1, f_2, \ldots, f_p)$, $\theta = (\theta_1, \theta_2, \ldots, \theta_q)$ is defined in Equation 3.13:

$$d\left(S_i(f,\theta), S_j(f,\theta)\right) = [\sum_{m=1}^{p} \sum_{n=1}^{q} (|S_i(f_m, \theta_n) - S_j(f_m, \theta_n)|^2)]^{1/2} \quad (3.13)$$

Then the *K*-means clustering method can be applied to create *K* clusters and obtain their corresponding *K* representative directional wave spectra.

E. Normalised H_s - T_e clustering method

This method is similar to the binning method A by first obtaining H_s and T_e for each hourly wave spectrum. Each of the sea states is considered as a two-dimensional data point *x* and H_s and T_e are the two coordinates of this data point [58]. However, the units of H_s and T_e are different. For H_s it is in meters and for T_e it is in seconds. Before the *K*-means clustering begins, H_s and T_e of each sea state is normalised by its total mean value respectively to eliminate the effect of different units. (It was found that the regrouping results by normalising by the mean value are better than by the maximum value. The details are discussed in Section 3.7). The difference between two wave spectra x_i and x_j can then be calculated from Equation 3.14:

$$\mathrm{d}(x_i, x_j) = (|x_{i1} - x_{j1}|^2 + |x_{i2} - x_{j2}|^2)^{1/2} \tag{3.14}$$

in which x_1 is the normalised H_s and x_2 is the normalised T_e .Then the *K*-means clustering method can be applied to obtain *K* clusters and *K* corresponding representative directional wave spectra.

F. Seven wave parameters clustering method

Method F is an extension of method E and uses seven different wave parameters rather than only H_s and T_e to represent an hourly wave spectrum. All of the seven wave parameters are considered of equal importance and normalised by their total mean value respectively [58]. These seven parameters are H_s and T_e, spectral bandwidth v, mean wave direction θ_m, wave power P, peak steepness S_p, directional spreading parameter σ_θ. The reason for using seven wave parameters is to guarantee more wave information is taken into consideration during the regrouping process. The definitions of the wave parameters are shown below:

Spectral bandwidth v is calculated by Equation 3.15 by using the spectral moments obtained from Equation 3.2 [161]:

$$v = \left(\frac{m_0 m_2}{m_1^2} - 1\right)^{1/2} \tag{3.15}$$

Wave power P is defined from Equation 3.16 [40]:

$$P = \frac{\rho g}{2} \int_0^\infty \frac{S(\omega) d\omega}{\omega} \tag{3.16}$$

in which ω is the wave angular frequency. The water depth is considered infinite.

Wave peak steepness S_p is calculated from Equation 3.17:

$$S_p = \frac{H_s}{\lambda_p} \tag{3.17}$$

where λ_p is the wavelength at the spectral peak, which can be calculated from Equation 3.18:

$$\lambda_p = \frac{2\pi}{k_p} \tag{3.18}$$

k_p is the wave number at the spectral peak. The relationship between $k_p$and the peak angular frequency ω_p is shown in Equation 3.19:

$$k_p = \frac{{\omega_p}^2}{g} \tag{3.19}$$

ω_p is the angular frequency of a non-directional wave spectrum at the spectral peak. Here the water depth is considered deep.

The wave directional spreading parameter σ_θ is calculated from Equation 3.20 [162]:

$${\sigma_\theta}^2 = \int_0^{2\pi} D(f,\theta)(\theta - {\theta_m}^2)d\theta \tag{3.20}$$

in which θ_m is the wave mean direction obtained from Equation 3.11.

The same as method E, each wave parameter is normalized by its total mean value respectively before taking part in the *K*-means clustering. The difference between two wave spectra can be calculated by the following Equation 3.21:

$$\mathrm{d}(x_i, x_j) = (|x_{i1} - x_{j1}|^2 + |x_{i2} - x_{j2}|^2 + \cdots + |x_{i7} - x_{j7}|^2)^{1/2} \qquad (3.21)$$

in which x_1, $x_2 \ldots$ x_7 represents the normalized seven wave parameters respectively. Then the *K*-means clustering method can be applied to obtain *K* clusters and the corresponding *K* representative directional wave spectra.

G. E+C combined two-stepped clustering method

Method G is a two-stepped clustering method. First by using method E, which is the normalised H_s - T_e *K*-means clustering method to obtain *K*/2 clusters. Method C is applied to divide each cluster from the first step into 2 sub-groups [58]. There are in total *K* groups created and corresponding *K* representative directional wave spectra obtained. The reason to use the two-step method is to combine two different methods together and to see the difference between the original methods E and C.

H. F+D combined two-stepped clustering method

Method H is also a two-stepped clustering method. First by using method F, which is the seven wave parameter clustering method to create *K*/2 clusters. Method D is applied to divide each cluster from the first step into 2 sub-groups [58]. There are in total *K* groups created and *K* representative directional wave spectra obtained.

3.3 Representative sea states from eight regrouping methods

The HF radar sea states and Long Island sea states introduced in Section 3.1 were regrouped by using eight regrouping methods introduced in Section 3.2.2. In order to compare the results easily, in this section, $K = 20$ was used for both data sets.

The HF radar sea states in 2012 with 3161 hourly sea states were used. A subset of the Long Island sea states from the year 2017 was used as a control group, which had 8402 hourly sea states (directional wave spectra).

As explained in Section 3.2.1, for binning methods A and B using large bins, each bin had the same size and the bin size depended on the range of H_s , T_e and θ_m. The number of bins chosen in H_s, T_e and θ_m was decided subjectively and it was hard to guarantee the number of non-empty bins after binning was equal to the target value of *K*. The number of H_s and T_e bins and the total non-empty bins after binning for both HF radar and buoy data are shown in Table 3.2 below:

Table 3.2: Creation of bins for HF radar and buoy data for binning methods A and B with target K = 20.

K = 20		H_s bins	T_e bins	θ_m bins	Non-empty bins
HF radar data	Method A	6	4	-	19
	Method B	4	3	3	21
Buoy data	Method A	6	4	-	18
	Method B	4	3	3	27

For Methods C to H, which were all based on the *K*-means clustering technique, the number of final groups obtained were all equal to *K*.

For all of the regrouping methods that were based on *K*-means clustering, the number of replicates was set to 100, which was larger than the recommended value of 50 to guarantee a high regrouping quality of the regrouping results.

After calculation and regrouping, the representative sea states from each regrouping method were plotted in H_s - T_e space together with their group members. Each dot represents an hourly sea state and the members within the same group use the same colour. The representative sea states are displayed using red circles. The results for K = 20 are shown in Figure 3.8 and Figure 3.9 below.

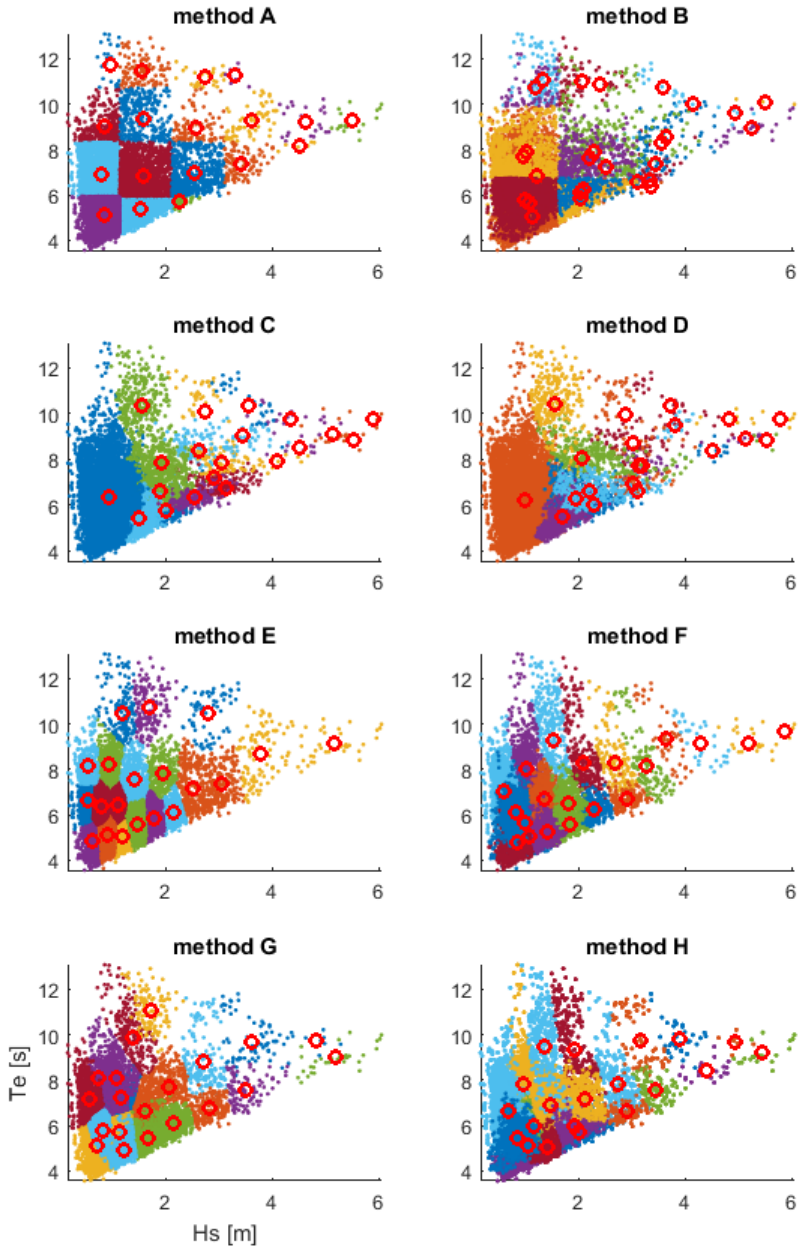

Figure 3.8: Hourly Sea states and the representative sea states of eight regrouping methods A to H in H_s - T_e space for Long Island Buoy data, K = 20.

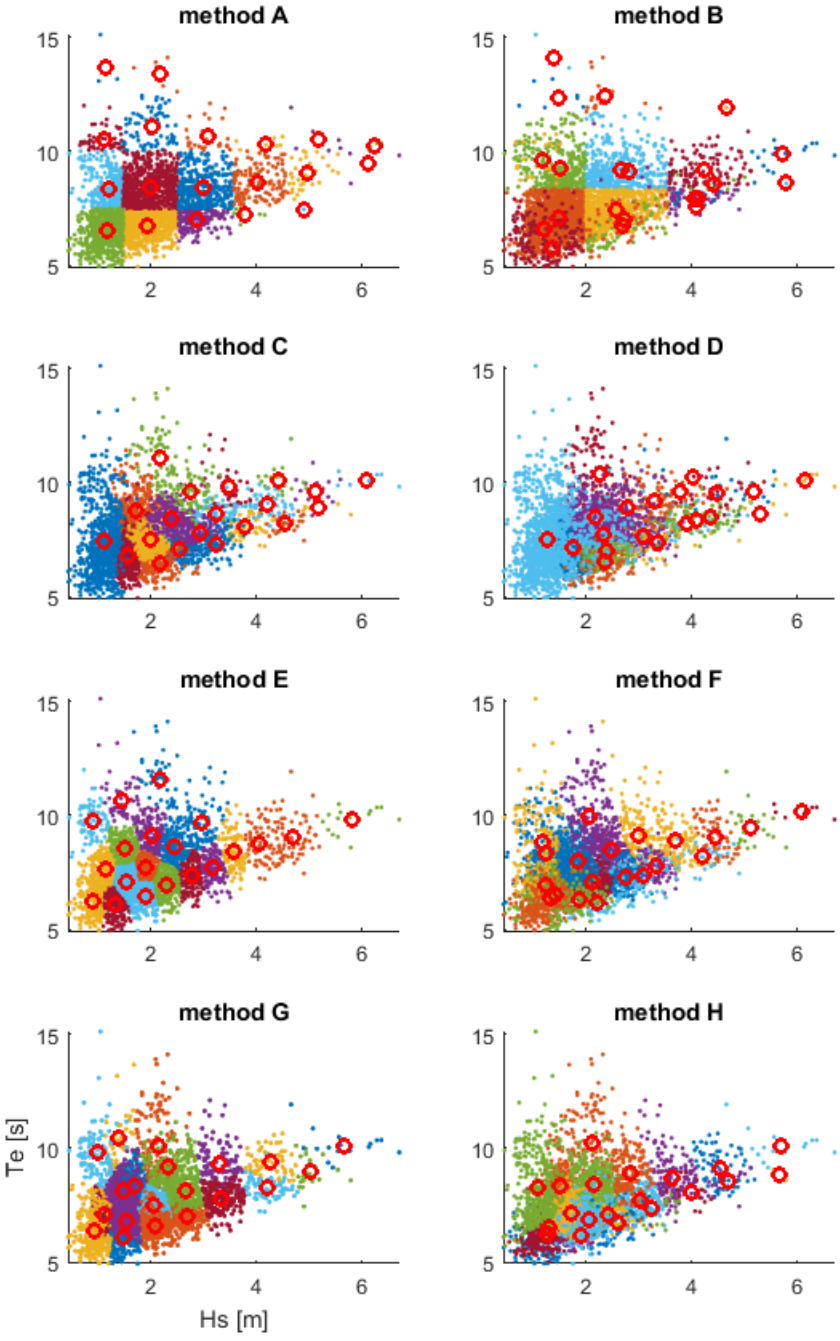

Figure 3.9: Hourly Sea states and the representative cases of eight regrouping methods A to H in H_s - T_e space for HF radar data, K = 20.

The representative sea states in $S(f)$ space for K = 20 of regrouping methods A to H are shown in Figure 3.10 and Figure 3.11 below:

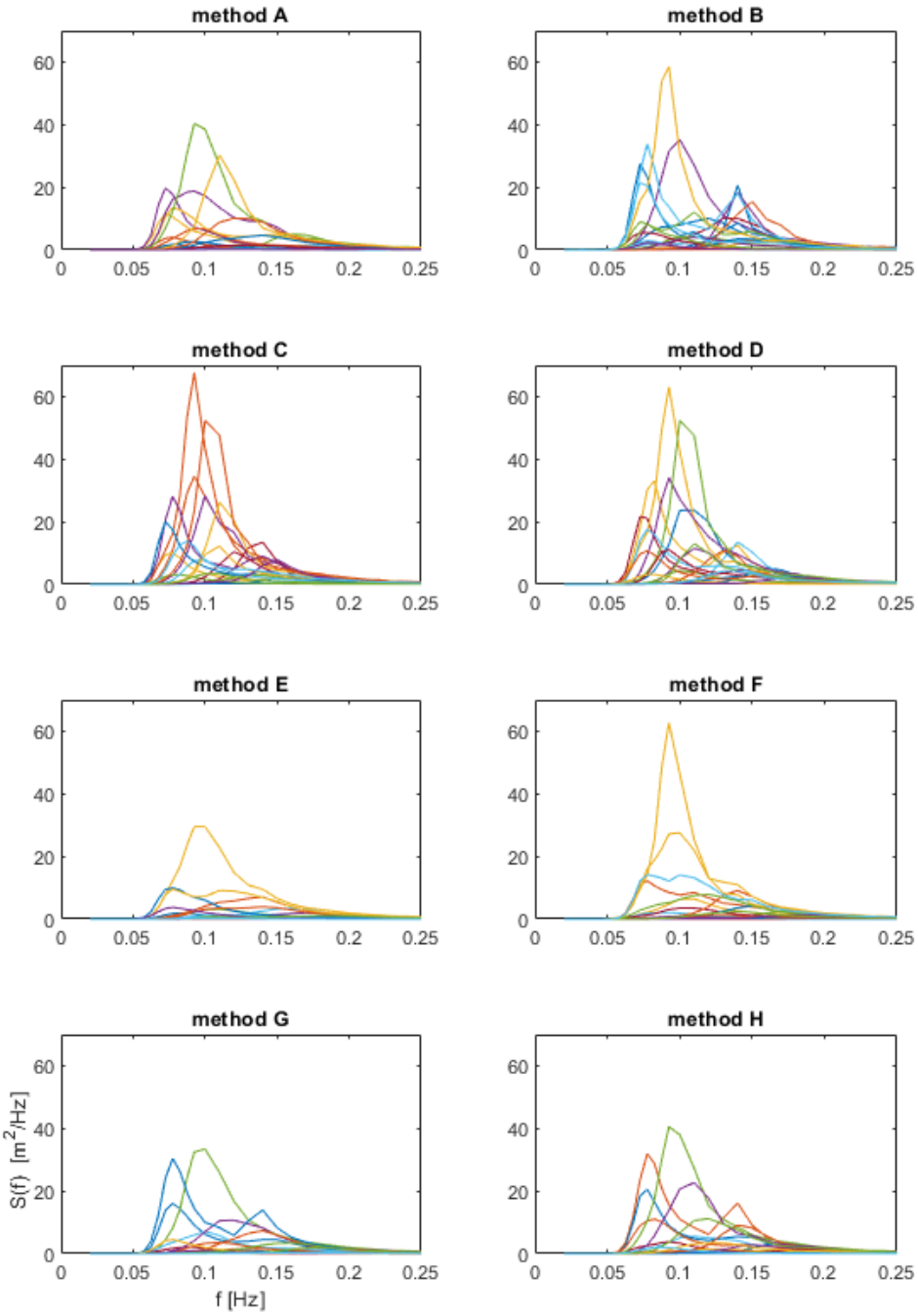

Figure 3.10: Representative sea states in $S(f)$ space for $K = 20$ for Long Island Buoy data. Each non-directional wave spectra plotted is the representative case from the group with the same colour in Figure 3.8.

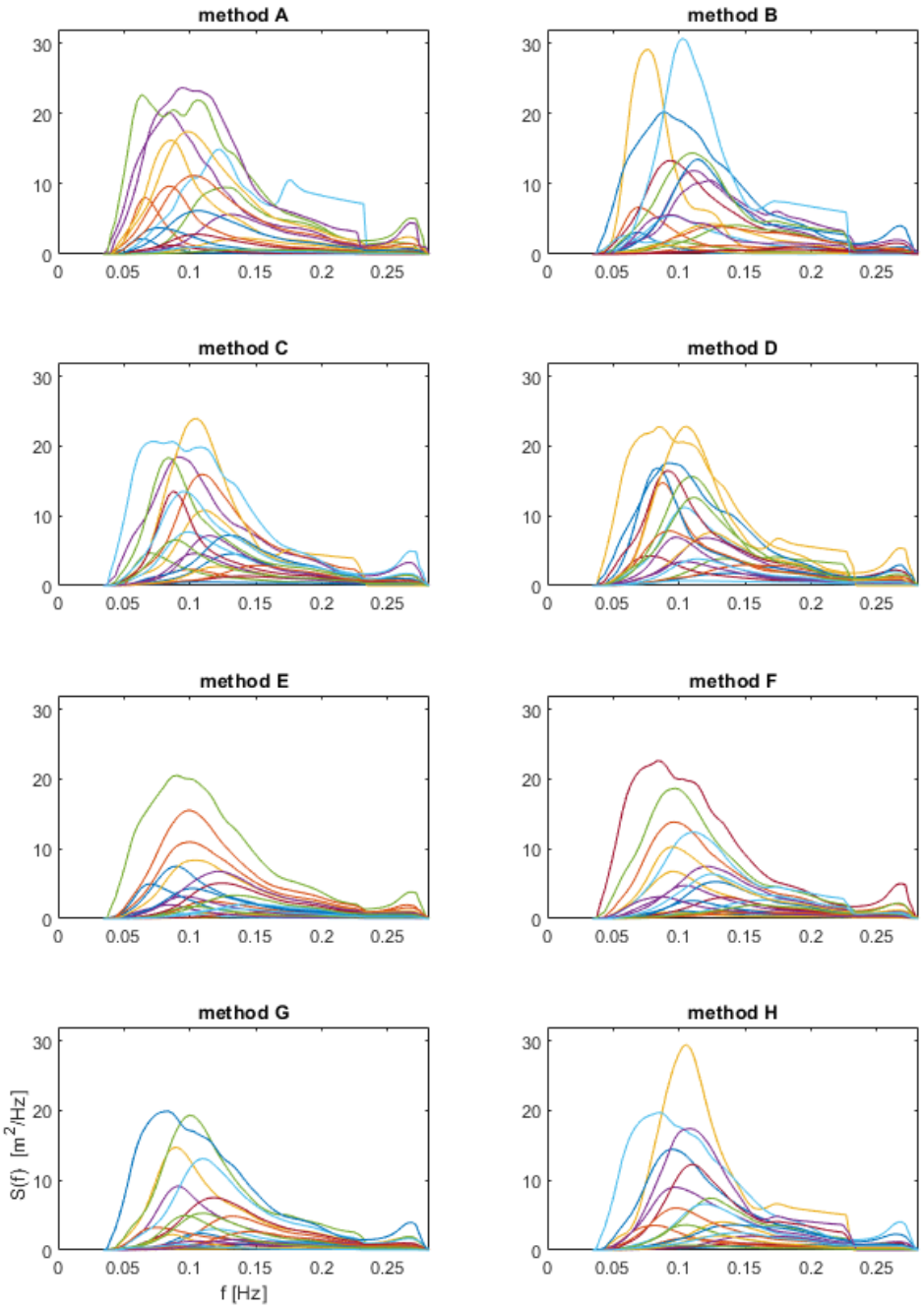

Figure 3.11: Representative sea states in $S(f)$ space for K = 20 for HF radar data. Each non-directional wave spectra plotted is the representative case from the group with the same colour in Figure 3.9.

From Figure 3.8 to Figure 3.11 shown above, it can be noticed that by using different regrouping methods, the group members and the representative sea states are completely different. It can be noticed for methods A and B, that the representative sea states in H_s - T_e space are relatively evenly distributed. It is because all the bins created are of the same

size. Some of the bins from methods A and B provide very large representative T_e values compared with other regrouping methods. From methods C to H, the representative sea states all have a relatively lower T_e value. For Long Island sea states, the highest and second highest T_e are 11.74 s (method A) and 11.05 s (method B), while other *K*-means methods range from 9.80 s (method H) to 10.75 s (method E). For HF radar sea states, the highest and second highest T_e are from 14.07 s (method B) and 13.69 s (method A), while other *K*-means methods range from 10.21 s (method H) to 11.61 s (method E).

It can be noticed from Figure 3.8 and Figure 3.9, that for methods C and D, a large number of sea state members are clustered inside one single group at the lower left corner. Regardless of whether the Long Island buoy data and HF radar data are used, the group with the lowest energy has the largest number of data members inside. Taking method C for example, for buoy data, there are 5,042 out of in total 8,408 members (59.97%) inside the lowest energy group. For HF radar data, there are 740 out of 3,161 members (23.41%) inside the lowest energy group. As explained in Section 3.2.1, *K*-means clustering put similar members inside the same group. As a result, those members with low energy are all considered similar and grouped together.

In order to compare the regrouping results in S(f) space between different regrouping methods, all the sea states together with their representative sea states of method A and method C are plotted. As shown in Table 3.2, for Buoy data, there are 18 non-empty bins for method A. For HF radar data, there are 19 non-empty bins for method A. All of the group members and their representatives are shown from Figure 3.12 to Figure 3.15. Groups display in the order of representative H_s in each plot from highest (top left) to lowest (bottom right).

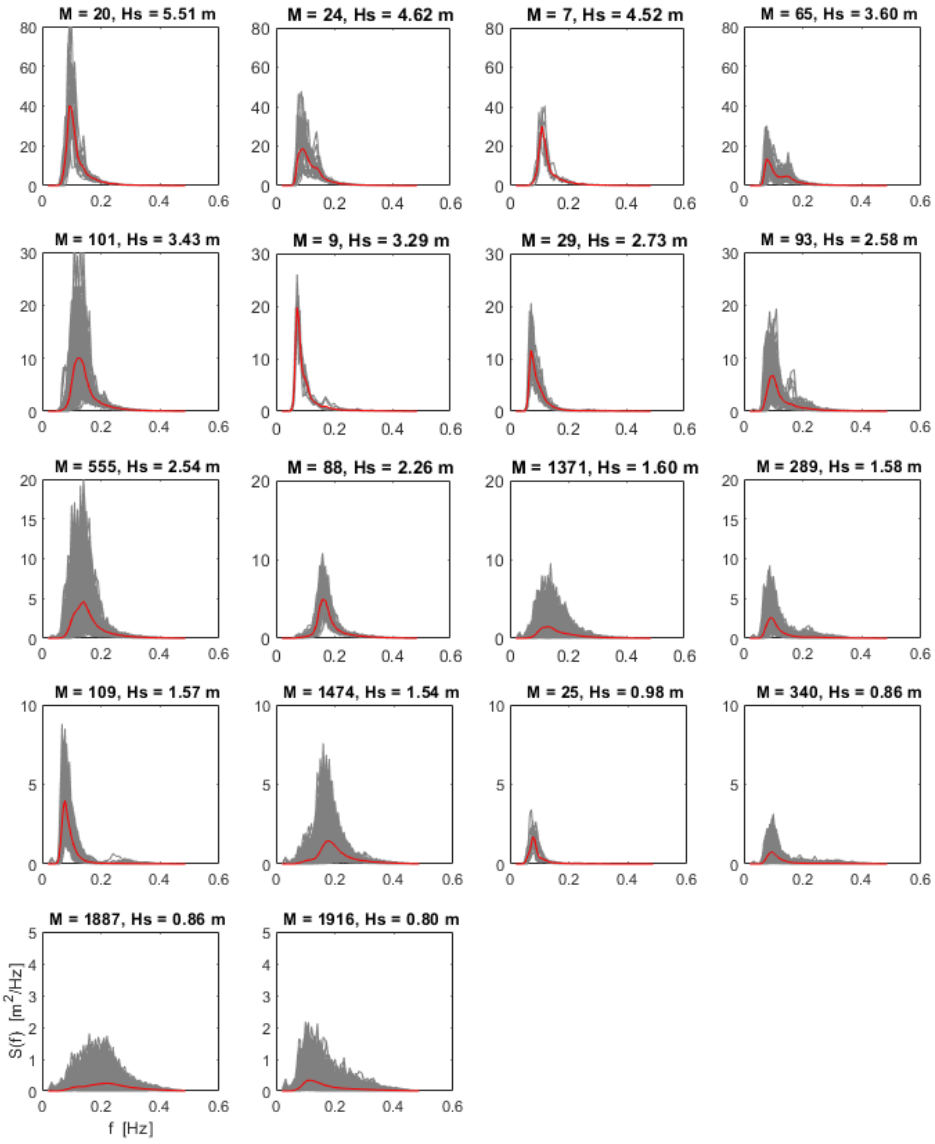

Figure 3.12: Representative sea states and each group's members in $S(f)$ space using method A for Long Island buoy measured data. Grey curves are the non-directional wave spectra of the group members. Red curves are the representative sea state of each group. M represents the number of wave members inside the group. H_s is the significant wave height of the representative sea state.

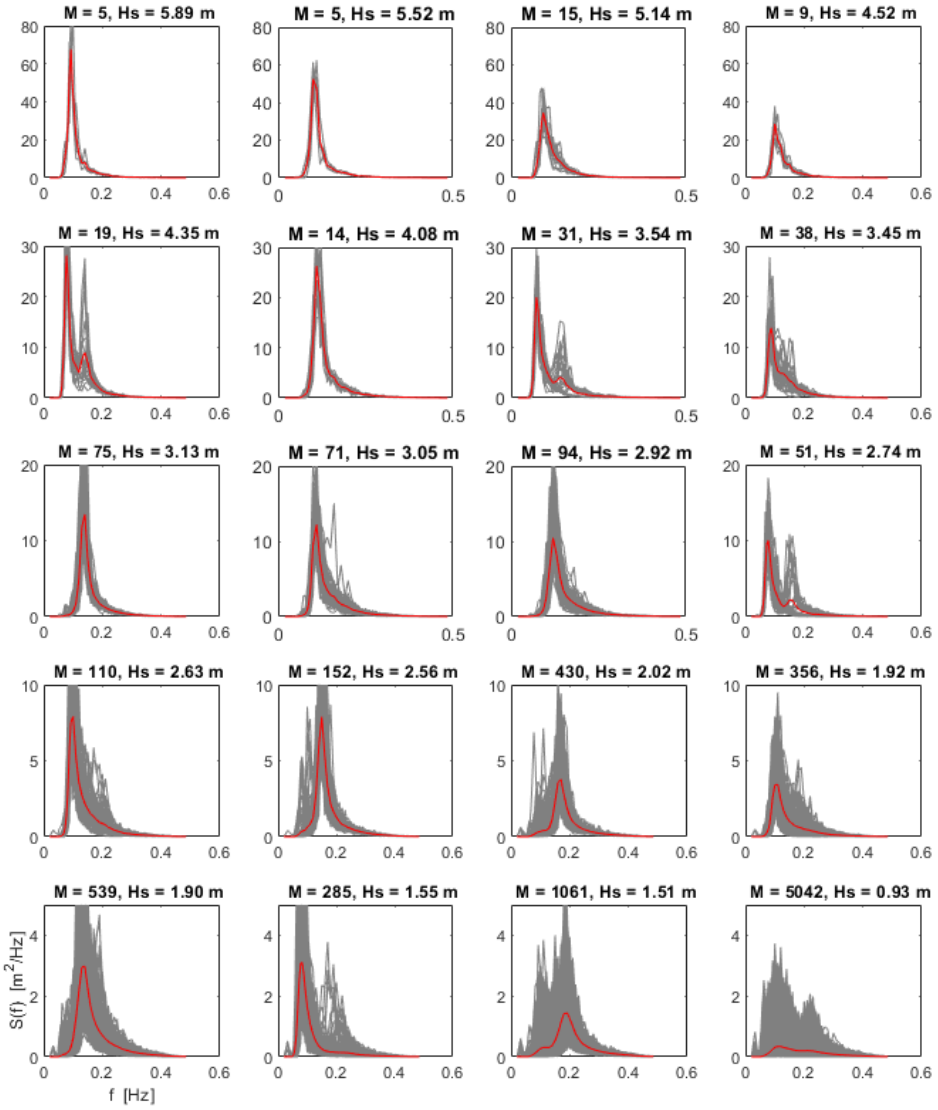

Figure 3.13: Representative sea states and each group's members in $S(f)$ space using method C for Long Island buoy measured data. Grey curves are the non-directional wave spectra of the group members. Red curves are the representative sea state of each group. M represents the number of wave members inside the group. H_s is the significant wave height of the representative sea state.

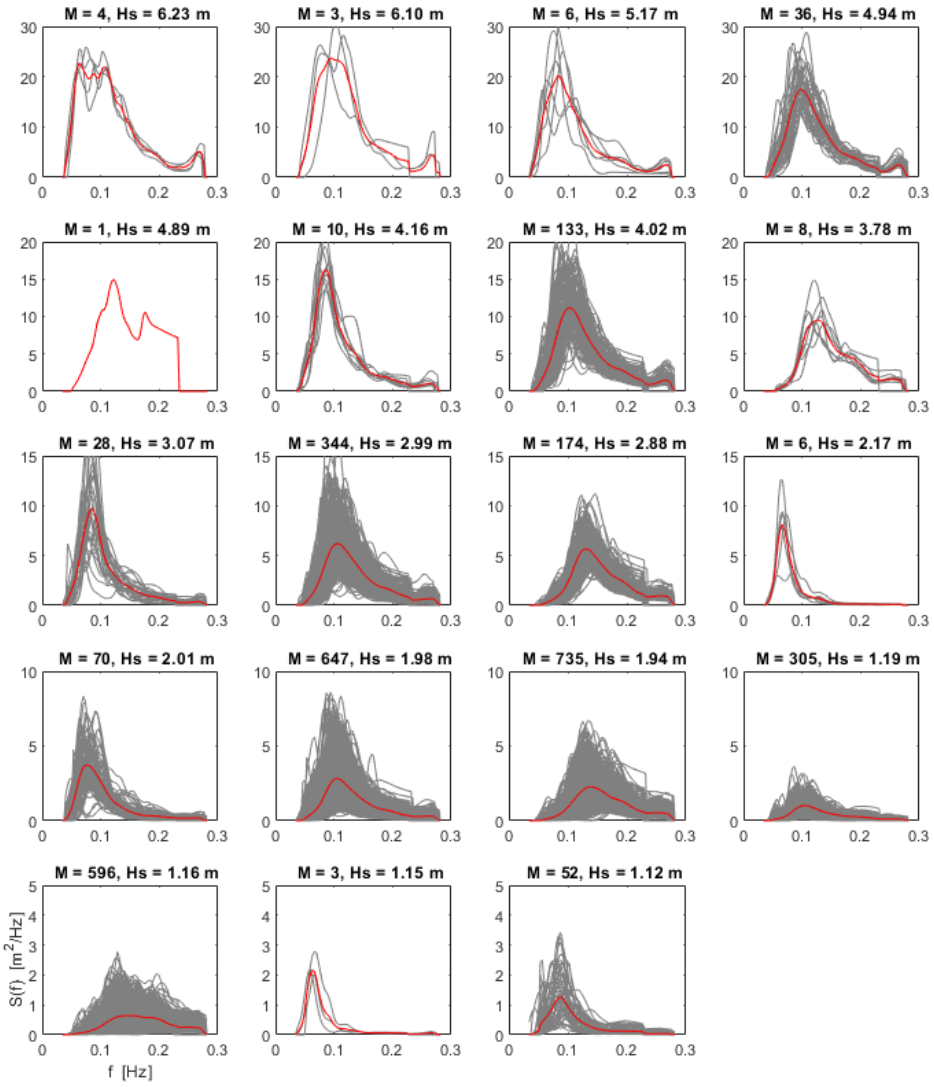

Figure 3.14: Representative sea states and each group's members in $S(f)$ space using method A for HF radar measured data. Grey curves are the non-directional wave spectra of the group members. Red curves are the representative sea state of each group. M represents the number of wave members inside the group. H_s is the significant wave height of the representative sea state.

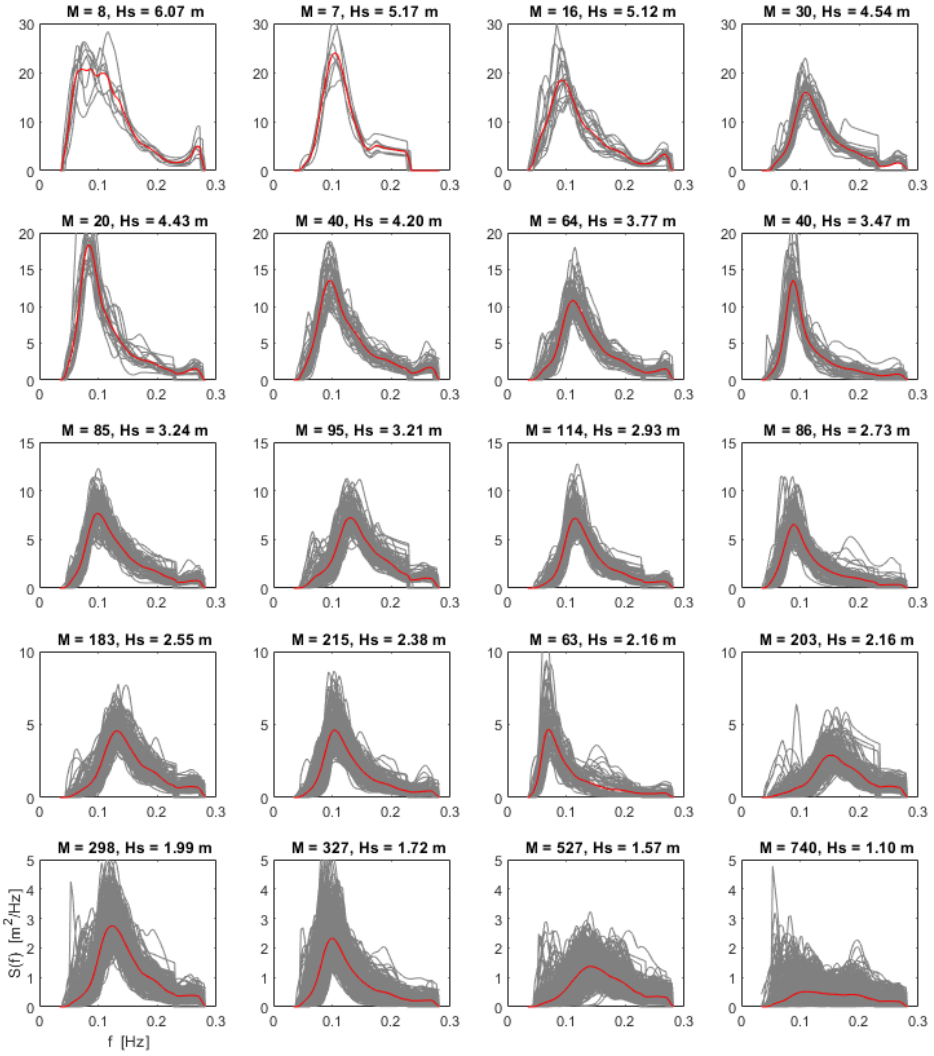

Figure 3.15: Representative sea states and each group's members in $S(f)$ space using method C for HF radar measured data. Grey curves are the non-directional wave spectra of the group members. Red curves are the representative sea state of each group. M represents the number of wave members inside the group. H_s is the significant wave height of the representative sea state.

As can be seen, (1) both methods created 20 (or close to 20 for binning method A) groups and thus gave 20 representative wave spectra; (2) each group had a different series of members inside; (3) the generated representative waves kept the real spectrum's shape recorded by the HF radar data or buoy data, which were shown to be different from the commonly used parametric/generic wave spectrum; (4) method C regrouped the sea states with similar wave spectrum S(f) in the same group automatically, which was not the case

for binning method A that members were grouped based on the defined bin size. (5) As mentioned earlier, compared to method A, method C tended to put a much larger number of low-energy wave cases into one single group with the lowest wave power.

It is obvious that the smaller the number of members in a group is, the more detailed the configuration of the representative $S(f)$. For method A, due to the fact that the bins were all evenly created, the bins located far away from most of the data members might have just several members inside. An example is shown in Figure 3.14, one group from method A of HF radar data contains only one single member inside it.

3.4 Introduction of two new regrouping methods

As can be seen from Figure 3.8 and Figure 3.9, when using methods based on the *K*-means clustering technique (method C to H), the range of the representative cases obtained was not evenly distributed in H_s - T_e space. For the physical model testing of WECs, it is better to test the model in sea states as different from each other as possible both in H_s and T_e space [36]. It is the reason why a H_s - T_e bivariate scatter table is widely used to select H_s and T_e pairs to create parametric/generic wave spectra (JONSWAP, PM i.e.). Another problem is that the maximum T_e of the representative cases obtained from *K*-means methods is relatively lower than that from the binning methods. In this section, two new two-stepped regrouping methods I and J were proposed to create a wider and more evenly distribution of T_e in the representative sea states, which are shown below:

A. The first step is to use method C (for method I) or method D (for method J) to create *K*/2 groups.

B. Based on the *K*/2 groups created in step one, step two is to create several sub-groups for each of the groups obtained from step one using a new clustering method, which is to guarantee the total number of groups created after step two is equal to *K*. The purpose of step two is to guarantee a broader range of representative cases in H_s - T_e space. There are two methods mentioned in Section 3.2.2 that can fulfil the task which are method A (binning method in H_s - T_e space) and method E (normalised H_s - T_e *K*-means clustering method). Both of the methods use H_s and T_e as key parameters to create groups that can guarantee a high distinctness in H_s - T_e space. Method A is excluded because the creation of H_s - T_e bins is highly subjective and the total number of non-empty bins from method A is hard to equal to *K* as explained in Section 3.2.1.

As a result, method E is selected to use for step two. However, similar to other methods based on *K*-means clustering, method E also provides a low T_e value of the representative sea states as shown in Figure 3.8 and Figure 3.9. In order to solve the problem, a new clustering method based on method E is introduced.

This new method is created by introducing a weighting parameter γ to method E. The influence of T_e on the clustering process can be amplified by this weighting parameter. For this modified method E, the difference between two members is calculated from Equation 3.22:

$$\mathrm{d}(x_i, x_j) = (|x_{i1} - x_{j1}|^2 + \gamma \cdot |x_{i2} - x_{j2}|^2)^{1/2} \quad (3.22)$$

in which x_1 and x_2 represent the normalized H_s and T_e respectively, and γ is the weighting parameter ($\gamma \geq 1$). When $\gamma = 1$, this method is equal to method E. After determining the difference between two members from Equation 3.22, the *K*-means clustering method can be applied to obtain sub-groups from each of the *K*/2 groups obtained from step one.

In order to explain the influence of γ on the clustering results, four different weighting parameters ($\gamma = 1, 2, 5, 10$) are used for the regrouping of Long island buoy data with *K* = 20 as an example. The clustering results and their representative sea states in H_s - T_e space are shown in Figure 3.16 below:

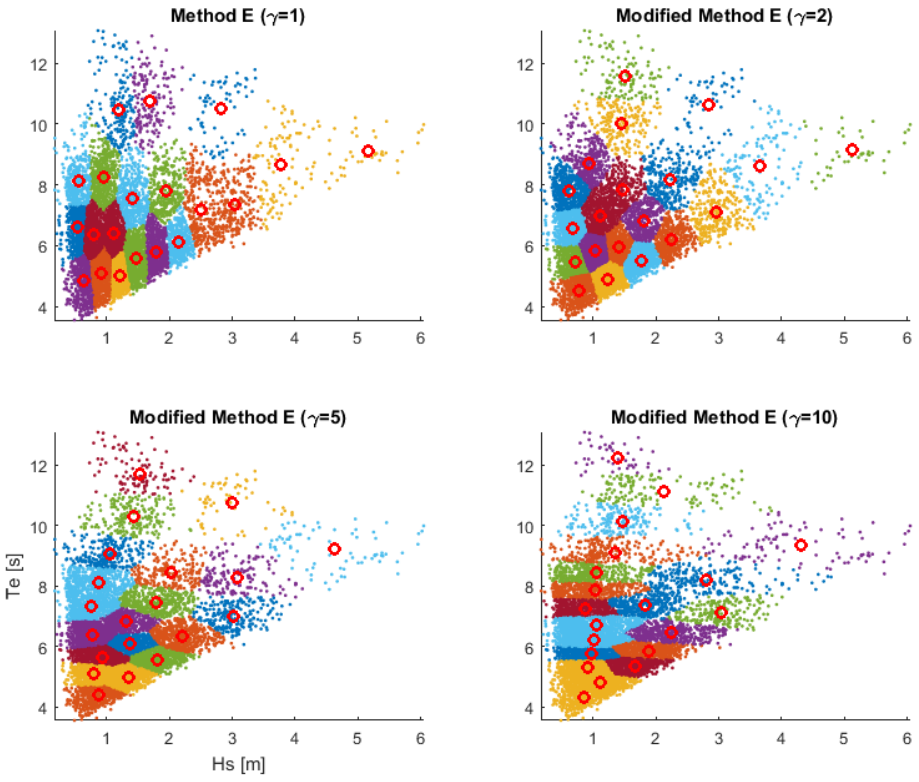

Figure 3.16: The influence of γ = 1, 2, 5, 10 on the modified method E regrouping results, Long Island buoy data, K = 20.

It can be seen that when increasing the weighting parameter γ, the value of the representative T_e increased. However, when the influence of T_e was amplified, the influence of H_s was reduced. This has shown that the influences of H_s and T_e were competing with each other. Increasing the influence of one wave parameter in K means clustering would automatically decrease the influence of the other wave parameter. As a result, it is important to find a suitable γ, which makes a balance between H_s and T_e.

In order to solve the non-even distribution problem for the representative cases in H_s - T_e space as shown in Section 3.2.2, the number of sub-groups based on the K/2 groups from step one needs to be decided carefully. By dividing a group from step one into more sub-groups, the distribution of the representative sea states in H_s - T_e space can be evenly

distributed. Here, three different methods are proposed to decide how many sub-groups based on the groups from step one are used for step two.

1. Evenly dividing method: By simply dividing each group from step one into two sub-groups. Since there are *K*/2 groups created in step one, after step two, there are in total *K* groups created.

2. Non-evenly dividing method based on the number of data members in each of the *K*/2 groups from step one: If a group from step one contains over 10% of the total sea state population, four sub-groups are created. Whereas if there are less than 1%, no sub-group is created. Other groups are all split into two sub-groups. This method is inspired by [58], in which a similar method was used to decide the number of sub-groups.

3. Non-evenly dividing method based on the range of T_e: After obtaining *K*/2 groups from step one, the group with the largest range of T_e is divided into more groups than other groups based on group members' T_e range.

In order to find out the optimal method from the three methods mentioned above, Long Island buoy data is used aiming to obtain 20 groups ($K = 20$). Method C is used in step one to create 10 groups and the modified method E with $\gamma = 10$ is used in step two. For step two, three different methods mentioned above are compared with each other.

For the third method (Non-evenly dividing method based on the range of T_e) to obtain sub-groups, based on the 10 groups obtained from step one, the group with the largest range of T_e is divided into 5 sub-groups; the second largest is divided into 4; the third largest is divided into 3 and the fourth is divided into 2. Other groups remain the same with no sub-groups created. After calculation, the regrouping results and their representative sea states with all the 3 methods were plotted together. The 10 groups obtained from step one and an ordinary one-stepped method C with K = 20 are also plotted for comparison. See the results in Figure 3.17 below:

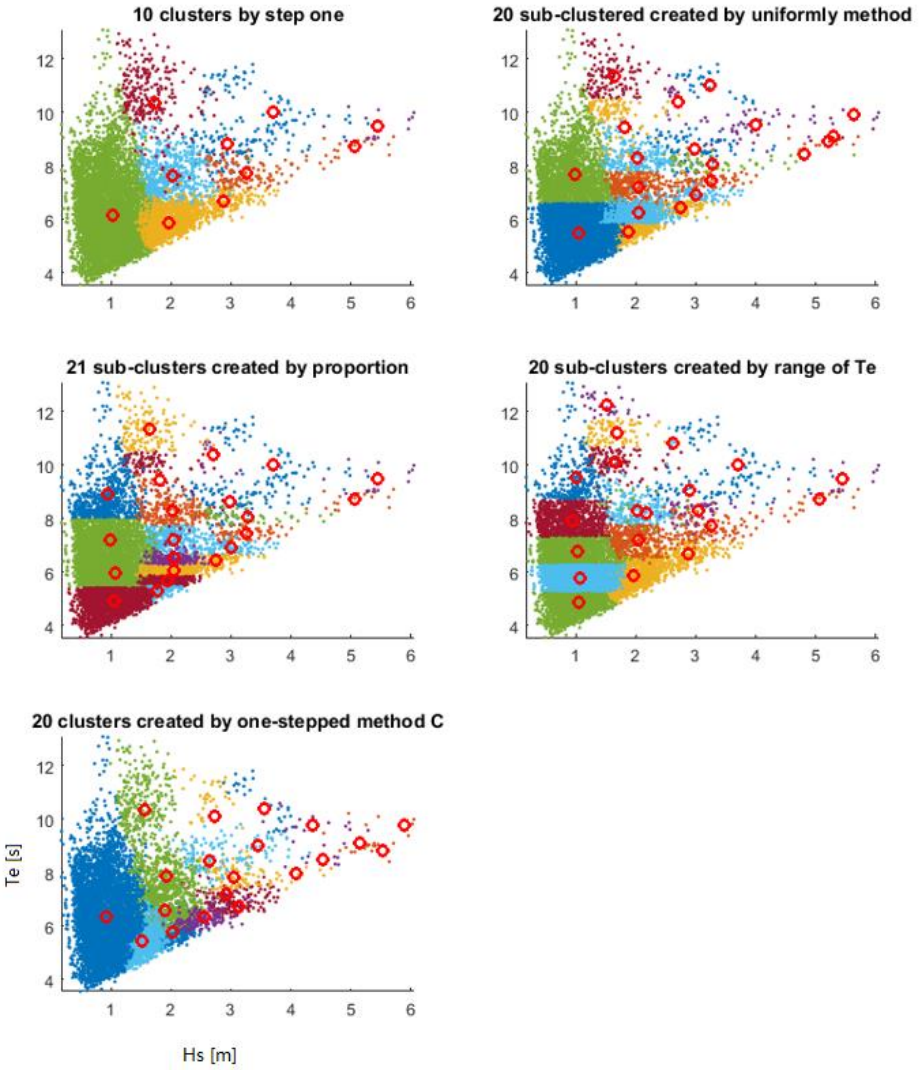

Figure 3.17: Long Island Buoy data with K = 20. 10 groups were created from step one and three modified methods E with γ =10 were used for step two. An ordinary one-stepped method C with K = 20 is also plotted for comparison.

As can be seen, the uniformity of the representative sea states in H_s - T_e space increased significantly using the 3 two-stepped methods compared with the ordinary one-stepped method C. The highest T_e value of the representative sea states is also increased significantly. The ordinary method C of K = 20 provides the highest T_e value of only 10.38s. The first method (evenly dividing method) provides a max T_e = 11.33s. The second method (non-evenly dividing method based on the number of data members in each group from step one) also provides a max T_e = 11.33s. The third method (Non-evenly sub-groups generated by the range of T_e) provides a max T_e = 12.22s, which is the highest maximum T_e for the representative cases among the 3 methods.

As a result, the third method to create sub-groups was chosen for step two for the two new clustering methods I and J. After regrouping, the representative sea states in H_s - T_e space and $S(f)$ space from methods I and J are shown in Figure 3.18 and Figure 3.19 below:

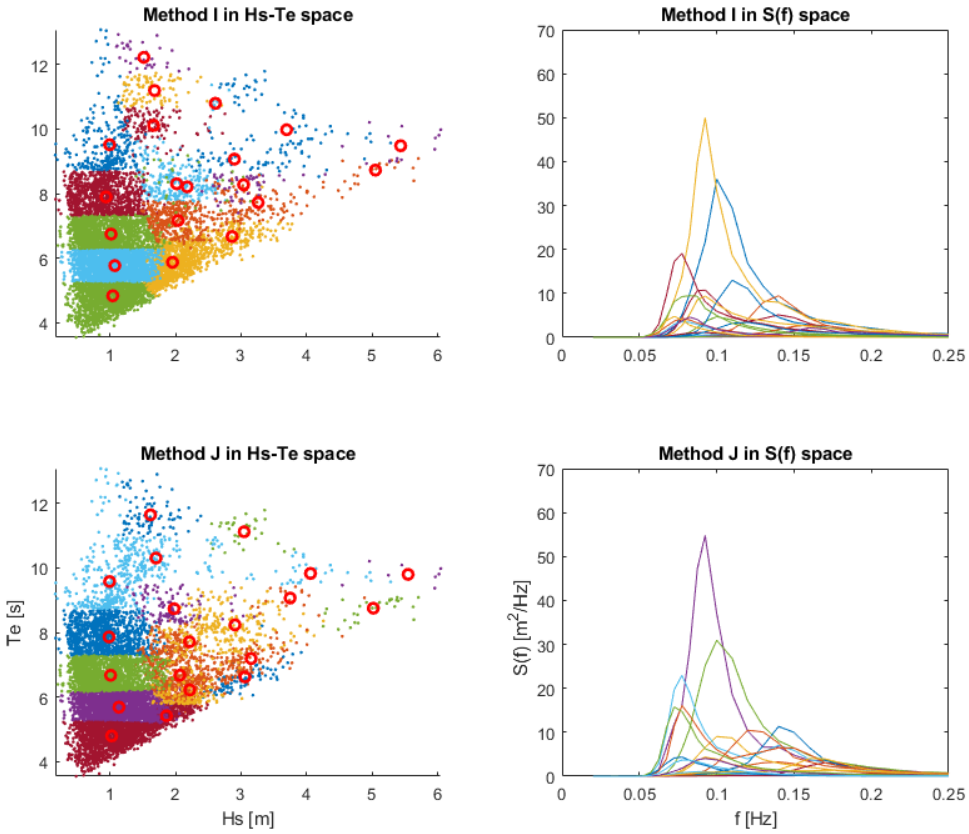

Figure 3.18: Representative sea states for Long Island buoy data from methods I and J in H_s - T_e and $S(f)$ space, K = 20.

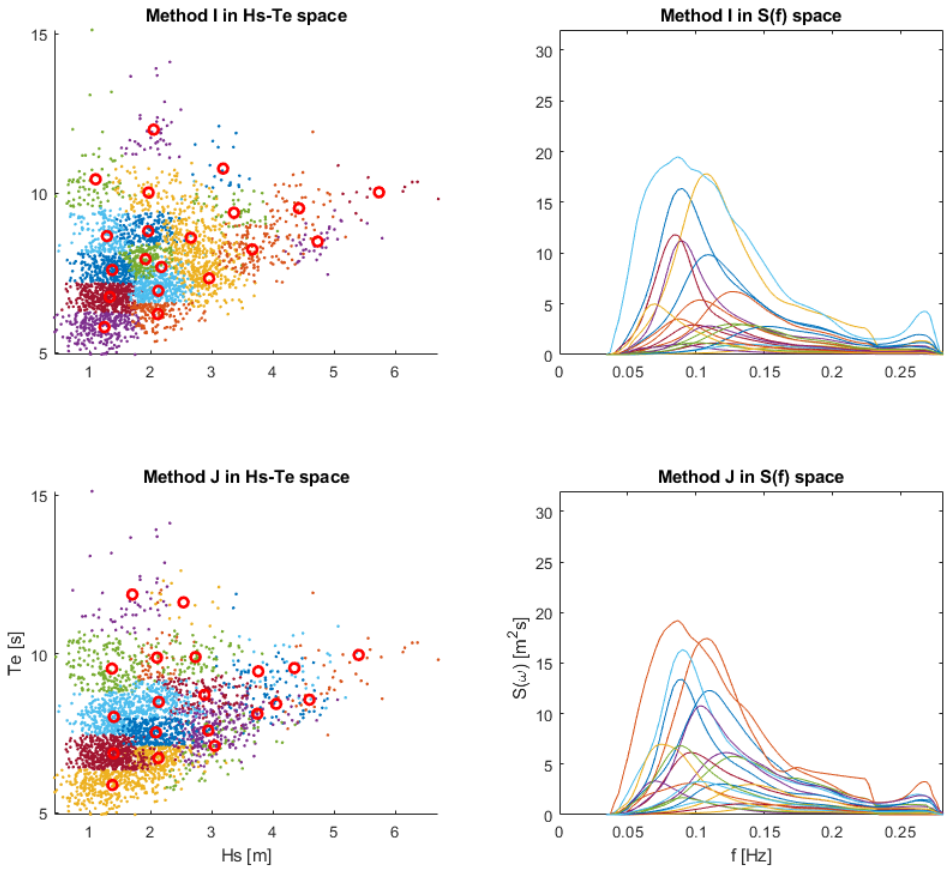

Figure 3.19: Representative sea states for HF radar data of methods I and J in H_s - T_e and $S(f)$ space, K = 20.

As shown above, methods I and J both created groups with an improved uniformity in H_s - T_e space and provided a relatively high representative T_e value compared with other methods C to H.

According to the industry standard [163], the WEC must have enough strength in Ultimate Limit State (ULS). It requires calculating the responses of WECs in extreme wave conditions. The commonly used method is to first calculate the extreme H_s of a certain ocean area ([164], [165]), then obtain the extreme wave period values. It can be achieved by using the joint probability methods such as the inverse-first order reliability

method (I-FORM) ([166], [167]). These methods create environmental contours relating to return periods (e.g. 100 years) and provide extreme $H - T$ combinations. They can be used as input of parametric wave spectrum such as JONSWAP wave spectrum.

For the ten regrouping methods A to J discussed, none of them obtains representative sea states that can be considered extreme wave conditions. It is because the data sets used are all measured from operational conditions. As a result, their representatives are not extreme either. This thesis focuses on operational conditions and extreme conditions are not discussed.

3.5 Two performance metrics

No matter what regrouping method is implemented, there has to be a metric to assess the regrouping quality. With each regrouping method used, there are K groups (or close to K groups for binning methods A and B) obtained. Each directional wave spectrum from the same group can be analysed and compared with their cluster mean (representative sea state) from the same group. They can be compared by using the same wave parameters (one-dimensional or multi-dimensional wave parameters) derived from them to access the regrouping quality.

Two metrics are used in this chapter. After the groups are created for a data set, metrics one and two can be used to assess the regrouping quality. For a regrouping method, metric one only calculated the average difference of a certain wave parameter between each

group member and the representative one within the same group. A low metric one value means a small average difference, which represents a good regrouping quality.

During physical model testing of WECs, for a fixed number of sea states to test, it is better to test the WEC models in as different wave environments as possible. It can guarantee the WECs models experience a broad range of wave conditions. As a result, it needs to consider not only the average difference inside the same group but also the average difference of the representative sea states from different groups. Metric two is used for this purpose.

3.5.1 Metric one

The equation of metric one can be found in [56]. As explained earlier, by using regrouping methods A to J from Sections 3.3 and 3.4, there are *K* groups created $(k = 1, \dots K)$. Each group *k* comprises a certain number of members $M(k)$. *m* represents each member's label in group k, $m = 1, \dots M(k)$; δ represents the wave parameter used for analysis, $\delta = H_s, T_e, \dots S(f), S(f,\theta)$; d represents how many discrete values δ has, $d = 1, \dots D(\delta)$. Metric one is shown in Equation 3.23:

$$Met(\delta) = \frac{1}{K}\sum_{k=1}^{K}\frac{1}{M(k)}\sum_{m=1}^{M(k)}\sum_{d=1}^{D(\delta)}\frac{|\delta_{k,m,d}-\mu_{k,d}(\delta)|}{\mu_{k,d}(\delta)} \tag{3.23}$$

in which $\mu(\delta)$ is the group mean for wave parameter δ. $\mu(\delta)$ is calculated from each group's representative directional wave spectrum.

The value $D(\delta)$ depends on the wave parameter δ to be analysed. For each of the one-dimensional wave parameter H_s, T_e, v, P and θ_m, $D(\delta) = 1$. For non-directional wave spectra $S(f)$ with $f = (f_1, f_2, \dots, f_p)$, $D(\delta) = p$. For directional wave spectra $S(f, \theta)$ with $f = (f_1, f_2, \dots, f_p)$ and $\theta = (\theta_1, \theta_2, \dots, \theta_q)$, $D(\delta) = p \times q$.

From Equation 3.23, it can be seen that the lower the metric one is, the better the regrouping quality. It is because when this metric one value is low, the average difference of a certain wave parameter between each group member and the representative one is small. The value of metric one ranges from 0 to 1.

3.5.2 Metric two

According to previous research [154], the within-group scatter matrix and the in-between-group scatter matrix are introduced to represent the intra-group regrouping quality and inter-group regrouping quality for a certain wave parameter respectively. The quotient of the two matrices is metric two.

To analyse a certain wave parameter, the within-cluster group matrix S_W is calculated as the summation of each group's total members' difference, see Equation 3.24:

$$S_W = \sum_{k=1}^{K} S_k \tag{3.24}$$

in which

$$S_k = \sum_{x \in C_k} (x - \mu_k)(x - \mu_k)^T \tag{3.25}$$

where *T* represents the transposition of the matrix. The in-between-group scatter matrix S_B is calculated from Equation 3.26:

$$S_B = \sum_{k=1}^{K} M(k)(\mu_k - \mu)\,(\mu_k - \mu)^T \tag{3.26}$$

in which μ is the total mean vector of all the members in the total data set *S*, which is defined by the following Equation 3.27:

$$\mu = \frac{1}{m_t} \sum_{k=1}^{K} M(k)\mu_k \tag{3.27}$$

where m_t is the total number of members in the total data set *S*. The eigenvalues of $S_w^{-1}S_B$ are $\lambda_1, \lambda_2, \ldots, \lambda_d$. A good regrouping is one in which the non-zero eigenvalues are large. The eigenvalues of $S_w^{-1}S_B$ are shown in Equation 3.28:

$$\mathrm{tr}[S_w^{-1}S_B] = \sum_{i=1}^{d} \lambda_i \tag{3.28}$$

To present this in simple terms, a good regrouping method according to metric two is the one with a small within-cluster difference S_W and a large in-between-cluster difference S_B. The larger the quotient value $S_w^{-1}S_B$ is, the better the regrouping result. The value of $S_w^{-1}S_B$ is metric two.

3.6 Comparison of ten regrouping methods using metric one

A. Discussion of metric one results for ten regrouping methods

As shown in Sections 3.3 and 3.4, ten regrouping methods have been tested on two data sets, each regrouping method created K = 20 (or close to K for binning methods A and B) groups. Metric one was then used to assess the regrouping quality for different wave parameters. The results are shown in Figure 3.20 and Figure 3.21 below:

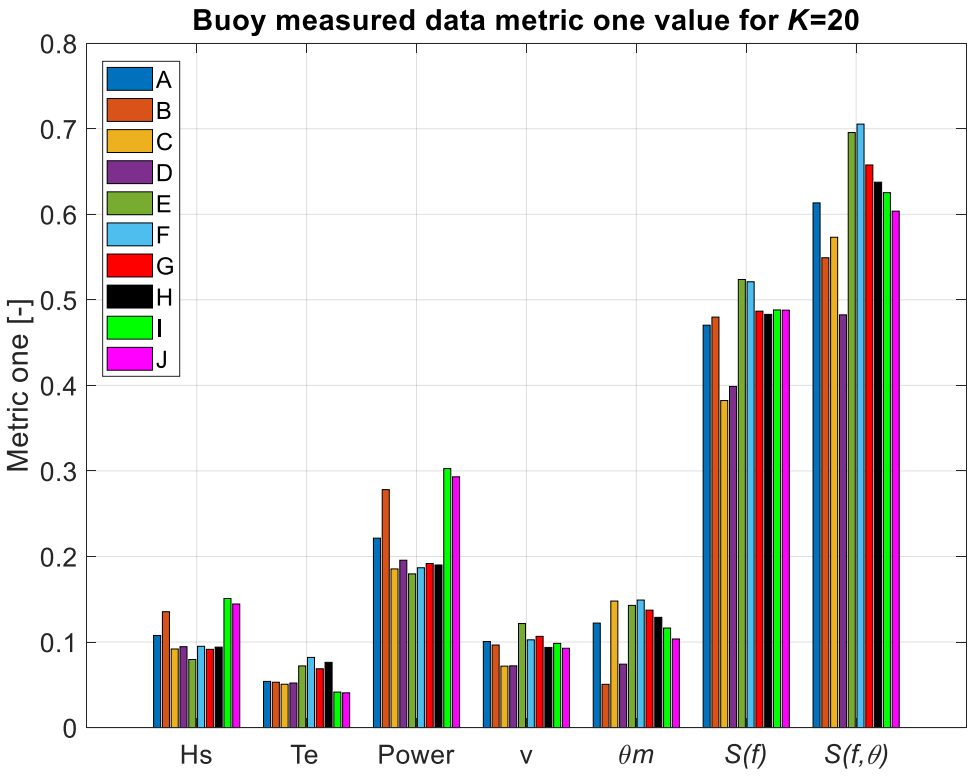

Figure 3.20: Metric one for different wave parameters for buoy data regrouping results from method A to J.

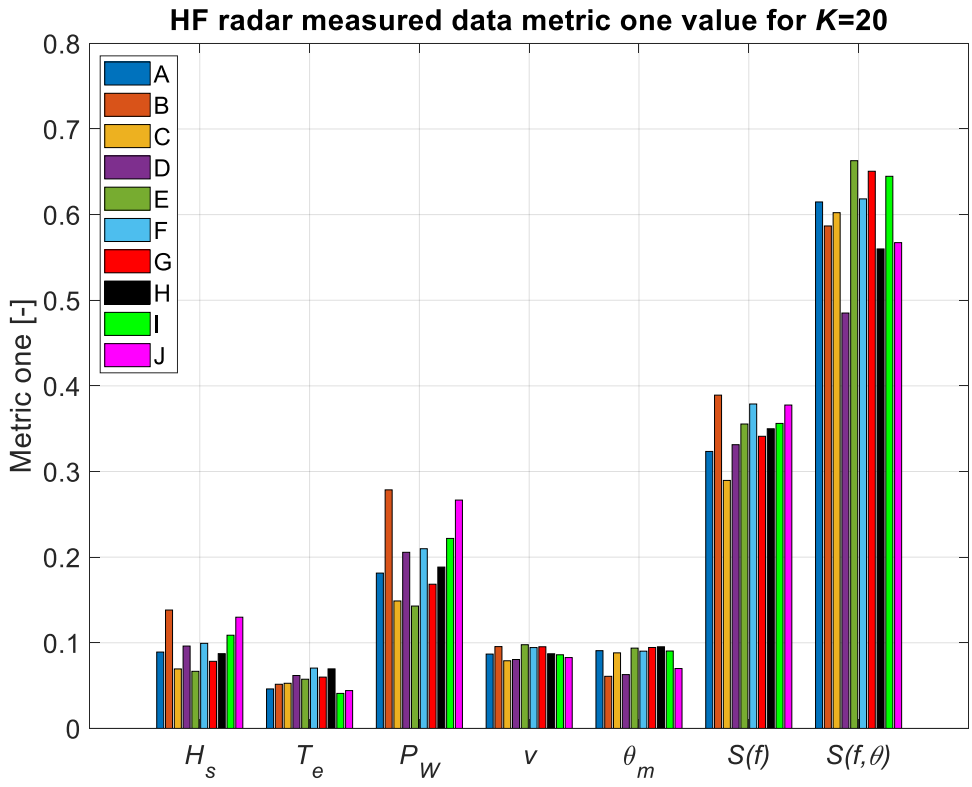

Figure 3.21: Metric one for different wave parameters for HF radar data regrouping results from method A to H.

It can be seen that the results from HF radar and Buoy data share high similarities. Metric one for one-dimensional wave parameters (H_s, T_e, P, ν, θ_m) is always lower than that for non-directional wave spectra $S(f)$. The wave parameter for non-directional wave spectra is always lower than that for the directional wave spectra $S(f,\theta)$. According to the definition of metric one, the difference between each group member with its cluster mean is defined as the summation of the absolute value of the differences between them. However, during the integration from $S(f,\theta)$ to $S(f)$ from Equation 3.1, the differences between different wave directions were eliminated. As a result, a part of the absolute differences between the two directional wave spectra was reduced. It is why the metric one result for $S(f)$ is always lower than that for $S(f,\theta)$. It is the same reason when

comparing metric one for the wave parameter $S(f)$ with the one-dimensional wave parameters. Part of the absolute differences was reduced during the integration process from $S(f)$ to the one-dimensional wave parameter. It is the reason metric one for one-dimensional wave parameters is always lower than that for $S(f)$.

In order to see the results from Figure 3.20 and Figure 3.21 clearly, the results of different regrouping methods were ranked based on their performance. For each wave parameter analysed, the highest representativeness of 10 regrouping methods (with the lowest value among ten methods) was ranked as '1', and the lowest representativeness (highest value) was ranked as '10', the results are shown in Table 3.3 to Table 3.6.

Table 3.3: The ranks of different methods of buoy data, metric one, by methods.

method	H_s	T_e	P_w	ν	θ_m	$S(f)$	$S(f,\theta)$	Total
A	7	6	7	7	5	3	5	40
B	8	5	8	5	1	4	2	33
C	3	3	2	1	9	1	3	22
D	5	4	6	2	2	2	1	22
E	1	8	1	10	8	10	9	47
F	6	10	3	8	10	9	10	56
G	2	7	5	9	7	6	8	44
H	4	9	4	4	6	5	7	39
I	10	2	10	6	4	8	6	46
J	9	1	9	3	3	7	4	36

Table 3.4: The ranks of different methods of buoy data, metric one, by rank values.

rank	H_s	T_e	P_w	v	θ_m	S(f)	S(f,θ)
1	E	J	E	C	B	C	D
2	G	I	C	D	D	D	B
3	C	C	F	J	J	A	C
4	H	D	H	H	I	B	J
5	D	B	G	B	A	H	A
6	F	A	D	I	H	G	I
7	A	G	A	A	G	J	H
8	B	E	B	F	E	I	G
9	J	H	J	G	C	F	E
10	I	F	I	E	F	E	F

Table 3.5: The ranks of different methods of HF radar data, metric one, by methods.

method	H_s	T_e	P_w	v	θ_m	$S(f)$	$S(f,\theta)$	Total
A	5	3	4	5	7	2	6	32
B	10	4	10	9	1	10	4	48
C	2	5	2	1	4	1	5	20
D	6	8	6	2	2	3	1	28
E	1	6	1	10	8	6	10	42
F	7	10	7	7	5	9	7	52
G	3	7	3	8	9	4	9	43
H	4	9	5	6	10	5	2	41
I	8	1	8	4	6	7	8	42
J	9	2	9	3	3	8	3	37

Table 3.6: The ranks of different methods of HF radar data, metric one, by rank values.

method	H_s	T_e	P_w	v	θ_m	$S(f)$	$S(f,\theta)$
1	E	I	E	C	B	C	D
2	C	J	C	D	D	A	H
3	G	A	G	J	J	D	J
4	H	B	A	I	C	G	B
5	A	C	H	A	F	H	C
6	D	E	D	H	I	E	A
7	F	G	F	F	A	I	F
8	I	D	I	G	E	J	I
9	J	H	J	B	G	F	G
10	B	F	B	E	H	B	E

By comparing ten different regrouping methods, it can be seen that among all of the seven wave parameters assessed, method C (clustering with non-directional wave spectra) provided the overall highest regrouping quality (highest representativeness) with the lowest total ranks. For buoy data, method C resulted in 22 total ranks which were the same as method D and both were the lowest values. For HF radar data, method C had a total rank of 20, which was also the lowest value. The overall performance of each method is plotted in Figure 3.22 below. It can be noticed that methods C and D provide the overall highest representativeness (with the lowest total ranks) among the ten methods, which is the same conclusion as [57]. It can also be noticed that the results of two completely different data set shared high similarities.

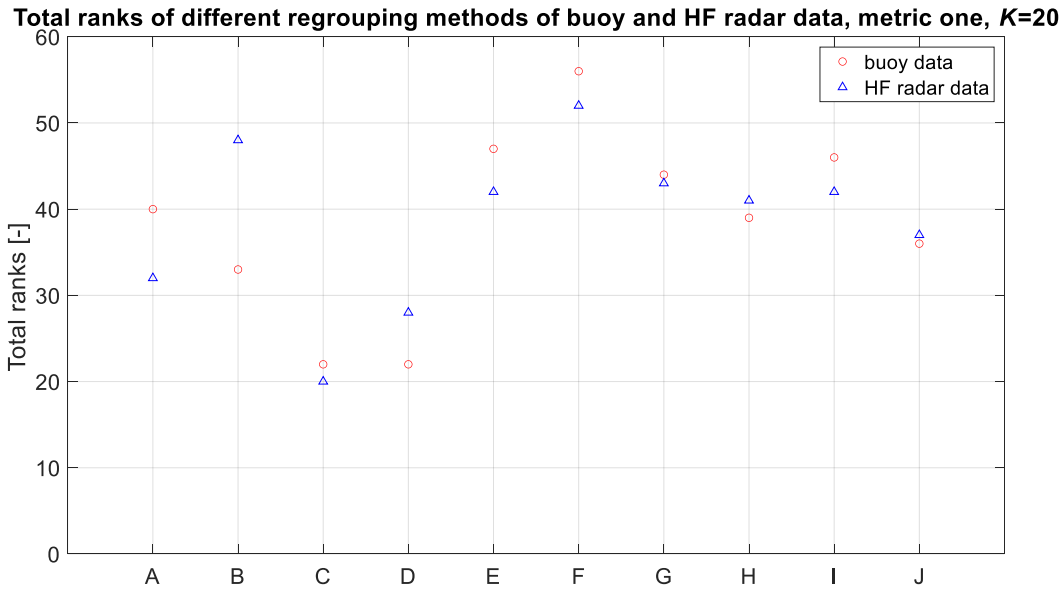

Figure 3.22: Total ranks of different regrouping methods of the buoy and HF radar data, metric one, K = 20.

From Table 3.3 and Table 3.5, it can be seen that there is a relationship between the quality of a wave parameter and the degree of participation of the same wave parameters in the regrouping process. Taking the mean wave direction θ_m as an example, method B

used θ_m directly for binning process and the representativeness of θ_m of method B was the highest compared with other regrouping methods (rank 1 for both buoy and HF radar sea states). It was a similar result for method D. Although method D used directional wave spectra for the clustering process without using θ_m directly. However, the directional information of waves was included in the directional wave spectra, which meant method D had wave directional information θ_m participating in the clustering process indirectly. It was why method D shows a high quality for wave parameter θ_m (both ranked 2nd for buoy and HF radar sea states). For tank testing of WEC models, if the WEC performance is not affected by the wave direction (e.g. point absorbers and attenuators), the inclusion of wave direction will lower other wave parameters' relative importance, which should be avoided. It means for this kind of WEC, method C is better than method D and vice versa.

From Figure 3.22, the result from method F is the worst (both the highest total ranks for buoy and HF radar sea states) and is the first to be eliminated. Other methods are all between the total ranks 30 to 50, which are much worse than methods C and D. It is because methods C and D both considered the influence of the wave spectrum as a whole, whereas other methods only considered several wave parameters and omitted much useful information. It is no surprise method C and D provides a much better overall performance than others.

Method E (the normalised H_s, T_e clustering method) provided very good quality for the wave parameter H_s which was of rank 1 for both buoy radar data and HF radar data. However, method E did not perform so well for the wave parameter T_e, which was of rank 8 for the buoy data and of rank 6 for the HF radar data. It is because, for method E,

the importance of the two different wave parameters H_s and T_e were different. Even though H_s and T_e were both normalised by their total mean value respectively, the differences of H_s between the two sea states were much larger than that of T_e. As a result, during the *K*-means iterations, the influence of H_s dominated over T_e. This part will be discussed in detail in the following section.

B. Discussion of the methods divided by their maximum values

As mentioned in Section 3.2.2, methods E, F, G, and H were all created by dividing each wave parameter by their total mean values (Methods A, B, C, D, I, and J were not influenced by it) before the *K*-means clustering calculation started. This prompts a question as to what the results are when divided by their total maximum values. This section is to show their difference.

Four new methods are introduced in this section, which are E-max, F-max, G-max, and H-max. The only difference is that each of the wave parameters in the calculation is divided by their total maximum values rather than their total mean values. To show this clearly, the metric one results are plotted with the original method E, F, G, and H results to compare, see Figure 3.23 below:

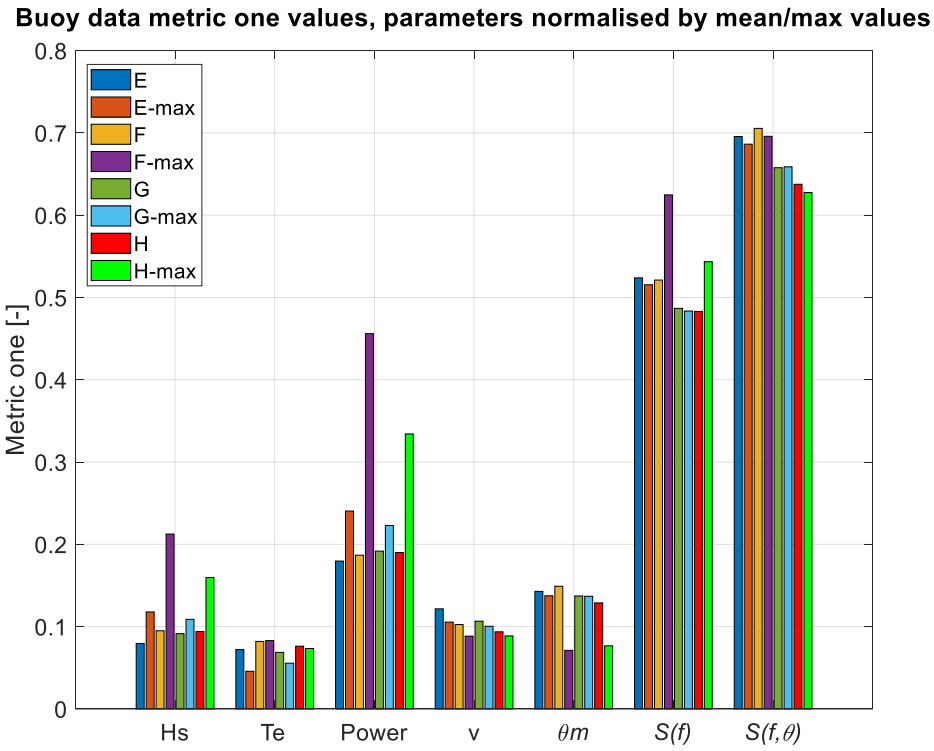

Figure 3.23: Buoy data metric one values, wave parameters normalised by their mean/maximum values.

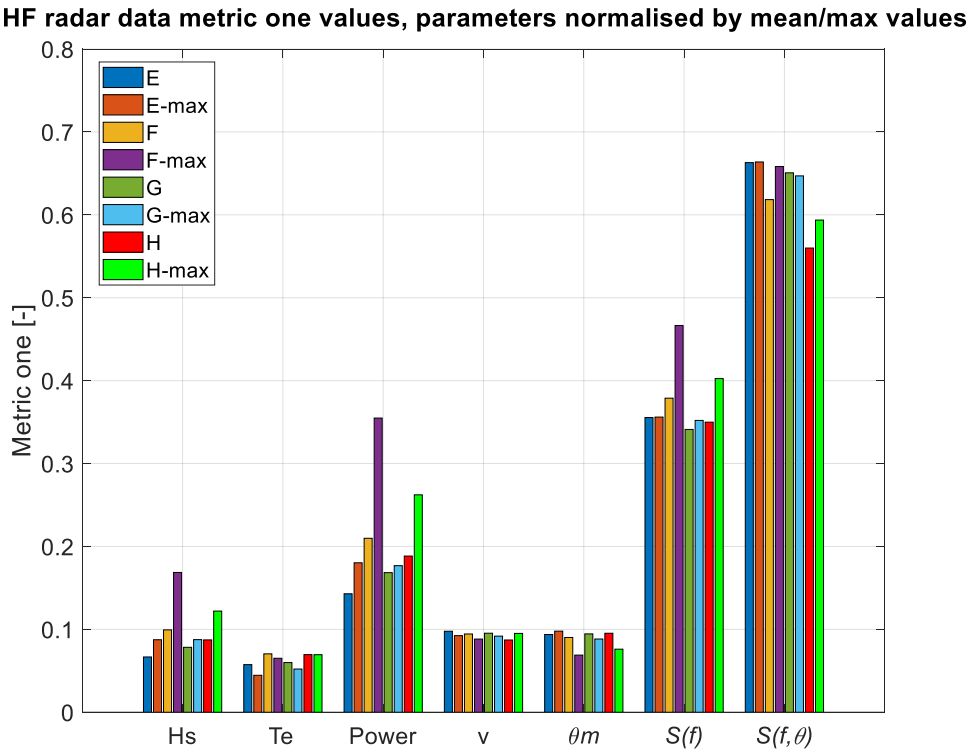

Figure 3.24: HF radar data metric one values, wave parameters normalised by their mean/maximum values.

The results were ranked from 1 (highest representativeness and lowest values) to the lowest 8 (lowest representativeness and highest values), which are shown in Table 3.7 below:

Table 3.7: The ranks of different methods of buoy data, divided by mean/max values

method	H_s	T_e	P_w	v	θ_m	$S(f)$	$S(f,\theta)$	Total
E	1	4	1	8	7	6	6	33
E-max	6	1	6	6	6	4	5	34
F	4	7	2	5	8	5	8	39
F-max	8	8	8	1	1	8	7	41
G	2	3	4	7	5	3	3	27
G-max	5	2	5	4	4	2	4	26
H	3	6	3	3	3	1	2	21
H-max	7	5	7	2	2	7	1	31

Table 3.8 The ranks of different methods of HF radar data, divided by mean/max value

method	H_s	T_e	P_w	v	θ_m	$S(f)$	$S(f,\theta)$	Total
E	1	3	1	8	5	4	7	29
E-max	4	1	4	4	8	5	8	34
F	6	8	6	5	4	6	3	38
F-max	8	5	8	2	1	8	6	38
G	2	4	2	7	6	1	5	27
G-max	5	2	3	3	3	3	4	23
H	3	7	5	1	7	2	1	26
H-max	7	6	7	6	2	7	2	37

The comparison of the total ranks is plotted in Figure 3.25 below:

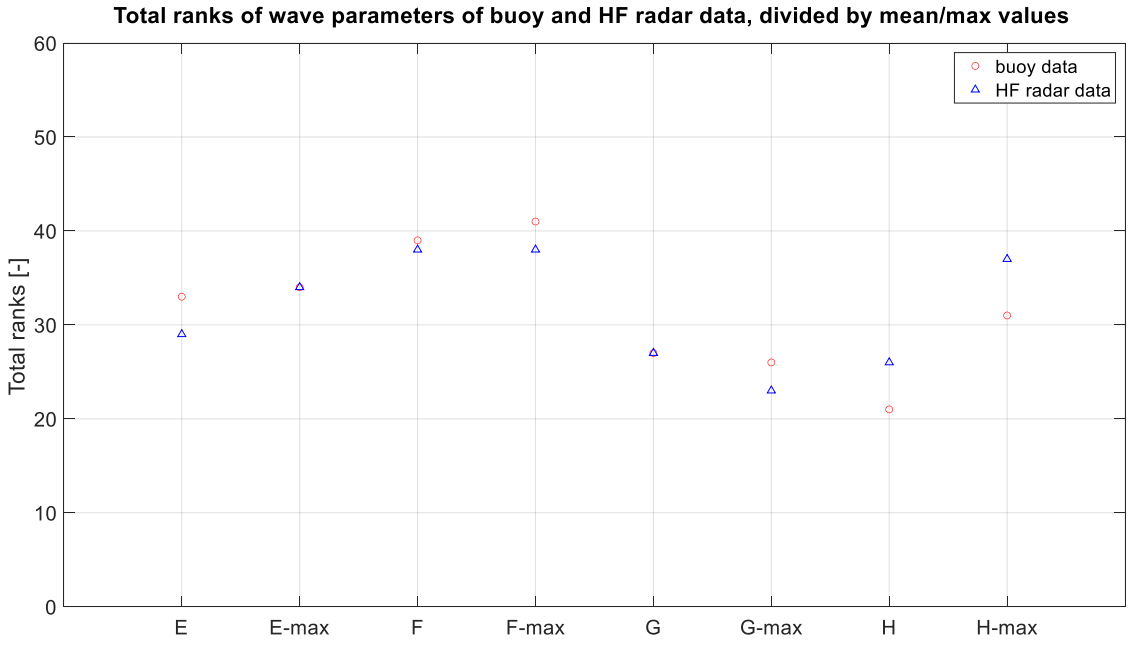

Figure 3.25: Total ranks of different regrouping methods, divided by mean value/ maximum values, buoy data, and HF radar data.

It can be seen from Figure 3.25 that regrouping methods from buoy data and HF radar data share high similarities. For both the buoy and HF radar data, the regrouping quality of methods E, F, and H was negatively affected when divided by the max value, with an

increase in the total ranks for E-max, F-max, and H-max. However, the results of method G have been improved with a decrease in the total ranks for G-max.

It can be noticed that from method E to E-max, the rank of H_s increased (from 1 to 4 for buoy data and from 1 to 6 for HF radar data) while the rank of T_e decreased (from 4 to 1 for buoy data and from 3 to 1 for HF radar data). It is a direct reflection of the change of the relative significance from method E to method E-max. Taking HF radar as an example, the total mean value of H_s was 2.03 m while the total maximum value was 6.70 m, and the total mean value of T_e was 7.72 s while the total maximum value of T_e was 15.12 s. It can be noticed that when changing from method E to E-max, the relative importance of H_s was decreased compared to T_e ($\frac{2.03}{6.70} < \frac{7.72}{15.12}$). It was why the representativeness of method E for parameter H_s was higher than method E-max and the representativeness of method E for parameter T_e was lower than method E-max.

From method F to F-max, it was more complicated. It can be noticed a significant increase in the metric one value for H_s for both the buoy data and HF radar data. The reason was that there were in total seven wave parameters participating in the regrouping procedure. When changing from method F to F-max, the relative importance of H_s was significantly reduced.

As a result, when using metric one, considering multiple wave parameters together for regrouping is not a good idea. It is very difficult to balance the relative importance of different wave parameters because these wave parameters are all of different units. Regardless of whether parameters are divided by the mean value or the maximum value,

the results are not as good as methods C and D. From this perspective, methods C and D are better than methods E, F, G, and H.

3.7 Comparison of ten regrouping methods using metric two

The same regrouping results (groups) from Sections 3.3 and 3.4 were assessed by using metric two of different wave parameters. As explained in Section 3.5.2, metric two considered both the difference between different groups and the differences within the same group. Although the groups created from each regrouping method A to J were the same as metric one, the results from metric two were completely different. The buoy data results and HF radar results for K = 20 are shown in Figure 3.26 and Figure 3.27 respectively. Opposite to metric one, a higher value for metric two indicates a better regrouping quality.

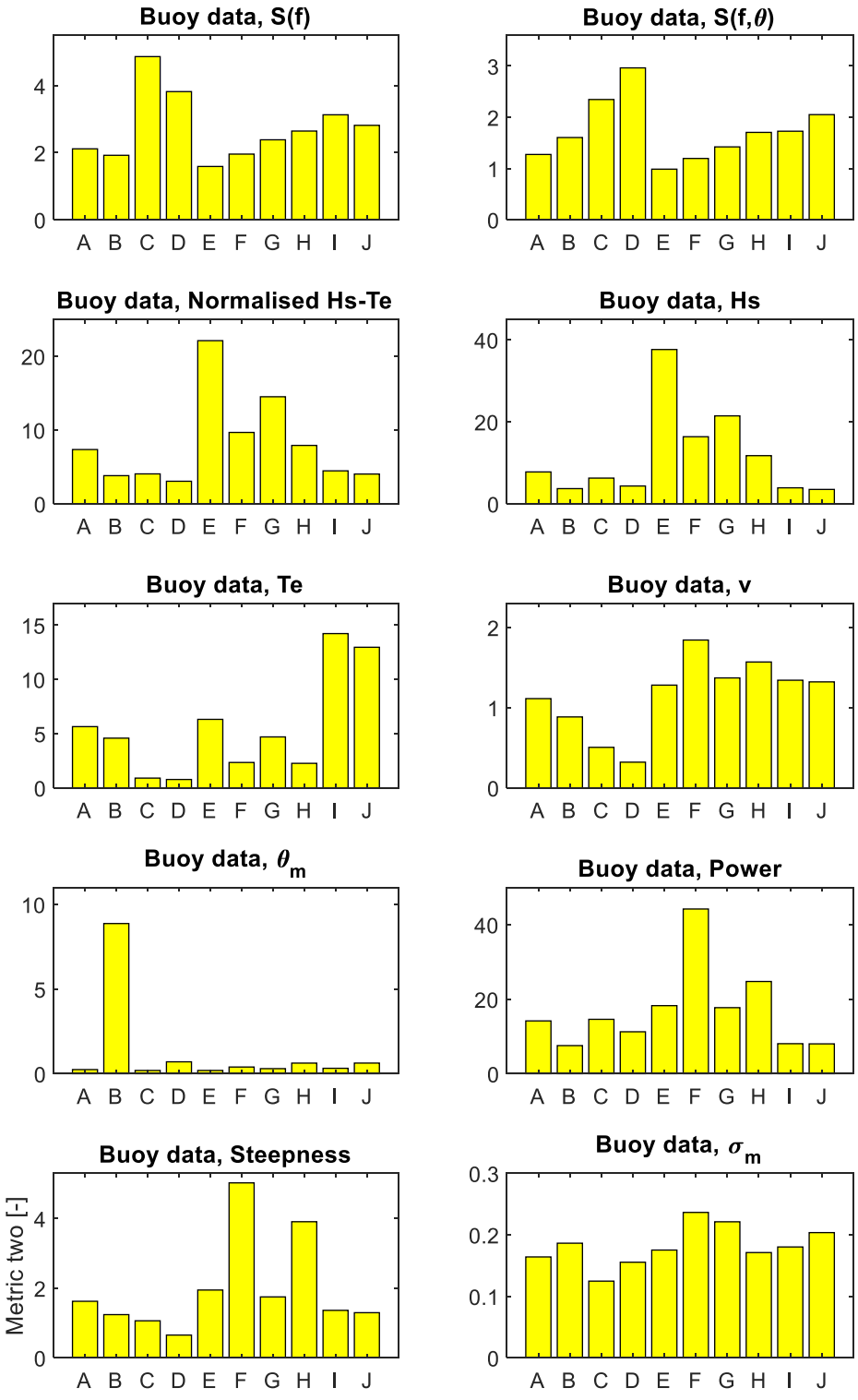

Figure 3.26: Metric two for Long Island buoy data results from method A to J with K = 20 for ten wave parameters.

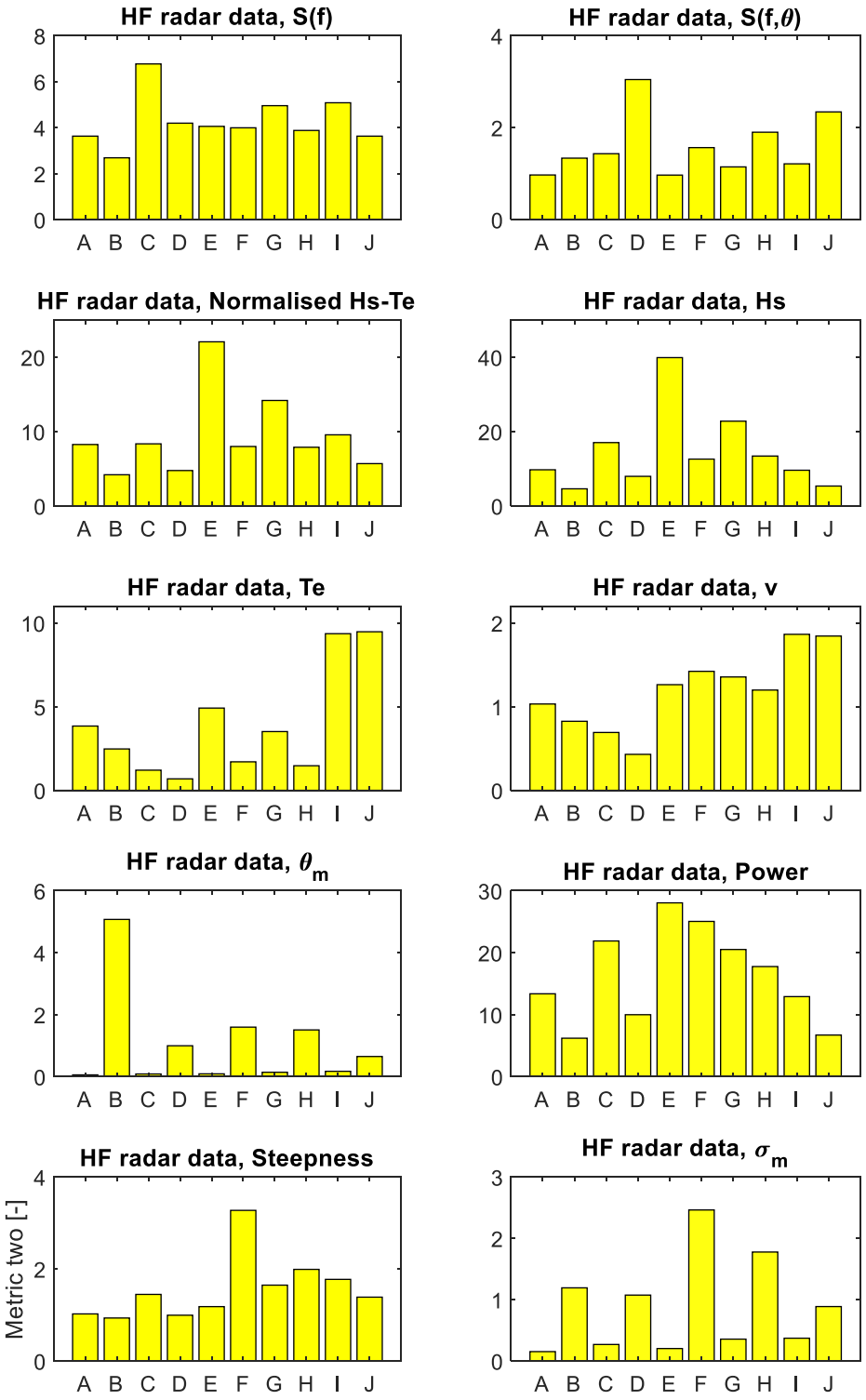

Figure 3.27: Metric two for HF radar data regrouping results from method A to J with K = 20 for ten wave parameters.

It can be seen that the values of metric two are different from metric one although the groups created are the same. In metric one, the values for different wave parameters range from 0 to 1. For metric two, the quotient values (S_B/S_W) vary a lot among ten different wave parameters. It is not suitable to plot metric two of different wave parameters together in the same figure as it has been done for metric one. For example, metric two value for H_s can go up to 40 while metric two value for σ_m can be only around 0.25. Instead, the subplots for metric two are plotted for different wave parameters as shown in Figure 3.26 and Figure 3.27.

The rank tables of buoy data and HF radar data were created. For each wave parameter, the highest representativeness (highest value) was ranked as 1 and the lowest representativeness (lowest value) was ranked as 10. The results are shown in Figure 3.8 to Figure 3.12 below:

Table 3.9: The ranks of different regrouping methods, buoy data, metric two, by methods.

method	$S(f)$	$S(f,\theta)$	normalised H_s - T_e	H_s	T_e	v	θ_m	P_w	S_p	σ_θ	Total
A	7	8	5	5	4	7	8	6	5	8	63
B	9	6	9	9	6	8	1	10	8	4	70
C	1	2	7	6	9	9	10	5	9	10	68
D	2	1	10	7	10	10	2	7	10	9	68
E	10	10	1	1	3	6	9	3	3	6	52
F	8	9	3	3	7	1	5	1	1	1	39
G	6	7	2	2	5	3	7	4	4	2	42
H	5	5	4	4	8	2	4	2	2	7	43
I	3	4	6	8	1	4	6	8	6	5	51
J	4	3	8	10	2	5	3	9	7	3	54

Table 3.10: The ranks of different regrouping methods, buoy data, metric two, by rank values.

rank	$S(f)$	$S(f,\theta)$	normalised H_s - T_e	H_s	T_e	ν	θ_m	P_w	S_p	σ_θ
1	C	D	E	E	I	F	B	F	F	F
2	D	C	G	G	J	H	D	H	H	G
3	I	J	F	F	E	G	J	E	E	J
4	J	I	H	H	A	I	H	G	G	B
5	H	H	A	A	G	J	F	C	A	I
6	G	B	I	C	B	E	I	A	I	E
7	A	G	C	D	F	A	G	D	J	H
8	F	A	J	I	H	B	A	I	B	A
9	B	F	B	B	C	C	E	J	C	D
10	E	E	D	J	D	D	C	B	D	C

Table 3.11: The ranks of different regrouping methods, HF radar data, metric two, by methods.

method	$S(f)$	$S(f,\theta)$	normalised H_s - T_e	H_s	T_e	ν	θ_m	P_w	S_p	σ_θ	Total
A	8	9	5	6	4	7	10	6	8	10	73
B	10	6	10	10	6	8	1	10	10	3	74
C	1	5	4	3	9	9	9	3	5	8	56
D	4	1	9	8	10	10	4	8	9	4	67
E	5	10	1	1	3	5	8	1	7	9	50
F	6	4	6	5	7	3	2	2	1	1	37
G	3	8	2	2	5	4	7	4	4	7	46
H	7	3	7	4	8	6	3	5	2	2	47
I	2	7	3	7	2	1	6	7	3	6	44
J	9	2	8	9	1	2	5	9	6	5	56

Table 3.12: The ranks of different regrouping methods, HF radar data, metric two, by rank values.

rank	$S(f)$	$S(f,\theta)$	normalised H_s - T_e	H_s	T_e	ν	θ_m	P_w	S_p	σ_θ
1	C	D	E	E	J	I	B	E	F	F
2	I	J	G	G	I	J	F	F	H	H
3	G	H	I	C	E	F	H	C	I	B
4	D	F	C	H	A	G	D	G	G	D
5	E	C	A	F	G	E	J	H	C	J
6	F	B	F	A	B	H	I	A	J	I
7	H	I	H	I	F	A	G	I	E	G
8	A	G	J	D	H	B	E	D	A	C
9	J	A	D	J	C	C	C	J	D	E
10	B	E	B	B	D	D	A	B	B	A

The comparison of buoy data and HF radar results are shown in Figure 3.28 below:

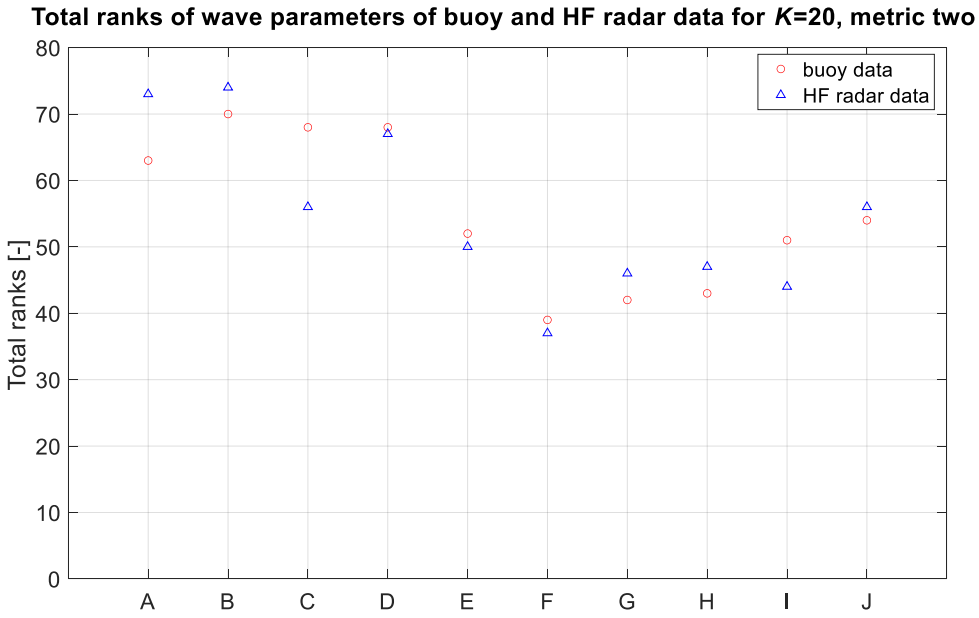

Figure 3.28: The total ranks of different methods of buoy data and HF radar data, metric two.

From the results, it can be seen that the relationship between the regrouping quality of a wave parameter and the degree of participation of the same wave parameter in the regrouping process is very clear. For example method C (*K*-means clustering by using $S(f)$) provides rank 1 for the wave parameter $S(f)$ and method D (clustering by using $S(f,\theta)$) provides rank 1 for wave parameter $S(f,\theta)$. However, methods C and D perform badly for almost all of the other parameters, which results in a total rank of the 7^{th} and 8^{th} of ten regrouping methods as shown in Figure 3.28.

From the definition of method B, the mean wave direction θ_m was used directly as an input of the binning process. From the results, it can be seen that method B was both of rank 1 for θ_m of buoy and HF radar sea states.

Another important thing that can be noticed is the significantly increased metric value for T_e from methods C and D (rank 9 and 10 for both buoy data and HF radar data) to methods I and J (rank 1 and 2 for buoy data and rank 2 and 1 for HF radar data). It means the distinctness has been greatly improved by the new methods introduced and the target to find a more even representative sea state distribution in H_s - T_e space has been successfully fulfilled. However, as a result of this, the representativeness of other parameters was negatively influenced. Taking H_s for example, the representativeness was reduced from methods C and D (rank of 6 and 7 for buoy data and rank of 3 and 8 for HF radar data) to methods I and J (rank of 8 and 10 for buoy data and rank of 7 and 9 for HF radar data). This phenomenon can also be noticed in metric one results. Some benefits of methods C and D were well preserved in methods I and J. For wave parameter $S(f)$, method I ranked 3 for buoy data and 2 for HF radar data. For wave parameter $S(f,\theta)$, method J ranked 3 for buoy data and 2 for HF radar data. It was because method I and method J used method C and method D as the first step respectively, which guaranteed a high quality for $S(f)$ and $S(f,\theta)$.

By using metric two, method F had the best overall performance, with both the lowest total ranks of buoy and HF radar data. It was completely different from the results of metric one, in which method F provided the lowest representativeness.

Another main difference between metric one and metric two is that methods C and D performed poorly using metric two. The main reason was that the inter-cluster differences S_B for methods C and D were low compared with other regrouping methods. From metric one it can be seen that methods C and D had the lowest intra-cluster differences which led to a low value of S_W for one-dimensional wave parameters. However, the values of S_B for methods C and D were also low, which led to low values of S_B/S_W. It explains why the regrouping quality for methods C and D according to metric two is low.

3.8 Discussion of the value of *K* on the regrouping quality

As mentioned in Section 2.2.4, based on the industrial standard [51], the time duration for irregular wave cases is 20 to 30 min for a full-scale prototype. In this thesis, for a full-scale WEC model testing, the time duration is 1 hour to guarantee the high quality of the testing results.

For example, for a typical TRL stage 1 model tested with a scaling factor of 25 (this scaling factor will be used in Chapter 5), according to Froude scaling law, the time duration of the model testing is 12 min. Considering the time spent for the wave to calm down between 2 adjacent wave cases (8 to 10 min), it is only available to test about 20 irregular wave cases per day. Considering the limited resources for tank testing, it is necessary to decide the total number *K* of sea states for WEC model testing carefully. In this section, the influence of *K* on the regrouping quality is discussed.

The total data set of Long Island's buoy measured directional wave spectra (74896 hourly sea states) was used as an example. The regrouping method chosen to use was method C (non-directional wave spectra *K*-means clustering method). The reason for using method C was because method C was a direct use of the *K*-means clustering method and presented the overall best regrouping quality. Both of the metrics were used to assess the regrouping quality with different *K* values.

As explained in Section 3.2.1, to obtain the optimal regrouping results, each *K*-means clustering calculation needed to be repeated a number of times to reduce the effect of the randomness introduced from the creation of the initial cluster centres. However, due to the large amount of total data set to process (74896 hourly sea states), the number of replicates for each *K* value was set to one (The total calculation time for the entire dataset using MATLAB is about 3 weeks with a 2.70 GHz CPU). After calculation, the regrouping results from $K = 2$ to $K = 356$ were obtained. For each regrouping result of a certain *K* value, the values of metric one of different wave parameters were calculated by Equation 3.23, which are shown in Figure 3.29 below:

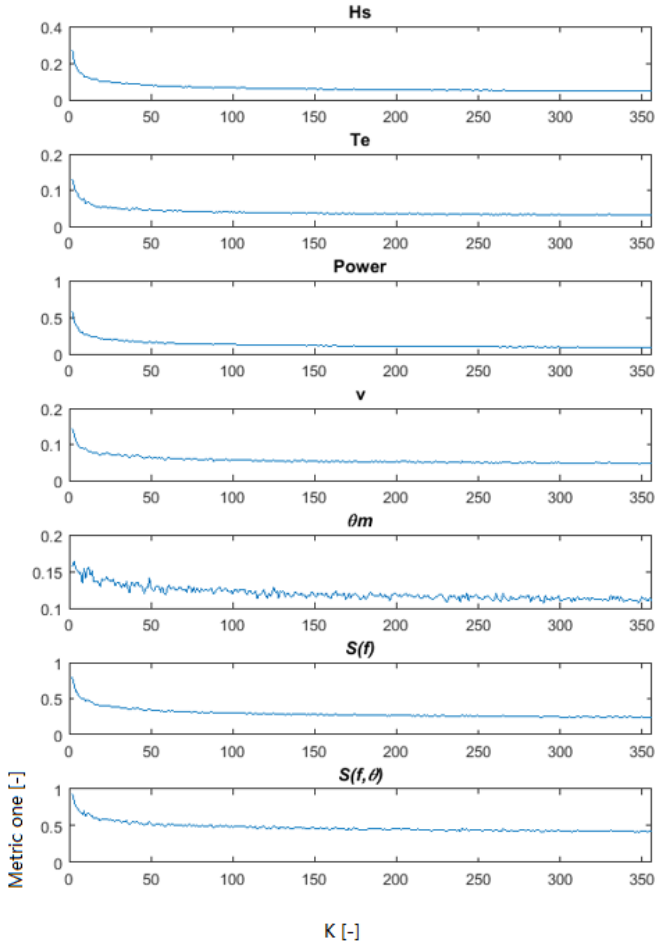

Figure 3.29: Metric one for different wave parameters with different *K* values (*K* = 2 to *K* = 356), Long Island sea states, method C, non-directional wave spectrum *K*-means clustering method.

It can be seen from Figure 3.29, that there is an obvious trend of decrease of the metric one value for all of the seven wave parameters when the number of groups *K* increases. There is a sharp decrease when *K* is small (from *K* = 2 to *K* = 20). It means for small *K* values, the decrease of metric value by increasing *K* is much faster than for large *K* values. According to the definition of metric one, the lower the value is, the better the regrouping quality. It means the regrouping results of the same total data set S can be improved by increasing the value of *K*.

It can be noticed that fluctuations appeared in some curves. This is believed to be due to the following reason. For each *K* value calculated (from 2 to 356), the number of *K*-means clustering replicates is calculated once. It is unlikely to achieve the optimal regrouping results through only one run due to the uncertainty which was introduced by creating the centres for the first iteration as explained in Section 3.2.1. It is possible that the clustering result of $K = n+1$ is no better than the result of $K = n$, which results in fluctuations in the curves. However, the overall trend of decrease of metric one values with the increase of *K* is obvious, which means the regrouping quality increases with the increase of *K*.

The same regrouping results were calculated using metric two, which is shown in Figure 3.30 below:

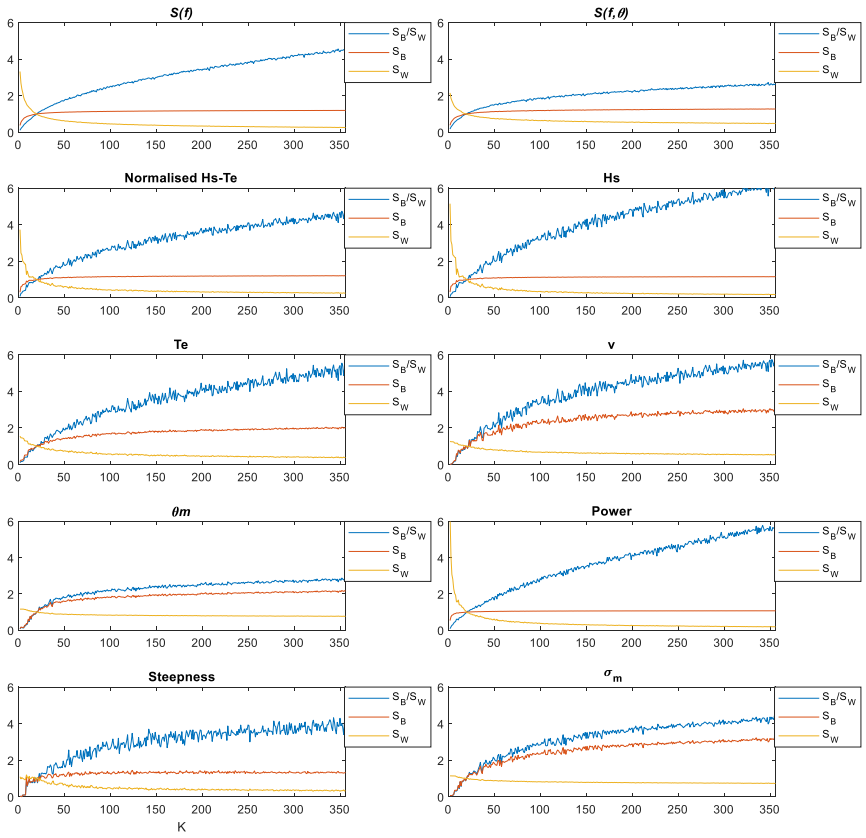

Figure 3.30: Metric two of different wave parameters with different K values (K = 2 to K = 356). Long Island sea states, method C, non-directional wave spectrum K-means clustering method, values have been normalised by the results of K = 20 respectively.

In order to see the trend for metric two easily, parameters were divided by the results calculated with K = 20. That is, S_B/S_W values were normalised by S_B/S_W with K = 20, S_B values were normalised by S_B with K = 20 and S_W were normalised by S_W with K = 20.

It can be seen clearly that for all of the ten wave parameters assessed, when K increased, the value of S_B/S_W (metric two) also increased. There were two reasons for that. The first one was the increase of the distinctness between different groups $S_B$and the second one was the decrease in the differences between the members and their cluster mean S_W

within the same group. S_B/S_W increased at a greater rate when *K* was small, which was the same as what was found with metric one. There were also fluctuations that can be seen in the curves for the same reason in metric one, which was due to a limited number of replicates in the *K*-means clustering process. According to the definition of metric two, the larger the value of S_B/S_W is, the better the regrouping result. From the results of metric one and metric two, it can be found that by increasing the number of groups *K* obtained from the same data set S, the quality of *K*-means clustering results can be increased. The increase in regrouping quality is much more obvious when *K* is lower than 20.

As a result, in order to use the *K*-means clustering method to obtain the representative sea states for WEC model testing, it is better to use a large *K* value than a small *K* value. However, the number of representative sea states for tank testing cannot be increased unlimitedly due to the limitation of resources.

3.9 Conclusion

The purpose of this chapter was to obtain a number of *K* representative sea states from a large data set for WEC model testing. Ten regrouping methods were compared based on their regrouping quality including two binning methods and eight *K*-means clustering methods.

Two metrics were utilized to assess the quality of ten regrouping methods from A to J using both Long Island buoy data and HF radar data set. It was shown that the regrouping results from two completely different data sets have great similarities, which means the

use of different regrouping methods is not limited to a certain ocean area. However, as shown in the wave rose plots in Figure 3.3 and Figure 3.5, both of the data sets used in this research were not highly directional with most of the waves coming from a narrow directional range. As a result, the following conclusion only applies to the ocean area used in this research with limited wave directionality.

If only considering the minimization of intra-group average differences (metric one), methods C and D provide the overall optimal results. However, if considering both the intra-group difference together with inter-group distinctness (metric two), method F provides the overall optimal performance. Methods I and J showed improved performance relative to methods C and D measured by metric two with a good balance between the representativeness of groups and the uniformity in H_s - T_e space. It also showed that the regrouping methods based on normalising certain wave parameters (method E, F, G, H and E-max, F-max, G-max, H-max) is not a good idea due to the difficulty in balancing the relative importance of wave parameters with different units.

It has been found that the regrouping quality of wave parameters depends on the degree of participation of the same wave parameters in the regrouping process. The increase in the relative importance of one wave parameter always leads to better representativeness but it will also lead to a decrease in the representativeness of other wave parameters. For WECs that are not influenced by wave directionality, method C is better than method D.

From the definition of ten regrouping methods, except for two binning methods A and B, methods C to J were all based on the *K*-means clustering technique. During the iteration

process, the *K*-means algorithm only focuses on minimizing the intra-group average difference, which had no direct relationship with the inter-group distinctness. It means metric one is in strict accordance with the definition of the *K*-means clustering technique while metric two is not. As a result, metric two is more applicable as an exploration tool and is used mainly to indicate the improvement of distinctness for methods I and J. From metric one, method C shows a great ability to obtain the representative sea states in $S(f)$ space and method D has a great ability to find the representative cases in $S(f, \theta)$ space compared with other methods.

4. Numerical analysis for the RM3 WEC using representative sea states

After obtaining the representative sea states from an ocean area, this chapter focuses on the power output performance of a WEC model in the representative sea states. In this chapter, $K = 20$ is used. Although there are numerous wave parameters used to assess the wave regrouping quality in Chapter 3, for WEC model performance, the main focus is on the average power output performance and the annual energy output estimation.

In this chapter, a point absorber numerical model from WEC-SIM is selected to use for this purpose. All of the representative sea states obtained from ten regrouping methods A to J from Chapter 3 are tested on this numerical model to assess the representativeness of the power output performance. The representative sea states are also used to predict the annual energy output.

Section 4.1 is the introduction of the RM3 WEC model and the testing of the representative sea states from ten regrouping methods A to J on the model to estimate the power output performances. Section 4.2 is to estimate the annual energy output by using the representative sea states from different methods and the impact of K. Section 4.3 is to assess the linearity of the RM3 WEC. Section 4.4 is the conclusion.

4.1 Average power output from representative sea states of different methods on RM3 WEC

4.1.1 RM3 point absorber

The U.S. Department of Energy established a reference model (RM) project to test a series of marine technologies including current (tidal, open-ocean, and river) turbines and WECs. The RM3 point absorber is the reference model built for the WEC study, which has been tested both numerically and experimentally, in order to assess the performance of this WEC and the potential for commercial applications [168].

The RM3 is a two-body point absorber that consists of a float and a spar plate. The relative heave movement of the two bodies in the waves drives a translation PTO to generate electricity. The geometric dimensions and mass properties of the full-scale prototype are shown in Figure 4.1 and Table 4.1 below [118]:

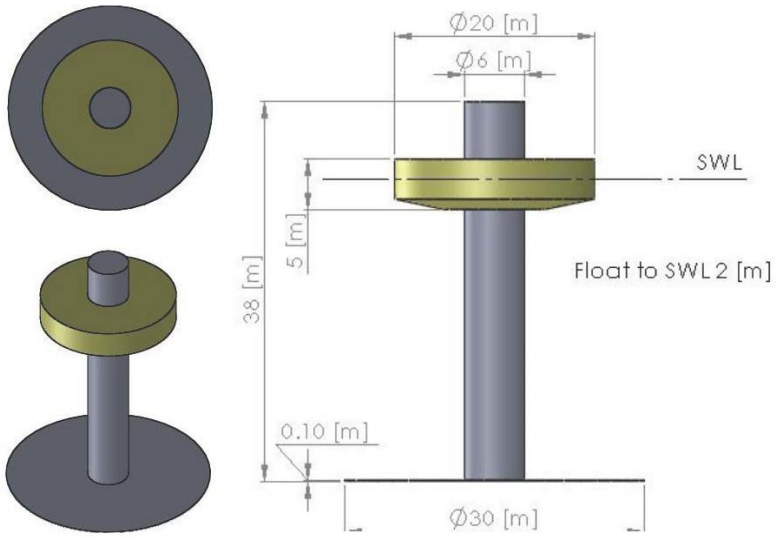

Figure 4.1: Geometric dimensions of the RM3 point absorber [118].

Table 4.1:Mass and geometric properties of the RM3 WEC [118].

Body	CoG [m]	Mass [tonne]	Direction	MOI [kg.m^2]		
Float	0	727.01	x	2.09E+07	0	0
	0		y	0	2.13E+07	0
	-0.72		z	0	0	3.71E+07
Spar plate	0	878.3	x	9.44E+07	0	0
	0		y	0	9.44E+07	0
	-21.29		z	0	0	2.85E+07

The numerical model of the RM3 point absorber was built in WEC-SIM. As was introduced in Section 2.4.1, WEC-SIM is an open-source WEC design tool based on the Simulink module in MATLAB [169]. It is a time domain analysis software that requires the frequency domain analysis results (hydrodynamic parameters) as input. By defining the sea states and mooring and PTO system using the Simulink model as shown in Figure 2.23, it can simulate the model responses in different wave conditions (regular/irregular). The numerical model of the RM3 point absorber is provided on the WEC-SIM official

website as a tutorial model and it has been tested and verified by experimental results [168]. Due to the simplicity of the model geometry, it is very efficient to run. Each irregular sea state with a 3600s repeat time in full scale only took about 2 minutes to finish with a 2.70 GHz CPU. As a result, the power output analysis using representative sea states is carried out using this RM3 model.

The numerical model of the RM3 point absorber is shown in Figure 4.2 below. The two bodies of the point absorber are considered rigid. The model floats still in the water when the analysis started and the equilibrium position of the CoG of both bodies (the float and the spar) is calculated automatically. The origin of the global reference system is on the still water level (SWL) with the z-axis pointing upwards. The incoming wave direction is the positive direction along the x-axis, i.e. from left to right in Figure 4.2.

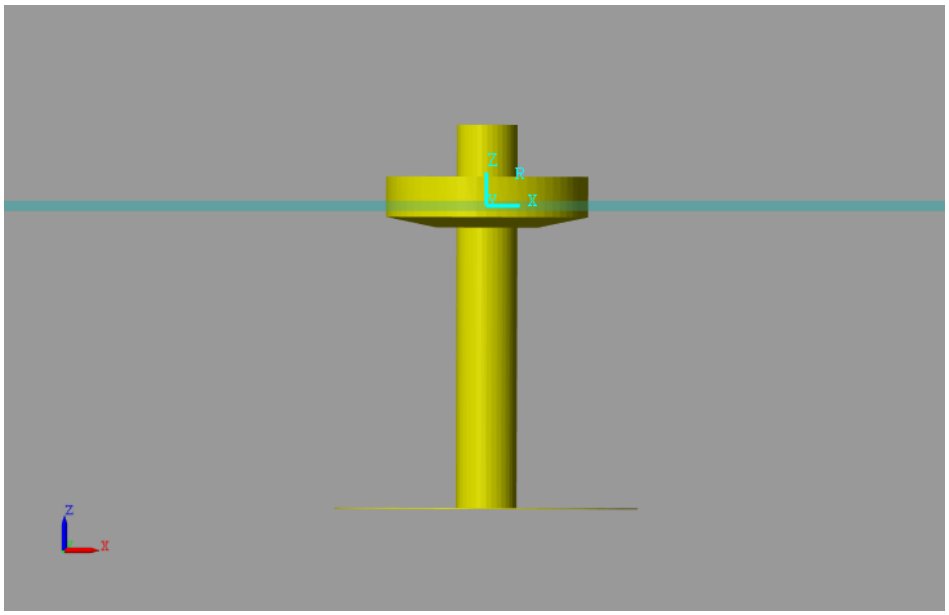

Figure 4.2: The RM3 point absorber model with the coordinate system.

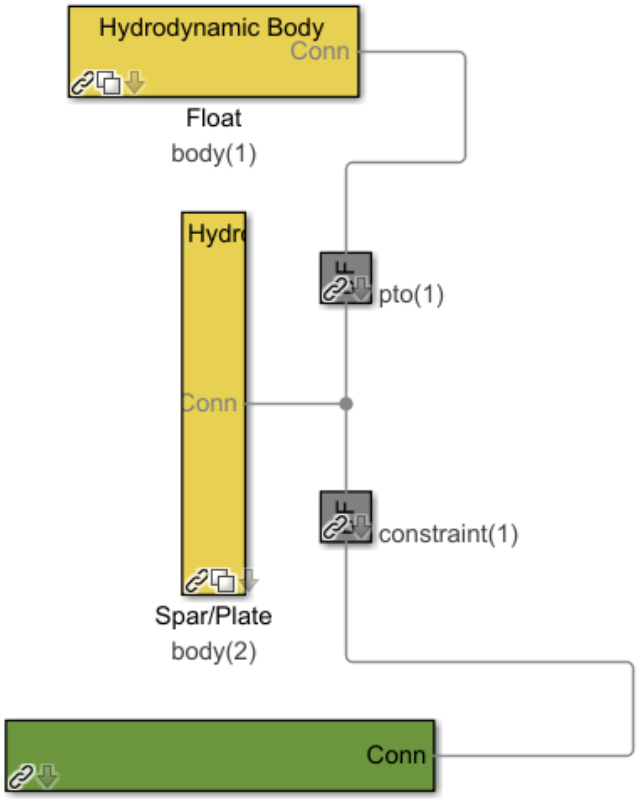

Figure 4.3: The Simulink model of RM3 point absorber.

The Simulink model is shown in Figure 4.3. According to the original model design, there are no mooring lines on this model. The hydrodynamic parameters were calculated using WAMIT. During the simulation, the model movement is constrained to surge, pitch, and heave for both of the bodies due to the symmetry of the model in the x-o-z and the y-o-z planes. The motion responses are the same for both the float and the spar plate in surge and pitch. However, there is a relative heave movement between the two bodies along the spar. There is a translational PTO with a translational damping parameter k_T between two bodies. The power output time series $p(t)$ of the WEC is calculated based on the following Equation 4.1 [170]:

$$p(t) = k_T \cdot \left|\overrightarrow{v_r(t)}\right| \cdot \left|\overrightarrow{v_r(t)}\right| \quad (4.1)$$

in which $v_r(t)$ is the relative velocity of the float and the spar plate, k_T is the translational PTO damping parameter which is 1.20e+06 N/m/s [171].

WEC-SIM supports different kinds of wave definitions. The user can create a regular wave by specifying wave height *H* and wave period *T*; create a non-directional irregular wave by importing the wave elevation signal directly; create a generic/parametric non-directional wave spectrum (e.g. JONSWAP, PM) by assigning significant wave height H_s and peak period T_p; or directly import a complex non-directional wave spectrum *S*(*f*) with a series of random phase angles ϵ for each frequency component *f*.

A simple WEC-SIM regular wave analysis is used as an example. In this example, a regular wave with *H* = 2.5 m and *T* = 8 s was created, the total time duration was 400 s with 100 s ramp-up time and the time step was 0.1 s. According to the wave theory [40], the wave elevation signal for a regular wave is calculated by the following Equation 4.2:

$$\eta(x,t) = \frac{H}{2} cos(\omega t - k_w x + \epsilon) \quad (4.2)$$

in which η is the wave elevation signal; *H* is the regular wave height; k_w is the wave number, ϵ is the phase angle; *x* is the distance from the origin of the coordinate system.

After analysis, the structural responses of both bodies including the position, velocity, acceleration, and forces were obtained. The relative velocity between two bodies was also obtained. The power output time series of the RM3 point absorber was calculated from Equation 4.1, which is shown in Figure 4.4 below:

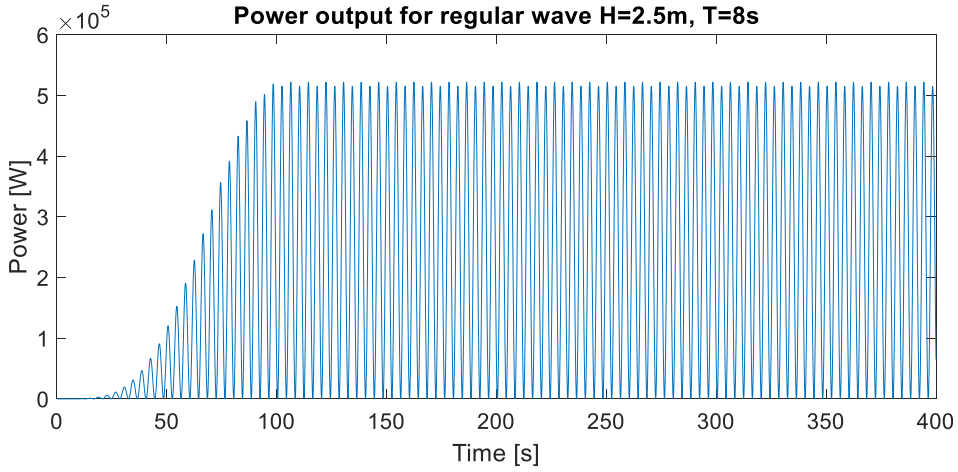

Figure 4.4: Power output time series for the regular wave with H = 2.5 m, T = 8 s, ramp up time = 100 s, run time = 400s.

The average power output $P_{average}$ in this wave condition is calculated from Equation 4.3:

$$P_{average} = \frac{1}{T_2 - T_1} \int_{T_1}^{T_2} p(t)dt \tag{4.3}$$

in which $p(t)$ is the power output time series shown in Figure 4.4. T_1 and T_2 are the lower and upper boundaries of the time window selected for the average power output calculation. In this example, the ramp-up time is 100 s. In order to get rid of the influence

from the ramp-up time and keep the stable part with an integer number of wave periods, a time window with T_1 = 100.4 s and T_2 = 396.5 s is used. After calculation, the average power output in this regular wave is 0.2739 MW.

In addition to the default time step 0.1s, other time steps of 0.01 s, 0.02 s, 0.05 s, and 0.2 s were also tested. It was found that there was a slight increase in the average power output with the decrease in the time step. However, the difference was within 1.5%. As a result, in the following analysis, the time step is still the default value of 0.1 s.

4.1.2 Average power output representativeness analysis

As shown in Chapter 3, in total ten regrouping methods A to J were examined and compared. Each regrouping method provided *K* (or close to *K* for binning methods A and B) groups and corresponding representative sea states. This section is to test the representative sea states on the RM3 model to obtain the average power output and assess the representativeness of the average power output.

Each representative sea state from ten regrouping methods A to J was imported to WEC-SIM for the average power output simulation in the form of the non-directional wave spectrum $S(f)$. Each frequency component of the non-directional wave spectrum was assigned with a random phase angle ranging from 0 to 2π.

The time duration for each non-directional wave was set to 3800s with 100s ramp time.

Taking one representative sea state from method C for example, this representative sea state was from the 13th sub-plot (group 13) containing 183 members from Figure 3.15. The non-directional wave spectrum of this sea state is shown in Figure 4.5.

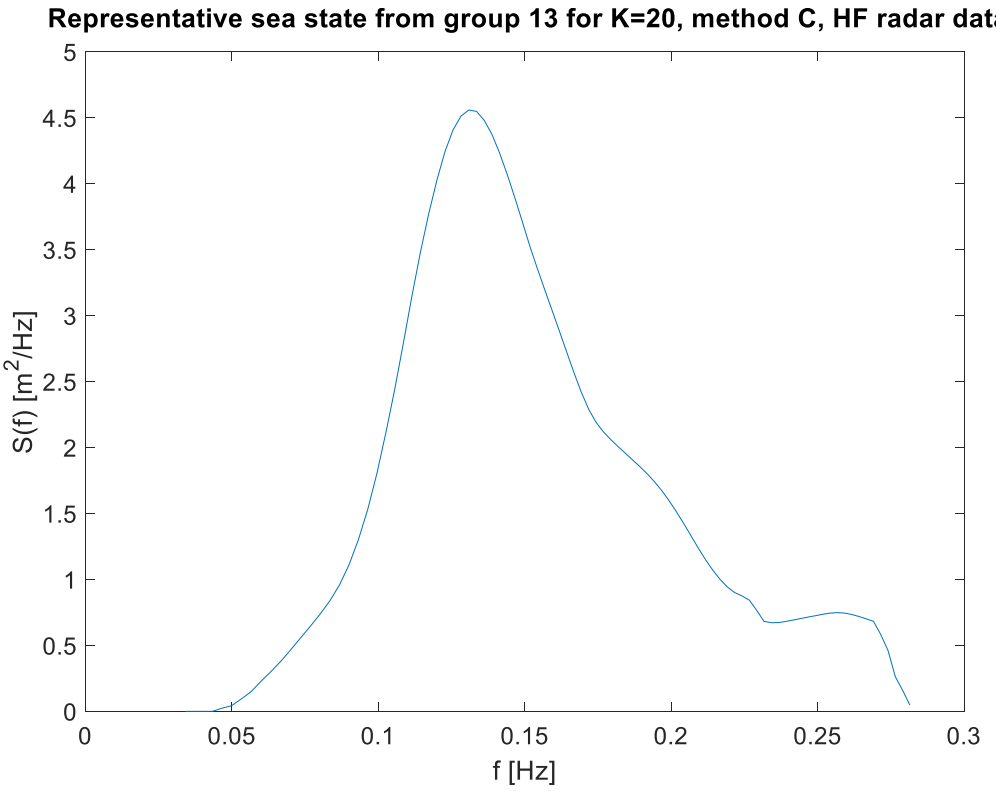

Figure 4.5: Representative sea state from group 13 with 183 members inside, method C, HF radar data. H_s = 2.55 m, T_e = 7.11 s.

By importing the representative sea state from group 13 into the WEC-SIM model and running, the power output time series for the RM3 point absorber was obtained from Equation 4.1. The power output time series is shown in Figure 4.6. Here the time window from T_1 = 200 s to T_2 = 3800 s was used to remove the influence of 100 s ramp-up time and to guarantee a 3600s time window length. The average power output was calculated from Equation 4.3. After calculation, for this representative sea state, the average power output was 0.1117 MW.

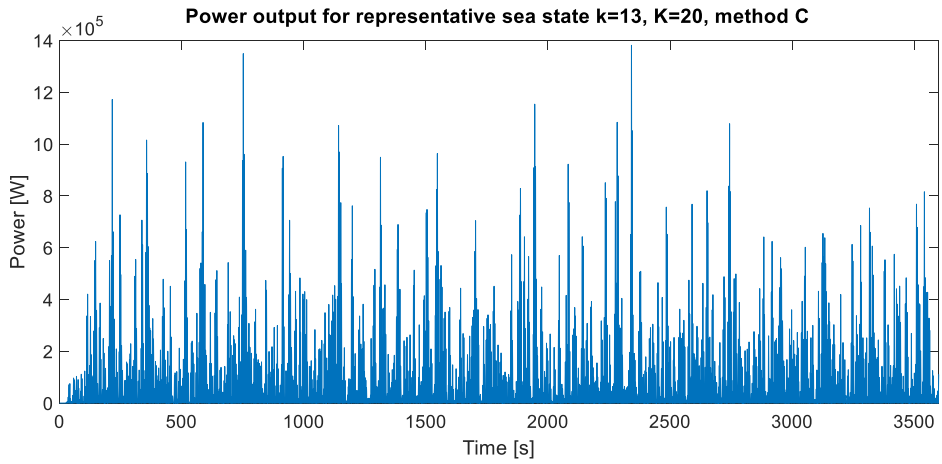

Figure 4.6: Power output of a representative sea state from group 13 of method C, HF radar sea state. H_s = 2.55 m, T_e = 7.11 s.

Each representative sea state's average power output was calculated accordingly with the same setup for regrouping methods A to J.

To estimate the representativeness of the power output performance, each of the 3161 HF radar sea states' average power output was calculated as well. This was done by inputting each of the hourly wave spectra into WEC-SIM using a loop in MATLAB.

The regrouping quality from different regrouping methods A to J for the average power output performance was assessed by using metric one from Equation 3.23 in Section 3.5.1. The result of metric one is shown in Figure 4.7.

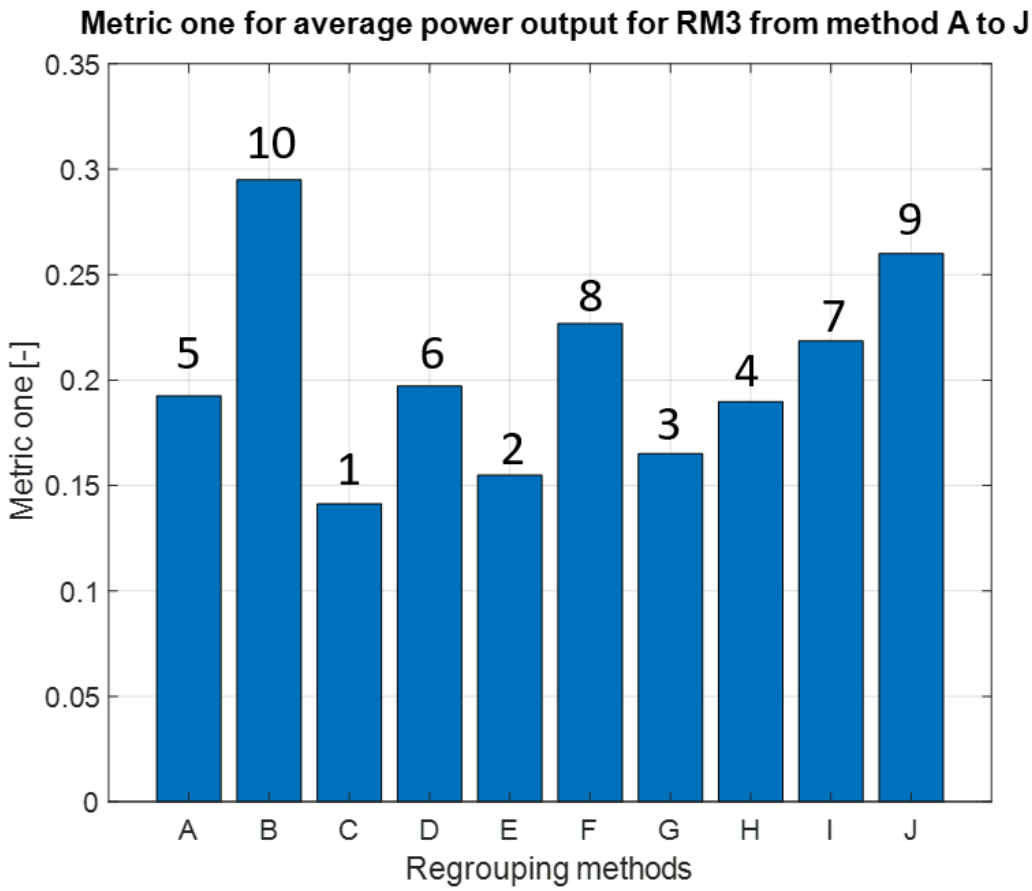

Figure 4.7: Metric one for the average power output of RM3 point absorber with different regrouping methods A to J. The rank of each method is plotted on top of each bar.

By comparing the results from different methods shown in Figure 4.7, method A (H_s - T_e binning methods) provides medium representativeness (rank 5) since it regroups sea states by only considering H_s and T_e with equally sized bins. Method B provides the worst representativeness (rank 10) and is the first to be eliminated from use. Method C (non-directional wave spectrum *K*-means clustering method) shows the highest representativeness (rank 1) for the average power output. Method D (directional wave spectrum clustering, rank 6) does not perform as well as method C both for incoming wave power representativeness (Figure 3.21) and WEC power output representativeness. According to previous analysis results from Chapter 3, taking into account one wave parameter in the *K*-means clustering process always reduces the influence of other wave

parameters. The RM3 WEC is not affected by wave direction, which explains why the metric one results for incoming wave power *P* from method D is not as good as method C. Method I and J both perform poorly (rank 7 and 9) when assessed using metric one. This is because methods I and J were created to obtain representative sea states with high distinctness of different groups as explained in Section 3.4. The representativeness is inevitably negatively affected.

From the results, method C provides the highest representativeness (rank 1) for the average power output from the RM3 numerical model. From Table 3.3, method C is of rank 2 for the incoming wave power. As a result, the representative sea states from method C are recommended for site-specific sea states physical model testing for the RM3 point absorber.

It is noticeable that the metric result from Figure 4.7 was very similar to the wave power parameter *P* metric one value in Figure 3.21. This will be discussed further in Section 4.3.

4.2. Annual energy output estimation with different regrouping methods.

4.2.1 Impact of *K* on annual energy output estimation

This section focuses on the annual (3161 hours) energy output estimation by using representative sea states with different *K* values. As explained in Section 3.1.1, the wave data with low signal-to-noise ratio were considered as low quality and have been removed, which left only 3161 hourly sea states available in the year analysed. However, the ability

to obtain the representative case by using *K*-means clustering was not affected by the size of the total data set. Although there are 8760 hours in total per year, the word 'annual' is still used to represent the total 3161 hours for the analysis.

In Section 3.8, the influence of *K* on the regrouping quality was discussed. In this section, a similar analysis has been conducted. The annual energy prediction with different *K* values was compared. Binning method A and *K*-means clustering method C were chosen for comparison. It was because method A was the traditional H_s - T_e binning method and method C was the novel *K*-means clustering method using H_s - T_e data points, which were suitable to compare with each other.

A. Generation of *K* groups using method C

It was straightforward to use method C to generate *K* groups. As explained in Section 3.2.2, by giving a *K* value, the corresponding *K* groups and the representative sea states were obtained.

B. Generation of *K* groups using Method A

Binning method A, as explained in Section 3.2.1, was more complex due to the existence of empty bins.

In order to obtain K non-empty bins, the number of T_e bins was decided based on the number of H_s bins. As shown in Table 4.2, the same number of H_s bins is filled using the same colour. For a certain number of H_s bins, the number of T_e bins starts from the value equal to the number of H_s bins and increases by 1 each time until it reaches the value of double the number of H_s bins.

Table 4.2: The K value for method A with different numbers of bins created.

Number of H_s bins	1	1	2	2	2	3	3	3	3	…
Number of T_e bins	1	2	2	3	4	3	4	5	6	…
Number of total bins	1	2	4	6	8	9	12	15	18	…
Non-empty bins K	1	2	4	5	7	8	9	11	14	…

Taking the number of H_s bins = 3 as an example, the number of T_e bins ranges from 3 to 6. For each case, the binning results for the HF radar data are shown in Figure 4.8 and Figure 4.9 below:

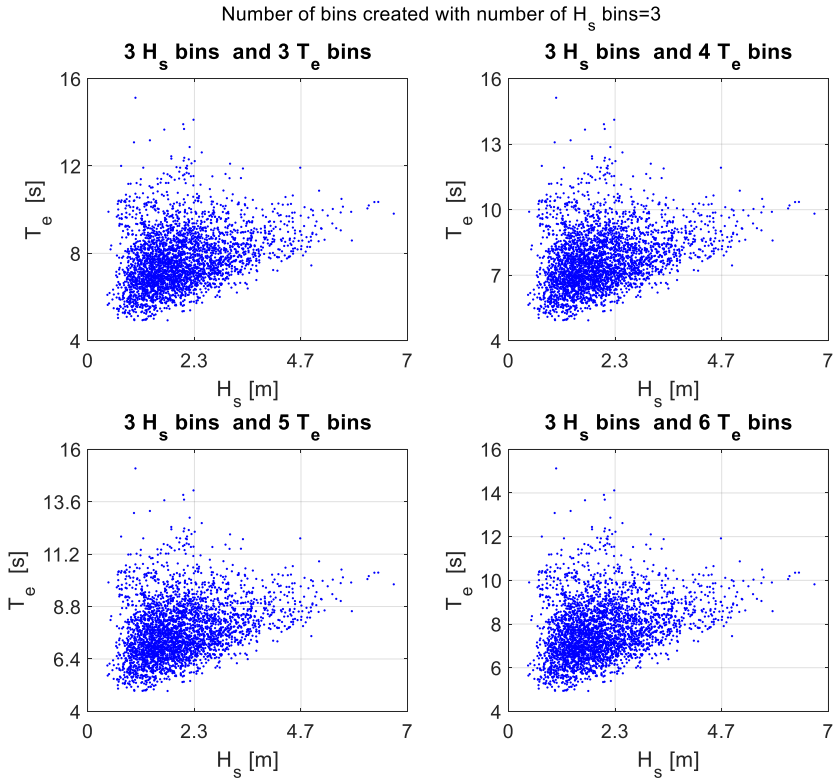

Figure 4.8: The number of bins created with the number of H_s bins = 3 and the number of T_e bins ranges from 3 to 6 for HF radar sea states. The grids of each figure represent the bins created.

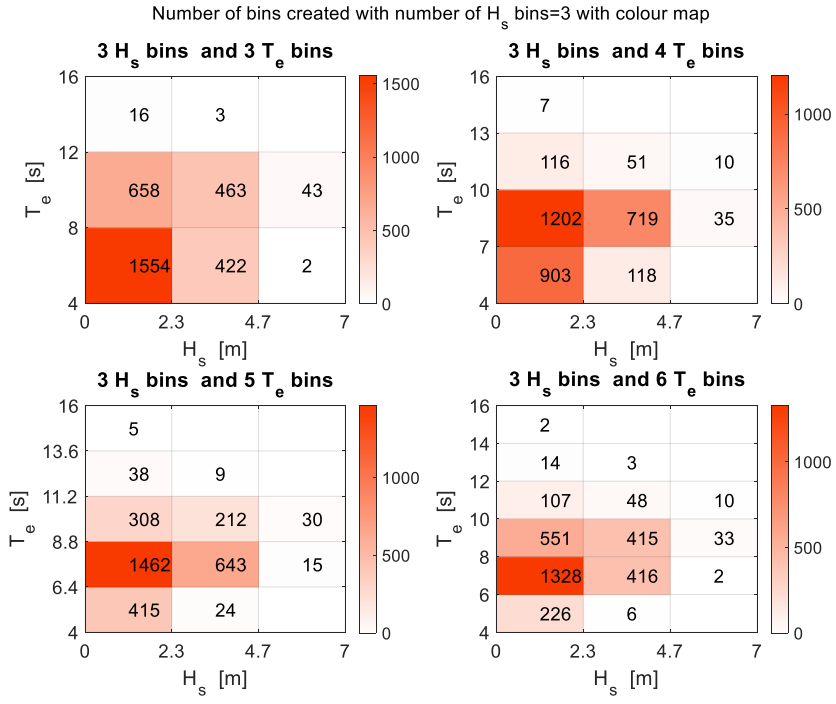

Figure 4.9: The number of bins created with the number of H_s bins = 3 with colour map and the number of sea states in each bin. The grids of each figure represent the bins created.

For the case with 3 T_e bins there are 8 non-empty bins; For the case with 4 T_e bins there are 9; For 5 T_e bins there are 11 and for 6 T_e bins there are 14. The number of non-empty bins for each case is considered as the value of *K*, which are the results for *K* = 8, 9, 11, 14 shown in Table 4.2.

All of the representative sea states from method A of each *K* value were obtained using this method.

C. Annual energy output estimation with different *K* for methods A and C

After obtaining different regrouping results (representative sea states) of different *K* values for methods A and C, the annual energy output was calculated. Each of the representative sea states was imported into the RM3 model for the average power output calculation as shown in Section 4.1.2.

Before comparing the annual energy output of methods A and C with different *K* values, it was necessary to calculate the actual annual energy output E_{actual}, which required the calculation and summation of every hourly sea state's average energy output. During the calculation of the metric one value of average power output in Section 4.1.2, each of the 3,161 sea state's average power outputs had already been calculated. By multiplying each of the average power outputs with one-hour time duration and summing up, the actual annual (3161 hours) energy output was obtained. After calculation, E_{actual} = 2.456e+05 kW.h.

The next step is to obtain the annual energy output by using representative sea states from different *K* values. For a certain value of *K*, the annual energy is calculated from Equations 4.4 and 4.5 below:

$$E_k = P_k \times M(k) * 3600 \tag{4.4}$$

and

$$E_{total} = \sum_{k=1}^{K} E_k \tag{4.5}$$

in which *k* is the label of the group (*k* = 1,2,3…*K*); $M(k)$ is the number of sea states in group *k*; P_k is the average power output of the representative sea state in group *k*, which is obtained from Equation 4.3; E_k is the energy output from $M(k)$ sea states (estimated by using the representative sea state) in group *k*; E_{total} is the annual energy output estimation for all of the *K* groups together, which is based on the available total data set (3161 hours) as it was explained at the beginning of Section 4.2.1. The unit of the energy obtained from Equation 4.5 is in J, which is converted into kW.h afterward.

For methods A and C, the average power output of each representative sea state from *K* = 1 to *K* = 170 was calculated. The total time spent on calculating both methods with different *K* values was about 3 weeks with a 2.70 GHz CPU using WEC-SIM. Then the annual energy output from each *K* value was calculated from Equation 4.4 and Equation 4.5. The annual energy output estimated for methods A and C with different *K* values is plotted together to compare, see Figure 4.10 below:

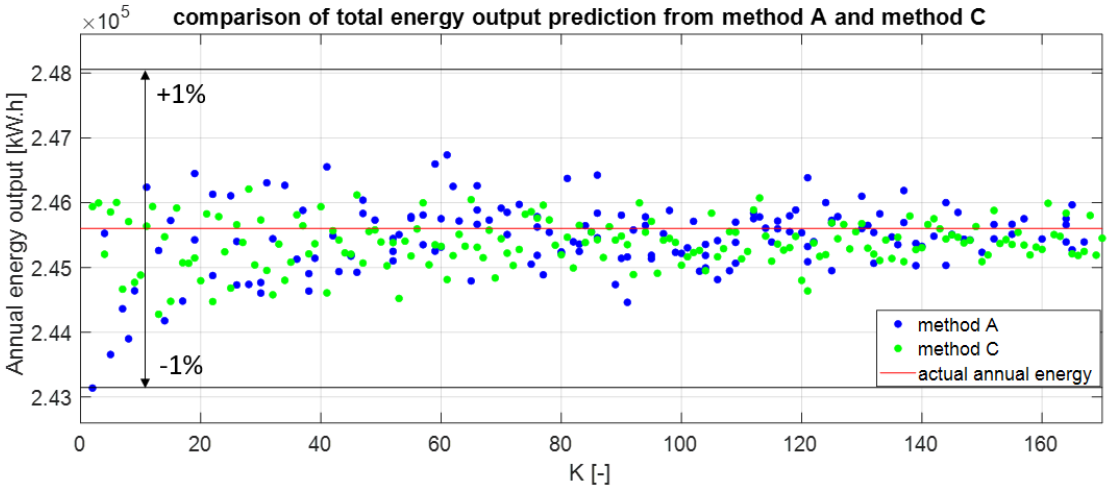

Figure 4.10: The annual energy output prediction from method A and method C with different *K* values. Actual annual energy is 2.456e+05 kW.h. The two black lines are the ±1% relative error limits with reference to the actual annual energy output.

From Figure 4.10, it can be seen that both methods A and C provide a very accurate annual energy output prediction with only ±1% relative error with the actual value no matter what *K* values were used. The relative error ψ_K from the actual annual energy for a certain *K* was calculated by the following Equation 4.6:

$$\psi_K = \frac{|E_{total} - E_{actual}|}{E_{Accurate}} \times 100\% \tag{4.6}$$

The difference in the annual energy output from different *K* values was introduced from the random phase angle generated in the WEC simulation process. It will be further discussed in Section 4.2.2.

4.2.2 Annual energy output estimation with different regrouping methods and comparison with generic JONSWAP spectrum results

In Chapter 3, ten regrouping methods A to J have been used to obtain the representative sea states with K = 20 using HF radar sea states. In this section, these representative sea states are used to estimate the annual energy output prediction. The average power output of the representative sea state is calculated using the same method shown in Section 4.1.2. To check the influence from the random phase angles generated in the WEC-SIM simulation each time, the calculation of each average power output was repeated in total 3 times. Equations 4.4 and 4.5 were used for the annual energy output estimation.

The calculation has shown that each regrouping method's annual energy output prediction was very close to each other. The results of all 3 repeats are shown in Table 4.3 below:

Table 4.3: Annual energy output prediction from method A to J with repeats [kW.h]

Method	A	B	C	D	E
1st repeat	2.444E+05	2.460E+05	2.456E+05	2.454E+05	2.457E+05
2nd repeat	2.464E+05	2.443E+05	2.454E+05	2.448E+05	2.451E+05
3rd repeat	2.455E+05	2.448E+05	2.448E+05	2.456E+05	2.449E+05
Method	F	G	H	I	J
1st repeat	2.457E+05	2.447E+05	2.465E+05	2.458E+05	2.455E+05
2nd repeat	2.444E+05	2.464E+05	2.446E+05	2.451E+05	2.450E+05
3rd repeat	2.448E+05	2.448E+05	2.453E+05	2.458E+05	2.450E+05

The results are plotted together with the actual annual energy output (2.456e+05 kW.h) in Figure 4.11 below:

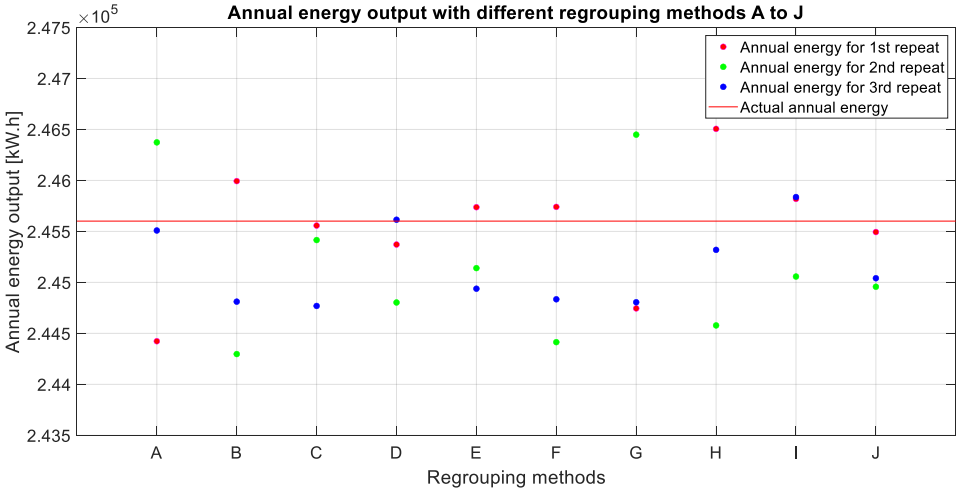

Figure 4.11: Annual energy output estimation from methods A to J for 3 repeats. Actual annual energy output is 2.456e+05 kW.h.

The relative error ψ_K between the accurate total energy output was calculated from Equation 4.6. The results are shown in Table 4.4 below:

Table 4.4: The relative error ψ_K with the accurate annual energy from method A to J [%], K = 20.

Method	A	B	C	D	E
1st run	-0.48	0.16	-0.02	-0.09	0.06
2nd run	0.31	-0.53	-0.08	-0.32	-0.19
3rd run	-0.04	-0.32	-0.34	0.01	-0.27
Mean value	-0.07	-0.23	-0.15	-0.13	-0.13
STD	0.32	0.29	0.14	0.14	0.14
Method	F	G	H	I	J
1st run	0.06	-0.35	0.37	0.09	-0.04
2nd run	-0.48	0.35	-0.42	-0.22	-0.26
3rd run	-0.31	-0.32	-0.11	0.1	-0.23
Mean value	-0.24	-0.11	-0.05	-0.01	-0.18
STD	0.23	0.32	0.32	0.15	0.1

From the results, it can be seen that each regrouping method provides a very accurate annual energy output estimation with a relative error ranging from -0.5% to +0.5%. This relative error is obviously introduced from the random phase angle generated for each repeat. It can be also noticed that no matter what regrouping method is used, the accurate annual energy output can be calculated from a small number (K = 20) of representative sea states.

In order to see the difference, the annual energy estimated using the H_s - T_p JONSWAP generic/parametric wave spectrum was obtained and compared with the annual energy estimation from the 1st repeat shown in Table 4.3. The equation for a JONSWAP wave spectrum was calculated from Equation 2.15 to 2.19 using Γ = 3.3 [50], with H_{m0} ,T_p from each representative sea state of different regrouping methods as input. For each representative sea state, the corresponding JONSWAP wave spectrum was calculated. Each JONSWAP wave spectrum was imported to WEC-SIM for average power output calculation as explained in Section 4.1.2. The annual energy output estimated by using the JONSWAP spectrum results was obtained from Equations 4.4 and 4.5, which are shown in Table 4.5.

Table 4.5: Annual energy output prediction from methods A to J using JONSWAP wave spectrum

Method	A	B	C	D	E
E_{total} [kW.h]	2.573E+05	2.644E+05	2.557E+05	2.578E+05	2.568E+05
Method	F	G	H	I	J
E_{total} [kW.h]	2.557E+05	2.527E+05	2.542E+05	2.557E+05	2.546E+05

The results were plotted together with the 1st repeat from Table 4.3 and the actual annual energy output result, see Figure 4.12 below:

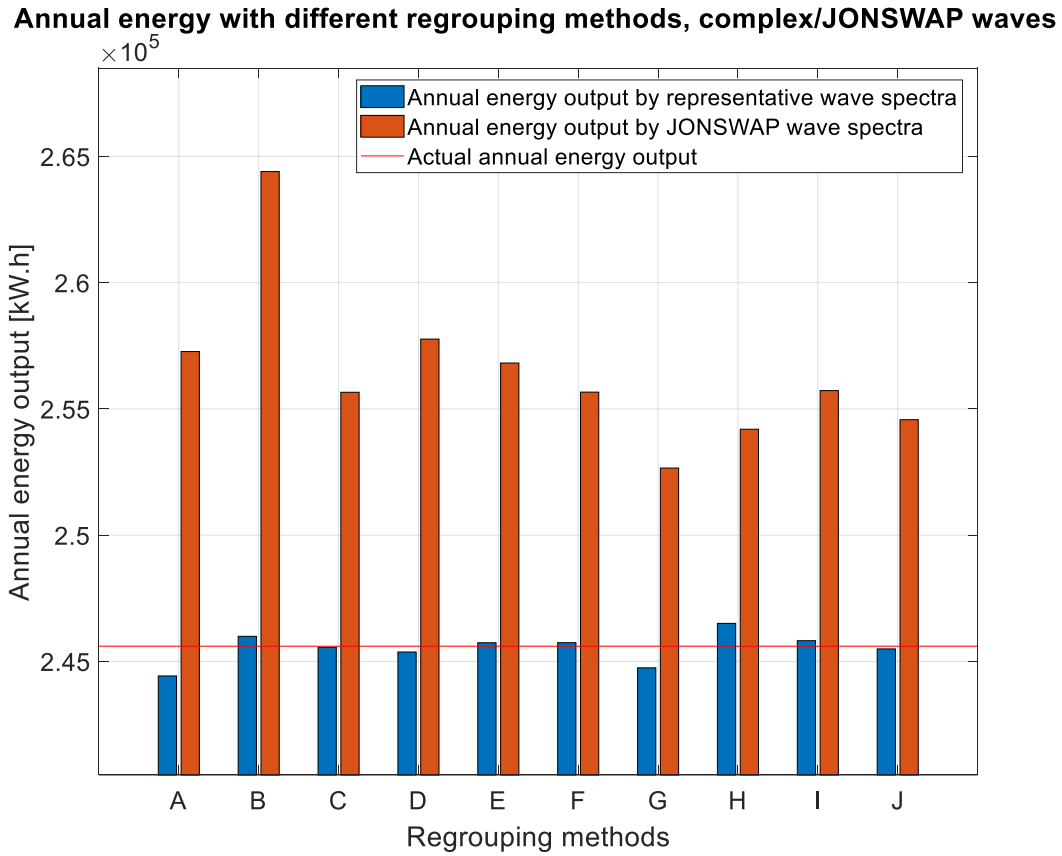

Figure 4.12: Comparison of annual energy output predicted from methods A to J using complex representative wave spectra and JONSWAP wave spectra. Actual annual energy is 2.456e+05 kW.h.

It can be noticed that when compared with the annual energy output estimated using the complex representative sea states, the annual energy output estimated from the JONSWAP wave spectra is significantly higher. The annual energy output prediction from JONSWAP waves is always over-predicted and the relative error between the actual annual energy output and the JONSWAP spectrum results ranges from 2.9% (method G) to 7.7% (method B), which is much larger than the annual energy predicted by using complex representative sea states (±0.5%).

Although each of the ten regrouping methods A to J can obtain an accurate annual energy output for the RM3 model with a ±0.5% error, it is not the case by using the traditional binning method shown as an example in Figure 2.18. In this example, the 15 bins selected in the figure for WEC model testing cannot represent all of the sea states as most of the sea states are left outside the bins. Even if the average power output from the 15 selected bins is obtained from physical/numerical analysis, it is less accurate to use them to estimate the annual energy output.

From Section 4.2, it can be seen that the input wave power and the output WEC power presented a highly linear relationship. It meant that regardless of how the sea states were grouped, the annual energy output predicted from the representative sea states was very accurate. The linearity of the RM3 model will be discussed in the next section.

4.3. Evaluation of the linearity of the RM3 WEC model

This section focuses on the discussion of the linearity of the RM3 WEC-SIM model. As explained in Section 2.2.2, the linearity of a WEC could be seen clearly from the regular wave RAO of different wave heights. In this section, a series of regular waves are tested to obtain the RAO.

4.3.1 The relative heave motion RAO for RM3 WEC in regular waves

As explained in Equation 2.6 from Section 2.2.2, the RAO for a floating body in a certain DoF in regular waves can be calculated by the following Equation 4.7:

$$RAO = \frac{a}{\zeta_a} \tag{4.7}$$

in which a is the amplitude of the movement in a certain DoF; ζ_a is the wave amplitude of the incoming regular wave. For the RM3 WEC model, the power output is from the relative heave motion between the float and the spar. As a result, the relative heave movement between two bodies is the most important parameter for the power output performance of the point absorber. The RAO for the relative heave motion needs to be calculated.

Based on the range of H_s and T_e of the HF radar measured sea states from Section 3.1, H ranging from 1 to 6 m and T ranging from 5 to 14 s were used to calculate the regular wave relative heave RAO. By using the wave period interval of 1 s and wave height interval of 1 m, there were in total 60 regular wave cases to analyse.

For each regular wave sea state of wave period T, the total time duration of $50\times T$ was used with a 100 s ramp-up time. When calculating the average relative heave amplitude, the time window was adjusted to contain an integer number of waves.

After calculation, all of the 60 regular wave cases' RAOs were obtained and plotted together, see Figure 4.13 below:

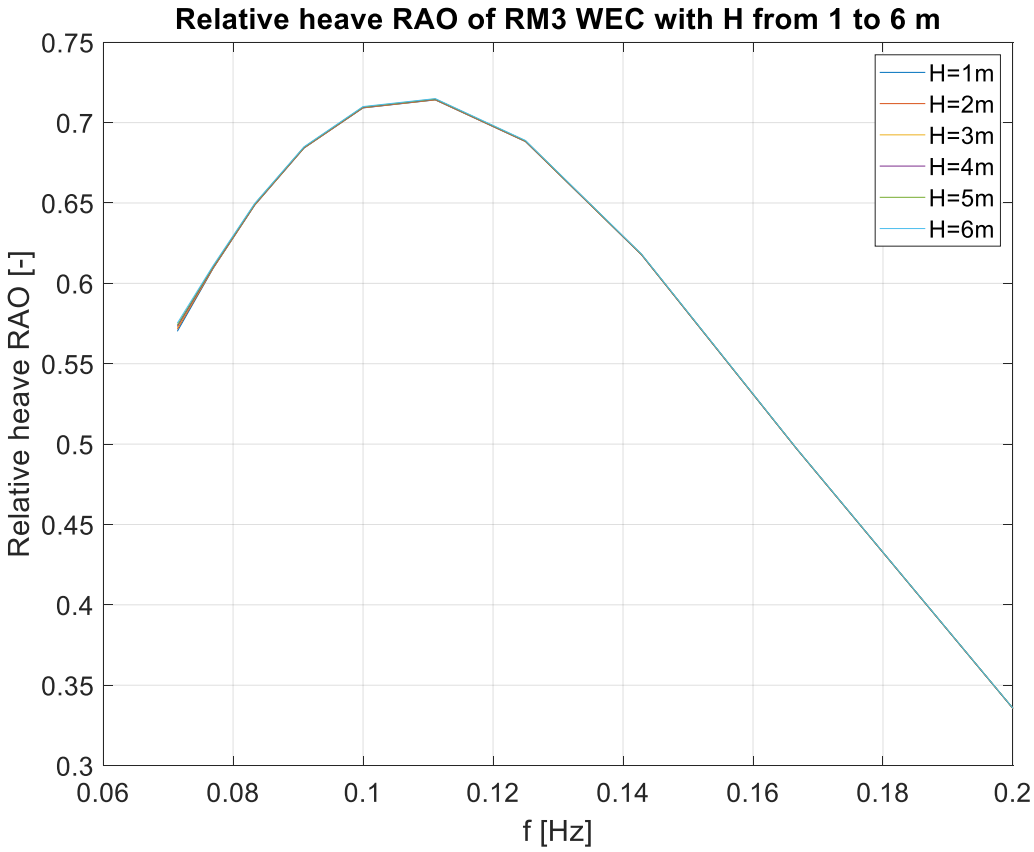

Figure 4.13: Relative heave RAO for RM3 model in 60 regular waves with *H* ranging from 1m to 6m.

It can be seen that no matter what the wave height *H* is, the RAO is almost identical and the relative RAO curves overlapped on top of each other. The average difference between different RAOs is lower than 0.1%, which means the RM3 WEC is a fully linear model.

4.3.2 The influence of the linearity of the RM3 model on the annual power output estimation.

As explained in Section 3.2, by using different regrouping methods A to J, each method provided *K* groups and each group consisted of *K* directional wave spectra. For a certain group *k* (*k* = 1,2,3…*K*) with *M*(*k*) hourly sea states in it, *m* represented each member's label in group *k*, $m = 1, \ldots M(k)$. The representative sea state from group *k*, which was $S_{rep-k}(f,\theta)$, was calculated by the following Equation 4.8:

$$S_{rep-k}(f,\theta) = \frac{1}{M(k)}(S_1(f,\theta) + S_2(f,\theta) + \cdots S_{M(k)}(f,\theta)) \tag{4.8}$$

in which $S_1(f,\theta)$, $S_2(f,\theta)\ldots$ to $S_{M(k)}(f,\theta)$ are the directional wave spectra inside group *k*. For the RM3 WEC non-directional wave spectrum WEC-SIM analysis, the representative sea state is transformed from a directional wave spectrum into a non-directional wave spectrum $S_{rep-k}(f)$, see Equation 4.9 below:

$$S_{rep-k}(f) = \int_0^{2\pi} S_{rep-k}(f,\theta)\, d\theta = \frac{1}{M(k)} \int_0^{2\pi} \left(\mathrm{S}_1(f,\theta) + \mathrm{S}_2(f,\theta) + \cdots S_{M(k)}(f,\theta)\right) d\theta \tag{4.9}$$

so

$$S_{rep-k}(f) = \frac{1}{M(k)} \int_0^{2\pi} \mathrm{S}_1(f,\theta) d\theta + \frac{1}{M(k)} \int_0^{2\pi} \mathrm{S}_2(f,\theta) d\theta + \cdots \frac{1}{M(k)} \int_0^{2\pi} \mathrm{S}_{M(k)}(f,\theta) d\theta \tag{4.10}$$

For any directional wave spectrum $S_m(f,\theta)$, the relationship with the non-directional wave spectrum $S_m(f)$ is:

$$S_m(f) = \int_0^{2\pi} S_m(f,\theta)\, d\theta \tag{4.11}$$

so

$$S_{rep-k}(f) = \frac{1}{M(k)}(S_1(f) + S_2(f) + \cdots S_{M(k)}(f)) \tag{4.12}$$

It can be seen that the non-directional representative sea state from a certain group *k* is the group mean of all group members' non-directional wave spectra.

For the RM3 point absorber WEC-SIM model, the relative heave motion represents the power output performance of the device. From Equation 4.7, for a regular wave component *j* with amplitude ζ_{a_j} and frequency f_j, the following Equation 4.13 is satisfied:

$$\mathrm{RAO}_j = \frac{a_j}{\zeta_{a_j}} = \frac{da_j/dt}{d\zeta_{a_j}/dt} = \frac{v_{rj}(t)}{d\zeta_{a_j}/dt} \tag{4.13}$$

then

$$v_{rj}(t) = \mathrm{RAO}_j \times \frac{d\zeta_{aj}}{dt} \tag{4.14}$$

in which a_j is the relative heave movement of the float and the spar plate due to regular wave j and $v_{rj}(t)$ is the relative heave movement velocity. $d\zeta_{a_j}/dt$ is the velocity of the water particle. According to wave theory [40], the water particle velocity for a regular wave j is proportional to the wave amplitude ζ_{a_j}, which can be easily proved from Equation 2.9. As a result, the following equation 4.15 is satisfied.

$$v_{rj}(t) \propto \mathrm{RAO}_j \times \zeta_{a_j} \tag{4.15}$$

From Equation 4.1, it can be found that Equation 4.16 is satisfied:

$$p_j(\mathrm{t}) \propto {\mathrm{RAO}_j}^2 \times {\zeta_{a_j}}^2 \tag{4.16}$$

In which $p_j(\mathrm{t})$ is the power output time series of regular wave j. From Equation 2.8, the average incoming wave power of a regular wave j, which is P_{wavej}, is also proportional to ${\zeta_{aj}}^2$. As a result, the wave power and the output WEC power satisfy the following Equation 4.17:

$$p_j(\mathrm{t}) \propto {\mathrm{RAO}_j}^2 \times P_{wavej} \tag{4.17}$$

From Equation 4.3, it can be found the average power output $P_{averagej}$ is satisfied:

$$P_{averagej} \propto \mathrm{RAO}_j{}^2 \times P_{wavej} \tag{4.18}$$

From Equation 2.11, it can be found that P_{wavej} is proportional to $S(f_j)$, then the following Equation 4.19 is satisfied:

$$P_{averagej} \propto \mathrm{RAO}_j{}^2 \times S(f_j) \tag{4.19}$$

It means for a linear RM3 WEC, each of the regular wave components j can be transformed into the average power output by multiplying by a constant value $\mathrm{RAO}_j{}^2$.

For an irregular wave which is the superposition of multiple regular waves, it can be found that if the total incoming wave power (or wave spectrum) is a fixed value of $S(f)$, the average power output $P_{average}$ is also a fixed value. Assuming wave spectrum $S_1(f)$, $S_2(f)$, $\ldots S_{M(k)}(f)$ from a group k has average power output P_1, $P_2 \ldots P_n$ respectively. From Equation 4.12, it can be easily found that the average power output P_{rep-k} from the representative sea states $S_{rep-k}(f)$ satisfies:

$$P_{rep-k} = \frac{1}{M(k)}(P_1 + P_2 + \cdots P_{M(k)}) \tag{4.20}$$

It explains why no matter how the sea states were grouped, as long as the WEC has a linear RAO, the annual energy can be accurately predicted by using a small number of representative sea states.

4.4. Conclusion

The annual HF radar sea states (3161 hourly sea states) together with the representative sea states from ten regrouping methods A to J obtained from Chapter 3 were imported to WEC-SIM for calculation. Each of the sea states was tested on a 1:1 RM3 point absorber WEC-SIM model to obtain the average power output value.

The results showed that method C (non-directional wave *K*-means clustering method) provided the highest representativeness for the average power output of the model (of rank 1). It means the representative sea states obtained from method C provide not only representative sea states in the ocean area measured but also the most test-worthy cases for the RM3 model, which are the most representative power output scenarios. The annual energy output prediction with representative sea states was also calculated and compared with the actual annual energy output value.

It was found that the annual energy prediction with different regrouping methods A to J or with different *K* values had very small differences (within ±1% limit). After analysis, it was found that the RM3 point absorber was highly linear, which explained why the different regrouping methods and different *K* values all provided an accurate annual energy output prediction.

To better understand the performance of WECs using representative sea states, physical tests of a realistic WEC scale model with full coupling and non-linearities in the wave basin are described in Chapter 5.

5. Experimental and numerical analysis of a 1:25 scale hinged-raft WEC model with HF radar representative sea states

In this chapter, a 1:25 hinged-raft was used for analysis. This model was designed and manufactured as part of the EU H2020 MaRINET 2 project. As part of the Round-Robin program, it was delivered and tested in the wave basins in four Universities in late 2020. The test plan was to test the model in multiple regular/JONSWAP irregular waves and still water for the free decay test. During the test in UoP, in addition to the original test plan, 31 additional representative sea states with different K values (K = 1, 5, 10, 15) of method C of HF radar sea states were tested on the model. To the best knowledge of the author, this was the first time the site-specific representative sea states from the K–means clustering method have been tested on a realistic WEC model. To build a reliable numerical model for the 1:25 hinged-raft in WEC-SIM, the MOI of both rafts and the stiffness coefficient of the tension spring used in the mooring system were carefully measured.

After all of the tests were finished, based on the physical model testing results, a 1:25 hinged-raft WEC-SIM numerical model was built and validated. The numerical model shows a good agreement with the physical model. It was then tested with the representative sea states obtained from ten different regrouping methods A to J from HF radar sea states to estimate the power output performance. The hinge angle spectral RAO

was calculated both physically and numerically to validate and show the linearity of the model.

Section 5.1 is to introduce the background of the model testing. Section 5.2 is the preparation work of the physical model testing, which includes the wave calibration for regular/irregular waves. Section 5.3 is to conduct the model testing in the wave basin of UoP. Section 5.4 is to analyse the physical model testing results in different wave conditions. Section 5.5 is to build a numerical model using WEC-SIM and carry out the numerical analysis. The physical and numerical results are compared. Section 5.6 is to carry out the annual power output estimation of the 1:25 hinged-raft using representative sea states from different regrouping methods. Section 5.7 is the conclusion.

5.1 The background of the 1:25 hinged-raft model testing

The main purpose of the EU H2020 project was to improve the quality and reliability of WEC model testing by testing and comparing the same model between different universities [172]. Based on this purpose, a round-robin testing program was designed. It aimed to obtain a reliable testing procedure and to share the open access model testing results obtained from different universities. A 1:25 hinged-raft model was designed and manufactured at Nantes University (ECN) and tested in the middle of 2020. It was then delivered to test at Plymouth University (UoP), Edinburgh University (UoE), and Cork University (UCC) from Sep 2020 to Dec 2020.

The design of the 1:25 hinged raft is shown in Figure 5.1. As an attenuator type of WEC, it consists of two rafts and has a rotational PTO system connecting both rafts through a hinge. A real-time embedded controller monitor controls the PTO to ensure the correct rotational damping value k_R (N.m/rad/s) in the testing. A mooring system with four mooring lines using calibrated tension springs and ropes was utilized to keep the model in position.

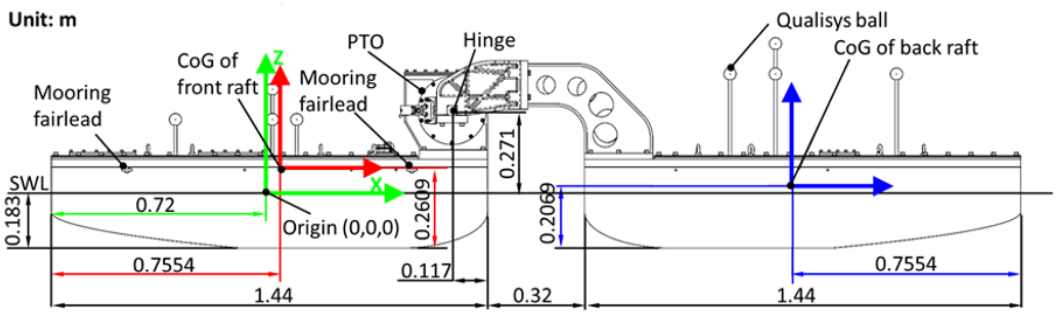

Figure 5.1: The geometric parameters of the 1:25 hinged-raft (front view) [173]. The front raft (left) and back raft (right)'s local coordinate systems and origins are marked.

Both bodies were made of aluminium and plastic and the hinge was made of machined aluminium. It was sealed with epoxy coating to protect the electrical device inside the bodies. Key geometric dimensions and parameters of the model are shown in Table 5.1:

Table 5.1: Key dimensions and parameters of the 1:25 hinged raft model

Measure	Units	Value
Length overall	m	3.2
Length front raft	m	1.44
Length back raft	m	1.44
Draft	m	0.183
Width	m	0.87
Mass overall	kg	399.5
Mass front raft	kg	199.8
Mass back raft	kg	199.7

The PTO system of the model consisted of a controllable motor in line with the hinge, which was mounted and sealed inside the front raft (see Figure 5.1). It was designed to provide torque up to 80 N.m with limited size and weight. A direct drive motor was used for this purpose [174]. When the PTO system was turned on, specified rotational damping k_R could be set on the motor through the control system, with adjustable damping values in the range from k_R = 0 to 80 N.m/rad/s. The relative rotation of the rafts generated torque at the hinge to simulate the power generator. An in-built torque metre was used to measure the generated torque. Before the experiment formally started, a series of k_R values ranging from 10 N.m/rad/s to 70 N.m/rad/s were tested with H = 0.05 m and 0.10 m by the manufacturer of the model to determine the optimal value of k_R. It was found that k_R = 20 N.m/rad/s was the optimal value. As a result, in the experiment, the value of k_R = 20 N.m/rad/s was used.

The whole test plan is shown in Table 5.2 below:

Table 5.2: 1:25 hinged-raft test plan in UoP

No.	Test type	Wave condition	PTO damping [N.m/rad/s]
1	Hinge angle free decay test	No wave	0 to 50
2	Regular wave test	Regular wave	20
3	JONSWAP wave test	Irregular wave	20
4	Representative HF radar sea states test	Irregular wave	20
5	Mooring spring tension coefficient	No wave	/
6	MOI of both rafts	No wave	/

The detailed test plan is shown in Appendix 9.1.

The free decay tests (No.1) focused on the hinge angle free oscillation of the rafts with different PTO damping parameters. Hinge rotational damping parameters k_R of 0, 10, 20, 30, 40, and 50 N.m/rad/s were tested and each test was repeated 3 times to reduce the uncertainty.

The model was tested in regular waves (No.2) with rotational damping parameters of k_R = 20 N.m/rad/s on the hinge. 49 regular wave cases with wave periods T ranging from 1 to 2.4 s and wave height H of 0.05m, 0.1m, 0.15m, and 0.2m were tested on the model. The time duration of each regular case was 120×T (which is longer than the normal standard of 50×T to 100×T as shown in Section 2.2.4.) to guarantee the quality of the experiment.

There were 12 long-crested JONSWAP irregular waves (No.3) tested with peak periods T_p ranging from 1.3 to 2.05 s and significant wave heights H_s of 0.05m, 0.1m, and 0.15m, and shape parameter Γ of 3.3. The repeat time of irregular wave cases was 12 minutes, which was calculated by the Froude scaling criterion from Section 2.2.1 with a scaling factor λ = 25 to have a full-scale model repeat time of 3600s (which was longer than the normal standard of 20 min to 30 min in full scale as shown in Section 2.2.4.) to guarantee the quality of the experiment.

There were 31 representative sea states from regrouping method C of HF radar measured sea states (No.4) with K = 1, K = 5, K = 10, K = 15 tested on the model with k_R = 20 N.m/rad/s. The repeat time of the representative irregular wave cases was the same as the repeat time of JONSWAP waves, which was 12 minutes with a scaling factor of 25. It was to guarantee a one-hour run time in full scale.

The tension coefficient for the tension spring k_{spring} used in the mooring line was also tested (No.5). The MOI of both the front and back rafts in roll, pitch, and yaw were also measured respectively (No.6).

5.2 The preparation work and final layout of the model in the wave tank

5.2.1 Model testing facility and the layout of the hinged-raft model testing

The model was tested in the Ocean basin located in the COAST laboratory at UoP. The Ocean Basin was 35 m long by 15.65 m wide with an adjustable basin floor that can be

used for different water depths of up to 3 m. The waves were generated through Wave Synthesizer software that controlled 24 hinged flap paddles individually with an active wave absorption system that reduces the reflections of waves [175]. Additionally, a parabolic absorbing beach was used on the other end of the basin. The paddles produced regular waves with an approximate maximum height of 0.9 m at 0.4 Hz. For irregular waves, the frequency range was from 0.1 Hz to 2 Hz [176]. The wave basin was able to produce regular, generic/parametric wave spectrum and site-specific complex wave spectrum.

Two gantries were free to move on top of the basin, which allowed the models and wave gauges to be deployed at suitable locations. A Qualisys motion capture system with multiple cameras was used to capture the movement of the model in each DoF. A picture of the wave basin is shown in Figure 5.2 below:

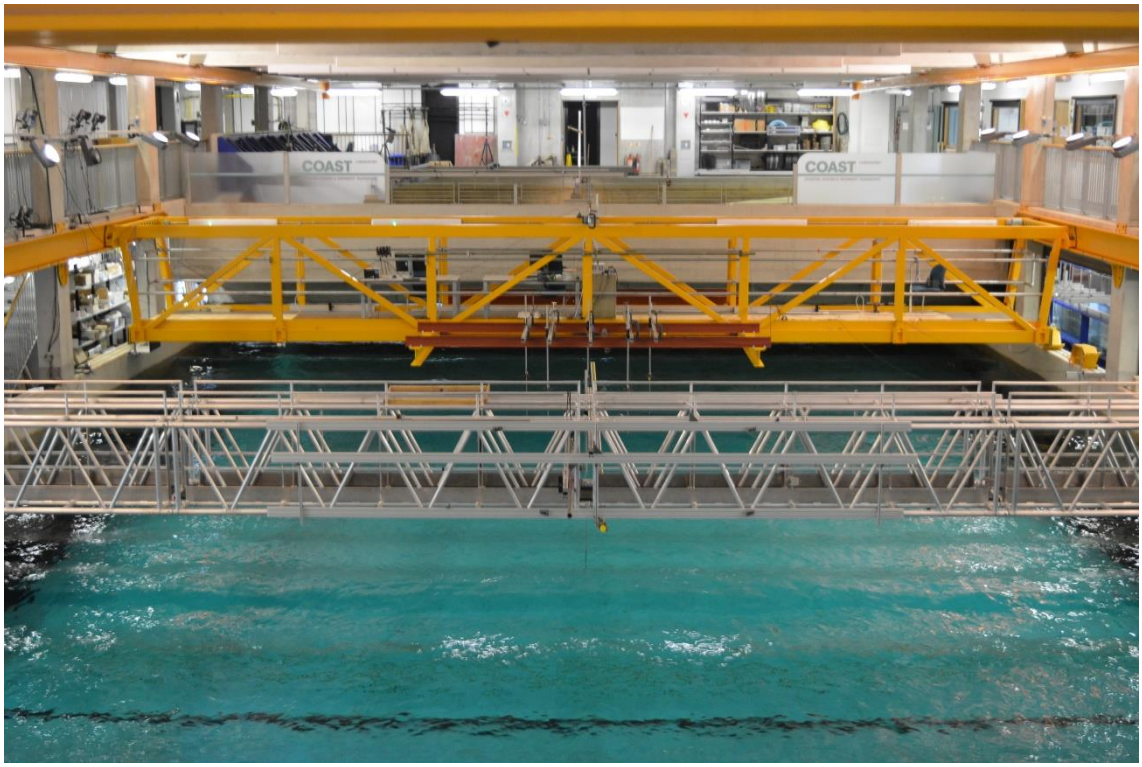

Figure 5.2: COAST laboratory in University of Plymouth [176].

To simulate the deep-water condition for the hinged-raft in waves, the water depth of the basin was set to the maximum value of 3 m, which was equal to 75 m at full scale.

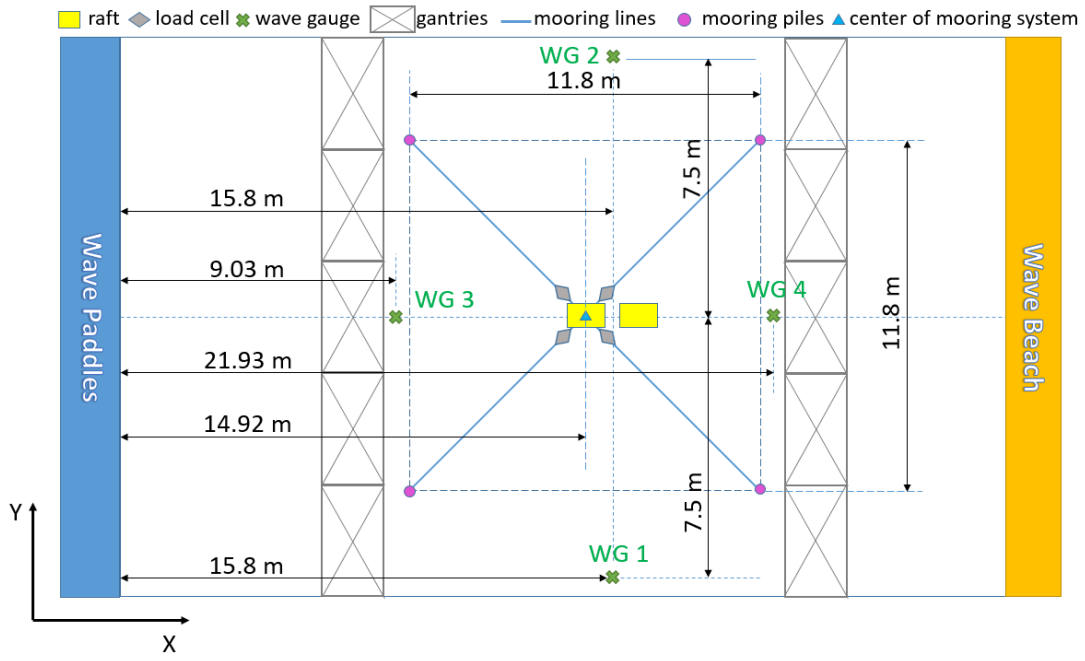

Figure 5.3: The layout of the hinged-raft physical model testing.

Considering the size of the 1:25 hinged-raft in Figure 5.1 and the existence of the mooring system, the mid-point between the two rafts was kept 15.8 m away from the wave paddles, see Figure 5.3. There were 4 aerial mooring lines installed with a 90^o angle interval around the front raft from a top view perspective. The anchor points of the mooring lines were 30cm above the SWL on the mooring piles and 7.79cm above the SWL on the front raft. The reason for keeping the mooring line with a small pitch angle rather than parallel to the SWL was to keep them away from the water during the model testing. Each mooring line consisted of a plastic rope and a tension spring. The total length of each mooring line was 7.325m. The model was kept following the wave direction (perpendicular to the wave paddles), which was based on the assumption that the model, which was an attenuator, would automatically rotate and operate parallel to the main wave direction [177].

Before the model installation, all of the wave conditions shown in Appendix 9.1 were created in the tank without the model in-situ and calibrated.

The layout of the wave gauges for wave calibration is shown in Figure 5.4 below with in total of 4 gauges used. Each wave gauge is a resistive type with a sampling frequency of 128 Hz. Wave gauge No. 2 (WG 2) is right at the position where the mid-point between two rafts locate, thus the measured wave elevation signals from WG 2 were used for wave calibration.

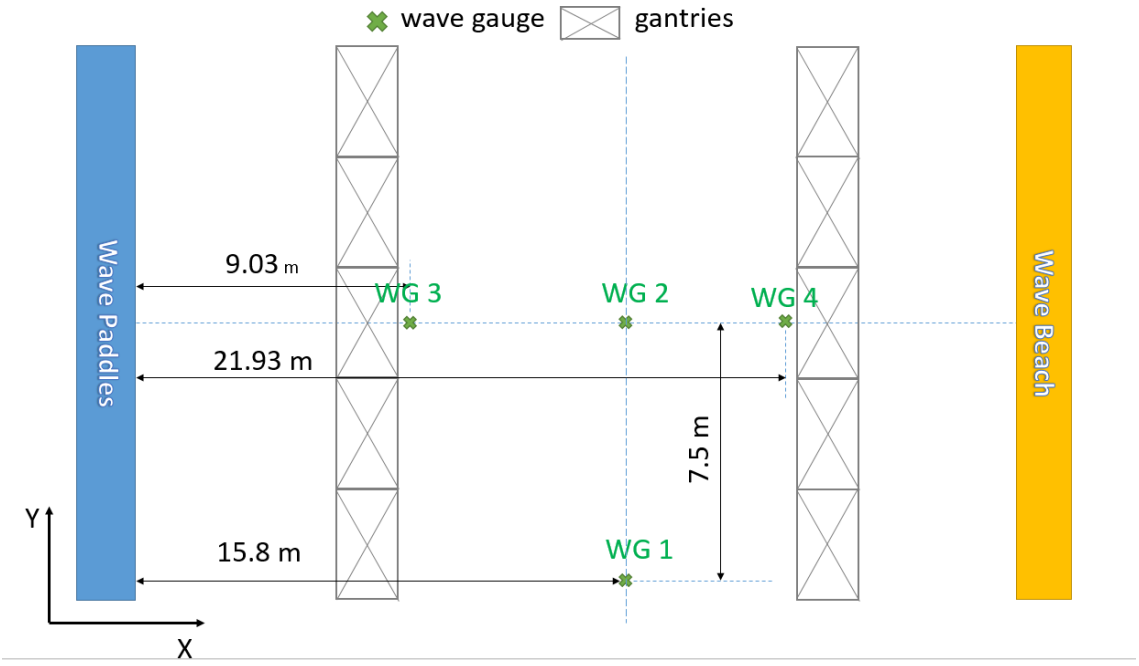

Figure 5.4: The layout of wave gauges in the tank without the model installed.

After the wave calibration and model testing, the measured data were analysed. The regular wave tank testing results were analysed in two parts. First, the RAOs for the rafts in different DoFs with k_R = 20 N.m/rad/s were analysed, and second, the Capture Width

Ratio (CWR) of the model with rotational damping parameter k_R = 20 N.m/rad/s was calculated.

Due to the difference between the RM3 point absorber used in Chapter 4 and the 1:25 hinged-raft, the RAO analysed for the hinged-raft was not only the heave RAO but also the pitch RAO and the hinge angle RAO for both rafts. To calculate the RAO, the amplitude of the movement of both rafts in heave and pitch and the amplitude of the hinge angle were obtained. For the heave RAO of both rafts, it provided a dimensionless characterisation [m/m]. For the pitch RAO and relative hinge angle RAO, it was expressed as hinge angle per unit wave amplitude [Degree/m].

The amplitude for the heave and pitch motion of each raft was obtained from the Qualisys motion capture system [178]. This system used multiple cameras to capture the position of the makers located on each raft. The makers of the rafts were shown in Figure 5.5 and the cameras used were shown in Figure 5.6. Each raft had a local coordinate system with the origin at the CoG of the raft, and the *x*-axis of the local coordinate system pointed towards the wave maker and the *z*-axis pointed upwards. Each raft had 4 markers installed. By comparing the movement of the markers relative to the global coordinate system (the earth), the displacement, velocity, and acceleration of each raft were obtained. The maximum capture distance was 35 m and the sampling frequency of the Qualisys system was 128 Hz.

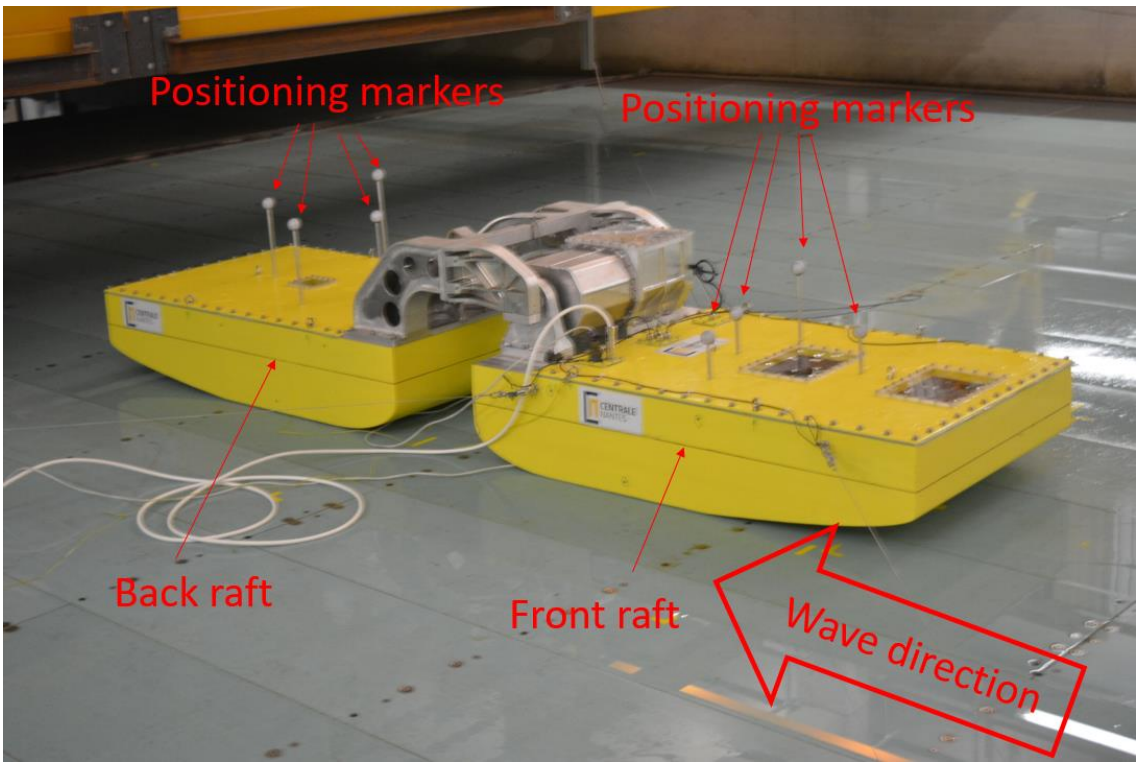

Figure 5.5: Assembly of both rafts and the installation of the positioning markers.

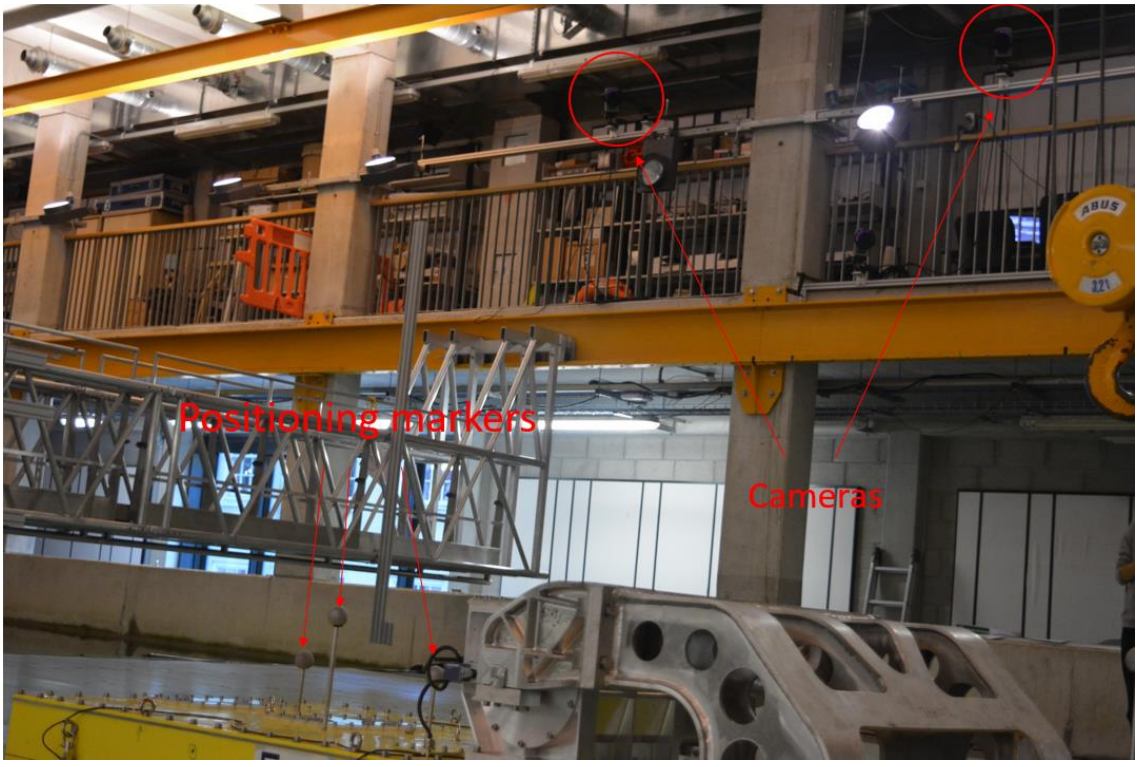

Figure 5.6: The Qualisys cameras used in the experiment.

There were different sensors installed inside the raft to measure the inner temperature, the real-time rotational angle of the hinge, the rotational angular velocity of the hinge, the temperature in the raft, the torque of the hinge, and the tension force in each mooring line. For each wave case tested, the measured data were recorded and saved in a .tdms format file inside the hard drive in the raft and transmitted to the PC for later analysis. The sampling frequency of the inbuilt recording system was 1000 Hz.

The wave amplitude used for incoming wave energy calculation was obtained from the wave gauge signal at the model location (WG2 in Figure 5.4) during the wave calibration process before the model was installed.

The average power output from the PTO system was the time average of the product of the hinge torque and the hinge angular velocity. For physical model testing, the hinge torque τ_{PTO} was measured by the previously introduced in-built recording system using a mechanical torque meter with a maximum capacity of 100 N.m [179].

After obtaining the torque from the PTO system, the power output time series $p_{PTO}(t)$ was calculated by Equation 5.1 below:

$$p_{PTO}(t) = -\tau_{PTO}(\mathrm{t}) \times v_{PTO}(t) \tag{5.1}$$

in which $v_{PTO}(t)$ is hinge angular velocity. The average power output $\overline{P_{PTO}}$ was calculated from Equation 4.3 by using an integer number of waves. For all of the power

output analyses, the time window from T_1 to T_2 was exactly the same as the time window that has been used in the regular wave calibration process.

After obtaining the average power output, the Capture Width Ratio (CWR) for the regular waves was calculated by normalizing the average power output from each wave case by the incoming wave energy per unit width of the model. The power of the incoming wave was calculated from Equation 5.2 below [40]:

$$\overline{Power_w} = c_g * \overline{E_w} \tag{5.2}$$

in which $\overline{Power_w}$ is the average wave power of a regular wave; c_g is the group velocity in limited water depth (3 m); $\overline{E_w}$ is the average total wave energy over a wave period, which is:

$$\overline{E_w} = \frac{H^2}{8}\rho g \tag{5.3}$$

in which H is the calibrated wave height; ρ is water density; g is the gravitational acceleration parameter. The CWR of a regular wave is calculated from Equation 5.4:

$$CWR = \frac{\overline{P_{PTO}}}{\overline{Power_w} * D} * 100\% \tag{5.4}$$

in which *D* is the width of the model.

The irregular wave analysis result is similar to the regular cases, which will be explained in Section 5.4.3.

5.2.2 Regular wave calibration

For regular wave calibration, it is necessary to calculate the wave amplitude from the stable part of the wave elevation signals and compared the result with the input target value. As explained by ITTC [180], two criteria need to be considered for the selection of the time interval of regular waves, which are:

A. The wave signal should start after the transients and it should end before the reflected waves reach the model. If the transients are long (long start-up). It may be necessary to accept the wave reflections. It is necessary to keep the reflections (mainly from the wave absorber) to a minimum for zero-speed tests. The choice of the interval can be made manually with a visual inspection process.

B. When calculating RAO, the numerical accuracy is improved by increasing the number of waves analysed.

These two criteria need to be balanced based on the main objective of the tests [181]. For the hinged raft, the hinge angle motion of the rafts was essential for the power output. As

a result, this research aimed to select an interval for which the pitch motion of the rafts was fully developed to obtain an accurate power output estimation. Thanks to the active wave absorption system in the wave generator, the wave amplitudes were quite stable in the wave basin with the reflection from the wave absorber almost unnoticeable. As a result, a long interval of $120 \times T$ s was used in this research. To guarantee the most stable part of the signal was used for analysis, the initial and final transients measured during the first and last few wave cycles of the wave elevation signal were abandoned and only the middle 70% of the total repeat time was used for the analysis. The boundaries were also carefully adjusted a little to make sure an integer number of regular wave signals are selected.

Two examples are given in Figure 5.7 and Figure 5.8. The first is a regular wave with H = 0.1 m, T = 1 s (shortest wave period), and the second is with H = 1 m, T = 2.4 s (longest wave period).

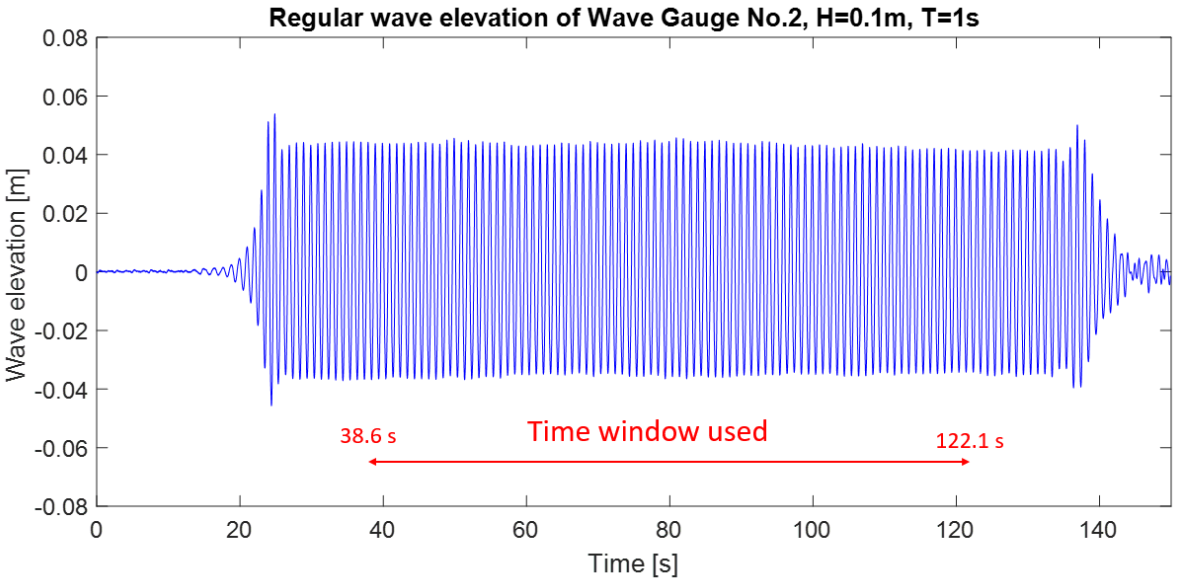

Figure 5.7: Wave elevation signal of WG No.2 of regular wave H = 0.1 m, T = 1 s. The time window used for wave calibration is marked.

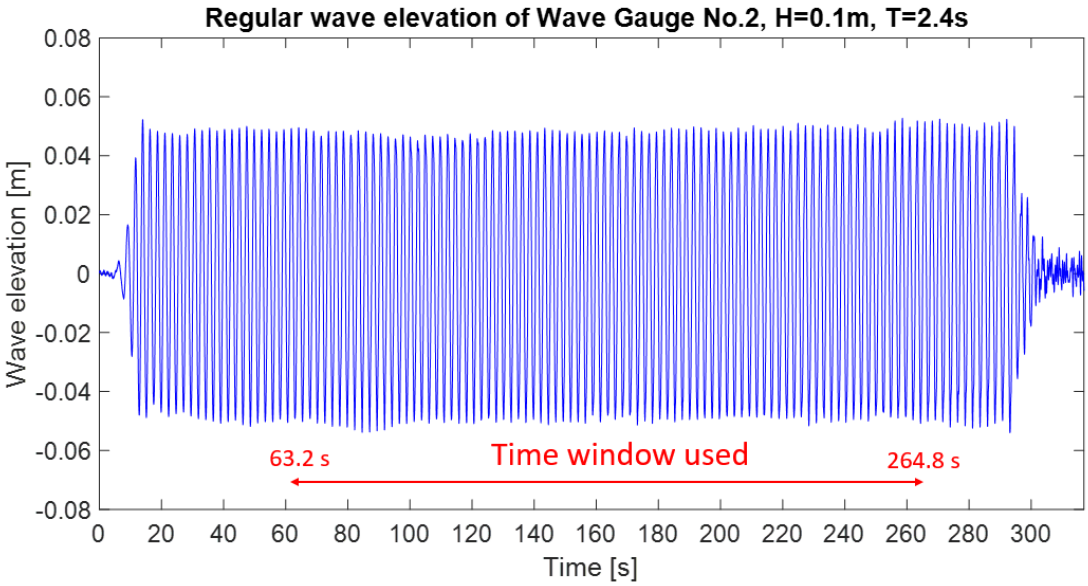

Figure 5.8: Wave elevation signal of WG No.2 of regular wave H = 0.1 m, T = 2.4 s. The time window used for wave calibration is marked.

It can be noticed that the sea states selected are stable in the time window selected.

The average wave amplitude was then calculated. The wave case with H = 0.1 m, T = 1 s is used as an example. For a regular wave, there is a positive peak and a negative trough in a full wave period T. The measured wave height H is the average magnitude between the peaks and troughs in the time window selected. In this example, H_{mean} = 0.0788 m.

Then the gain value φ used to correct the input wave amplitude was calculated by the following Equation 5.5:

$$\varphi = \frac{H_{target}}{H_{mean}} \tag{5.5}$$

in which H_{target} is the target wave amplitude. For this wave case H_{target} = 0.1 m. Then φ = 1.269. It means the input wave amplitude needs to be amplified to meet the target value.

After obtaining the gain value, it was applied to the input wave amplitude to correct it and the wave case was run the second time in the wave basin. Usually, it would guarantee the measured wave and the target amplitude's relative error are smaller than 5%. If not, the wave would be further calibrated for a 2nd time or even more times until the measured wave was within the 5% error. For this regular wave, the 2nd run had an average wave amplitude of 0.0508 m. The corresponding gain value φ was 0.9850, which was within the range of 0.95 to 1.05 (5% error). Thus the calibration stopped.

All of the regular waves were calibrated accordingly. The gain values of each regular wave are shown in Appendix 9.1.

5.2.3 JONSWAP irregular wave calibration

There were 12 JONSWAP irregular waves in the test plan. After the wave generation of each wave case in the empty tank, the wave elevation signals from WG No.2 was processed with MATLAB and transformed into frequency domain signal by using Direct Fourier Transformation (DFT) to obtain the measured wave spectrum. It was compared with the target JONSWAP wave spectrum to obtain a gain signal $\varphi(f)$ in the frequency domain to calibrate the input wave spectrum.

Taking an irregular wave as an example, the target H_s was 0.1 m, T_p was 1.8 s, and Γ was 3.3.

In order to remove the influence of ramp-up time and the part after the paddles stopped working, only the data from time window 10s to 729s was used to guarantee a full 12 min analysis time, see Figure 5.9 below:

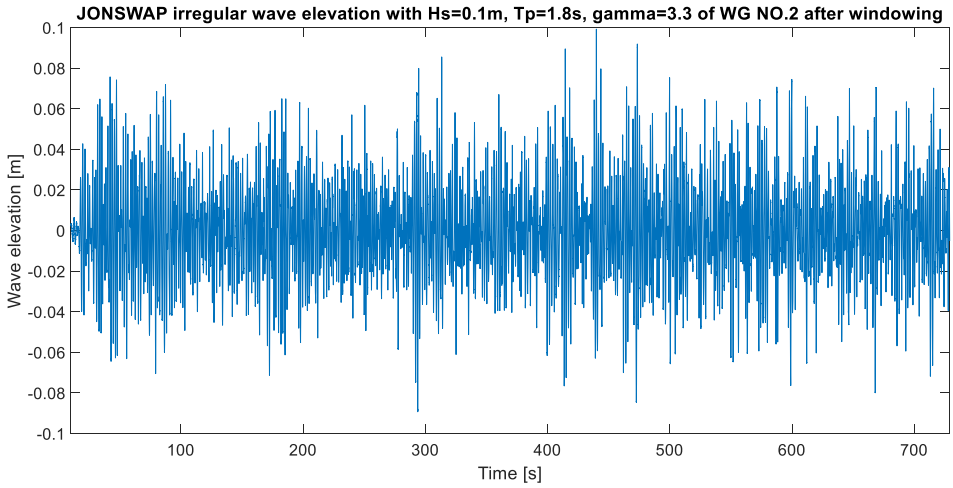

Figure 5.9: JONSWAP irregular wave elevation for case H_s = 0.1 m, T_p = 1.8 s after windowing.

The windowed wave elevation signal was then transformed by using DFT to obtain the non-directional wave spectrum, which was then compared with the target JONSWAP wave spectrum. The relative error between the target and measured non-directional wave spectrum φ_S was calculated from the following Equation 5.6:

$$\varphi_S = \frac{\int_0^\infty [S(f) - S_{measured}(f)]df}{\int_0^\infty S(f)df} * 100\% \quad (5.6)$$

in which $S(f)$ is the target JONSWAP wave spectrum and $S_{measured}(f)$ is the measured wave spectrum from DFT. For this case, the relative error φ_S is 10.72%.

The input wave spectrum was calibrated according to the measured wave spectrum. For different frequency components *f*, the difference between the input wave spectrum and the target wave spectrum $D_{PSD}(f)$ is shown in Equation 5.7 below:

$$D_{PSD}(f) = \frac{S(f)}{S_{measured}(f)} \tag{5.7}$$

From linear wave theory, the relationship between the non-directional wave spectrum of a frequency component *f* and the regular wave amplitude at this frequency component is:

$$S(f)\ \Delta f = \frac{\zeta_a(f)^2}{2} \tag{5.8}$$

in which Δf is the frequency step, $\zeta_a(f)$ is the wave amplitude of a regular wave with frequency *f*. The gain value obtained to calibrate the input wave spectrum is shown below:

$$\varphi(f) = \frac{A(f)}{A_{measured}(f)} = \sqrt{\frac{S(f)}{S_{measured}(f)}} = \sqrt{D_{PSD}(f)} \tag{5.9}$$

For some frequency components, the target JONSWAP spectrum *S*(*f*) and $S_{measured}(f)$ could be close to zero. It means $\varphi(f)$ was meaningless at those frequencies. To avoid this, only the wave frequency within the range *S*(*f*) that satisfies the following Equation 5.10 is taken into consideration.:

$$S(f) > \frac{S_{peak}}{100} \tag{5.10}$$

in which S_{peak} is the peak value of the input JONSWAP spectrum. For this wave case, the gain value $\varphi(f)$ is shown in Figure 5.10 below:

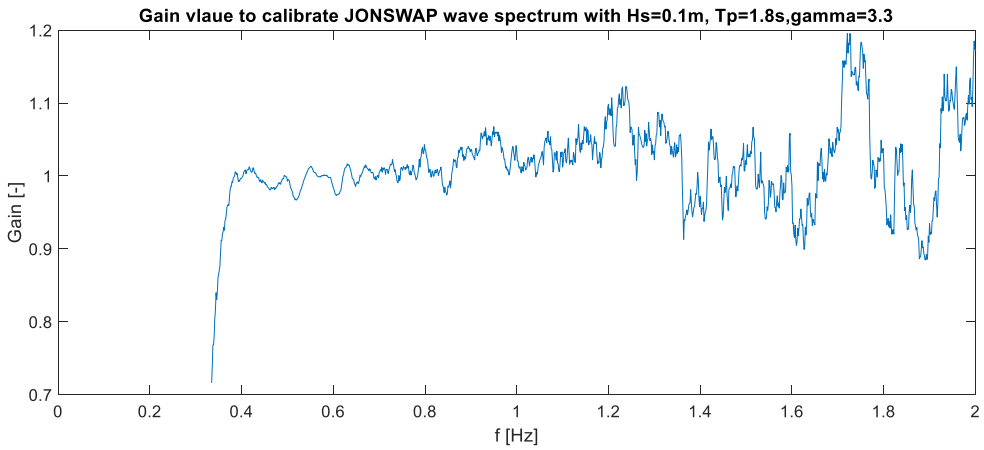

Figure 5.10: Gain value to calibrate JONSWAP wave with H_s = 0.1 m, T_p = 1.8 s, gamma = 3.3

This gain value was then imported to Wave Synthesizer and applied to the input target JONSWAP wave spectrum. The calibrated wave was run the 2nd time and the error value φ_S was calculated again from Equation 5.6. If this error was in the range of ±5%, the calibration was stopped. If not, the wave was calibrated further on until it was within the error limit. The measured wave spectrum before calibration, the target wave spectrum, and the calibrated wave spectrum are shown in Figure 5.11 below:

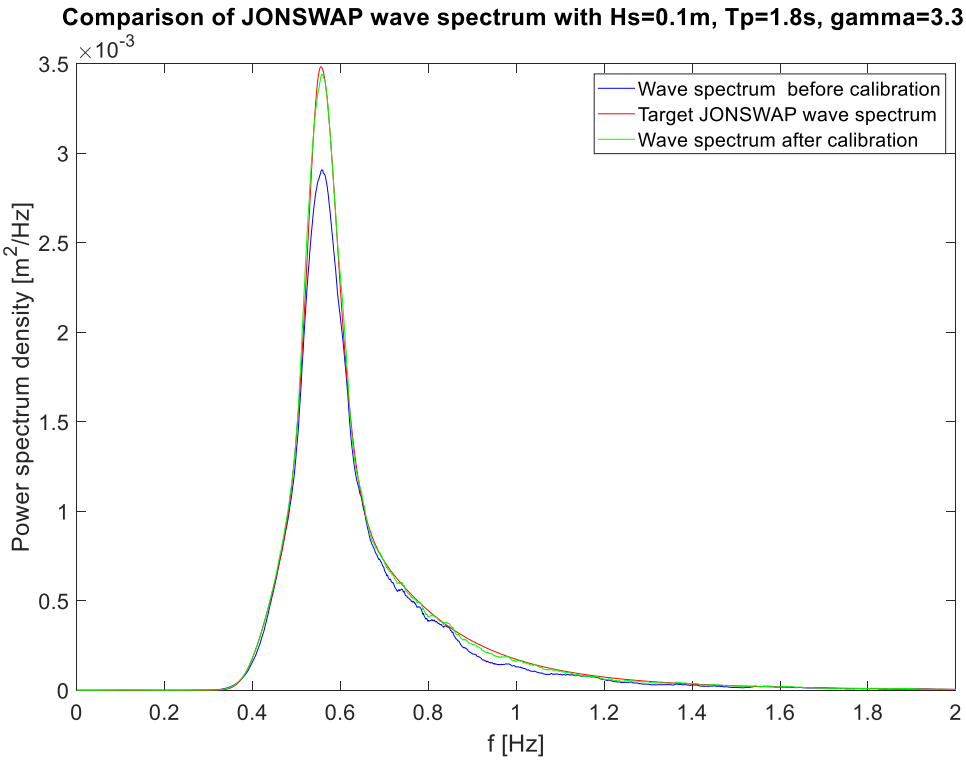

Figure 5.11: Comparison of the measured wave spectrum before calibration and the target JONSWAP spectrum with H_s = 0.1 m, T_p = 1.8 s, and gamma = 3.3 and the spectrum after wave calibration.

All of the 12 JONSWAP waves were calibrated accordingly.

5.2.4 HF radar measured representative sea states calibration

For HF radar measured sea states, each *K* value's corresponding bivariate scatter plot in H_s - T_e space and the representative sea states in *S*(*f*) space is shown in Figure 5.12 below:

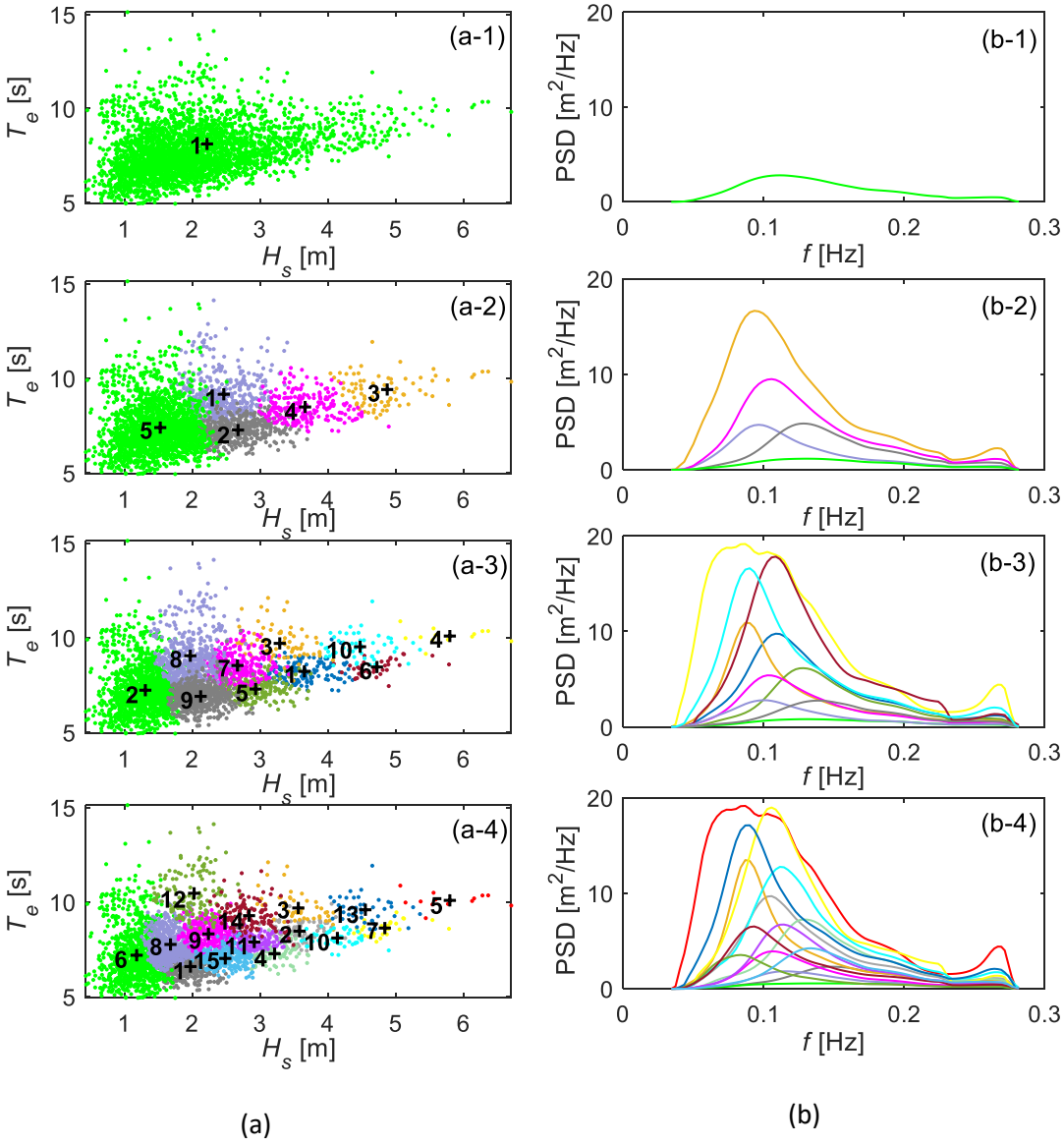

Figure 5.12: Full-scale representative sea states for HF radar data obtained using method C. (a) H_s - T_e space. (a-1) to (a-4) represent results obtained under K = 1, 5, 10 and 15, respectively. The sea states from the same group are marked in the same colour and the displayed values represent the group number k. The representative sea states are marked with black '+'. (b) $S(f)$ space. (b-1) to (b-4) represent results obtained under K = 1, 5, 10 and 15, respectively. The representative non-directional wave spectra are marked in solid lines using the same group colour described in H_s - T_e space.

Before being imported into the Wave Synthesizer for wave generation in the empty tank, the representative sea states were processed. Since the HF radar sea state was measured in full-scale from Wave Hub, in order to be tested on a 1:25 model, each representative sea state was scaled down according to Froude scaling law. Taking the case k = 1 of K = 1 as an example, in this case, there was only one representative sea state, which was the

average non-directional wave spectrum from all of the 3,161 hourly sea states. This representative sea state in *S*(*f*) space in full scale is shown in Figure 5.13 below:

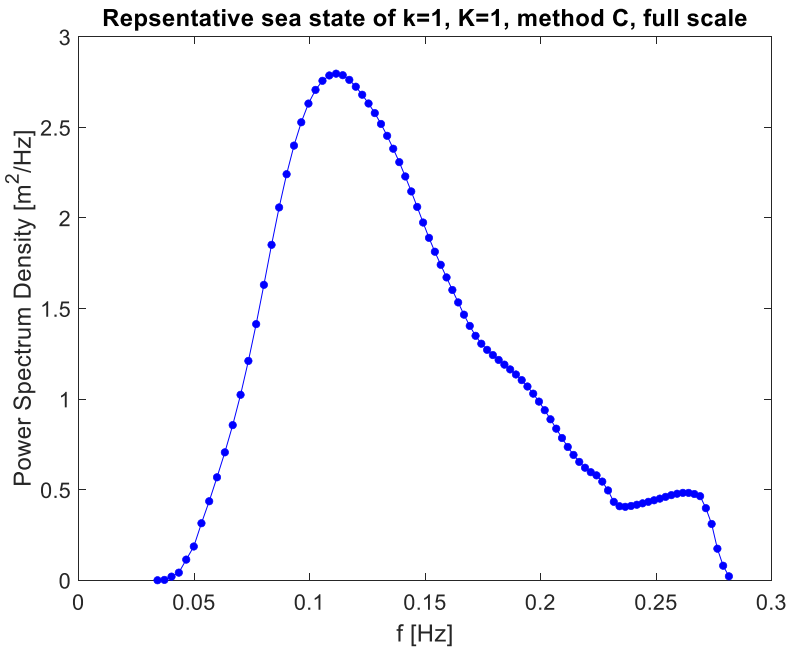

Figure 5.13: The representative sea state for k = 1, K = 1, method C of HF radar data in full scale.

According to the Froude scaling law, the scaled frequency f_{scaled}, the scaled power spectrum $S_{scaled}(f_{scaled})$, and the original frequency f and $S(f)$ follow the following Equations 5.11 and 5.12:

$$f_{scaled} = f \times \sqrt{\lambda} \tag{5.11}$$

and

$$S_{scaled}(f) = \frac{S(f)}{\lambda^{2.5}} \tag{5.12}$$

In the Wave Synthesizer, the repeat time T_{repeat} is directly related to the frequency step f_{step} of the imported non-directional wave spectrum, see Equation 5.13 below:

$$T_{repeat} = \frac{1}{f_{step}} \tag{5.13}$$

For the full-scale prototype, the repeat time was one-hour. For the model scale, the repeat time was 12 min. Then f_{step} in the model scale was obtained, which was 1/720 Hz.

The scaled non-directional wave spectrum $S_{scaled}(f_{scaled})$ was interpolated using the new frequency step. After interpolation, the model scale wave spectrum is shown in Figure 5.14 below:

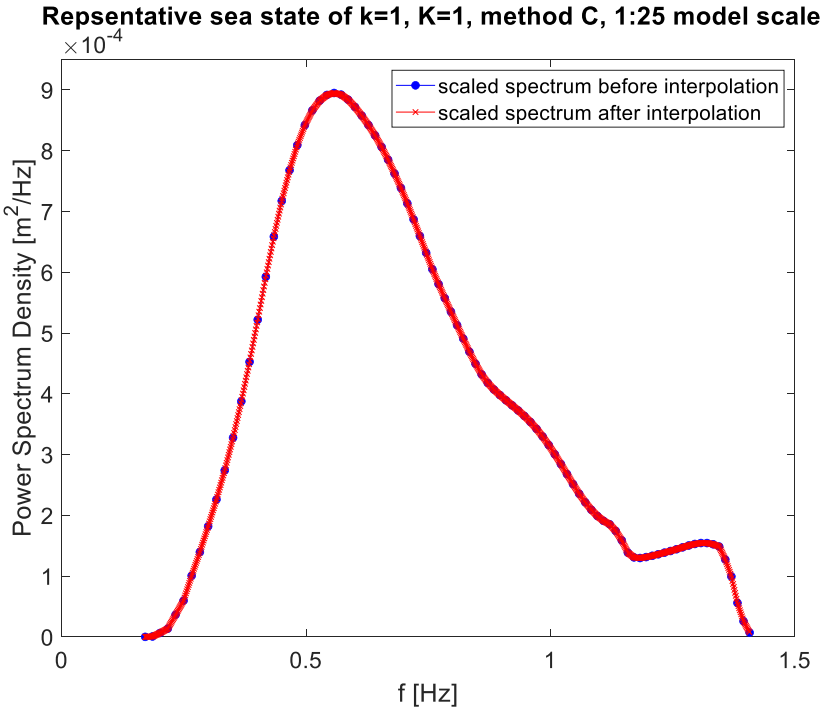

Figure 5.14: The representative sea state for *K* = 1, method C in 1:25 model scale

This wave spectrum was imported to Wave Synthesizer to be created in the wave basin. The wave elevation signal taken from WG No.2 was selected for wave calibration. All 31 HF radar sea states were calibrated following the same process as described in Section 5.2.3 to have a relative error with the target spectra below ±5%.

5.3 Tank testing with model installed

After the calibration for all of the sea states, both of the rafts were put in the correct location and assembled as shown in Figure 5.3. WG 2 was moved from the original position in Figure 5.4 to make room for the model.

As mentioned in Section 5.2.1, for model motion capturing, the Qualisys system was used. The layout of the local/global coordinate system is shown in Figure 5.15.

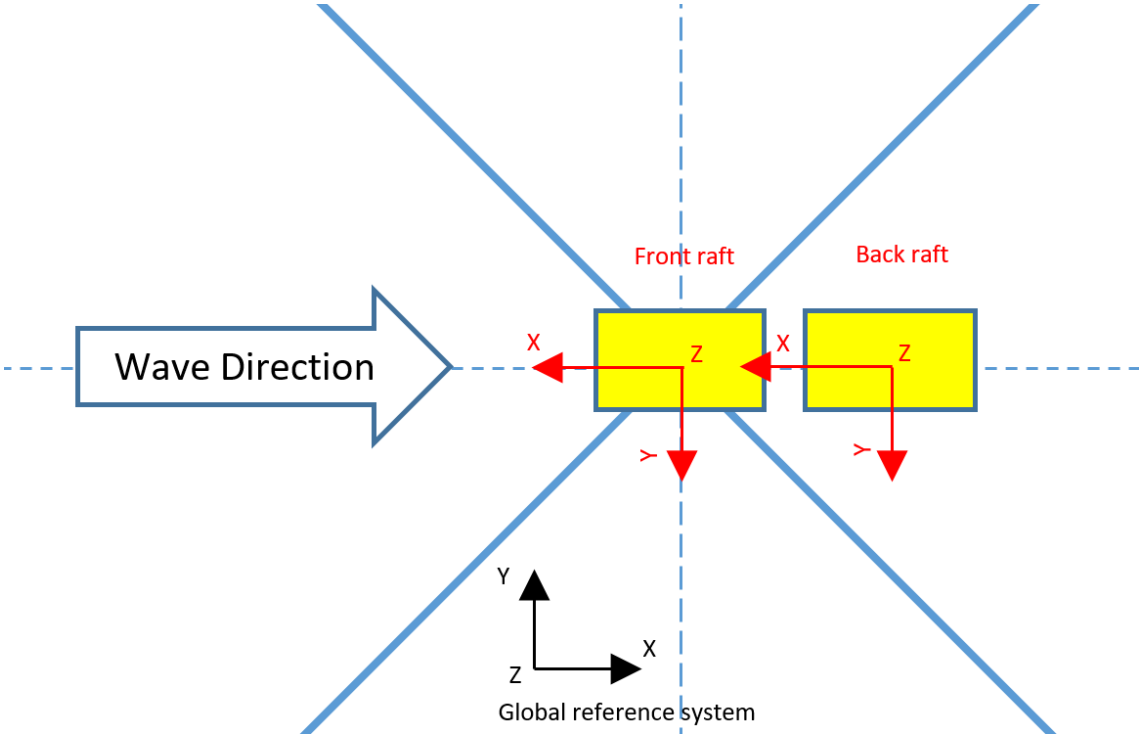

Figure 5.15: Local and global reference system for motion capture positioning.

The mooring system of the model is shown in Figure 5.3. Each mooring line consisted of a tension spring and a polypropylene rope. The rope end of the mooring line was connected to the mooring fairleads on the front raft, see Figure 5.16 below. The mooring force in each mooring line was measured by a load cell installed on the front raft.

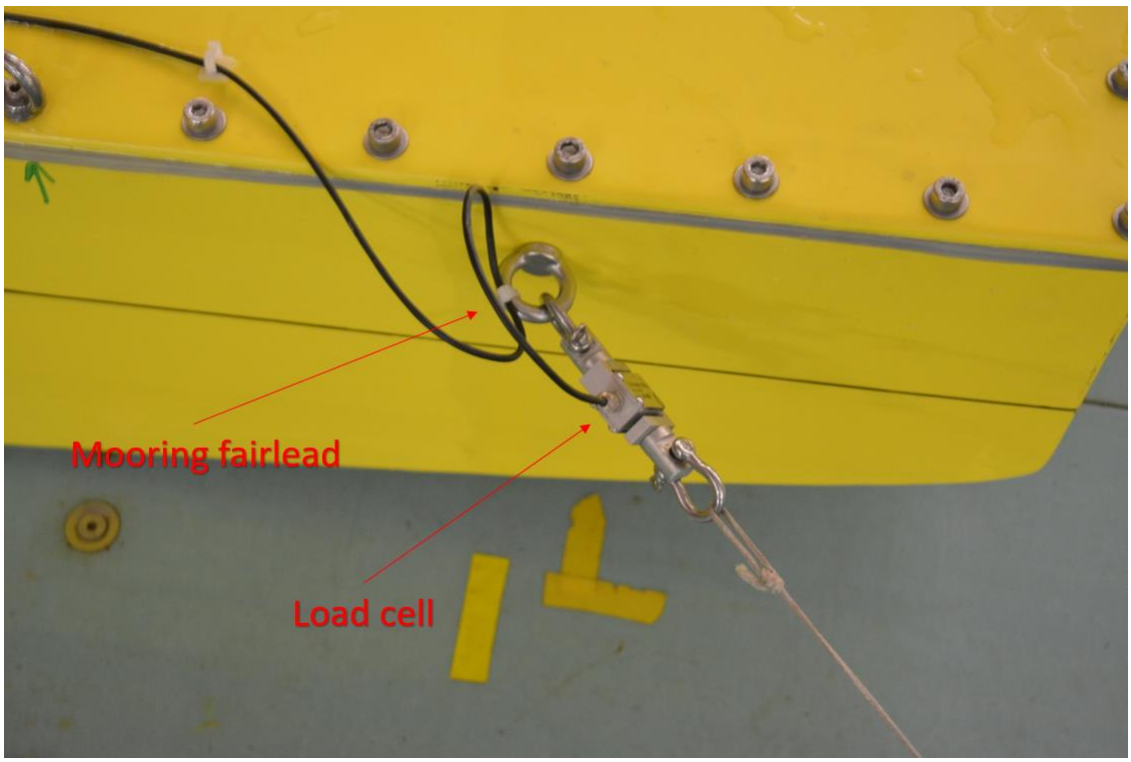

Figure 5.16: Mooring fairleads and load cell on the front raft

There were two cables connected to the raft, which were a power supply cable and a data transmission cable, see Figure 5.17 below:

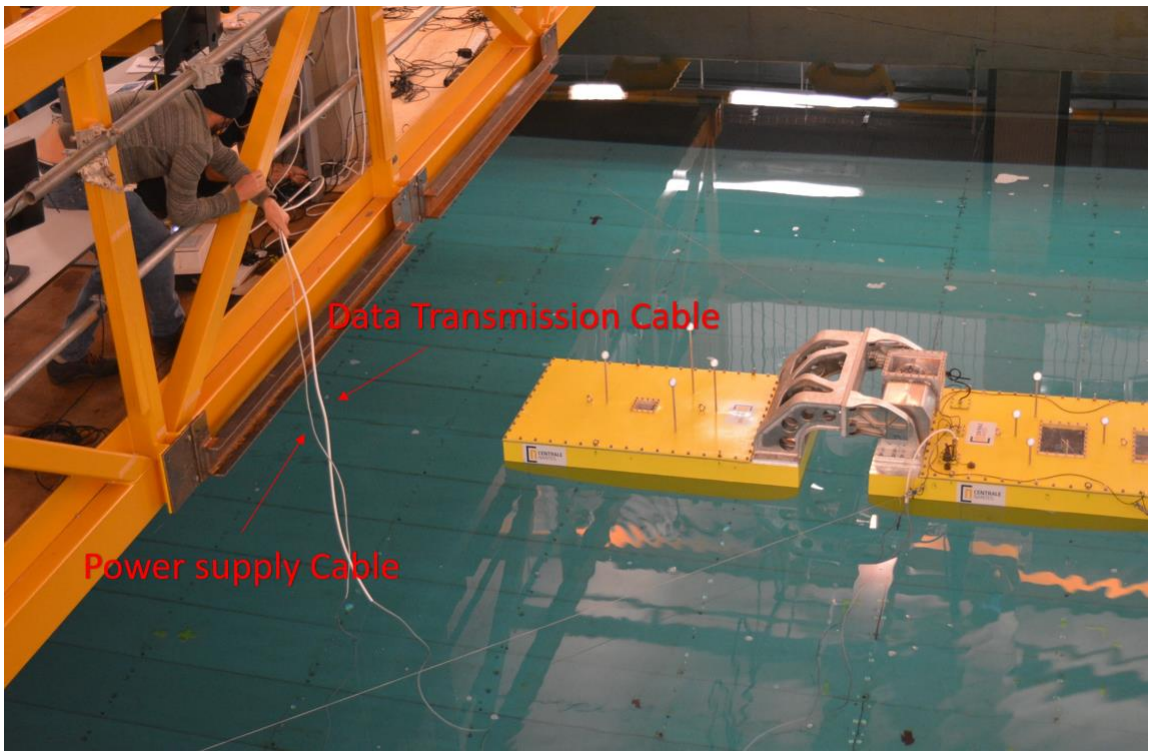

Figure 5.17: The connection of the power cable and data transfer cables.

An example model testing case in the wave basin is shown in Figure 5.18 below:

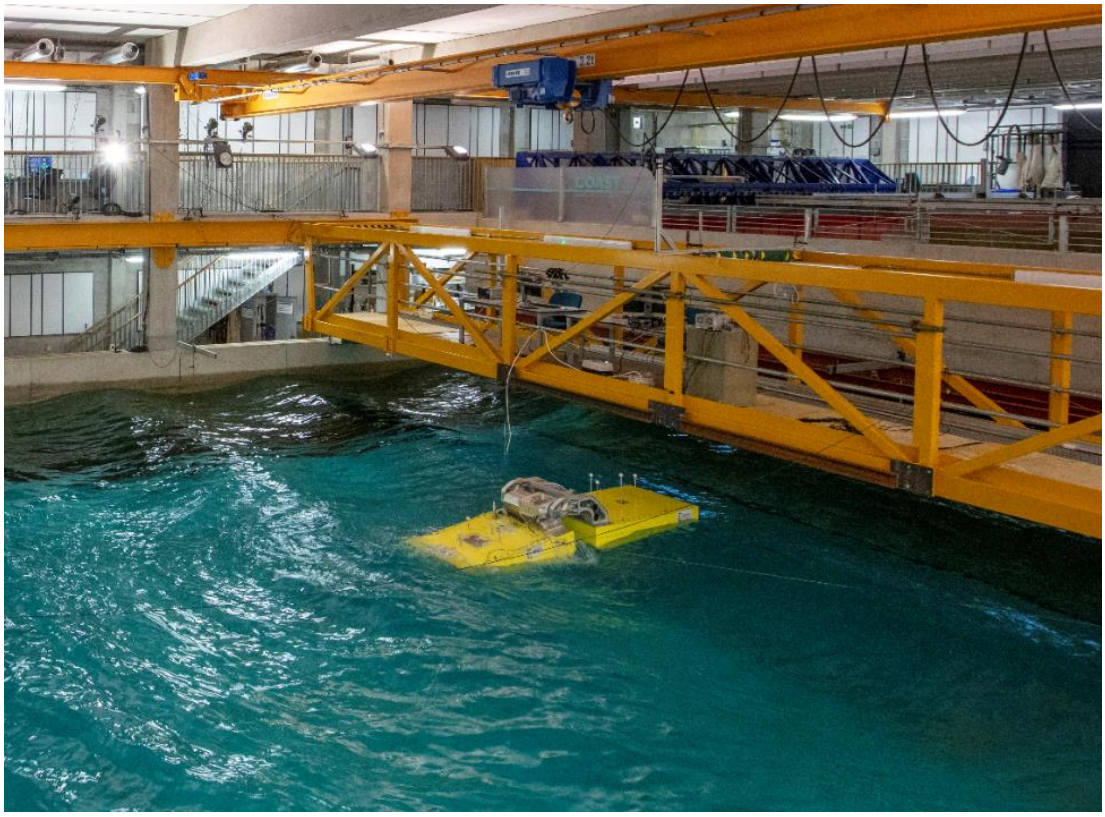

Figure 5.18: 1:25 hinged-raft model testing process in the wave basin.

For each wave case tested, the wave gauge system, the Qualisys system, and the raft inbuilt recording system started recording simultaneously.

Each of the wave cases from Appendix 9.1 was tested one after another. In order to guarantee the quality of the tank testing results, after each run, it took about 8 to 10 min for the water to calm down with the average wave amplitude in the wave basin smaller than 2 mm. From the observations of the tank testing process, for some sea states with large wave heights, there existed an obvious overtopping phenomenon on the front raft, which definitely influenced the model testing results. It will be discussed in Section 5.5.

The free decay tests of the model were conducted in a still water condition. A rope tied on the hinge was used to give the model an initial displacement by lifting the model up and releasing it. A set of k_R values ranging from 0 to 50 N.m/rad/s with 10 N.m/rad/s step interval were tested. Each of the free decay tests was repeated 3 times.

The measurement of the stiffness of the tension spring used in the mooring lines was conducted. The coordinates of both ends of the mooring lines were already known from Figure 5.3. The total length of the mooring line (including the spring and the rope) without any tension force was 732.5 cm. The only parameter that needed to be measured was the stiffness constant k_{spring}.

According to Hooke's law, for a linear spring, the following Equation 5.14 is satisfied:

$$F_{restoring} = -k_{spring} \times x \tag{5.14}$$

in which $F_{restoring}$ is the restoring force of the tension spring and x is the extension of the tension spring. To simplify the measurement procedure, the spring was hung up and different standard weights were added to the lower end of the spring each time.

This experiment was conducted twice (two run sets). Each time the total weight of the standard weights and the weight hanger together was measured by an electronic scale before they were attached to the lower end of the spring. During the measurement, the coordinate of the lower end of the spring on the tape measure with the total weight applied

was recorded. The coordinate of the lower end with zero weight added was also recorded as the initial position. After each measurement, the weight was removed and replaced with a new weight.

During the test, it was found that different from the linear spring assumption, the tension spring measured needed a minimum weight to start extension. It meant when the weight was lower than a limit value, there was no extension no matter what the weight was. As a result, all of the weights used needed to be large enough to give an extension. The extension force (gravitational force of total weight) and the extension of the tension spring satisfy:

$$F_{restoring} = -k_{spring} \times x + F_{initial} \tag{5.15}$$

in which $F_{initial}$ is the lowest force for the spring to start extension. After measurement, the coordinates of the lower end of the spring were subtracted by the coordinate with zero weight applied to obtain the extension of the spring. The data points were fitted into a straight line for each run set, which is shown in Figure 5.19 below:

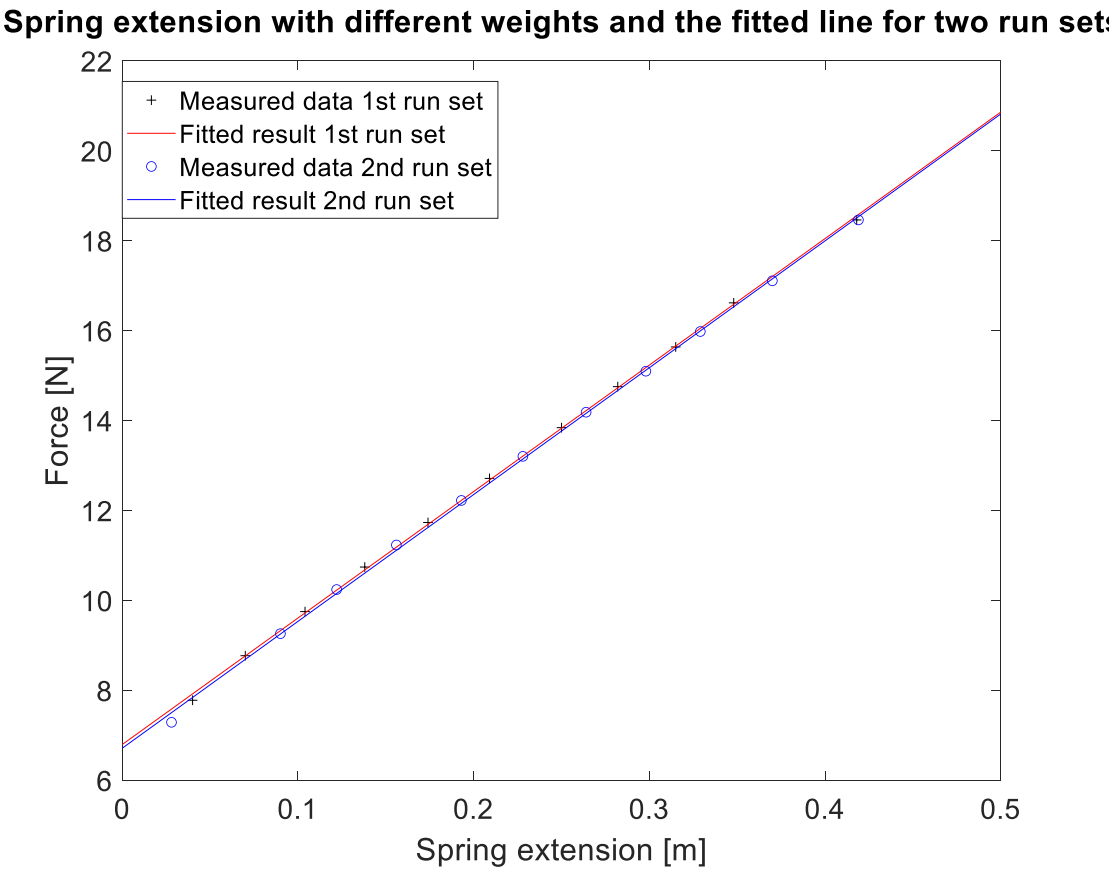

Figure 5.19: Spring extension with different weights and the fitted straight lines for two run sets.

It can be noticed a clear linear relationship between the applied total weight and the extension of the spring. Both run sets showed similar spring responses although the standard weights were added with different weight increments. After the linear regression calculation using MATLAB, the spring constant k_{spring} from the first run was 28.13 N/m and $F_{initial}$ was 6.80 N, with a linear correlation factor of 99.98%. For the second run, the spring constant k_{spring} was 28.21 N/m and $F_{initial}$ was 6.71 N, with a linear correlation factor of 99.97%. The average of k_{spring} was 28.17 N/s and $F_{initial}$ was 6.75 N.

During the physical model testing of the hinged-raft, the pretension force of each of the mooring lines was 20 N in the neutral position (no waves), which was much larger than $F_{initial}$. The whole mooring system can be considered linear and k_{spring} will be used in MoorDyn in the numerical model in Section 5.5.

After the measurement of the tension spring parameter, the tests for the MOI for both rafts were conducted. To calculate the MOI in different DoF, it was necessary to know the mass of the raft and the gyroradius (radius of gyration) in each DoF. The gyroradius in each DoF was calculated using a bifilar suspension method [182]. Each of the rafts was hung up by suspension lines and given an initial movement in roll, pitch, and yaw respectively to allow it to move freely. The free oscillation period in each DoF was measured using Qualisys. The gyroradius in each DoF (k_{xx}, k_{yy} and k_{zz}) was calculated from the free oscillation period, the distance from the hanging point to the CoG of the model (k_{xx} and k_{yy}), the length of the suspension lines, and the distance between the suspension points (k_{zz}). The MOI in each DoF was calculated from the following Equation 5.16:

$$I_{DoF} = M{k_{DoF}}^2 \tag{5.16}$$

in which k_{DoF} is the gyroradius in each DoF; I_{DoF} is the MOI in each DoF; *M* is the mass of the raft. After calculation, the MOI of both rafts is shown in Table 5.3 below:

Table 5.3: MOI for both of the rafts

Body	Direction	MOI [kg.m^2]		
Front raft	x	15.8	0	0
	y	0	66.0	0
	z	0	0	71.5
Back raft	x	15.8	0	0
	y	0	66.0	0
	z	0	0	71.5

5.4 Physical model testing results analysis

After the physical model testing of the hinged-raft, the experimental data measured from the wave gauges, Qualisys, and the in-built recording system were obtained and processed. Two papers collaborated among different universities have been written and published ([174], [181]).

5.4.1 Hinge angle free decay analysis

The hinge angle free decay test was used to determine the natural frequency of the model. In the neutral position in still water, the hinge angle of both rafts was zero degrees. The free decay test with rotational damping of k_R = 0 N.m/rad/s was taken as an example. After windowing, the time series for the hinge angle is shown in Figure 5.20 below.

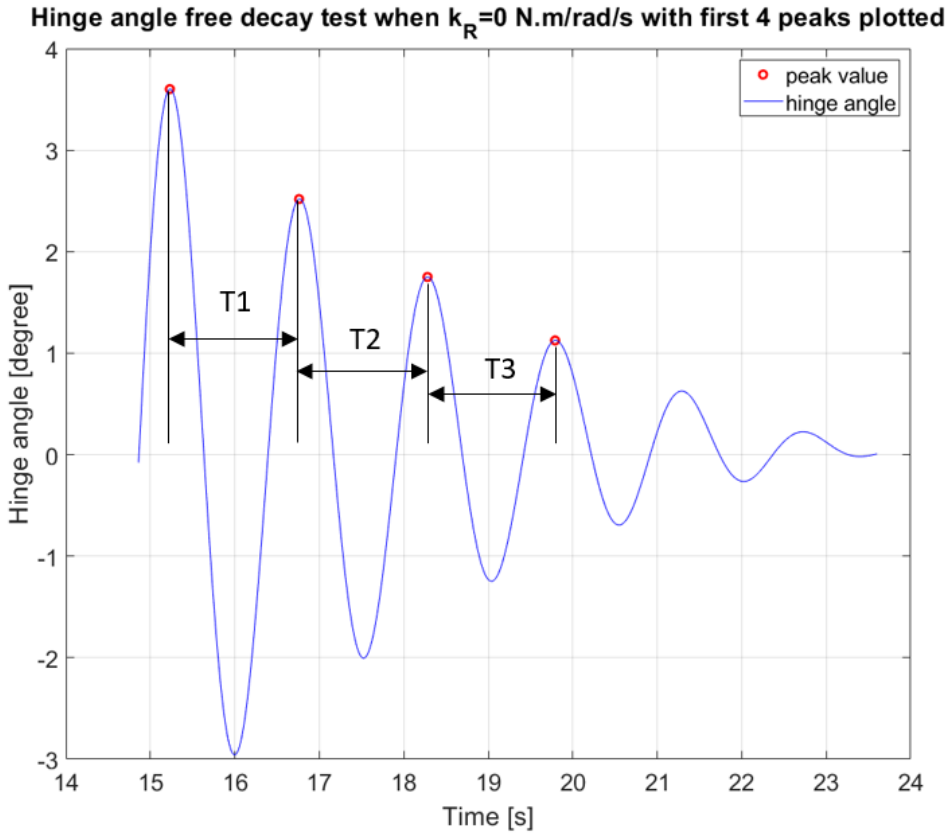

Figure 5.20: The hinge movement free decay test when k_R = 0 N.m/rad/s after windowing with the first 4 peaks and 3 free decay periods marked.

In order to calculate the average free decay period of the hinge angle, the free decay periods of T1, T2 and T3 were averaged. The other method was to use the first 3 peaks of the same signal, which only had 2 free decay periods T1, and T2 averaged.

Similarly, for other rotational damping values k_R, the peaks and free decay periods were obtained using the same method, see Appendix 9.2. It can be noticed that hinge angle movement damps out faster with a higher rotational damping parameter k_R as expected. Since the free decay tests were repeated 3 times, there were in total 3 sets of results of each k_R value. The results are shown in Table 5.4 and Table 5.5:

Table 5.4: Average hinge angle free decay periods using 4 oscillations (4 peaks)

Average hinge period [s]	k_R = 0 [N.m/rad/s]	k_R = 10 [N.m/rad/s]	k_R = 20 [N.m/rad/s]	k_R = 30 [N.m/rad/s]	k_R = 40 [N.m/rad/s]	k_R = 50 [N.m/rad/s]
first run	1.520	1.537	1.537	1.530	1.573	1.613
second run	1.547	1.523	1.540	1.563	1.567	1.560
third run	1.520	1.543	1.540	1.550	1.533	1.573
average	1.529	1.534	1.539	1.548	1.558	1.582

Table 5.5: Average hinge angle free decay periods using 3 oscillations (3 peaks)

Average hinge period [s]	k_R = 0 [N.m/rad/s]	k_R = 10 [N.m/rad/s]	k_R = 20 [N.m/rad/s]	k_R = 30 [N.m/rad/s]	k_R = 40 [N.m/rad/s]	k_R = 50 [N.m/rad/s]
first run	1.525	1.540	1.545	1.545	1.570	1.575
second run	1.560	1.530	1.550	1.585	1.585	1.580
third run	1.520	1.560	1.540	1.555	1.555	1.590
average	1.535	1.543	1.545	1.562	1.570	1.582

The results are plotted in Figure 5.21 below for comparison:

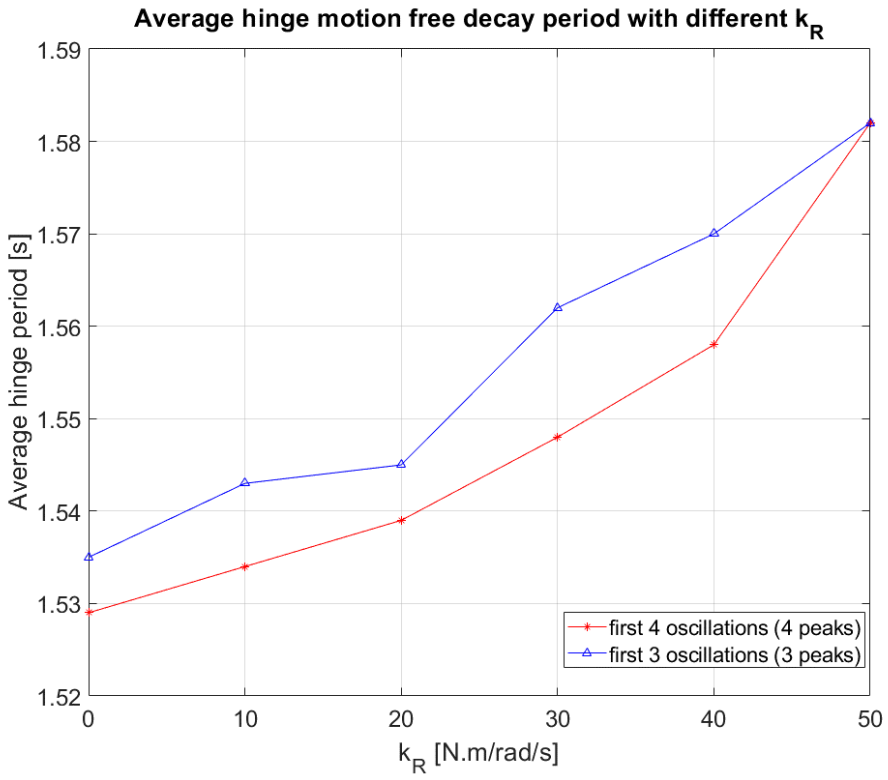

Figure 5.21: Comparison of the average hinge motion free decay period with different k_R.

The mean value and the standard deviation (STD) of the hinge motion's natural frequency are shown in Figure 5.22 below:

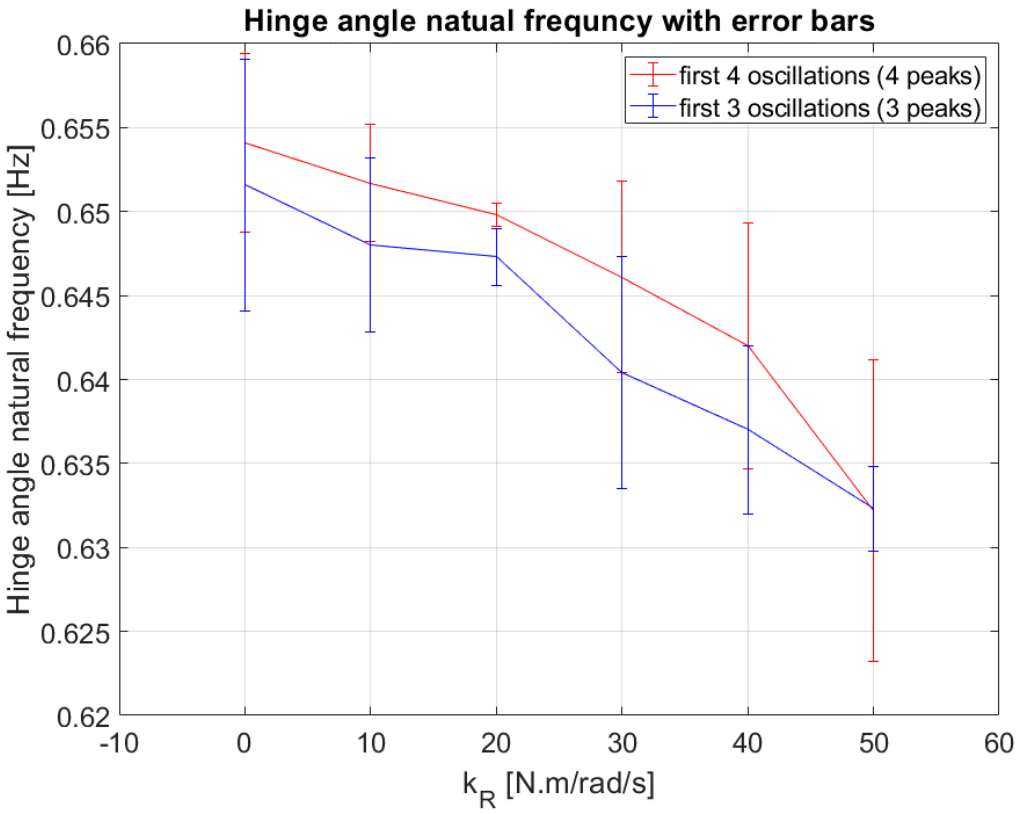

Figure 5.22: Hinge angle natural frequency with error bars.

The model testing results have shown a gradual decrease of the free decay hinge angle frequency with the increase of k_R. However, the absolute values of the pitch periods are very stable, ranging from about 1.53 s to 1.58 s. The differences between using 4 oscillations (4 peaks) and 3 oscillations (3 peaks) are quite small. The slight increase of natural period with the increase of k_R meets the expectations as explained in [183], where the increase of damping will cause the decrease of natural frequency for a free oscillating system.

5.4.2 Regular wave analysis results

As explained in Section 5.2.1, the regular waves with k_R = 20 N.m/rad/s in Appendix 9.1 were analysed to obtain the regular wave RAO.

After calculation, the heave RAO, pitch angle, and pitch RAO for both rafts and the hinge angle RAO in the 1:25 model scale are plotted from Figure 5.23 to Figure 5.29 below.

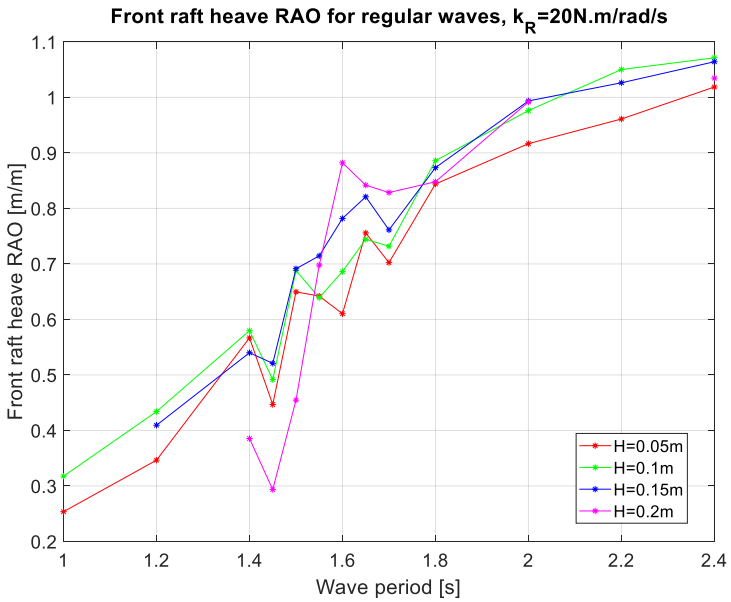

Figure 5.23: Front raft heave RAO with k_R = 20 N.m/rad/s

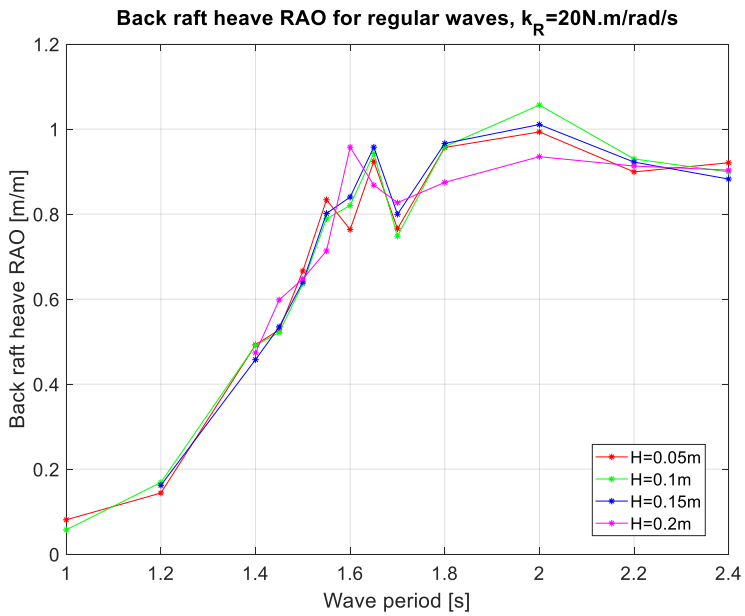

Figure 5.24: Back raft heave RAO with k_R = 20 N.m/rad/s

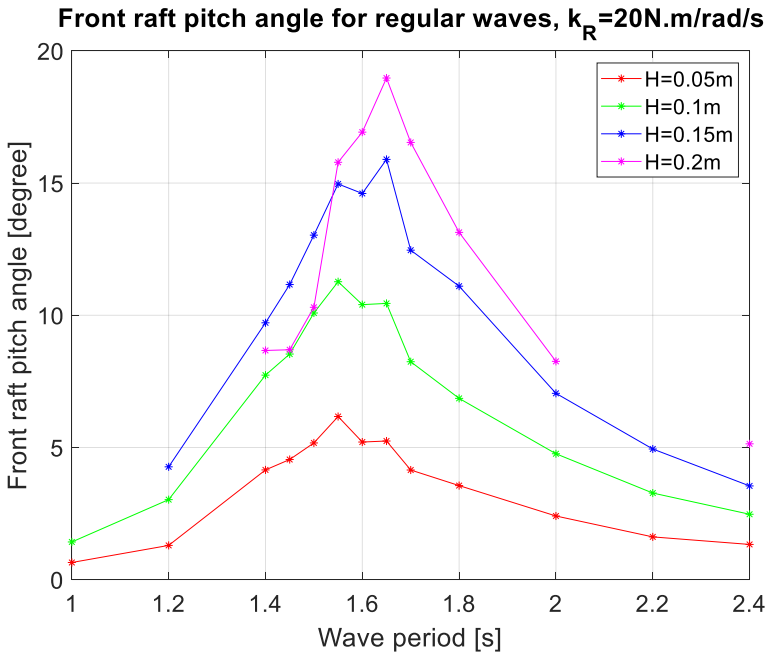

Figure 5.25: Front raft pitch angle with k_R = 20 N.m/rad/s

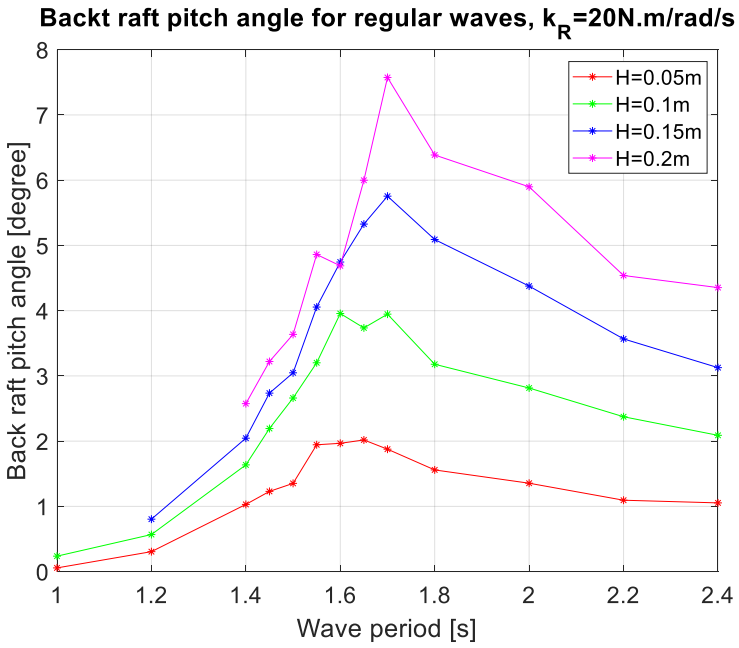

Figure 5.26: Back raft pitch angle with k_R = 20 N.m/rad/s

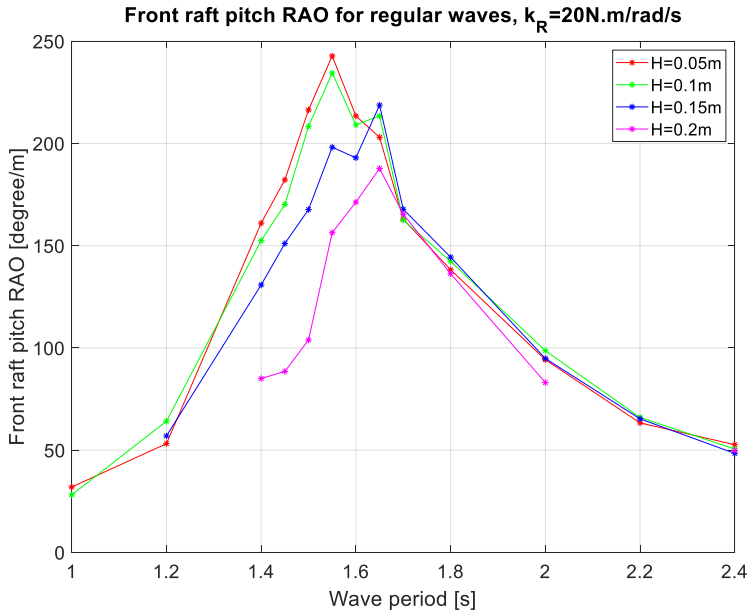

Figure 5.27: Front raft pitch RAO with k_R = 20 N.m/rad/s

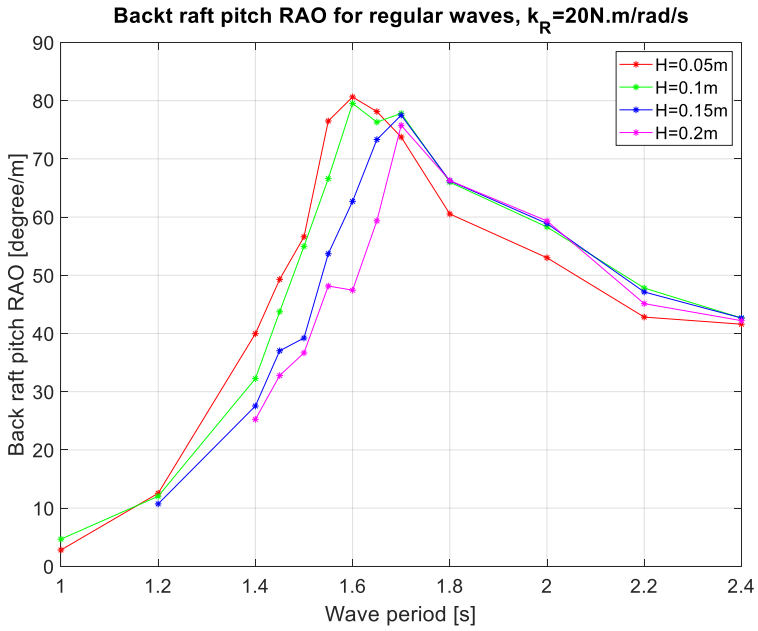

Figure 5.28: Back raft pitch RAO with k_R = 20 N.m/rad/s

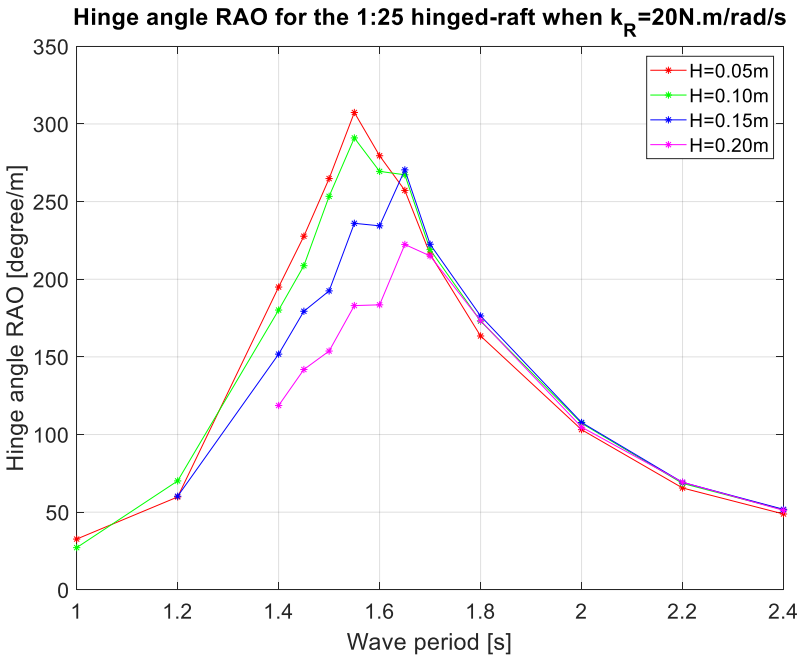

Figure 5.29: Regular wave hinge angle RAO with k_R = 20 N.m/rad/s

For the regular wave case with H = 0.2 m and T = 2.2 s, due to the technical issue, the motion capture for the front raft failed. As a result, the RAO curve for front raft heave and pitch with H = 0.2 m has one data point missing at T = 2.2 s.

From Figure 5.23 and Figure 5.24, it can be noticed that the heave RAO of both rafts are similar no matter what wave height H is used. For the front raft, the heave RAO increases with the increase of the wave period with a peak at about T = 1.60 s and followed by a decrease and increases again after T = 1.70 s. For the back raft, the heave RAO also increases with the increase of the wave period with a peak also at about T = 1.60 s and a decrease afterward. It also increases again after T = 1.70 s and becomes stable after T = 1.80 s. From the free decay test result, the natural period of the device (1.54 s for 4 peaks to 1.55 s for 3 peaks as shown in Figure 5.21) with k_R = 20 N.m/rad/s is close to 1.60 s. As a result, the fluctuations of the heave RAO of both rafts are due to the resonance of the device.

For the front raft, the pitch RAO increases with the increase of T until it reaches the peak value at about T = 1.55 s (H = 0.05 m) to 1.65 s (H = 0.20 m) and followed by a constant decrease. For the back raft, the pitch RAO also increases with the increase of T until it reaches the peak value at 1.60 s (H = 0.05 m) to 1.70 s (H = 0.20 m) wave period and is followed by a constant decrease. It can be found that the peak period of the pitch RAO of the front raft with H = 0.05 m and H = 0.10 m is about 1.55 s and it is exactly what the resonance period of the model is. However, it can be noticed when H is larger (H = 0.15 m and H = 0.20 m), the peak value of the pitch RAO happens with a larger T at 1.65 s. It can be found that the back raft reached its peak RAO value at a larger T than the front raft.

The pitch RAO values for both rafts are obviously affected by *H*. The pitch RAO for both rafts with smaller wave heights is higher than that with larger wave heights. It means the pitch response of the hinged raft with a lower *H* is much more responsive than that with a higher *H*. It means the hinged raft may have a higher CWR in lower *H* than a higher *H*. The pitch RAO for the front raft is much larger than the back raft as expected.

For the hinge angle RAO, it increases with the increase of wave period *T* until it reaches the peak value at *T* = 1.55s (*H* = 0.05 m) to *T*= 1.65 s (*H* = 0.20 m), which shows a clear relationship with the free decay period (1.54 s to 1.55 s with k_R = 20 N.m/rad/s) of the device. It is followed by a constant decrease afterward. It can be noticed that the hinge angle RAO decreases with the increase of *H* and the peak RAO period increased with the increase of the wave height. From the hinge angle RAO, it can be noticed an obvious non-linear response of the WEC as explained in Section 2.2.2. The hinge angle RAO depends not only on the incoming wave period *T* but also on the wave height *H*.

The CWR for the model was calculated from Equation 5.1 to Equation 5.4. All of the regular wave cases were processed accordingly, and the CWR curves are plotted in Figure 5.30 below:

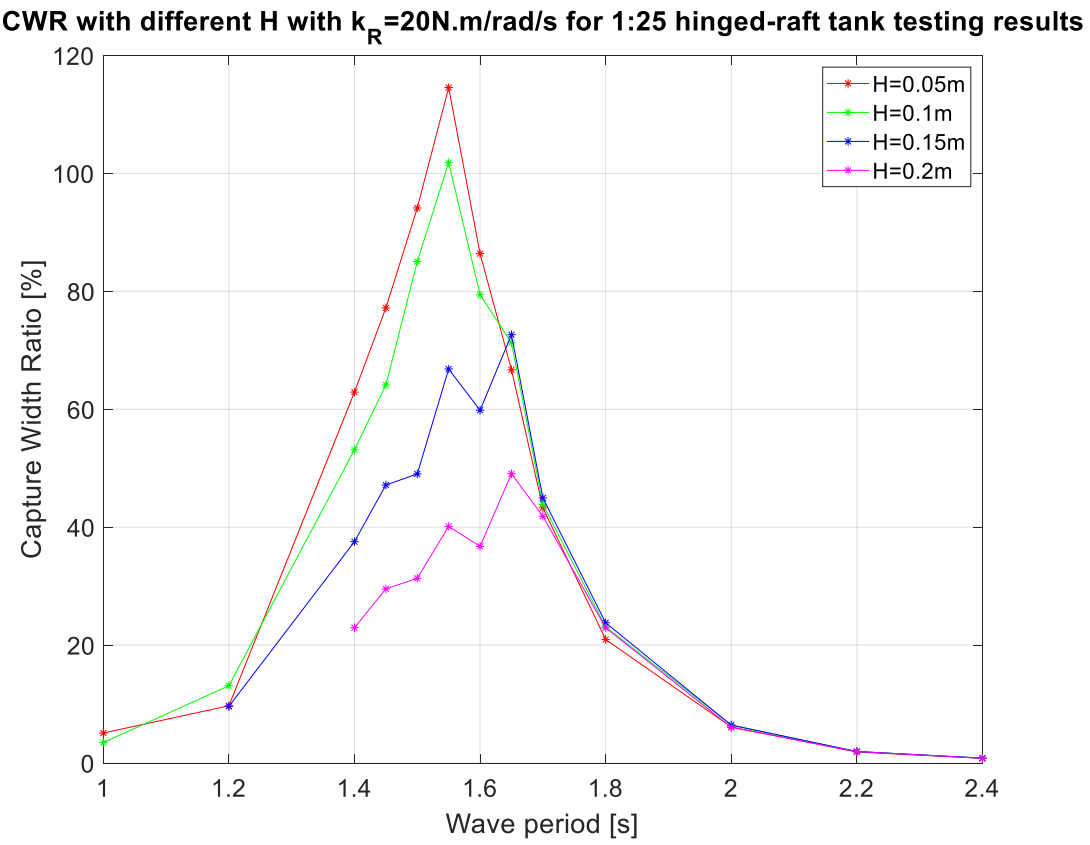

Figure 5.30: CWR of 1:25 hinged raft tank testing results.

From the results, it can be seen that the CWR increases with the increase of T until it reaches the peak value at T = 1.55 s (H = 0.05 m) to 1.65 s (H = 0.2 m) and followed by a constant decrease afterward.

For the same wave period T, the CWR of a smaller wave height is larger than a larger wave height. The CWR values with H = 0.15 m and H = 0.20 m is significantly lower than that with H = 0.05 m and H = 0.10 m. The speculation from the pitch RAO results that the CWR with a lower H is higher than that with a higher H has been confirmed.

For H = 0.05 m and H = 0.1 m, the CWR peaks at T = 1.55 s. While for H = 0.15 m and H = 0.2 m, the CWR peaks at T = 1.65 s. The wave period at the peak values of CWR ranges from 1.55 s to 1.65 s, which is where the natural period of the model is. According to the dispersion relationship in a limited water depth of 3 m, the wavelength corresponding to the wave period of 1.55 s was 3.75 m. The wavelength corresponding to the wave period of 1.65 s was 4.25 m and the total length of the model was 3.2 m. Thus the resonance of the model occurs when the incoming wavelength was from 17% to 33% larger than the model length.

The influence of wave steepness on the hinged angle RAO is shown in Figure 5.31 below. The steepness of the regular waves ranges from 0.003 to 0.03. It was found that the linear correlation factor of the wave steepness and the hinge angle RAO was very small (31.9%), which meant there was no relationship between the wave steepness and the hinge angle RAO.

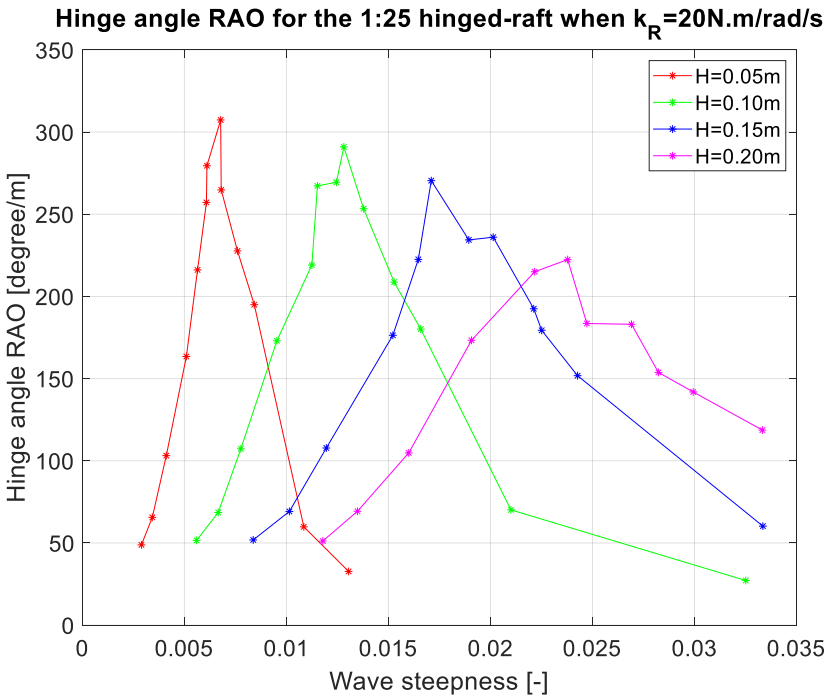

Figure 5.31: Regular wave hinge angle RAO with k_R = 20 N.m/rad/s with wave steepness.

From the regular wave analysis results, it can be noticed that the 1:25 hinged-raft was a non-linear model, the RAO depends on the wave height *H*, which was different from the linear model RM3 used in Chapter 4.

5.4.3 JONSWAP irregular wave analysis results

The analysis of JONSWAP waves focused on the average power output and the spectral RAO of the hinge angle. According to the test plan in Appendix 9.1, there were in total 12 JONSWAP waves tested on the model.

A. Average power output analysis

Similar to the regular wave model testing, each of the 12 JONSWAP waves' average power output was calculated from Equation 5.3, see Figure 5.32 below:

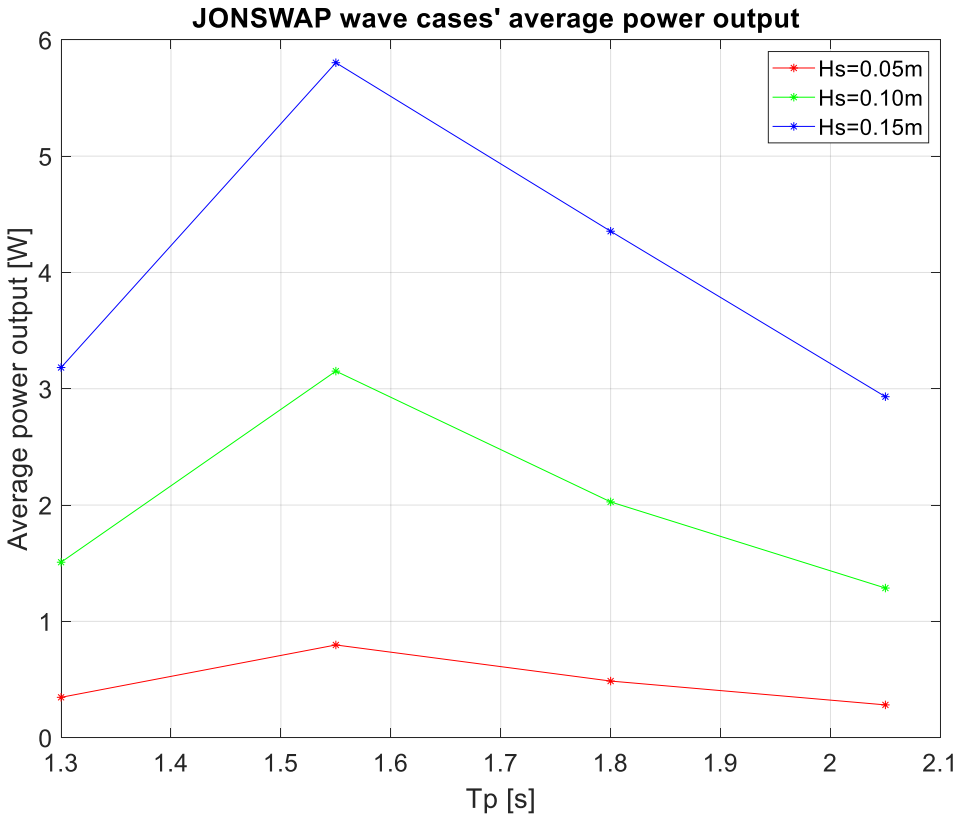

Figure 5.32: 12 JONSWAP sea states' average power output

It can be noticed that all of the JONSWAP sea states' power outputs reached the peak value at T_p = 1.55 s, which was equal to the resonance period of the model. The average power output from a large significant wave height was always larger than that from a small significant wave height as expected.

B. Spectral RAO analysis for the hinge motion

The hinge angle spectral RAO for the model is calculated from Equation 5.17 below:

$$RAO = \sqrt{\frac{S_{hinge}}{S_{\eta}}} \tag{5.17}$$

in which S_{hinge} is the hinge movement spectrum of the WEC and S_{η} is the spectrum for the incoming irregular wave. Both of them were calculated using DFT. The time window used was the same as the wave calibration process with a 720 s time duration. As mentioned in Section 5.2.1, the sampling frequency of the wave gauges used was 128 Hz. According to the definition of the Nyquist frequency in [184] and [185], the Nyquist frequency is one-half of the sampling frequency. For the wave gauges used in this research, it was 64 Hz. As shown in the test plan in Section 5.1, of all the 12 JONSWAP waves and 31 representative waves tested, the frequency range of interest was much lower than the Nyquist frequency (less than 3 Hz). Examples can be found in Figure 5.11 and Figure 5.14. As a result, the signals measured were free of the distortion known as aliasing.

The non-directional wave spectrum was calculated using MATLAB. It was required to specify the number of data points for the DFT calculation. For each irregular wave signal, there were in total of 720×128 = 92160 data points. The number of data points used for DFT calculation was the same as the signal length. There was no window weighting function applied [186] and a default rectangular window was used for the DFT calculation. For the hinge angle motion, it provided a dimensional value (hinge angle [degree]/ wave amplitude [m]).

All of the 12 JONSWAP wave spectra's spectral RAO were obtained and plotted, see the figure below:

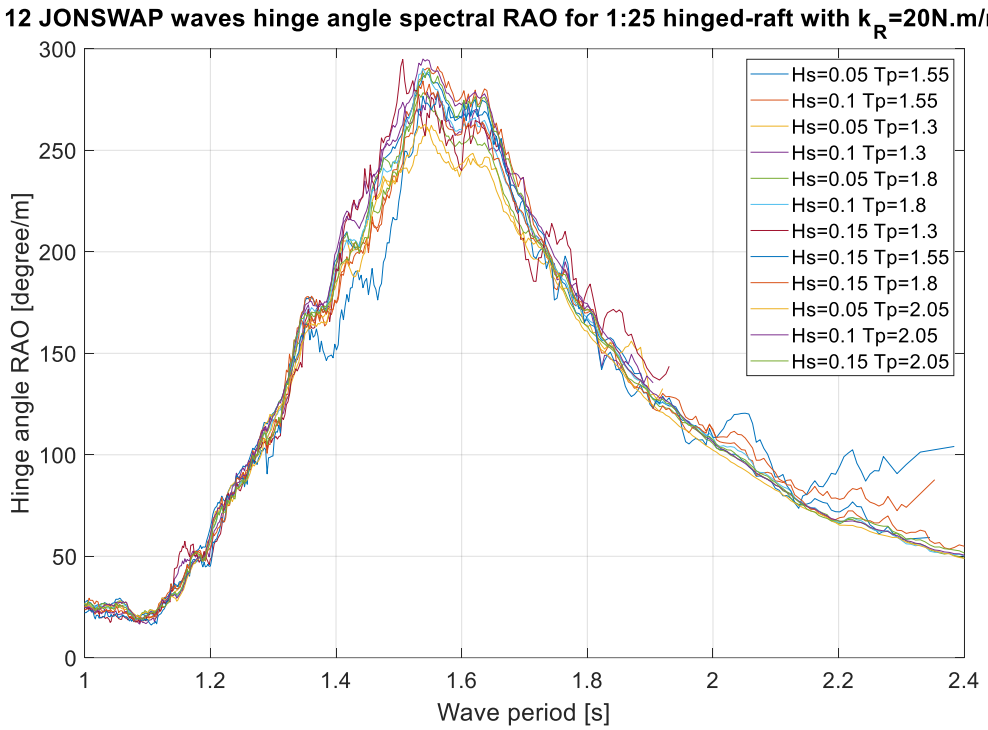

Figure 5.33: Hinge angle spectral RAO for all 12 JONSWAP waves.

From the results, it can be noticed that 12 JONSWAP wave cases' hinge angle spectral RAO were obviously different from each other. The highest peak value 294.6 deg/m was from H_s = 0.1 m, T_p = 2.05 s at T = 1.55 s, which was 12.3% higher than the lowest peak value 262.3 deg/m from H_s = 0.05 m, T_p = 1.3 s at T = 1.55 s. It confirmed the non-linearity of the 1:25 hinged-raft. However, the non-linearity was only obvious in the range from T = 1.55s to T = 1.65 s when the wave period was close to the resonance period. For the wave periods far away from the resonance period, the hinge RAO mostly presented a linear behaviour.

It can be noticed that the JONSWAP wave hinge angle spectral RAO was different from the regular waves hinge angle RAO. To compare, the JONSWAP hinge angle spectral RAO and regular wave hinge angle RAO were plotted together, see Figure 5.34 below:

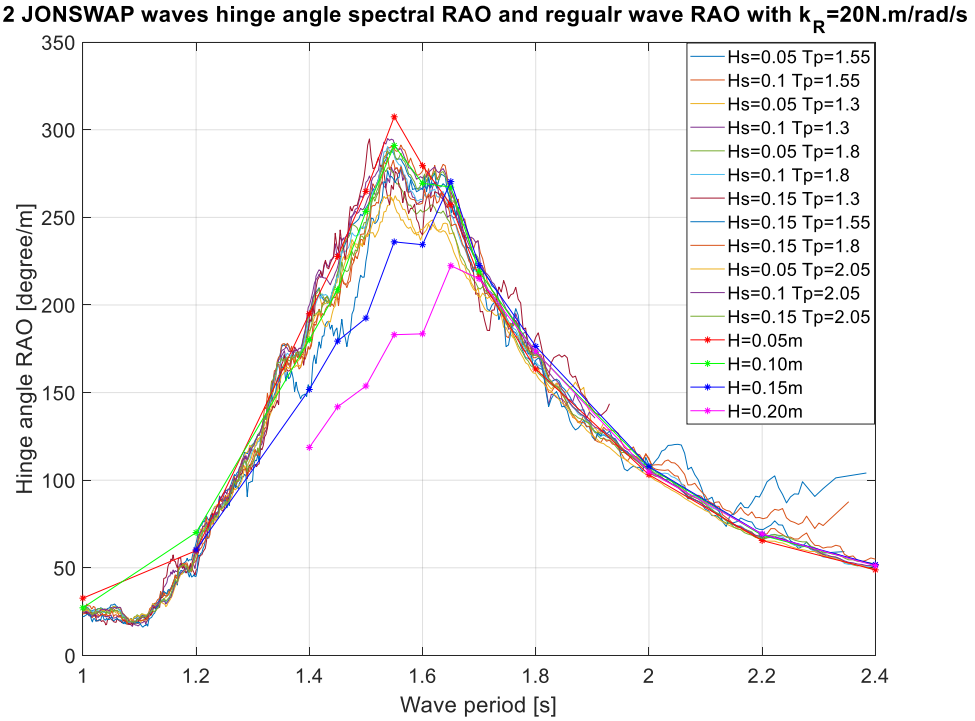

Figure 5.34: Hinge angle RAO for both regular and JONSWAP irregular waves.

It can be found that the JONSWAP wave hinge angle spectral RAO and regular wave hinge angle RAO matched well when H was small (0.05 m and 0.10 m), but not the case for H = 0.15 m and 0.2 m. The non-linearity of the 1:25 hinged-raft increased with the increase of wave height and became obvious when H > 0.15 m. For the 12 JONSWAP waves tested, even the highest H_s was only 0.15 m. From the definition of significant wave height (the average wave height of the 1/3 highest waves), for an irregular wave with H_s = 0.15 m, the average wave height was much lower than 0.15 m. It was why the non-linearity for 12 JONSWAP waves was not as obvious as the regular wave cases with

H = 0.15 m. Similarly, the average wave steepness of JONSWAP waves was even smaller than the regular waves. As a result, the influence of wave steepness was considered unimportant.

In previous research [187], the reflection coefficient C_R, which was defined as the reflected wave height as a proportion of the incident wave height at a certain wave period, was measured in the wave basin of the University of Plymouth. The result is shown in Figure 5.35.

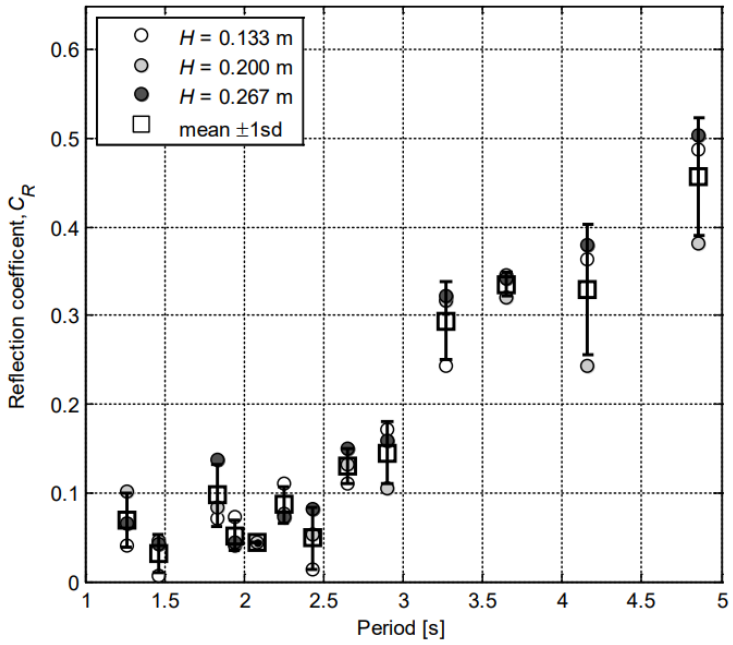

Figure 5.35: Reflection coefficients calculated for a range of regular wave periods and three wave heights in the wave basin, University of Plymouth [187].

It can be noticed that the wave height H had little effect on C_R. However, C_R was heavily influenced by the incoming wave period. There was a large increase in value at wave periods from 2.5 s to 3.5 s.

According to the test plan in Section 5.1, the regular waves tested were with wave periods ranging from 1 s to 2.4 s. For JONSWAP waves tested, T_p ranged from 1.3 s to 2.05 s. As a result, the influence of wave reflection was very small due to the existence of the parabolic absorbing beach in the wave basin and the active wave absorption system in the wave paddles.

5.4.4 HF radar representative sea states analysis results

All of the 31 representative sea states tested on the hinged-raft with K = 1, K = 5, K = 10, and K = 15 from method C, HF radar sea states were analysed to obtain the spectral RAO and the average power output.

A. Hinge angle spectral RAO for representative sea states with K = 15

Only the representative sea states hinge angle spectral RAO for K = 15 are shown in this section. The sea states tested with K = 15 are shown in Figure 5.36 and Figure 5.37 below:

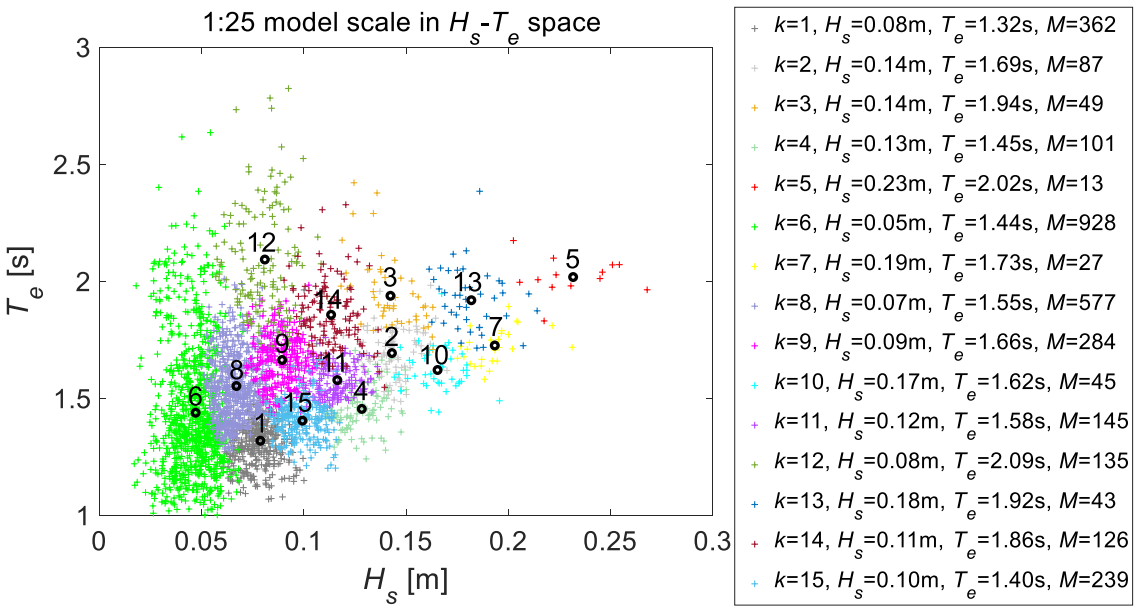

Figure 5.36: Representative sea states for K = 15 (k = 1, 2, 3…15) in H_s - T_e space with scaling factor 25, members in the same group are with the same colour, 15 black circles are the 15 representative sea states. M represents the number of members in group k.

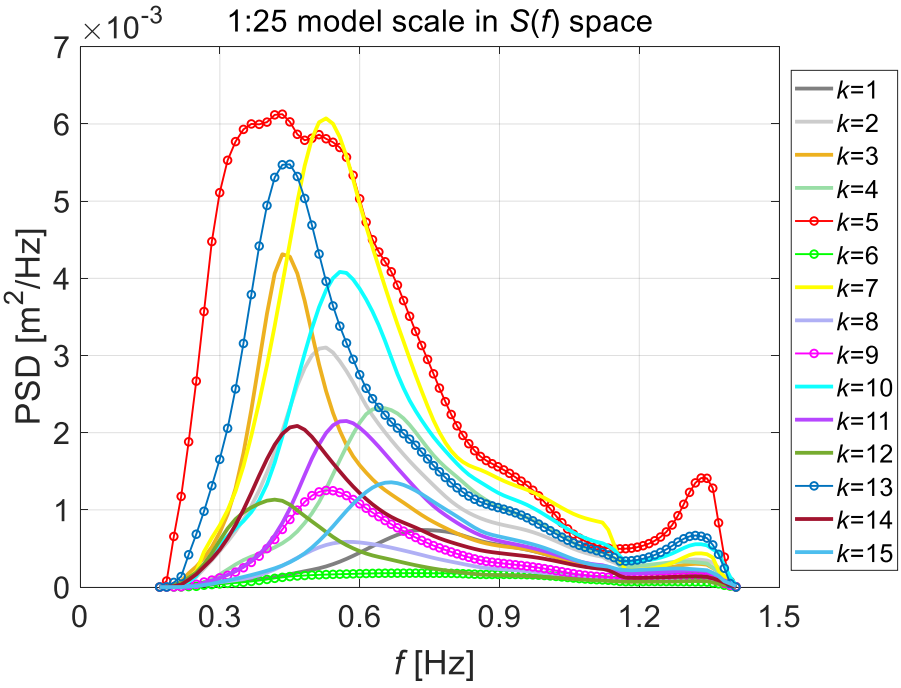

Figure 5.37: Representative sea states from HF radar data set of group k for K = 15 in $S(f)$ space with scaling a factor of 25. 15 lines represent 15 representative sea states.

From Figure 5.37, it can be found that when K = 15, the representative sea state with the highest significant wave height is from the 5th group (k = 5) with target H_s = 0.23 m, T_e = 2.02 s, number of members $M(k)$ = 13. From the T_e values of the representative sea states, it can be found that the reflection of the waves is unimportant in this research based on Figure 5.35.

Similar to the JONSWAP wave analysis, each representative wave case's incoming wave spectrum and hinge angle spectrum were obtained by using DFT.

After calculation, all of the 15 hinge angle spectral RAOs for K = 15 were obtained, which are shown in Figure 5.38 below:

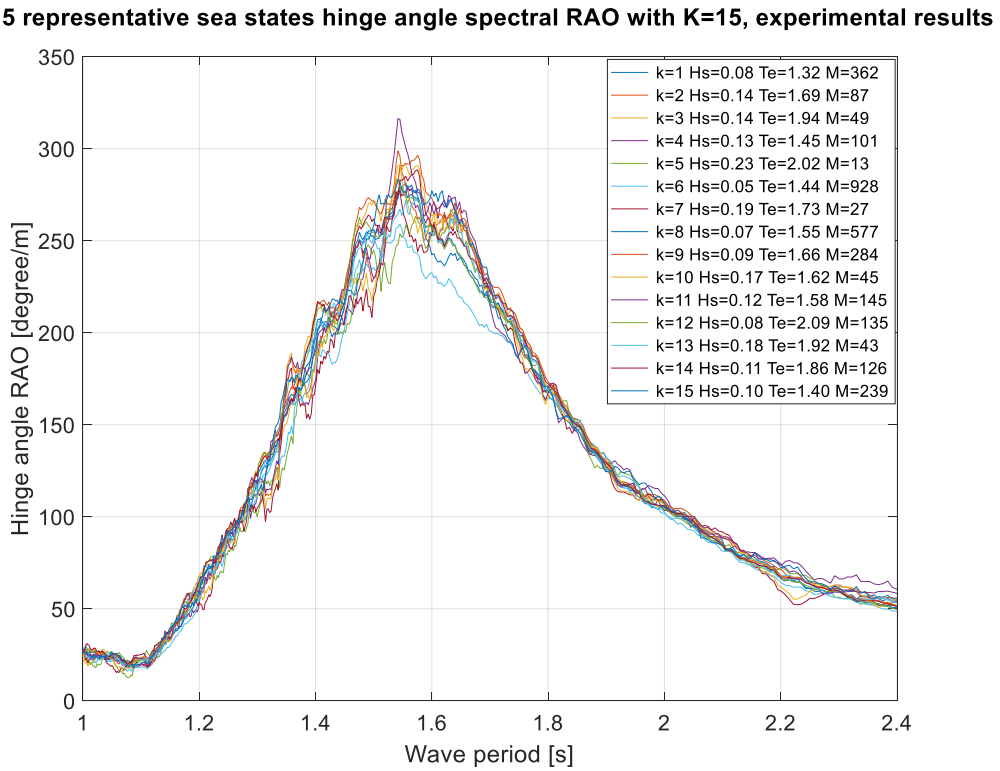

Figure 5.38: All 15 representative sea states' hinge angle spectral RAO for K = 15, 1:25 model scale.

It can be noticed that the same as 12 JONSWAP irregular wave results, 15 representative sea states' hinge angle spectral RAO for K = 15 also showed obvious non-linearity close to the resonance period.

The highest peak value (316.37 deg/m) for the hinge angle spectral RAO among 15 representative sea states of K = 15 occurred when k = 11 with target H_s = 0.12 m, T_e = 1.58 s, M = 145. The lowest peak value (262.33 deg/m) occurred for wave k = 6 with H_s = 0.05 m, T_e = 1.44 s, M = 928. It was different from what has been found from the regular wave hinge angle RAO results shown in Figure 5.29, in which the smaller wave height provided a higher spectral RAO peak value than the wave with a larger wave height. This will be explained in Sections 5.5.2 and 5.5.3.

B. Annual energy output estimation using representative sea states with different *K*

The focus of the power output analysis was the average power output from each of the 31 representative sea states. The average power output calculation procedure was the same as the JONSWAP waves. By using Equation 4.3, the average power output for each representative sea state was obtained. After analysis, all of the 31 representative sea states' average power output for physical model testing is shown in Table 5.6.

Table 5.6: Summary of the obtained physical average power outputs for method C with *K* = 1, 5 10, and 15.

K	***k***	***M***	P_{phy} **[W]**	***k***	***M***	P_{phy} **[W]**
1	1	3161	1.32			
5	1	424	1.355	4	221	3.245
	2	496	2.255	5	1939	0.584
	3	81	4.63			
10	1	143	3.466	6	36	5.545
	2	1310	0.363	7	262	1.956
	3	78	1.92	8	468	0.857
	4	13	6.001	9	565	1.255
	5	232	2.742	10	54	3.692
15	1	362	0.92	9	284	1.607
	2	87	3.185	10	45	4.566
	3	49	2.309	11	145	2.699
	4	101	3.234	12	135	0.647
	5	13	6.031	13	43	3.758
	6	928	0.263	14	126	1.69
	7	27	5.613	15	239	1.979
	8	577	0.815			

According to the industry design standards [163], the WEC needs to have enough fatigue life to satisfy the Fatigue Limit State (FLS). It means the WEC must not fail in the life

span. In this research, due to the time limitation. The fatigue or failure of the component of the WEC was not taken into consideration. The WEC was assumed with enough fatigue life.

The annual energy output of 3,161 hours on the 1:25 model scale can be obtained by using the following Equations 5.18 and 5.19:

$$E_k = P_k \times M(k) \times 720 \tag{5.18}$$

and

$$E_{total} = \sum_{k=1}^{K} E_k \tag{5.19}$$

in which P_k is the average power output from the physical tank testing results in group k shown in Table 5.6. $M(k)$ is the number of members inside group k. The time used to calculate energy output is 720 s according to the Froude scaling law. E_{total} is the total energy output estimated for the 1:25 model rather than full scale. After calculation, E_{total} of different K values are shown in Table 5.7 below:

Table 5.7: Annual energy output of the hinged-raft of different *K* estimated from tank testing results, 1:25 scaled model.

K	Annual energy output [kW.h]
1	0.8345
5	0.7836
10	0.7714
15	0.7964

According to the Froude scaling law, the full-scale annual energy output and the model scale annual energy output satisfy the following Equation 5.20:

$$E_{full\ scale} = E_{model} \times \lambda^4 \tag{5.20}$$

The annual energy output for a full-scale hinged-raft was obtained, which is shown in Table 5.8.

Table 5.8: Annual energy output estimation by using different *K*, full-scale model.

Group number	Annual energy output [kW.h]
K = 1	325962.80
K = 5	306085.91
K = 10	301319.32
K = 15	311106.44

For *K* = 1, 5, 10 and 15 results, the mean value for the annual energy output was 3.11e+05 kW.h with the standard deviation of 1.07e+04 kW.h. The coefficient of variation (STD/mean) was 3.4%, which meant the variation of the annual energy output estimation

from different *K* values was small. Although there was obvious non-linearity that can be noticed from the hinge angle spectral RAO as shown in Figure 5.38, the influence of *K* on the annual output estimation was small, which was similar to the fully linear RM3 model. The reason will be discussed in detail in Section 5.6.

Due to the limitation of the time and cost of the physical model testing, it was impossible to test all of the 3,161 HF radar sea states on the hinged-raft model in the wave basin, which means that the estimation of the actual annual energy output and the representativeness assessment of different regrouping methods impossible. This part of the work was carried out using a WEC-SIM numerical model, which is shown in Section 5.5.

5.5 A 1:25 numerical hinged-raft model built in WEC-SIM

After the physical model testing of the 1:25 hinged-raft model, a WEC-SIM numerical model was built and validated based on the physical testing results.

As explained in Section 2.4. The WEC-SIM numerical model started with the building of the 3D model by using Solidworks 2019 [128], which is shown in Figure 5.39 below. The WEC-SIM model was also with a scaling factor of 25. The geometrical dimensions, the draft of the hinged-raft, and the relative distance of both rafts were the same as the design shown in Figure 5.1 and Table 5.1. For the numerical model, the superstructure of the model above the SWL, which included the hinge, the cables, and positioning markers was

considered with no direct interaction with water, therefore the geometrical details of them were omitted. The 3D model built is shown in Figure 5.39 below:

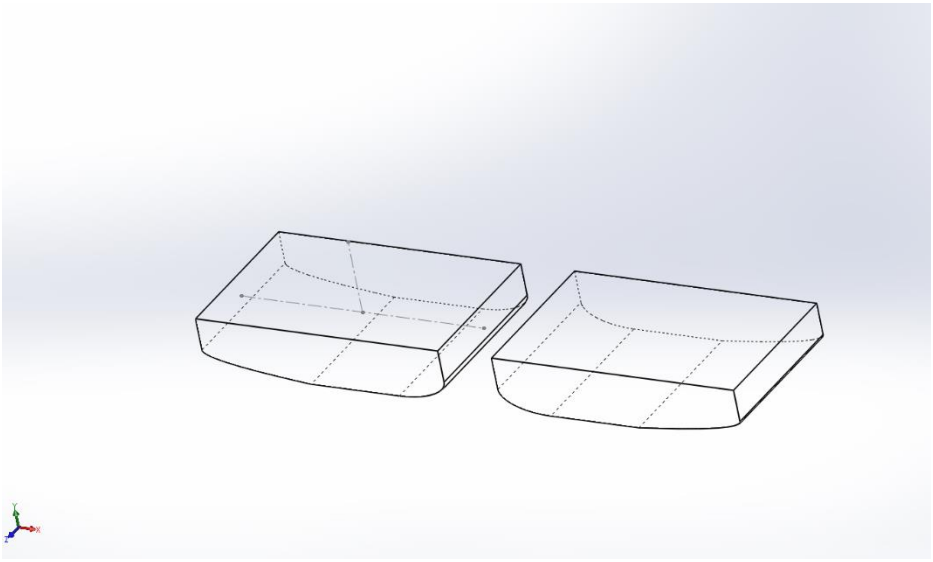

Figure 5.39: The 3D model of the 1:25 hinged raft built in Solidworks 2019.

The water depth used for the 1:25 numerical model was 3 m, which was the same as that in the physical model testing.

The 3D model of the hinged-raft was imported to AQWA to calculate the hydrodynamic coefficients as explained in Section 2.4.2. The coefficients were calculated on each node of the 3D model, thus it needed to create mesh elements for the model. In AQWA, the maximum wave frequency that can be used was dependent on the size of the mesh. The denser the mesh that was created, the higher the wave frequency that can be used. For the 1:25 hinged-raft model, the maximum element size was 0.032 m, which allowed the maximum wave frequency of 3.258 Hz, which was enough for the numerical analysis.

After meshing, there were in total 20952 nodes and 20948 mesh elements created, which is shown in Figure 5.40 below.

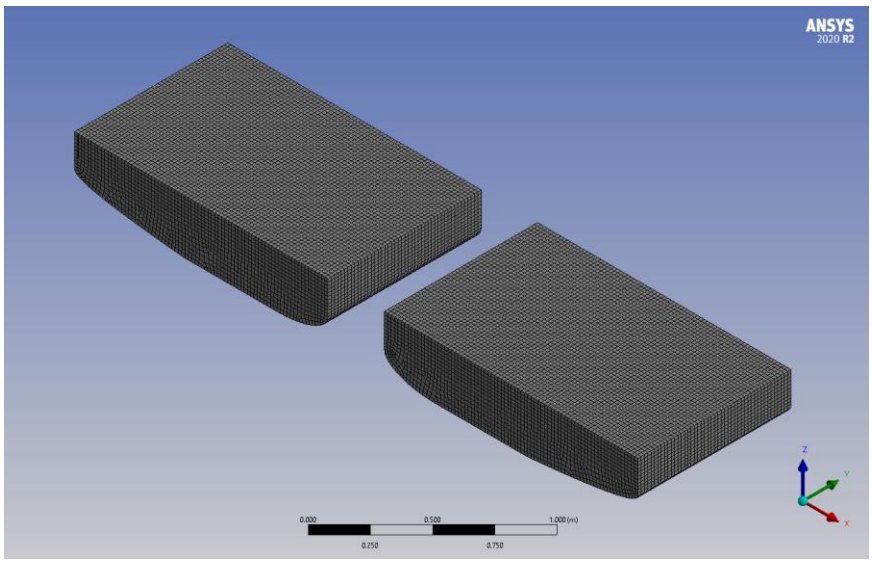

Figure 5.40: The mesh and nodes created for the 1:25 hinged-raft in AQWA.

The meshed model of the hinged-raft was simulated in a series of wave frequency components with 0-degree incoming wave direction (non-directional waves) in AQWA to obtain the hydrodynamic coefficients for each wave frequency.

After calculation, the added mass term A, damping term B, restoring term C, the excitation force vector F_e, and the radiation force vector F_{rad} at each wave frequency were obtained. The hydrodynamic frequency domain coefficients were written into an HDF5 format (.h5) file through the BEMIO script to be later used in WEC-SIM as it was shown in Figure 2.23.

The MATLAB Simulink model for the 1:25 hinged-raft was built, as is shown in Figure 5.41. At this stage, the PTO system and mooring system were added. A rotational PTO module was used in the Simulink model. The mooring system was defined in MoorDyn and the stiffness of the tension spring in the mooring lines and the coordinates of mooring points were from the test conducted in Section 5.3.

The boundary condition for both rafts was defined, in which both of the rafts are free to move in heave, surge, and pitch due to the symmetry of the model in the x-o-z plane shown in Table 5.14.

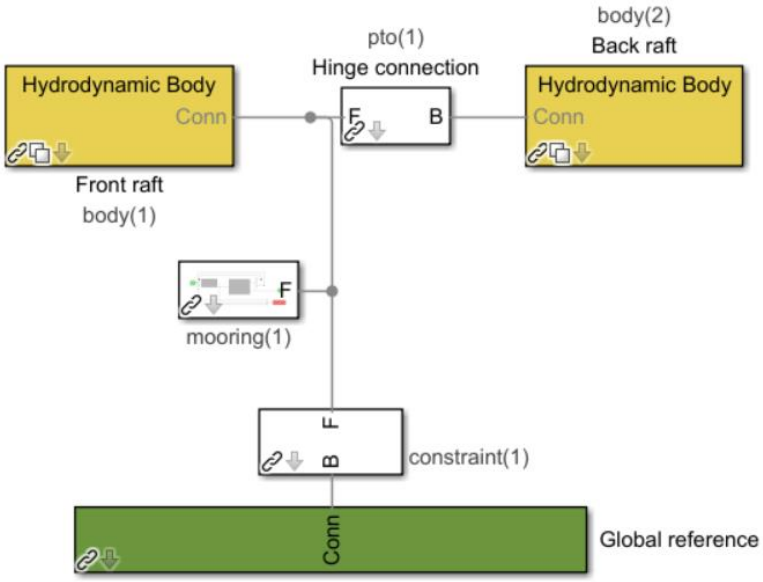

Figure 5.41: Simulink model for the 1:25 hinged-raft.

In the WEC-SIM numerical model, the wave direction was along the *x*-axis, which was the same as the wave direction in the physical model testing, see Figure 5.42 below:

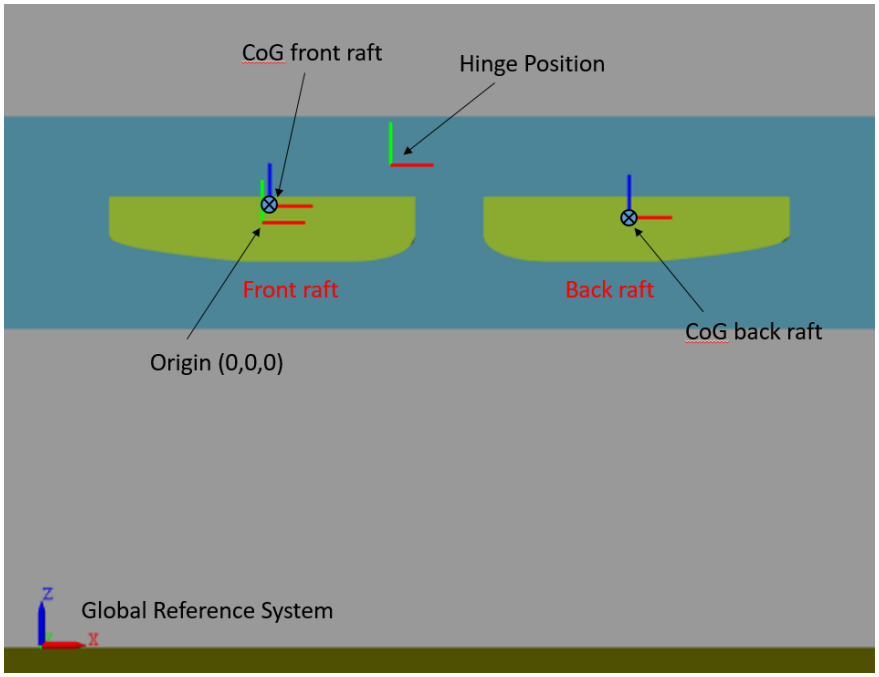

Figure 5.42: the model set up in WEC SIM, with COG of both rafts and the location of PTO marked.

The rotational damping parameter k_R used in the PTO module was 20 N.m/rad/s. The MOI values were specified in the input file.

The results from the physical model testing were compared with the results from the WEC-SIM numerical simulation. This section focuses on the hinge angle spectral RAO and the average power output performance.

5.5.1 Regular wave analysis for the numerical model.

The regular sea states tested physically on the 1:25 hinged-raft were inputted to the WEC-SIM model for numerical analysis. The time duration and the time window used were the

same as the physical testing conditions. In order to illustrate the results clearly, only the results for H = 0.05 m and H = 0.2 m are shown in Figure 5.43 below.

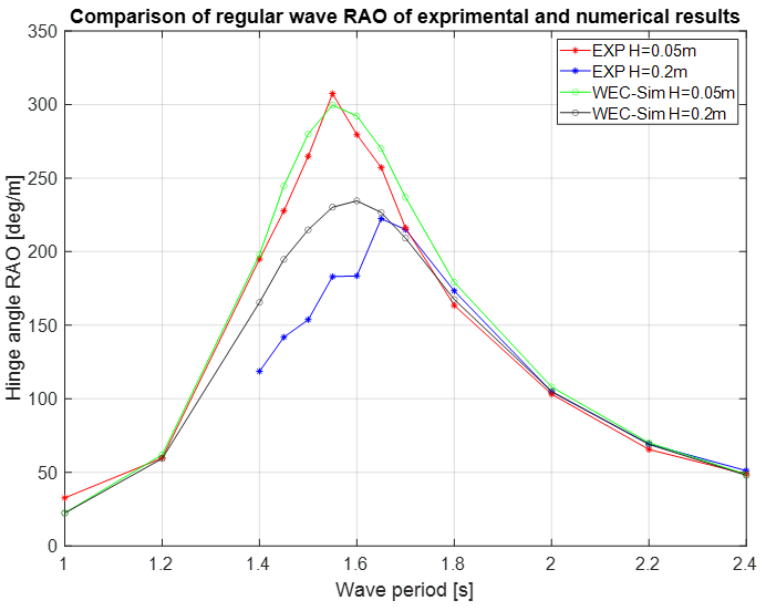

Figure 5.43: The comparison of regular sea states hinge angle RAO of experimental and WEC-SIM numerical results.

It can be noticed that the WEC-SIM model and the tank testing results agree with each other very well at small wave heights with H = 0.05 m. The non-linearity of the hinged-raft is well presented in the numerical model. However, it can be noticed that when H = 0.2 m, there exists an obvious difference between the experimental and WEC-SIM numerical results. As introduced in Section 5.3, it was because of large wave heights, that there was a strong overtopping phenomenon on the front raft, which influenced the performance of the device seriously. Due to the limitation of the numerical model, this phenomenon cannot be reproduced and it was why the hinge angle RAO results for large H were different.

From Figure 5.43, it was found that the influence of wave steepness is very small and can be neglected. Taking the RAO results at T = 1.2 s as an example, it can be found that RAO results for different H = 0.05 m and H = 0.2 m were the same. However, the wave steepness of them was completely different. Similar results can be found at T = 2.4 s. As a result, the influence of wave steepness was not important. The important factor that influences the RAO is the incoming wave period.

5.5.2 JONSWAP irregular wave analysis for the numerical model.

The spectral RAOs of all 12 JONSWAP irregular waves were obtained using Equation 5.17. Each JONSWAP sea state was scaled down by the scaling factor of 25 according to Table 2.1 and tested on the numerical model. The same time duration and time window in the physical testing were used for the calculation. The results for 12 JONSWAP waves' hinge angle spectral RAO are shown in Figure 5.44 below:

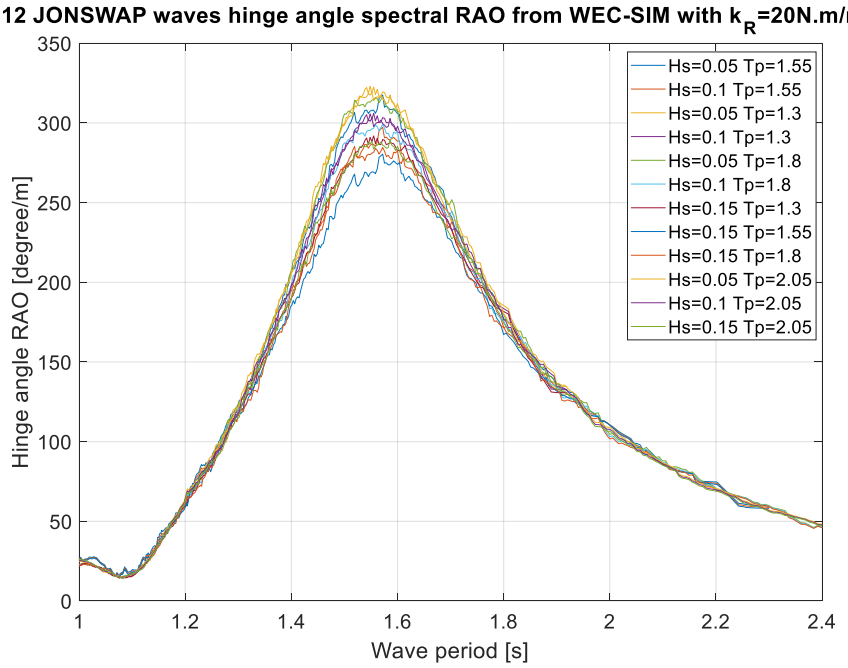

Figure 5.44: Hinge angle spectral RAO of 12 JONSWAP waves from WEC-SIM analysis with k_R = 20 N.m/rad/s for 1:25 hinged-raft.

By comparing Figure 5.44 with Figure 5.33, it can be noticed that the hinge angle spectral RAO from WEC-SIM analysis and the results from physical testing are similar.

In order to see the results clearly, taking three JONSWAP waves to compare, which are H_s = 0.10 m, target T_p = 2.05 s, H_s = 0.15 m, target T_p = 1.55 s and H_s = 0.05 m, target T_p = 1.3 s, the hinge angle RAO from physical/numerical results are plotted in Figure 5.45 below:

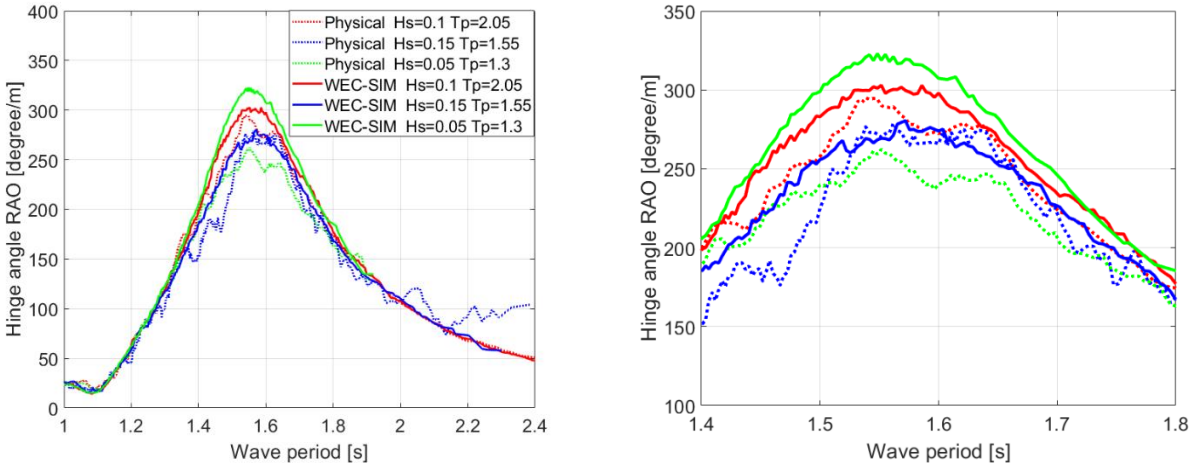

Figure 5.45: Physical and numerical hinge angle RAOs for three JONSWAP irregular waves. The left figure shows the results in full range and the right shows the close-up. Physical results are shown in dashed lines and numerical results are shown in solid lines.

The WEC-SIM numerical model shows clearly a non-linear behaviour from Figure 5.44 at the wave period close to 1.55 s, which is the resonance period of the model. What is different from the physical testing results is that the sea state with a smaller target H_s always provides a higher peak RAO value and vice versa. As shown in Figure 5.45, for the numerical results, the highest peak value (322.97 deg/m) for the hinge angle spectral RAO occurs with target H_s = 0.05 m, target T_p = 1.3 s. The lowest peak value (280.46 deg/m) occurs with target H_s = 0.15 m, target T_p = 1.55 s. This agrees with the hinge angle RAO result from regular wave testing shown in Figure 5.43 and also the results from physical model testing in regular waves shown in Figure 5.29. However, it is not the case for physical results with JONSWAP wave target H_s = 0.05 m, target T_p = 1.3 s. This can be the reason that it is relatively hard to calibrate the wave accurately when H_s is quite small in the physical basin for irregular waves. From the introduction of the model shown in Figure 5.1, the mass and size of this hinged raft WEC are significant compared to the small H_s of 0.05 m. Therefore, the physical response can be contaminated by uncertainties such as un-calmed waves between wave cases and the reflection in the

physical basin, especially under small waves, which are, however, absent in the numerical WEC-Sim model.

It can be noticed that the numerical results (red, blue, and green solid lines) match that from physical testing (red, blue, and green dotted lines) well, with just slight over predictions. It can lead to a higher average power output value from the numerical model.

5.5.3 HF radar representative sea states analysis for the numerical model.

Next, the 31 representative sea states (K = 1, K = 5, K = 10, and K = 15) from method C obtained from HF radar sea states were tested on the numerical model. The representative sea states were scaled down with the scaling factor of 25 and inputted to WEC-SIM for analysis. After calculation, all 31 hinge angle spectral RAO from the numerical model were obtained. Only the results for K = 15 were shown in this section, see Figure 5.46 below.

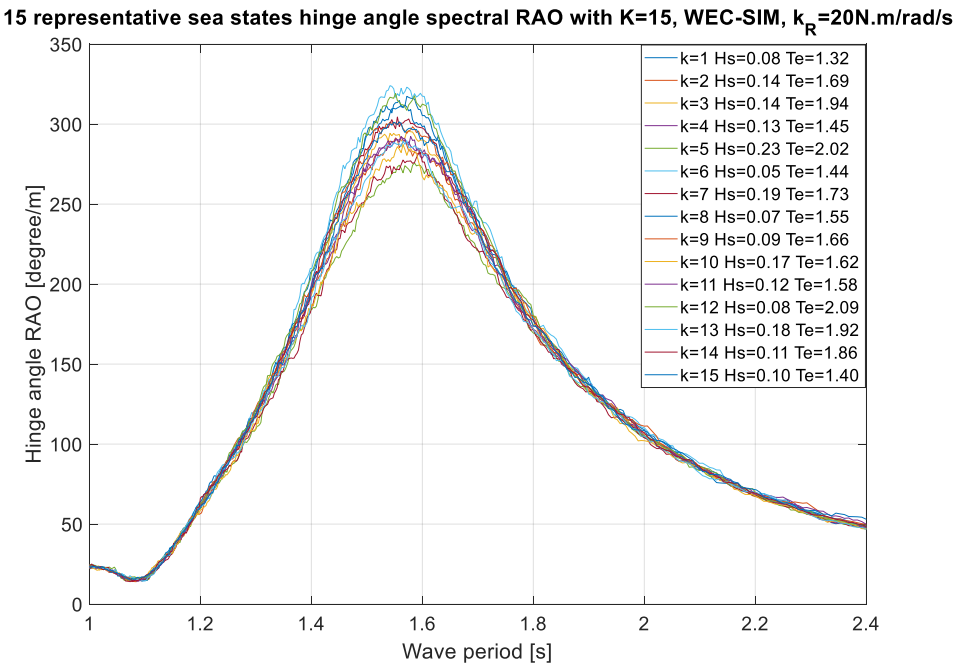

Figure 5.46: Hinge angle spectral RAO of 15 representative sea states with K = 15 from numerical model with k_R = 20 N.m/rad/s for 1:25 hinged-raft.

To show the results clearly, 3 representative sea states of K = 15 as shown in Figure 5.36 and Figure 5.37 are selected for comparison. The representative sea states of k = 5 (the highest H_s and smallest number of members M), k = 6 (the lowest H_s and largest number of members M), and k = 9 (in the middle) are plotted in Figure 5.47 below:

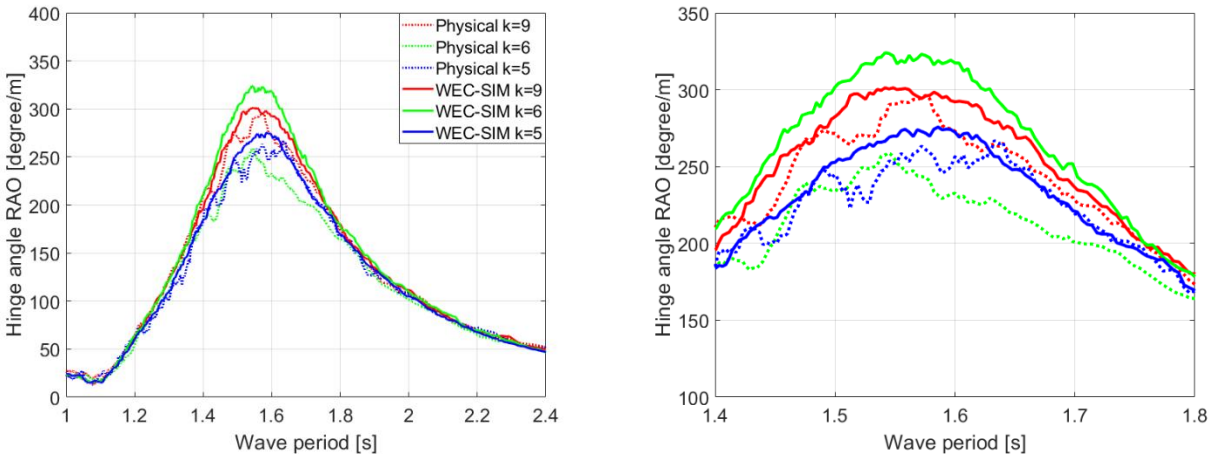

Figure 5.47: Physical and numerical hinge angle RAOs for the smallest and largest number of representative sea states under k = 5 (H_s = 0.23 m and T_e = 2.02 s, blue) and k

= 6 (H_s = 0.05 m and T_e = 1.44 s, green), as well as k = 9 (H_s = 0.09 m and T_e = 1.66 s, red). The left figure shows the results in full range and the right shows the close-up. Physical results are shown in dashed lines and numerical results are shown in solid lines.

From Figure 5.46, The WEC-SIM numerical model shows clearly a non-linear behaviour when wave period T is close to the resonance period of the model. Similar to the JONSWAP waves results, for the numerical model, the highest peak RAO value (324.05 deg/m) for the hinge angle spectral RAO occurs with group number k = 6, with target H_s = 0.05 m, target T_e = 1.44 s. The lowest peak value (275.71 deg/m) occurs with group number k = 5, with target H_s = 0.23 m, target T_e = 2.02 s. This also agrees with the hinge angle RAO result from regular wave testing shown in Figure 5.43. Similar to JONSWAP wave results shown in Figure 5.45, the spectral RAO for the small wave with k = 6, H_s = 0.05 m, and T_e = 1.44 s presents a relatively large error with the physical results. It can be noticed that the numerical hinge angle spectral RAO results are slightly higher than that from physical testing results, which means the power output can be slightly over predicted.

The resonance period of 31 representative sea states for the numerical model can also be obtained. From the numerical results of the model, the lowest resonance period is from the lowest H_s and vice versa. H_s of 31 representative sea states range from 0.05 m to 0.23 m as shown in Figure 5.36. Then the highest resonance period 1.60 s is from the representative wave with group number k = 5 with target H_s = 0.23 m and T_e = 1.44 s. The lowest resonance period of 1.54 s is from the wave case with group number k = 6 with H_s = 0.05 m and T_e = 1.44 s. So the resonance period for 31 representative sea states ranges from 1.54 s to 1.60 s.

From the results above, it can be seen the non-linear WEC-SIM 1:25 hinged-raft model matched the physical model very well although the hinge angle spectral RAO was slightly higher than the physical model result. The non-linearity of the physical model was presented clearly in the numerical model results. This suggests that the WEC-SIM numerical model can be used for the annual power output performance analysis, which is shown in Section 5.6.

5.6 Power output analysis using representative sea states on a 1:25 hinged-raft WEC-SIM numerical model

Since the numerical model has been built and verified in Section 5.5, the power output performance analysis using the representative sea states obtained from different regrouping methods A to J was carried out.

The average power output results from physical and numerical model testing of 31 representative sea states were calculated using Equation 5.1 and Equation 4.3. The relative error between the numerical result and the physical result δ_P is shown in Equation 5.21 below:

$$\delta_P = \frac{P_{num} - P_{phy}}{P_{phy}} \times 100\% \tag{5.21}$$

in which P_{num} is the average power output from the WEC-SIM numerical simulation. P_{phy} is average power output from tank testing with the same sea state. The results are shown in Table 5.9 below, with the physical results from Table 5.6 to compare.

Table 5.9: Summary of the obtained physical and numerical average power outputs for method C with K = 1, 5 10, and 15.

K	***k***	***M***	P_{phy} **[W]**	P_{num} **[W]**	δ_P **[%]**	***k***	***M***	P_{phy}**W]**	P_{num} **[W]**	δ_P **[%]**
1	1	3161	1.320	1.413	7.076					
5	1	424	1.355	1.512	11.591	4	221	3.245	3.530	8.767
	2	496	2.255	2.367	4.979	5	1939	0.584	0.672	15.040
	3	81	4.630	5.046	8.990					
10	1	143	3.466	3.814	10.054	6	36	5.545	5.880	6.043
	2	1310	0.363	0.480	32.175	7	262	1.956	2.019	3.233
	3	78	1.920	2.040	6.210	8	468	0.857	1.005	17.247
	4	13	6.001	6.450	7.482	9	565	1.255	1.402	11.674
	5	232	2.742	2.949	7.554	10	54	3.692	3.806	3.1086
15	1	362	0.920	1.087	18.122	9	284	1.607	1.573	-2.162
	2	87	3.185	3.358	5.455	10	45	4.566	4.818	5.500
	3	49	2.309	2.387	3.381	11	145	2.699	2.831	4.907
	4	101	3.234	3.448	6.629	12	135	0.647	0.741	14.459
	5	13	6.031	6.419	6.447	13	43	3.758	3.908	3.995
	6	928	0.263	0.346	31.439	14	126	1.690	1.825	8.003
	7	27	5.613	5.8362	3.984	15	239	1.979	2.107	6.499
	8	577	0.815	0.943	15.701					

As can be seen from Table 5.9, the numerical and physical results agree with each other well. Considering ±15% as a limit, for K = 1, the error of the only representative sea state

is 7.08%, which lies within the limit range; For K = 5, 4 out of 5 sea states lie within the limit range; For K = 10, 8 out of 10 cases lie within the limit range; For K = 15, 12 out of 15 cases lie within the limit range. It can be noticed that the WEC-SIM results over predicted the average power output almost for every sea state. The results agreed with the hinge angle RAO results from Section 5.5.3, in which the numerical hinge angle spectral RAO was always slightly higher than the physical model results.

As observed, these 6 sea states with the relative error δ_P out of the limit range are all from the largest groups for a certain K value. For K = 5, it is the group k = 5 with 1939 members (61.3%) out of 3161. For K = 10, they are the groups k = 2 with 1310 (41.4%) and k = 8 with 468 (14.8%) members respectively. For K = 15, they are groups k = 1 with 362 (11.5%), k = 6 with 928 (29.4%) and k = 8 with 577 (18.3%) members. From Figure 5.12, it can be noticed that all of these large groups are of small representative waves of H_s < 0.08 m under the model scale. As discussed earlier, the physical response could be affected by the un-calmed wave between wave cases and the reflection under small wave conditions, which was absent from the numerical model. It was possible that the representative sea states tested physically with a small target H_s had large relative errors compared to the numerical results, which can lead to large relative errors in the average power output compared to the numerical results.

Overall, the validated non-linear WEC-Sim numerical model represented the physically observed performance of this device well. The effect of different regrouping methods on WEC performance estimation will be evaluated using this model.

A. Annual energy output performance with different *K*

The annual energy output estimation with different *K* values from the 1:25 numerical model was obtained from Equation 5.18 and Equation 5.19. After calculation, the annual energy output in the 1:25 model from WEC-SIM is shown in Table 5.10 below:

Table 5.10: Annual energy output for the 1:25 hinged raft with different *K*, numerical results.

K	Annual power output in model scale [kW.h]
1	0.893514
5	0.861429
10	0.861955
15	0.866462

The annual energy output for a full-scale prototype was obtained by using Equation 5.20 with the Froude scaling law. The annual energy output estimation from physical model testing results in Section 5.4.4 in Table 5.8 are shown to compare, see Table 5.11 below:

Table 5.11: Physical and numerical model annual energy output, full scale.

K	Annual energy output physical [kW.h]	Annual energy output numerical [kW.h]	Relative error [%]
1	325962.8	349028.8	7.076
5	306085.9	336495.7	9.935
10	301319.3	336701.3	11.742
15	311106.4	338461.6	8.793

From the results, it can be noticed that the annual energy predicted from WEC-SIM and the results from model testing are with a relative error of 12%.

As shown in Section 5.4.4, for the annual energy output from physical model testing, the average value with K = 1, 5, 10, and 15 was 3.11e+05 kW·h with an STD of 1.07e+04 kW.h. The coefficient of variation was 3.4%. For the annual energy output from numerical model testing, the average value with K = 1, 5, 10, and 15 was 3.40e+05 kW·h with an STD of 5.97e+03 kW·h. The coefficient of variation was only 1.76%. Therefore, it can be noticed that the influence of the K value on the total energy output prediction was not significant, according to the hinged raft WEC studied in this work. In other words, the annual energy output could be accurately predicted by using just a few representative sea states with $K \leq 15$, although the 1:25 hinged-raft numerical model was non-linear.

Each of the 3,161 hourly sea states was imported to WEC-SIM for the average power output calculation.

After calculation, the actual annual energy output of 3,161 sea states for the 1:25 WEC-SIM numerical model was calculated by the following Equation 5.22:

$$E_{model\ actual} = \sum_{i=1}^{3161} P_i \times 720 \tag{5.22}$$

in which $E_{model\ actual}$ is the actual annual energy output from 3,161 sea states on the 1:25 model scale; P_i is the average power output of each of the 3,161 sea states. 720 s is the

time duration for a 1: 25 model corresponding to the one-hour duration for a full-scale model using the Froude scaling law. The actual annual energy in full scale was obtained by using the Froude scaling law in the following Equation 5.23:

$$E_{full\ actual} = E_{model\ actual} \times \lambda^4 \tag{5.23}$$

in which λ = 25.

After calculation, the actual annual energy output from the WEC-SIM numerical model at full scale was 334997.9 kW.h. It can be found that the annual energy output estimations using the representative sea states with K = 1, K = 5, K = 10, and K = 15 from WEC-SIM were all very close to this actual value, see Table 5.12 below:

Table 5.12: Annual power output prediction with different K from WEC-SIM compared with the actual value in full-scale.

K	Annual energy output [kW.h]	Actual annual energy output [kW.h]	Relative error [%]
1	349028.8	334997.9	4.188
5	336495.7	334997.9	0.447
10	336701.3	334997.9	0.508
15	338461.6	334997.9	1.034

It is noticeable that the relative error between the WEC-SIM analysis and the accurate value is very small and within the error limit of 5%. From previous Section 5.5.3, the input wave power and the output WEC power for the 1:25 hinged-raft numerical model had an obvious non-linear relationship. However, the annual total energy output can be

accurately predicted by using just a few representative sea states. The reason is that although the 1:25 hinged-raft is a non-linear model, the non-linearity occurs only when the wave frequency component is close to the resonance period of the device, which ranges from 1.54 s to 1.60 s for the numerical model as explained in Section 5.5.3. From Figure 5.46 it can also be noticed that the non-linearity is obvious only when H_s is larger than 0.15 m. The total data set of HF sea states measured from Wave Hub and the range in which the non-linearity is important is shown in Figure 5.48 below:

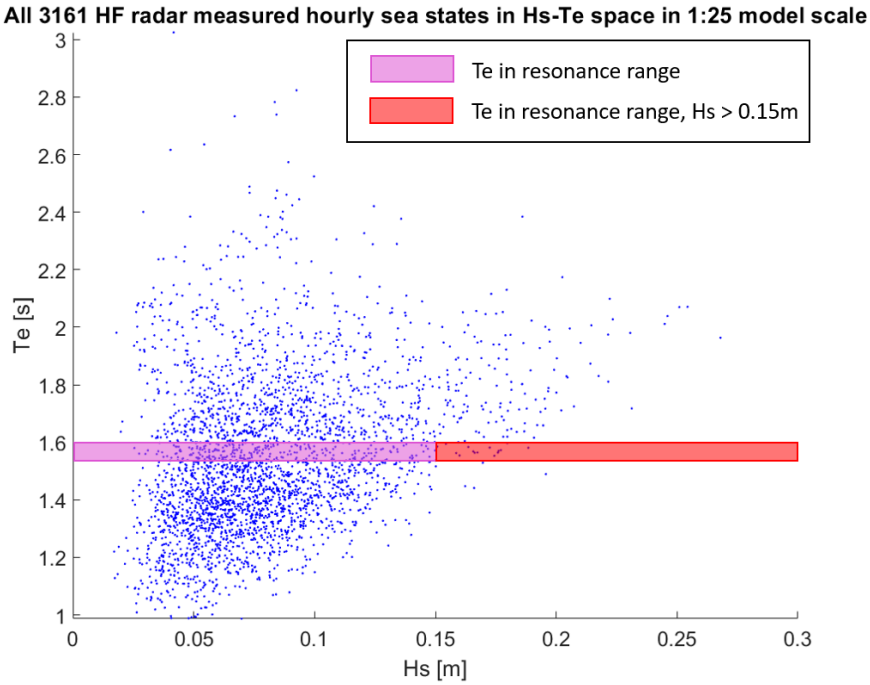

Figure 5.48: Resonance range of the hinged-raft WEC for the HF radar measured Wave Hub site with all of 3161 hourly sea states in H_s-T_e space. 1:25 model scale.

From Figure 5.48 it can be noticed that most of the 3161 hourly sea states measured from HF radar are with an energy period far away from the resonance period and only a small number of the sea states are with the energy period in the resonance range. After calculation, only 254 out of 3161 sea states are with energy period between 1.54 s to 1.60 s, among which only 15 sea states are with H_s larger than 0.15 m.

As a result, the influence of the nonlinearity on the annual energy estimation is very limited, which means Equation 4.19 can be considered valid for the hinged-raft. The annual energy output can be estimated accurately by using only a few numbers ($K \leq 15$) of representative sea states.

B. Power output representativeness analysis with different regrouping methods.

The representativeness of different regrouping methods A to J was calculated. Following the RM3 point absorber analysis, all of the representative sea states measured from HF radar were obtained with $K = 20$. For each regrouping method, 20 (or close to 20 for binning methods A and B) representative sea states were obtained from Sections 3.3 and 3.4. The representative sea states from different regrouping methods were imported to WEC-SIM to obtain the average power output for each of the representative sea states ($k = 1,2,3…20$).

By using metric one from Equation 3.23, the representativeness of the power output performance from different regrouping methods A to J was obtained. To compare, the metric one values were plotted with the power output metric values from the RM3 point absorber (Figure 4.7) and the wave power metric value for HF radar sea states (Figure 3.21) together, see Figure 5.49 below:

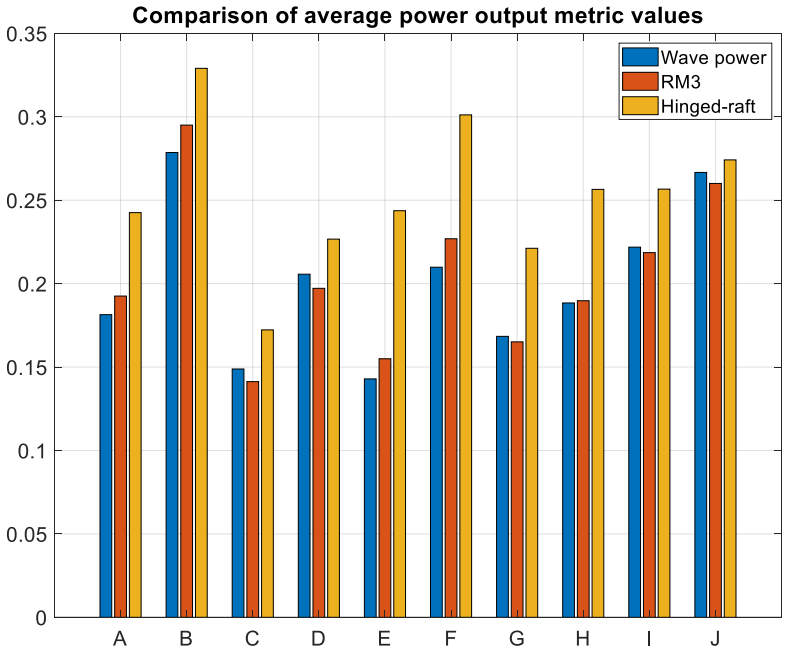

Figure 5.49: Comparison of metric one values from wave energy from HF radar data, RM3 WEC, and 1:25 hinged-raft power output performance.

The ranks of the representativeness of the wave power, the average power output of the RM3, and the hinged-raft are shown in Table 5.13 below, in which rank 1 represents the highest representativeness (with the lowest metric value) and rank 10 represents the lowest (with the highest metric value).

Table 5.13: The ranks of the power output representativeness of different methods from methods A to J.

	A	B	C	D	E	F	G	H	I	J
Wave power	4	10	2	6	1	7	3	5	8	9
RM3	5	10	1	6	2	8	3	4	7	9
Hinged-raft	4	10	1	3	5	9	2	6	7	8

To show the results clearly, the ranks of different methods are plotted together, which is shown in Figure 5.50 below:

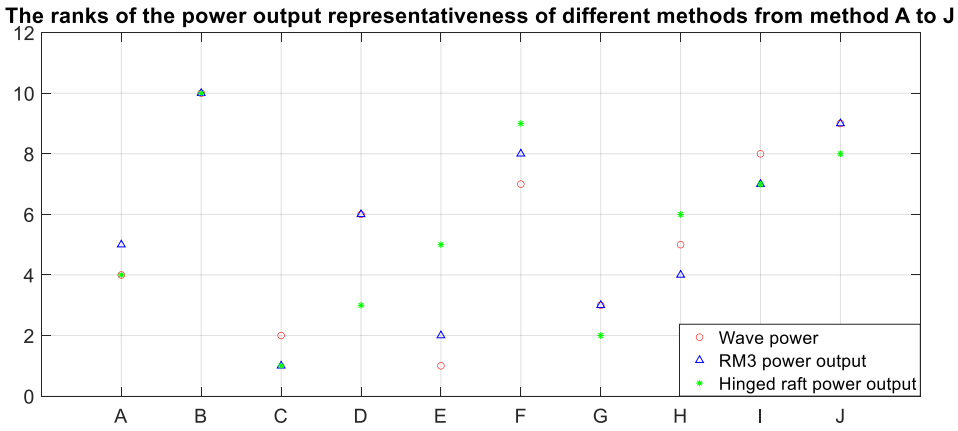

Figure 5.50: The ranks of the power output representativeness of different methods from method A to J.

Although the average power output from the RM3 point absorber and the hinged-raft within the same representative sea state are completely different due to the different design of the device, from Figure 5.49, it can be noticed that the metric one for both devices has great similarities. Most importantly, the representative sea states from method C (as shown in Figure 3.9) provide the average power output estimations of the two WEC devices with the highest representativeness (both rank 1). Therefore, method C using *K*-means clustering is the most recommended for conducting model testing to predict power outputs of both of the devices from HF radar sea states, instead of the widely used binning method (A/B). It means when conducting model testing of both devices to assess their yearly power output performance in the Wave Hub testing site, the sea states obtained from method C are the most test-worthy cases.

From Figure 5.49 and Figure 5.50, it can be noticed that the metric values for the wave power and the power output from the RM3 point absorber are very similar to each other and the rank difference of different regrouping methods is within 1 limit. As explained in

Section 4.3, the RM3 device was highly linear and the difference between the metric values could be attributed to the influence of the randomized phase angles introduced during the WEC-SIM simulation, which meant the power output from the RM3 device could be considered as a direct reflection from the input wave power. However, the metric values and ranks of the wave power showed much larger differences with the power output from the 1:25 hinged-raft, which was due to the existence of relatively stronger non-linearity that has been explained in Section 5.5.3.

B. Annual energy output estimation using different regrouping methods

The annual energy estimation from different regrouping methods A to J with $K = 20$ was compared. For each regrouping method, the average power output for each representative sea state was calculated. By using Equations 5.18, 5.19, and 5.20, the annual energy output estimations for the full-scale prototype from different regrouping methods were obtained, which are shown in Table 5.14 below. They were compared with the actual annual energy output value (334997.9 kW.h) to calculate the relative error.

Table 5.14: Annual energy estimation from different regrouping methods for the full-scale hinged-raft model.

Different methods	Total energy [kW.h]	Actual annual energy [kW.h]	Relative error [%]
A	338978.7	334997.9	1.188
B	338569.4	334997.9	1.066
C	336297.7	334997.9	0.388
D	335957.5	334997.9	0.286
E	335336.3	334997.9	0.101
F	337069.9	334997.9	0.619
G	334755.2	334997.9	0.072
H	337094.5	334997.9	0.626
I	335090.1	334997.9	0.028
J	338846.5	334997.9	1.149

From the results, it can be noticed that similar to the RM3 point absorber results, regardless of what regrouping method is used, the total energy output can be accurately identified with an error of about 1%. Considering the influence of the random phase angles on the average power output is about 1%, although the impact of non-linearity on the average power output can be seen from metric one results from Figure 5.49, its influence is almost unnoticeable on the annual energy output performance. This is because the hinged raft WEC studied in this work was not optimally designed for the Wave Hub. The device performed with a narrow resonance range (from the period of 1.54 s to 1.60 s) and the influence of non-linearity on the power output was very limited. As a result, the annual energy output prediction was not sensitive to K or the regrouping method used, which was similar to the RM3 point absorber result.

5.7 Conclusions of the hinged raft study

In this chapter, a 1:25 hinged-raft WEC model with a rotational PTO and a mooring system was tested in the COAST facility at the University of Plymouth. The model was tested in regular waves, 12 JONSWAP irregular waves, and 31 representative waves (K = 1, 5, 10, and 15) from HF radar measured data. For each sea state, the wave was carefully calibrated before testing to guarantee a ±5% relative error.

After the physical model testing, the regular wave RAO of both rafts in different DoFs, the hinge angle RAO, the CWR, and irregular wave spectral RAO for the 1:25 hinged-raft were calculated. The WEC showed a clear non-linear behaviour when the wave period was close to the resonance period.

The tank testing results were used to build and validate a 1:25 hinged-raft numerical model using WEC-SIM. The regular wave hinge RAO showed good agreement with the physical results except for large wave heights due to the existence of the overtopping phenomenon in the physical model testing. For irregular representative wave cases, the numerical model was accurate with a relative error below 15% when H_s of the target wave was larger than 0.08 m. After analysis, the relatively large error for H_s lower than 0.08 m may be due to the relatively large disturbances (un-calmed waves between wave cases) on the physical testing.

The numerical model results were compared with the physical testing results. They showed that the difference in the annual energy output estimation between the physical

results for K = 1, 5, 10, and 15 was all within the 12% limit range, which also indicated the level of accuracy of the numerical model. It was found that for both the physical and the numerical results, the influence of K on the annual energy output estimation was very small. For the physical model, the coefficient of variation of the energy output from different K was 3.4%. For the numerical model, the coefficient of variation was only 1.76%. It meant that the annual energy output estimation was insensitive to K, which was similar to the results of RM3 WEC from Chapter 4.

The numerical model was used to calculate the actual annual energy output by summing up all of the 3161 sea states' energy output. It was then used to be compared with the numerical results for the power output prediction with K = 1, 5, 10, and 15. The results have shown that the difference between the actual value between the values from different K was only 5%. Ten regrouping methods' representative sea states for K = 20 were tested on the model. It was found that the relative error between the actual value and each method's annual energy output estimation was only 1%. The results showed that the annual energy output was insensitive to the regrouping methods used, which was also similar to the linear RM3 model used in Chapter 4. However, for this hinged-raft model, the average power output representativeness from different regrouping methods was influenced by the non-linearity of the model, which was different from the RM3 model. As explained in Chapter 4, the power output of the RM3 model was a linear transformation of the incoming wave power.

Both the physical testing results and WEC-SIM numerical results showed that the 1:25 hinged-raft model was non-linear. However, the hinged raft WEC studied in this work was not optimally designed for the sea states from Wave Hub. The influence of non-

linearity was limited due to the fact that most of the sea states are with T_e outside the resonance range (1.54s to 1.60s) of the model or within the range but with a small H_s (H_s < 0.15 m) that making the non-linearity unimportant. For this 1:25 hinged raft model in HF radar measured sea states, the annual energy was accurately predicted (±1% relative error) by using just a few (K = 20) representative sea states regardless of which regrouping method was used, which was similar to the highly linear RM3 model used in Chapter 4.

Based on the numerical WEC-SIM model analysis results, the representative sea states obtained from method C (non-directional wave spectrum *K*-means clustering method) showed the highest representativeness for the power output performance. This means that the representative sea states from method C are recommended for physical model testing of the hinged-raft when giving an overall assessment of the annual energy output performance.

6. Discussion

In this discussion chapter, Section 6.1 is to explain the value of this Ph.D. research and how the results may fit into the work of other authors and the comparison. The application of the research results that may contribute to the tank testing of WECs, the annual energy assessment, and fatigue analysis will be shown in Section 6.2. The limitations of this Ph.D. research will be discussed in Section 6.3. A discussion of future work is given in Section 6.4.

6.1. Position of the research

This study mainly consists of two parts, the first part is to find a regrouping method that can be used to obtain a small number of sea states that can best represent the character of an ocean area. This part was inspired by the previous research ([57], [56], [58]), which used 64974 hourly sea states measured from January 2010 to December 2013 that characterised the EMEC's Billa Croo wave test site. The sea states were with an average H_s of 11.5 m and an average T_e of 15 s. The directional spreading ranged from 275° to 340°. Different regrouping methods based on *H*-*T* binning method and the *K*-means clustering method were used to obtain the representative sea states and two metrics were used to assess the performance of each method.

In this Ph.D. research, similar methods and metrics were used on two different test sites, which are the Wave Hub and the Long Island test sites. It has been found that the regrouping quality using the same method from two testing sites was highly similar to the results from the previous research using the EMEC data set. For example, the regrouping methods based on the binning method were less good than the methods based on the *K*-means clustering method, with a higher relative difference between each wave case and their cluster mean. The methods based on the wave spectrum *K*-means clustering were much better than the method only using wave parameters *K*-means clustering, with a much lower relative difference between each wave case and their cluster mean [58].

The previous research ([57], [56], [58]) has shown the K-means clustering method is able to obtain the representative sea states that can best present the EMEC testing site. In this latest work, these conclusions are extended to that regardless of the testing site, the regrouping methods based on the K-means clustering method are able to obtain the most representative sea states of the ocean area, which are the most suitable wave cases for the WEC model testing in limited resources.

There were also differences found between the results presented here and the previous research. From previous research in [58], it was found that when using metric 2, there was no regrouping method that showed a clear advantage over other methods. However, from the current research results shown in Table 3.9 and Table 3.11, it can be seen clearly that the *K*-means clustering method using seven wave parameters showed the best overall regrouping quality. It was because, in this research, an innovative ranking system was created that can indicate the quality of each regrouping clearly, which was absent in the

previous research [58]. Without the ranking system, it would be very difficult to judge if a regrouping method is better than another.

The second part of this Ph.D. research is to estimate the responses (RAO) and the annual energy output performance using WEC models. In addition to the linear numerical model of the RM3 point absorber WEC, a non-linear 1:25 hinged-raft model was tested and analysed in different wave conditions. The model test results were compared with those obtained at Nantes University, Edinburgh University, and Cork University as part of the Marinet2 project Round-Robin tests. The comparison with other data shows good agreement of the RAO in surge, heave, pitch, hinge-angle, and power output results with a 5 to 10% relative error in the mean power output [174]. Despite many local differences in the testing facilities, the global trends that came out of the Round-Robin tests were the same across all basins [181]. For each target wave amplitude, the period at which the RAO reaches its maximum is similar in all basins. The evolution of the power production with the wave height is consistent across the basins. The data generated by the project was made publicly available [188], and the research carried out as part of this thesis contributed to the model testing of the hinged-raft type WEC and contributed data to the Round Robin study.

A lot of research has been done using WEC-SIM previously, however, most studies apply to point absorbers or OSWECs ([189], [118], [190]). In this research, a numerical model of the hinged raft was developed in WEC-SIM and validated using 1:25 physical model data from experiments. The new model included a PTO system with adjustable rotational damping parameters, a mooring system with four mooring lines, and a complex recording system to record the performance of the model in detail. The relative difference in the

RAO and the average power output between the physical model and the numerical model was very small (within 10%). The non-linear responses of the physical model were well preserved in the numerical model.

6.2 Applications of the research results

This research reported here has proposed a new method that shows improved representativeness in obtaining the representative sea states to the traditional *H* - *T* binning method ([191], [192]) to select the most suitable sea states for the model testing of WECs in the wave basin with a limited incoming wave direction (within 90^o).

For a given WEC model that is insensitive to the incoming wave direction (e.g. point absorber, attenuator), when doing tank testing, the first task is to calculate the time duration for each irregular wave case according to the scaling factor λ and the Froude scaling law as introduced in Section 2.2.1. It is necessary to guarantee a one-hour runtime in full scale. From the runtime and the total time length of the model testing project, one can obtain the value of *K*, which is the number of irregular wave cases for the model testing.

Then applying the non-directional *K*-means clustering method (method C) to the total data set (e.g. annual hourly sea states) with the *K* value calculated to obtain *K* representative sea states. From Chapter 3, these sea states are the most test-worthy sea states for the WEC model. The responses of the model can best represent the performance of the model in this ocean area.

If targeting a balance between the traditional binning method and the novel *K*-means clustering method, the new two-step method I developed here can be used, which is able to obtain the representative sea states with high representativeness and high representativeness with an even distribution in H_s and T_e space.

After model testing, the average power output of each representative sea state is obtained. It is possible to estimate the annual energy output accurately according to Section 5.6.

It is also possible to estimate the fatigue damage of the WEC model. Similar to the annual energy output estimation, each of the *K* groups' fatigue damage can be calculated by using the representative sea states from the physical model testing. The fatigue damage of one group can be estimated as the number of members *M* multiplying the fatigue damage from the representative sea state in the group. The annual accumulated fatigue damage can be calculated by adding up all of the *K* group's fatigue damage ([193], [194]). Due to the limitation of the research reported here, this part was not explained in detail.

6.3 Limitations of the research

As shown in Figure 3.3 and Figure 3.5, the wave roses of both locations show different levels of directionality, but neither is very high (less than 90^o). For Wave Hub sea states, the incoming ware direction ranged from 245° to 275°. For Long Island sea states, it ranged from 115° to 195°. Although both of the sea states used in this research were directional, the incoming wave direction was limited to a narrow range. Additionally, for

the Wave Hub sea states, there were no waves with H_s below 0.43 m, which may result in an incomplete understanding of the WEC performance in small waves.

Another limitation of the research presented here is the use of an unrealistic mooring system on the 1:25 hinged-raft. As shown in Figure 5.5, the hinged-raft was held in position by four aerial mooring lines, which was unrealistic in real life, but useful to isolate the mooring forces in a way that could be readily replicated and understood. For the attenuator type of WECs, the commonly used mooring systems are the Catenary Anchor Leg Mooring (CALM) and the Single Anchor Leg Mooring (SALM), which is to moor the WEC to a catenary moored buoy (CALM) or to a single anchored taut buoy (SALM). Both the mooring designs allow the WEC to yaw freely with the incoming waves [195]. The reason for using the aerial mooring lines for hinged-raft was that for the Round-Robin testing carried out in different facilities, the water depth was different. A CALM or SALM mooring system with different water depths might introduce unnecessary errors. As a result, the aerial mooring system was used. However, this means that the annual energy output obtained from the hinged-raft model testing may not be representative of the actual annual energy output in real life.

Another limitation that was not covered in this thesis was the fatigue analysis of the WECs. The analysis of the annual power output performance of the hinged-raft was based on the assumption that the structural failure due to the fatigue damage never happened in the time scope analysed. However, it was unrealistic in real life. From previous research in [196] and [197], the fatigue consideration was very important for WECs. The fatigue limits might be exceeded quickly in the wave and load conditions, especially in the mooring system.

From the previous research in [198], three WECs (Pelamis, AquaBuOY, and Wave Dragon) were analysed in five locations off the coast of Brittany, France numerically using the sea states from 2004 to 2011. It was found that there existed high annual and seasonal variations of the wave conditions even for the same location. In this research, the HF radar data set only consists of 3161 hourly sea states measured in 2011, which means the representative sea states obtained can only represent these 3161 hours. To better understand the character of an ocean area, it is better to use a larger data set that covers a longer period (e.g. 10 years).

In this research, the hinged-raft WEC analysis assumes that the model rotates freely and follows the main wave direction, which is based on the definition of the attenuators. However, this assumption might not apply when the WEC operates in a wave-current joint condition. The effect of currents will apply additional load to the moorings and structure and may also directly influence H_s. According to [198], the tidal currents resulted in the semi-diurnal variations of the H_s by nearly 30%. This may affect the performance of the WECs.

The performance of the hinged-raft model was tested in the regular/JONSWAP/site-specific waves physically. However, other types of waves (e.g. Bretschneider wave spectrum) were not tested due to the limited time. It is worthy to test the model in different wave spectra to better understand the performance of the WEC in different conditions.

6.4 Future work

In the future, the following research should be conducted:

1. In the future, a larger data set (e.g. 10 years) is needed to indicate the annual and seasonal variations. A new data set that includes smaller H_s needs to be used to better understand the responses of the WECs in small waves. If possible, the WEC needs to be analysed in a wave-current joint condition.

2. The representative sea states used to estimate the annual energy output was based on the assumption that the model would not break in the long run. The fatigue damage on the WEC must be taken into consideration in future work.

3. The representative sea states obtained from different regrouping methods can be used to estimate the annual power output performance of WECs. However, they are not able to estimate the responses of the WECs in extreme wave conditions. It is necessary to develop a new method that can be used for the ULS estimation. For example, by combining the site-specific sea states with the commonly used joint probability methods such as the inverse-first order reliability method (I-FORM), a similar approach can be found in [199].

4. The hinged raft WEC studied in this work was not optimally designed for the Wave Hub wave conditions. The non-linearity in the model was relatively small. It is necessary

to test the influence of non-linearity on the power output performance using a specifically designed WEC in a considered ocean area with a broader resonance range.

5. The RM3 point absorber and hinged-raft were both assumed wave direction insensitive in this research. It is necessary to test the representative sea states on other types of WECs that are wave direction sensitive (e.g. OSWEC, overtopping device) to find out the influence of the wave direction. It is expected that the representative sea states from method D (directional wave *K*-means clustering method) provide the highest power output performance for this kind of WEC.

7. Conclusion

Obtaining a small number of sea states but with high representativeness is very important for conducting physical model testing of a WEC in a wave tank.

The first part (Chapter 1 to 3) of the thesis was to introduce the background of this study and to investigate a regrouping method, which is able to obtain *K* representative sea states from a large data set that presents the overall highest representativeness for an ocean area. Ten different regrouping methods A to J were tested on two completely different ocean area annual data sets taken from different instruments (HF radar measured Wave Hub sea states and buoy measured Long Island sea states). Both of the data sets used were with limited wave directionality. The metric results showed that method C (non-directional wave spectrum *K*-means clustering method) provided the overall highest representativeness and maintained the wave characteristics well by providing the lowest metric one values (highest representativeness). The results of two different data sets showed great similarities,

To evaluate the impact of different regrouping methods on the WEC performance, the second part (Chapter 4) of the thesis was to test the representative sea states obtained from regrouping methods A to J on a full-scale numerical model (RM3 point absorber) using WEC-SIM. It has shown that the representative sea states obtained from method C

presented the highest overall representativeness for the power output performance among 10 regrouping methods. Additionally, the annual (3,161 hours) energy output was accurately predicted by using the representative sea states no matter how many groups or what regrouping methods were used. The RAO results showed that the RM3 numerical model was a highly linear model, which meant the input wave power and output WEC power had a linear relationship. The annual energy output could therefore be estimated accurately using just a few representative sea states' average power output results.

The third part (Chapter 5) of the thesis was to test the representative sea states on a realistic non-linear WEC model, which was a 1:25 hinged-raft model from the MaRINET 2 Round-Robin project. The model was physically tested in different wave conditions. The results were used to build and validate a WEC-SIM numerical model of the 1:25 hinged-raft. After comparison, the numerical model showed good agreement with the physical model, and the non-linearity of the physical model was well presented in the numerical model.

Both the physical and numerical results have shown the annual energy output can be accurately predicted by using a small number (K = 20) of representative sea states regardless of which regrouping method was used. This was because the hinged raft WEC studied in this work was designed for the Round-Robin testing, not specifically for the Wave Hub testing. From the spectral RAO results of the model, the incoming wave energy and output WEC energy presented a linear relationship for most of the sea states. The non-linearity in both the physical and numerical model became obvious only when the wave energy period of the sea state was close to the resonance period range (from 1.54 s to 1.60 s in model-scale and from 7.7 s to 8 s in full-scale) and with a significant

wave height higher than 0.15 m. For the HF radar sea states, it has been found that only a small number of sea states were located in this range annually therefore the influence from non-linearity was very limited. Although the power output representativeness from the representative sea states of different regrouping methods was different and the influence of non-linearity on the average power output representativeness can be clearly noticed, the annual energy output can be accurately predicted (within ±1% relative error) no matter which regrouping method was used.

The numerical analysis results have shown that the representative sea states from method C presented the highest representativeness for the average power output performance of the hinged-raft. Considering method C also provided the highest representativeness for the average power output for a linear WEC model (RM3 point absorber) and the overall best performance in the sea states regrouping, it was the preferred method to obtain the sea states for a wave direction insensitive WEC tank testing.

The main contributions of this thesis are:

1. It has been shown that the preferred regrouping method C (non-directional wave spectrum *K*-means clustering method) can be used on the ocean areas regardless of the location with limited wave directionality to obtain the representative sea states for tank testing of WECs. Given limited resources for model testing, these representative sea states were the most test-worthy cases rather than the wave cases obtained from the traditional binning method.

2. New regrouping methods I (using method C as step one) and J (using method D as step one) showed improved distinctness and uniformity in H_s - T_e space. However, the representativeness of methods I and J was inevitably negatively affected compared with methods C and D.

3. It has been shown that as long as the WEC model presented a highly linear relationship between the incoming wave power and output WEC power, or the influence from non-linearity is minor, the annual energy output can be accurately estimated (within a 5% error) by using a small number of ($K \geq 20$) representative sea states.

8. References

[1] *The official webpage of the Paris Agreement*. Available: https://unfccc.int/process-and-meetings/the-paris-agreement/the-paris-agreement

[2] G. Mork, S. Barstow, A. Kabuth, and M. T. Pontes, "Assessing the Global Wave Energy Potential," 2010. Available: https://doi.org/10.1115/OMAE2010-20473

[3] F. Mahnamfar and A. Altunkaynak, "Comparison of numerical and experimental analyses for optimizing the geometry of OWC systems," *Ocean Engineering,* vol. 130, pp. 10-24, 2017/01/15/ 2017.

[4] K. Koca *et al.*, *Recent Advances in the Development of Wave Energy Converters*. 2013.

[5] EPSRC. (2020). *Wave Energy Road Map - Realising the potential of Wave Energy in the next 10 to 15 years*. Available: https://www.supergen-ore.net/outputs

[6] R. M. F. Robin Pelc, "Renewable energy from the ocean," *Marine Policy,* vol. 26, pp. 471–479, 2002.

[7] "House of Commons，Science and technology-seventh report: wave and tidal energy," LondonApril 30, 2001.

[8] *The official webpage from UK Government for Digest of UK Energy Statistics (DUKES)*. Available: https://www.gov.uk/government/collections/digest-of-uk-energy-statistics-dukes

[9] G. Lopez, D. C. Conley, and D. Greaves, "Calibration, Validation, and Analysis of an Empirical Algorithm for the Retrieval of Wave Spectra from HF Radar Sea Echo," *Journal of Atmospheric and Oceanic Technology,* vol. 33, no. 2, pp. 245-261, 2016/02/01 2015.

[10] *Official website of MaRINET 2* Available: https://cordis.europa.eu/project/id/731084

[11] D. Ross, "Power from sea waves," ed. United Kingdom,Oxford University Press, 1995.

[12] Y. Masuda, "Experimental full scale result of wave power machine KAIMEI in 1978," *Proceedings. 1st Symposium on Wave Energy Utilization, 1979 (Proc 1st Symp Wave Energy Util 1979)* pp. 349-363, 1979.

[13] A. Falcao and J. Henriques, "Oscillating-water-column wave energy converters and air turbines: A review," *Renewable Energy,* vol. 85, pp. 1391-1424, 01/01 2016.

[14] S. H. Salter, "Wave power," *Nature,* vol. 249, p. 720, 06/21/online 1974.

[15] A. Clément *et al.*, "Wave energy in Europe: current status and perspectives," *Renewable and Sustainable Energy Reviews,* vol. 6, no. 5, pp. 405-431, 2002/10/01/ 2002.

[16] H. P. Nguyen, C. M. Wang, Z. Y. Tay, and V. H. Luong, "Wave energy converter and large floating platform integration: A review," *Ocean Engineering,* vol. 213, p. 107768, 2020/10/01/ 2020.

[17] A. F. d. O. Falcão, "Wave energy utilization: A review of the technologies," *Renewable and Sustainable Energy Reviews,* vol. 14, no. 3, pp. 899-918, 2010/04/01/ 2010.

[18] H. Ohneda, S. Igarashi, O. Shinbo, S. Sekihara, K. Suzuki, and H. Kubota, "Construction procedure of a wave power extracting caisson breakwater," *Proc. 3rd Symp. Ocean Energy Utilization,* pp. 171-179, 1991.

[19] T. V. Heath, "Chapter 334 - The Development and Installation of the Limpet Wave Energy Converter," in *World Renewable Energy Congress VI*, A. A. M. Sayigh, Ed. Oxford: Pergamon, 2000, pp. 1619-1622.

[20] C. Boake, T. Whittaker, M. Folley, and H. Ellen, "Overview and Initial Operational

Experience of the LIMPET Wave Energy Plant," *Proceedings of the International Offshore and Polar Engineering Conference,* vol. 12, 01/01 2002.
[21] A. Falcao, *The shoreline OWC wave power plant at the Azores*. 2000, pp. 42-47.
[22] K. Collins *et al.*, "A Physical Mooring Comparison for a Floating OWC," 2017.
[23] T. Whittaker, D. Collier, M. Folley, M. Osterried, A. Henry, and M. Crowley, *The development of Oyster–A shallow water surging wave energy converter*. 2007.
[24] T. Mäki, M. Vuorinen, and T. Mucha, "Waveroller one of the leading technologies for wave energy conversion," in *Proceedings of the 4th International Conference on Ocean Energy (ICOE)*, 2014.
[25] K. Edwards and M. Mekhiche, "Ocean power technologies powerbuoy®: system - level design, development and validation methodology," 2014.
[26] R. H. Hansen and M. M. Kramer, "Modelling and control of the wavestar prototype," in *Proceedings of the 9th European Wave and Tidal Energy Conference, EWTEC 2011*, 2011: University of Southampton.
[27] E. Mehlum, "TAPCHAN," in *Hydrodynamics of Ocean Wave-Energy Utilization*, Berlin, Heidelberg, 1986, pp. 51-55: Springer Berlin Heidelberg.
[28] *The official webpage of Ocean Wave Energy Harvesters – A very brief review*. Available: https://apotheoseblog.wordpress.com/2017/05/14/ocean-wave-energy-harvesters-a-very-brief-review/
[29] J. P. Kofoed, P. Frigaard, E. Friis-Madsen, and H. C. Sørensen, "Prototype testing of the wave energy converter wave dragon," *Renewable Energy,* vol. 31, no. 2, pp. 181-189, 2006/02/01/ 2006.
[30] R. Henderson, "Design, simulation, and testing of a novel hydraulic power take-off system for the Pelamis wave energy converter," *Renewable Energy,* vol. 31, no. 2, pp. 271-283, 2006/02/01/ 2006.
[31] *The official Website of Mocean Energy*. Available: http://www.moceanenergy.com/
[32] *The official Website of Sea Power Ltd* Available: http://www.seapower.ie
[33] R. Taylor, P. Taylor, and P. K. Stansby, "A coupled hydrodynamic–structural model of the M4 wave energy converter," *Journal of Fluids and Structures,* vol. 63, pp. 77-96, 05/01 2016.
[34] E. Angelelli, B. Zanuttigh, and J. Kofoed, "Numerical modelling of the hydrodynamics around the farm of Wave Activated Bodies (WAB)," in *4th International Conference on Ocean Energy, October, Dublin*, 2012.
[35] M. Héder, "From NASA to EU: the evolution of the TRL scale in Public Sector Innovation."
[36] EMEC. (2009). *Tank Testing of Wave Energy Systems Marine Renewable Energy Guides*. Available: http://www.emec.org.uk/standards/
[37] D. M. Ingram, *Protocols for the equitable assessment of marine energy converters*. 2011.
[38] H. Fernandez *et al.*, "The new wave energy converter WaveCat: Concept and laboratory tests," *Marine Structures,* vol. 29, no. 1, pp. 58-70, 2012/12/01/ 2012.
[39] V. Heller. (2012). *Model-Prototype Similarity*. Available: http://www.drvalentinheller.com/Dr%20Valentin%20Heller_files/Heller_Model-Prototype%20Similarity.pdf
[40] O. Faltinsen, *Sea loads on ships and offshore structures*. Cambridge university press, 1993.
[41] A. Babarit, J. Hals, M. J. Muliawan, A. Kurniawan, T. Moan, and J. Krokstad, "Numerical benchmarking study of a selection of wave energy converters," *Renewable Energy,* vol. 41, pp. 44-63, 2012/05/01/ 2012.
[42] L. Martinelli *et al.*, "Power Umbilical for Ocean Renewable Energy Systems-Feasibility and Dynamic Response Analysis," in *Proc. Int Conf Ocean Energy*, 2010.
[43] M. Lawson, Y.-H. Yu, A. Nelessen, K. Ruehl, and C. Michelen, "Implementing nonlinear buoyancy and excitation forces in the WEC-Sim wave energy converter modeling tool," in *ASME 2014 33rd International Conference on Ocean, Offshore and Arctic Engineering*, 2014, pp. V09BT09A043-V09BT09A043: American Society of Mechanical Engineers.

[44] M. S. Longuet-Higgins, "The Directional Spectrum of Ocean Waves, and Processes of Wave Generation," *Proceedings of the Royal Society of London. Series A, Mathematical and Physical Sciences,* vol. 265, no. 1322, pp. 286-315, 1962.
[45] W. J. Pierson Jr and L. Moskowitz, "A proposed spectral form for fully developed wind seas based on the similarity theory of SA Kitaigorodskii," *Journal of geophysical research,* vol. 69, no. 24, pp. 5181-5190, 1964.
[46] R. J. Seymour, "Estimating wave generation on restricted fetches," *ASCE J of the Waterway, Port, Coastal & Ocean Div,* vol. 103, no. ASCE 12924 Proceeding, 1977.
[47] K. Hasselmann *et al.*, "Measurements of wind-wave growth and swell decay during the Joint North Sea Wave Project (JONSWAP)," *Ergänzungsheft 8-12,* 1973.
[48] *The official website of WEC-SIM*. Available: https://wec-sim.github.io/WEC-Sim/master/theory/theory.html#irregular-waves
[49] "The definition of peak enhancement factor."
[50] K. Hasselmann *et al.*, "Measurements of wind-wave growth and swell decay during the Joint North Sea Wave Project (JONSWAP)," *Ergaenzungsheft zur Deutschen Hydrographischen Zeitschrift, Reihe A,* 1973.
[51] EMEC, "Tank Testing of Wave Energy Conversion Systems, Marine Renewable Energy Guides," 2018.
[52] B. Holmes, *Tank testing of wave energy conversion systems: marine renewable energy guides*. European Marine Energy Centre, 2009.
[53] R. Carballo and G. Iglesias, "A methodology to determine the power performance of wave energy converters at a particular coastal location," *Energy Conversion and Management,* vol. 61, pp. 8-18, 2012/09/01/ 2012.
[54] L. J. Hamilton, "Characterising spectral sea wave conditions with statistical clustering of actual spectra," *Applied Ocean Research,* vol. 32, no. 3, pp. 332-342, 2010/07/01/ 2010.
[55] L. J. Hamilton, "Clustering of cumulative grainsize distribution curves for shallow-marine samples with software program CLARA," *Australian Journal of Earth Sciences,* vol. 54, no. 4, pp. 503-519, 2007/06/01 2007.
[56] S. Draycott, T. Davey, D. Ingram, J. Lawrence, A. Day, and L. Johanning, "Applying site specific resource assessment: Methodologies for replicating real seas in the FLOWAVE facility," presented at the International Conference on Ocean Energy (ICOE), 2014-11-06, 2014.
[57] S. Draycott, T. Davey, D. M. Ingram, J. Lawrence, A. Day, and L. Johanning, "Applying Site-Specific Resource Assessment: Emulation of Representative EMEC seas in the FloWave Facility," 2015/7/27/,
[58] S. Draycott, "On the Re-creation of Site-Specific Directional Wave Conditions," 2017.
[59] M. S. Longuet-Higgins, "Observations of the directional spectrum of sea waves using the motions of a floating buoy," *Ocean wave spectra,* 1961.
[60] H. Mitsuyasu *et al.*, "Observations of the directional spectrum of ocean WavesUsing a cloverleaf buoy," *Journal of Physical Oceanography,* vol. 5, no. 4, pp. 750-760, 1975.
[61] M. Tucker, "Interpreting directional data from large pitch-roll-heave buoys," *Ocean Engineering,* vol. 16, no. 2, pp. 173-192, 1989.
[62] K. Steele, C.-C. Teng, and D. Wang, "Wave direction measurements using pitch-roll buoys," *Ocean Engineering,* vol. 19, no. 4, pp. 349-375, 1992.
[63] H. H. Shih, C. Long, M. Bushnell, and K. Hathaway, "Intercomparison of Wave Data Between Triaxys Directional Wave Buoy, ADCP, and Other Reference Wave Instruments," no. 41960, pp. 655-663, 2005.
[64] R. B. Long and K. Hasselmann, "A variational technique for extracting directional spectra from multi-component wave data," *Journal of Physical Oceanography,* vol. 9, no. 2, pp. 373-381, 1979.
[65] A. Lygre and H. E. Krogstad, "Maximum entropy estimation of the directional distribution in ocean wave spectra," *Journal of Physical Oceanography,* vol. 16, no. 12, pp. 2052-2060, 1986.

[66] F. P. Brissette and I. K. Tsanis, *Estimation of Wave Directional Spectra from Pitch-Roll Buoy Data*. 1994.

[67] *Introduction of two types of ADCP*. Available: http://sedexp.net/equipment/acoustic-doppler-current-profiler-adcp

[68] E. A. Terray, B. H. Brumley, and B. Strong, "Measuring waves and currents with an upward-looking ADCP," in *Proceedings of the IEEE Sixth Working Conference on Current Measurement (Cat. No.99CH36331)*, 1999, pp. 66-71.

[69] P. A. Work, "Nearshore directional wave measurements by surface-following buoy and acoustic Doppler current profiler," *Ocean Engineering,* vol. 35, no. 8, pp. 727-737, 2008/06/01/ 2008.

[70] E. Terray, R. L. Gordon, and B. Brumley, "Measuring wave height and direction using upward-looking ADCPs," in *Oceans '97. MTS/IEEE Conference Proceedings*, 1997, vol. 1, pp. 287-290 vol.1.

[71] "Observations of the directional spectrum of sea waves using the motions of a floating buoy: Longuet-Higgins, M. S., D. E. Cartwright and N. D. Smith, 1963. In: Ocean Wave Spectra, Proc. Conf., Easton, Md., May 1–4, 1961, Prentice-Hall, N.J., 111–132," *Deep Sea Research and Oceanographic Abstracts,* vol. 12, no. 1, p. 53, 1965/02/01/ 1965.

[72] H. E. Krogstad, R. L. Gordon, and M. C. Miller, "High-Resolution Directional Wave Spectra from Horizontally Mounted Acoustic Doppler Current Meters," *Journal of Atmospheric and Oceanic Technology,* vol. 5, no. 2, pp. 340-352, 1988.

[73] T. H. C. Herbers, R. L. Lowe, and R. Guza, *Field Verification of Acoustic Doppler Surface Gravity Wave Measurements*. 1991, pp. 17023-17035.

[74] A. J. F. Hoitink, H. C. Peters, and M. Schroevers, "Field verification of ADCP surface gravity wave elevation spectra," *Journal of Atmospheric and Oceanic Technology,* vol. 24, no. 5, pp. 912-922, 2007.

[75] J. C. Nieto Borge and C. Guedes Soares, "Analysis of directional wave fields using X-band navigation radar," *Coastal Engineering,* vol. 40, no. 4, pp. 375-391, 2000/07/01/ 2000.

[76] J. Nieto Borge, G. R. Rodríguez, K. Hessner, and P. I. González, "Inversion of marine radar images for surface wave analysis," *Journal of Atmospheric and Oceanic Technology,* vol. 21, no. 8, pp. 1291-1300, 2004.

[77] H. Dankert and W. Rosenthal, "Ocean surface determination from X‐band radar‐image sequences," *Journal of Geophysical Research: Oceans,* vol. 109, no. C4, 2004.

[78] F. Ziemer, C. Brockmann, R. A. Vaughan, J. Seemann, and C. Senet, *Radar survey of near shore bathymetry within the oroma project*. 2004.

[79] J. N. Borge, G. R. Rodríguez, K. Hessner, and P. I. González, "Inversion of Marine Radar Images for Surface Wave Analysis," *Journal of Atmospheric and Oceanic Technology,* vol. 21, no. 8, pp. 1291-1300, 2004.

[80] I. Young, W. Rosenthal, and F. Ziemer, *A three-dimensional analysis of marine radar images for the determination of ocean wave directionally and surface currents*. 1985, pp. 1049-1060.

[81] J. c. Nieto-Borge, K. Hessner, P. Jarabo-Amores, and D. D. L. Mata-moya, "Signal-to-noise ratio analysis to estimate ocean wave heights from X-band marine radar image time series," *IET Radar, Sonar & Navigation,* vol. 2, no. 1, pp. 35-41, 2008.

[82] S. F. Barstow, J.-R. Bidlot, and S. Caires, "Measuring and analysing the directional spectrum of ocean waves," ed: COST Office, 2005.

[83] D. D. Crombie, "Doppler spectrum of sea echo at 13.56 Mc./s," *Nature,* vol. 175, no. 4459, p. 681, 1955.

[84] D. E. Barrick, "The interaction of HF/VHF radio waves with the sea surface and its implications," in *AGARD Conference Proceedings, Sprinfield*, 1970.

[85] G. Lopez, "Evaluation, analysis, and application of HF radar wave and current measurements," 2017.

[86] D. E. Barrick, "HF radio oceanography—a review," *Boundary-Layer Meteorology,* vol. 13, no. 1-4, pp. 23-43, 1978.

[87] H.-H. Essen, K.-W. Gurgel, and T. Schlick, "Measurement of ocean wave height and direction by means of HF radar: an empirical approach," *Deutsche Hydrografische Zeitschrift,* vol. 51, no. 4, pp. 369-383, 1999.
[88] R. Chapman *et al.*, "On the accuracy of HF radar surface current measurements: Intercomparisons with ship‐based sensors," *Journal of Geophysical Research: Oceans,* vol. 102, no. C8, pp. 18737-18748, 1997.
[89] J. T. Kohut and S. M. Glenn, "Improving HF radar surface current measurements with measured antenna beam patterns," *Journal of Atmospheric and Oceanic Technology,* vol. 20, no. 9, pp. 1303-1316, 2003.
[90] D. Savidge *et al.*, "Assessment of WERA long-range HF-radar performance from the user's perspective," in *Current, Waves and Turbulence Measurements (CWTM), 2011 IEEE/OES 10th*, 2011, pp. 31-38: IEEE.
[91] D. E. Barrick, "The ocean waveheight nondirectional spectrum from inversion of the HF sea-echo Doppler spectrum," *Remote Sensing of Environment,* vol. 6, no. 3, pp. 201-227, 1977.
[92] L. R. Wyatt, "A relaxation method for integral inversion applied to HF radar measurement of the ocean wave directional spectrum," *International Journal of Remote Sensing,* vol. 11, no. 8, pp. 1481-1494, 1990.
[93] N. Hashimoto and M. Tokuda, "A Bayesian approach for estimation of directional wave spectra with HF radar," *Coastal Engineering Journal,* vol. 41, no. 02, pp. 137-149, 1999.
[94] Y. Hisaki, "Development of HF radar inversion algorithm for spectrum estimation (HIAS)," *Journal of Geophysical Research: Oceans,* vol. 120, no. 3, pp. 1725-1740, 2015.
[95] G. Voulgaris *et al.*, "Waves initiative within SEACOOS," *Marine Technology Society Journal,* vol. 42, no. 3, pp. 68-80, 2008.
[96] K. Gurgel, H. Essen, and T. Schlick, "An Empirical Method to Derive Ocean Waves From Second-Order Bragg Scattering: Prospects and Limitations," *IEEE Journal of Oceanic Engineering,* vol. 31, no. 4, pp. 804-811, 2006.
[97] L. R. Wyatt, "Limits to the Inversion of HF Radar Backscatter for Ocean Wave Measurement," *Journal of Atmospheric and Oceanic Technology,* vol. 17, no. 12, pp. 1651-1666, 2000.
[98] J. J. Green and L. R. Wyatt, "Row-Action Inversion of the Barrick–Weber Equations," *Journal of Atmospheric and Oceanic Technology,* vol. 23, no. 3, pp. 501-510, 2006.
[99] *Introduction of the WERA system in University of Plymouth*. Available: https://www.plymouth.ac.uk/research/hf-radar
[100] L. R. Wyatt, J. J. Green, and A. Middleditch, "HF radar data quality requirements for wave measurement," *Coastal Engineering,* vol. 58, no. 4, pp. 327-336, 2011/04/01/ 2011.
[101] H. E. Krogstad and S. F. Barstow, "Satellite wave measurements for coastal engineering applications," *Coastal Engineering,* vol. 37, no. 3, pp. 283-307, 1999/08/01/ 1999.
[102] K. Hasselmann and S. Hasselmann, "On the nonlinear mapping of an ocean wave spectrum into a synthetic aperture radar image spectrum and its inversion," *Journal of Geophysical Research: Oceans,* vol. 96, no. C6, pp. 10713-10729, 1991.
[103] H. E. Krogstad, O. Samset, and P. W. Vachon, "Generalizations of the non‐linear ocean‐SAR transform and a simplified SAR inversion algorithm," *Atmosphere-Ocean,* vol. 32, no. 1, pp. 61-82, 1994.
[104] P. Heimbach, S. Hasselmann, and K. Hasselmann, "Statistical analysis and intercomparison of WAM model data with global ERS‐1 SAR wave mode spectral retrievals over 3 years," *Journal of Geophysical Research: Oceans,* vol. 103, no. C4, pp. 7931-7977, 1998.
[105] G. Chen, Q. Xiong, P. J. Morris, E. G. Paterson, A. Sergeev, and Y. Wang, "OpenFOAM for computational fluid dynamics," *Notices of the AMS,* vol. 61, no. 4, pp. 354-363, 2014.
[106] B. Sanderse, S. P. van der Pijl, and B. Koren, "Review of computational fluid dynamics for wind turbine wake aerodynamics," *Wind Energy,* vol. 14, no. 7, pp. 799-819, 2011.
[107] J. Johansen, N. N. Sørensen, J. A. Michelsen, and S. Schreck, "Detached-eddy simulation

of flow around the NREL Phase VI blade," *Wind Energy,* vol. 5, no. 2-3, pp. 185-197, 2002.
[108] J. Davidson, M. Karimov, A. Szelechman, C. Windt, and J. Ringwood, *Dynamic mesh motion in OpenFOAM for wave energy converter simulation*. 2019.
[109] C. Eskilsson, J. Palm, J. P. Kofoed, and E. Friis-Madsen, "CFD study of the overtopping discharge of the Wave Dragon wave energy converter," *Renewable Energies Offshore,* pp. 287-294, 2015.
[110] J. Palm, C. Eskilsson, L. Bergdahl, and G. M. Paredes, "CFD study of a moored floating cylinder: Comparison with experimental data," in *Proc. 1st Int. Conf. on Renewable Energies Offshore (Renew 2014), Lisbon*, 2014.
[111] A. Iturrioz, R. Guanche, J. A. Armesto, C. Vidal, and I. J. Losada, "Experimental and numerical development of a floating multi-chamber OWC device," in *Proceedings of the 10th European Wave and Tidal Energy Conference*, 2013.
[112] P. Schmitt *et al.*, "Hydrodynamic loading on a bottom hinged oscillating wave surge converter," in *The Twenty-second International Offshore and Polar Engineering Conference*, 2012: OnePetro.
[113] J. B. Thomsen, A. Têtu, and H. Stiesdal, "A Comparative Investigation of Prevalent Hydrodynamic Modelling Approaches for Floating Offshore Wind Turbine Foundations: A TetraSpar Case Study," *Journal of Marine Science and Engineering,* vol. 9, no. 7, p. 683, 2021.
[114] M. A. Bhinder, M. Karimirad, S. Weller, Y. Debruyne, M. Guérinel, and W. Sheng, "Modelling mooring line non-linearities (material and geometric effects) for a wave energy converter using AQWA, SIMA and Orcaflex," in *Proceedings of the 11th European Wave and Tidal Energy Conference, Nantes, France*, 2015, pp. 6-11.
[115] D. Kim, S. K. Poguluri, H. S. Ko, H. Lee, and Y. H. Bae, "Numerical and experimental study on linear behavior of salter's duck wave energy converter," *Journal of Ocean Engineering and Technology,* vol. 33, no. 2, pp. 116-122, 2019.
[116] D. Bull and P. Jacob, "Methodology for creating nonaxisymmetric WECs to screen mooring designs using a Morison Equation approach," in *2012 Oceans*, 2012, pp. 1-9: IEEE.
[117] S. Chandrasekaran and V. V. S. Sricharan, "Numerical analysis of a new multi-body floating wave energy converter with a linear power take-off system," *Renewable Energy,* vol. 159, pp. 250-271, 2020/10/01/ 2020.
[118] M. Lawson, Y.-H. Yu, K. Ruehl, and C. Michelen, "Development and demonstration of the WEC-Sim wave energy converter simulation tool," 2014.
[119] Y. Wei, J. J. Barradas-Berglind, M. van Rooij, W. A. Prins, B. Jayawardhana, and A. I. Vakis, "Investigating the adaptability of the multi-pump multi-piston power take-off system for a novel wave energy converter," *Renewable Energy,* vol. 111, pp. 598-610, 2017/10/01/ 2017.
[120] J. Ringwood *et al.*, "The Wave Energy Converter Control Competition: Overview," in *ASME 2019 38th International Conference on Ocean, Offshore and Arctic Engineering*, 2019, vol. Volume 10: Ocean Renewable Energy, V010T09A035.
[121] R. So, C. Michelen, B. Bosma, P. Lenee-Bluhm, and T. K. A. Brekken, "Statistical Analysis of a 1:7 Scale Field Test Wave Energy Converter Using WEC-Sim," *IEEE Transactions on Sustainable Energy,* vol. 8, no. 3, pp. 1118-1126, 2017.
[122] B. Bosma, T. Brekken, P. Lomonaco, B. DuPont, C. Sharp, and B. Batten, "Array modeling and testing of fixed OWC type Wave Energy Converters," *International Marine Energy Journal,* vol. 3, no. 3, pp. 137-143, 2020.
[123] S. Sirnivas, Y.-H. Yu, M. Hall, and B. Bosma, "Coupled Mooring Analyses for the WEC-Sim Wave Energy Converter Design Tool," in *ASME 2016 35th International Conference on Ocean, Offshore and Arctic Engineering*, 2016, vol. Volume 6: Ocean Space Utilization; Ocean Renewable Energy, V006T09A023.
[124] S. Chandrasekaran and V. V. S. Sricharan, "Analysis of a Floating Wave Energy Converter With Hydraulic-Mechanical Power Take-Off Using WEC-Sim and SIMSCAPE," in *ASME*

2020 39th International Conference on Ocean, Offshore and Arctic Engineering, 2020, vol. Volume 9: Ocean Renewable Energy, V009T09A032.

[125] V. V. S. Sricharan and S. Chandrasekaran, "Time-domain analysis of a bean-shaped multi-body floating wave energy converter with a hydraulic power take-off using WEC-Sim," *Energy,* vol. 223, p. 119985, 2021/05/15/ 2021.

[126] R. So, S. Casey, S. Kanner, A. Simmons, and T. K. A. Brekken, "PTO-Sim: Development of a power take off modeling tool for ocean wave energy conversion," in *2015 IEEE Power & Energy Society General Meeting*, 2015, pp. 1-5.

[127] M. Lawson, Y.-H. Yu, A. Nelessen, K. Ruehl, and C. Michelen, "Implementing Nonlinear Buoyancy and Excitation Forces in the WEC-Sim Wave Energy Converter Modeling Tool," in *ASME 2014 33rd International Conference on Ocean, Offshore and Arctic Engineering*, 2014, vol. Volume 9B: Ocean Renewable Energy, V09BT09A043.

[128] *The official Website of Solidworks*. Available: https://www.solidworks.com/

[129] Q. Qi, T. Zhang, P. Wen, and T.-g. LIU, "Numerical simulation of FPSO mooring systems based on AQWA," *Ship Science and Technology,* vol. 33, no. 12, pp. 14-18, 2011.

[130] M. A. Bhinder, M. Karimirad, S. Weller, Y. Debruyne, M. Guérinel, and W. Sheng, "Modelling mooring line non-linearities (material and geometric effects) for a wave energy converter using AQWA, SIMA and Orcaflex."

[131] S. R. Samaei, F. Azarsina, and M. A. Ghahferokhi, "Numerical simulation of floating pontoon breakwater with ANSYS AQWA software and validation of the results with laboratory data," *Bulletin de la Société Royale des Sciences de Liège,* vol. 85, pp. 1487-1499, 2016.

[132] *Official website of WAMIT*. Available: https://www.wamit.com/

[133] Y.-H. Eng, C.-S. Chin, and M. W.-S. Lau, "Added mass computation for control of an open-frame remotely-operated vehicle: Application using WAMIT and MATLAB," *Journal of Marine Science and Technology,* vol. 22, no. 4, p. 1, 2014.

[134] M. Frederick, "Hydrodynamic Modeling of Pelamis® P1-750 Wave Energy Converters using WAMIT software," *Master of Science Plan B Research Paper, Dept. of Ocean and Resources Engineering, University of Hawaii,* 2014.

[135] S. J. Lee, M. Kim, D. Lee, J. Kim, and Y. Kim, "The effects of LNG-tank sloshing on the global motions of LNG carriers," *Ocean Engineering,* vol. 34, no. 1, pp. 10-20, 2007.

[136] M. Penalba, T. Kelly, and J. Ringwood, "Using NEMOH for modelling wave energy converters: A comparative study with WAMIT," 2017.

[137] *Official website of NEMOH*. Available: https://lheea.ec-nantes.fr/valorisation/logiciels-et-brevets/nemoh-presentation

[138] G. Verao Fernández, V. Stratigaki, and P. Troch, "Irregular Wave Validation of a Coupling Methodology for Numerical Modelling of Near and Far Field Effects of Wave Energy Converter Arrays," *Energies,* vol. 12, no. 3, p. 538, 2019.

[139] F. Nelli *et al.*, "Reconstructing Sea-States in the Southern Ocean Using Ship Motion Data," in *ASME 2021 40th International Conference on Ocean, Offshore and Arctic Engineering*, 2021, vol. Volume 6: Ocean Engineering, V006T06A027.

[140] M. Hall, "MoorDyn user's guide," *Orono, ME: Department of Mechanical Engineering, University of Maine,* 2015.

[141] W. M. West, A. J. Goupee, C. Allen, and A. M. Viselli, "Floating Wind Turbine Model Test to Verify a MoorDyn Modification for Nonlinear Elastic Materials," *Journal of Offshore Mechanics and Arctic Engineering,* pp. 1-41, 2021.

[142] *The official website of Wave Hub WEC testing site* Available: https://www.theguardian.com/environment/2010/sep/07/wave-hub-installed-cornish-coast

[143] *The official webpage of Celtic Sea Power drives floating offshore wind ambitions*. Available: https://businesscornwall.co.uk/latest-news/2021/07/celtic-sea-power-drives-floating-offshore-wind-ambitions/

[144] K.-W. Gurgel, H.-H. Essen, and S. Kingsley, "High-frequency radars: physical limitations

and recent developments," *Coastal engineering,* vol. 37, no. 3-4, pp. 201-218, 1999.
[145] *The official website of National Data Buoy Centre (NDBC)*. Available: https://www.ndbc.noaa.gov/
[146] J. Lavelle and J. P. Kofoed, "Power production analysis of the OE buoy WEC for the cores project," 2011.
[147] R. Pascal, A. Torres, and A. Gonzalez, "Going further than the scatter diagram: tools for analysing the wave resource and classifying sites," in *Proceedings of the 11th European Wave and Tidal Energy Conference, Nantes, France*, 2015, pp. 6-11.
[148] V. Venugopal *et al.*, "EquiMar. Deliverable D2. 2. Wave and tidal resource characterisation," 2011.
[149] J. Lavelle and J. P. Kofoed, "Power production analysis of the oe buoy wec for the cores project," *Department of Civil Engineering, Aalborg University,* 2011.
[150] D. Arthur and S. Vassilvitskii, "k-means++: The advantages of careful seeding," Stanford2006.
[151] S. Lloyd, "Least squares quantization in PCM," *IEEE transactions on information theory,* vol. 28, no. 2, pp. 129-137, 1982.
[152] G. A. Seber, *Multivariate observations*. John Wiley & Sons, 2009.
[153] H. Spath, *The cluster dissection and analysis theory fortran programs examples*. Prentice-Hall, Inc., 1985.
[154] O. Maimon and L. Rokach, *Data Mining and Knowledge Discovery Handbook*. Springer-Verlag, 2005.
[155] J. Han and M. Kamber, "Data Mining: Concepts and Techniques, chapter Mining association rules in large databases," ed: Morgan Kaufmann Publisher, 2001.
[156] K. Krishna and M. N. Murty, "Genetic K-means algorithm," *IEEE Transactions on Systems, Man, and Cybernetics, Part B (Cybernetics),* vol. 29, no. 3, pp. 433-439, 1999.
[157] A. Likas, N. Vlassis, and J. J. Verbeek, "The global k-means clustering algorithm," *Pattern recognition,* vol. 36, no. 2, pp. 451-461, 2003.
[158] M.-C. Su and C.-H. Chou, "A modified version of the K-means algorithm with a distance based on cluster symmetry," *IEEE Transactions on pattern analysis and machine intelligence,* vol. 23, no. 6, pp. 674-680, 2001.
[159] P. Fränti and S. Sieranoja, "How much can k-means be improved by using better initialization and repeats?," *Pattern Recognition,* vol. 93, pp. 95-112, 2019/09/01/ 2019.
[160] *Official Website of MATLAB*. Available: https://uk.mathworks.com/products/matlab.html
[161] M. J. Tucker and E. G. Pitt, *Waves in ocean engineering* (no. Volume 5). 2001.
[162] P. Frigaard *et al.*, "Proceedings of the 27th IAHR Congress, San Francisco, 10-15 August 1997 : IAHR Seminar : Multidirectional Waves and their Interaction with Structures," presented at the The 27th IAHR Congress -San Francisco, California, United States, 10 Aug 1997 → 15 Aug 1997, 1997.
[163] *DNV OSS-312 Certification of Tidal and Wave Energy Converters*. Available: https://rules.dnv.com/docs/pdf/dnvpm/codes/docs/2008-10/Oss-312.pdf
[164] S. Coles, J. Bawa, L. Trenner, and P. Dorazio, *An introduction to statistical modeling of extreme values*. Springer, 2001.
[165] N. Teena, V. Sanil Kumar, K. Sudheesh, and R. Sajeev, "Statistical analysis on extreme wave height," *Natural hazards,* vol. 64, no. 1, pp. 223-236, 2012.
[166] S. Haver and K. A. Nyhus, "A wave climate description for long term response calculations," in *International offshore mechanics and arctic engineering. Symposium. 5*, 1986, pp. 27-34.
[167] J. C. Berg, "Extreme Ocean Wave Conditions for Northern California Wave Energy Conversion Device," Sandia National Lab.(SNL-CA), Livermore, CA (United States); Sandia National …2011.
[168] Y. Yu, M. Lawson, Y. Li, M. Previsic, J. Epler, and J. Lou, "Experimental wave tank test for reference model 3 floating-point absorber wave energy converter project," National

Renewable Energy Lab.(NREL), Golden, CO (United States)2015.
[169] K. Ruehl, C. Michelen, S. Kanner, M. Lawson, and Y.-H. Yu, "Preliminary verification and validation of WEC-Sim, an open-source wave energy converter design tool," in *International Conference on Offshore Mechanics and Arctic Engineering*, 2014, vol. 45547, p. V09BT09A040: American Society of Mechanical Engineers.
[170] Y.-H. Yu, M. Lawson, Y. Li, M. Previsic, J. Epler, and J. Lou, "Experimental wave tank test for reference model 3 floating-point absorber wave energy converter project," National Renewable Energy Lab.(NREL), Golden, CO (United States)2015.
[171] *Official website of RM3 point absorber WEC-SIM numerical model*. Available: https://wec-sim.github.io/WEC-Sim/master/user/tutorials.html
[172] S. Gueydon *et al.*, "A heuristic approach for inter-facility comparison of results from round robin testing of a floating wind turbine in irregular waves," *Journal of Marine Science and Engineering,* vol. 9, no. 9, p. 1030, 2021.
[173] *Model design of the hinged-raft ''E180402-SE000-PE01 Nomenclature M2_RR-RAFT'',2019.*
[174] T. Davey *et al.*, "Round Robin Testing: Exploring Experimental Uncertainties through a Multifacility Comparison of a Hinged Raft Wave Energy Converter," *Journal of Marine Science and Engineering,* vol. 9, no. 9, p. 946, 2021.
[175] H. A. Schäffer and G. Klopman, "Review of multidirectional active wave absorption methods," *Journal of waterway, port, coastal, and ocean engineering,* vol. 126, no. 2, pp. 88-97, 2000.
[176] *The official website of COAST laboratory in Plymouth University*. Available: https://www.plymouth.ac.uk/research/institutes/marine-institute/coast-laboratory
[177] EMEC. *The definition of different WECs*. Available: https://www.emec.org.uk/marine-energy/wave-devices/
[178] *Offical website of Qualisys motion capture system*. Available: https://www.qualisys.com/cameras/
[179] ECN, "Raft's Quick Start Guide," 2020.
[180] "The official webpage of ITTC, Analysis Procedure for Model Tests in Regular Waves."
[181] J. Ohana *et al.*, "Round robin tests on a hinged raft wave energy converter," *EWTEC,* 2021.
[182] P. F. Hinrichsen, "Bifilar suspension measurement of boat inertia parameters," *Journal of Sailing Technology,* vol. 3, no. 12, pp. 1-37, 2014.
[183] B. M. Sumer, *Hydrodynamics around cylindrical strucures*. World scientific, 2006.
[184] W. H. Press, W. T. Vetterling, S. A. Teukolsky, and B. P. Flannery, *Numerical Recipes Example Book (FORTRAN)*. Cambridge University Press Cambridge, 1992.
[185] J. H. Horne and S. L. Baliunas, "A prescription for period analysis of unevenly sampled time series," *The Astrophysical Journal,* vol. 302, pp. 757-763, 1986.
[186] G. Heinzel, A. Rüdiger, and R. Schilling, "Spectrum and spectral density estimation by the Discrete Fourier transform (DFT), including a comprehensive list of window functions and some new at-top windows," 2002.
[187] K. Collins, G. Iglesias, D. Greaves, A. Toffoli, and S. Stripling, "The New Coast Laboratory at Plymouth University: A World-Class Facility for Marine Energy," in *From Sea to Shore–Meeting the Challenges of the Sea: (Coasts, Marine Structures and Breakwaters 2013)*, 2014, pp. 1326-1335: ICE Publishing.
[188] *The official webpage of the e-Infrastructures*. Available: https://wayback.archive-it.org/12090/20170401084642/https://ec.europa.eu/digital-single-market/en/e-infrastructures
[189] T. Tosdevin *et al.*, "On the calibration of a WEC-Sim model for heaving point absorbers," 2020.
[190] M. Choiniere, J. Davis, N. Nguyen, N. Tom, M. Fowler, and K. Thiagarajan, "Hydrodynamics and load shedding behavior of a variable-geometry oscillating surge wave energy converter (OSWEC)," *Renewable Energy,* 2022.
[191] D. Wang, D. Conley, M. Hann, K. M. Collins, and D. Greaves, "Use of HF radar for

replciating wave-current combined wave conditions for testing of wave energy converters," 2019.
[192] D. Wang, D. Conley, M. Hann, K. Collins, S. Jin, and D. Greaves, "Power output estimation of WEC with HF radar measured complex representative sea states," *International Marine Energy Journal,* 2022.
[193] A. Fatemi and L. Yang, "Cumulative fatigue damage and life prediction theories: a survey of the state of the art for homogeneous materials," *International journal of fatigue,* vol. 20, no. 1, pp. 9-34, 1998.
[194] S. Marco and W. Starkey, "A concept of fatigue damage," *Transactions of the American Society of Mechanical Engineers,* vol. 76, no. 4, pp. 627-632, 1954.
[195] R. E. Harris, L. Johanning, and J. Wolfram, "Mooring systems for wave energy converters: A review of design issues and choices," *Marec2004,* 2004.
[196] P. R. Thies, L. Johanning, and G. H. Smith, "Lifecycle fatigue load spectrum estimation for mooring lines of a floating marine energy converter," 2012: ASME.
[197] P. R. Thies, L. Johanning, V. Harnois, H. C. Smith, and D. N. Parish, "Mooring line fatigue damage evaluation for floating marine energy converters: Field measurements and prediction," *Renewable Energy,* vol. 63, pp. 133-144, 2014.
[198] N. Guillou and G. Chapalain, "Annual and seasonal variabilities in the performances of wave energy converters," *Energy,* vol. 165, pp. 812-823, 2018/12/15/ 2018.
[199] S. Draycott, T. Davey, and M. D. Ingram, "Simulating Extreme Directional Wave Conditions," *Energies,* vol. 10, no. 11, 2017.

9. Appendix

9.1: Test plan of the hinged-raft model

No.	Test type	Repeat time (s)	T/Tp [s]	H/Hs [m]	Gamma	Rotational Damping [N.m/rad/s]	Gain for regular	Comments
1	Free Decay	/	/	/	/	0	/	
2	Free Decay	/	/	/	/	10	/	
3	Free Decay	/	/	/	/	20	/	
4	Free Decay	/	/	/	/	30	/	
5	Free Decay	/	/	/	/	40	/	
6	Free Decay	/	/	/	/	50	/	
7	RW	120	1	0.05	/	20	1.2558	
8	RW	144	1.2	0.05	/	20	0.9955	
9	RW	168	1.4	0.05	/	20	1.061	
10	RW	174	1.45	0.05	/	20	0.9983	
11	RW	180	1.5	0.05	/	20	1.0538	
12	RW	186	1.55	0.05	/	20	1.125	
13	RW	192	1.6	0.05	/	20	1.0098	
14	RW	198	1.65	0.05	/	20	1.0909	
15	RW	204	1.7	0.05	/	20	0.9894	
16	RW	216	1.8	0.05	/	20	1.0852	
17	RW	240	2	0.05	/	20	1.091	
18	RW	264	2.2	0.05	/	20	1.0238	
19	RW	288	2.4	0.05	/	20	1.0676	
20	RW	120	1	0.1	/	20	1.2683	
21	RW	144	1.2	0.1	/	20	1.0102	
22	RW	168	1.4	0.1	/	20	1.0482	
23	RW	174	1.45	0.1	/	20	0.9943	
24	RW	180	1.5	0.1	/	20	1.0212	
25	RW	186	1.55	0.1	/	20	1.0441	
26	RW	192	1.6	0.1	/	20	1.0217	
27	RW	198	1.65	0.1	/	20	1.0469	
28	RW	204	1.7	0.1	/	20	0.9707	
29	RW	216	1.8	0.1	/	20	1.0422	
30	RW	240	2	0.1	/	20	1.0737	

31	RW	264	2.2	0.1	/	20	1.0302	
32	RW	288	2.4	0.1	/	20	1.017	
33	RW	144	1.2	0.15	/	20	1.0931	
34	RW	168	1.4	0.15	/	20	1.0763	
35	RW	174	1.45	0.15	/	20	0.9824	
36	RW	180	1.5	0.15	/	20	1.0469	
37	RW	186	1.55	0.15	/	20	1.1242	
38	RW	192	1.6	0.15	/	20	1.002	
39	RW	198	1.65	0.15	/	20	1.0614	
40	RW	204	1.7	0.15	/	20	0.9772	
41	RW	216	1.8	0.15	/	20	1.1044	
42	RW	240	2	0.15	/	20	1.0837	
43	RW	264	2.2	0.15	/	20	1.034	
44	RW	288	2.4	0.15	/	20	1.0161	
45	RW	168	1.4	0.2	/	20	1.0307	
46	RW	174	1.45	0.2	/	20	1.0395	
47	RW	180	1.5	0.2	/	20	1.0226	
48	RW	186	1.55	0.2	/	20	1.068	
49	RW	192	1.6	0.2	/	20	1.0508	
50	RW	198	1.65	0.2	/	20	1.058	
51	RW	204	1.7	0.2	/	20	0.9877	
52	RW	216	1.8	0.2	/	20	0.979	
53	RW	240	2	0.2	/	20	1.0453	
54	RW	264	2.2	0.2	/	20	1.0106	
55	RW	288	2.4	0.2	/	20	1.0755	
56	IW	720	1.55	0.05	3.3	20	/	JONSWAP
57	IW	720	1.55	0.1	3.3	20	/	JONSWAP
58	IW	720	1.3	0.05	3.3	20	/	JONSWAP
59	IW	720	1.3	0.1	3.3	20	/	JONSWAP
60	IW	720	1.8	0.05	3.3	20	/	JONSWAP
61	IW	720	1.8	0.1	3.3	20	/	JONSWAP
62	IW	720	1.3	0.15	3.3	20	/	JONSWAP
63	IW	720	1.55	0.15	3.3	20	/	JONSWAP
64	IW	720	1.8	0.15	3.3	20	/	JONSWAP
65	IW	720	2.05	0.05	3.3	20	/	JONSWAP
66	IW	720	2.05	0.1	3.3	20	/	JONSWAP
67	IW	720	2.05	0.15	3.3	20	/	JONSWAP
68	IW k=1	720	/	/	/	20	/	K=1
69	IW k=1	720	/	/	/	20	/	K=5
70	IW k=2	720	/	/	/	20	/	K=5
71	IW k=3	720	/	/	/	20	/	K=5
72	IW k=4	720	/	/	/	20	/	K=5
73	IW k=5	720	/	/	/	20	/	K=5
74	IW k=1	720	/	/	/	20	/	K=10
75	IW k=2	720	/	/	/	20	/	K=10
76	IW k=3	720	/	/	/	20	/	K=10
77	IW k=4	720	/	/	/	20	/	K=10
78	IW k=5	720	/	/	/	20	/	K=10

79	IW k=6	720	/	/	/	20	/	K=10
80	IW k=7	720	/	/	/	20	/	K=10
81	IW k=8	720	/	/	/	20	/	K=10
82	IW k=9	720	/	/	/	20	/	K=10
83	IW k=10	720	/	/	/	20	/	K=10
84	IW k=1	720	/	/	/	20	/	K=15
85	IW k=2	720	/	/	/	20	/	K=15
86	IW k=3	720	/	/	/	20	/	K=15
87	IW k=4	720	/	/	/	20	/	K=15
88	IW k=5	720	/	/	/	20	/	K=15
89	IW k=6	720	/	/	/	20	/	K=15
90	IW k=7	720	/	/	/	20	/	K=15
91	IW k=8	720	/	/	/	20	/	K=15
92	IW k=9	720	/	/	/	20	/	K=15
93	IW k=10	720	/	/	/	20	/	K=15
94	IW k=11	720	/	/	/	20	/	K=15
95	IW k=12	720	/	/	/	20	/	K=15
96	IW k=13	720	/	/	/	20	/	K=15
97	IW k=14	720	/	/	/	20	/	K=15
98	IW k=15	720	/	/	/	20	/	K=15

9.2. 1:25 hinged-raft free decay test results

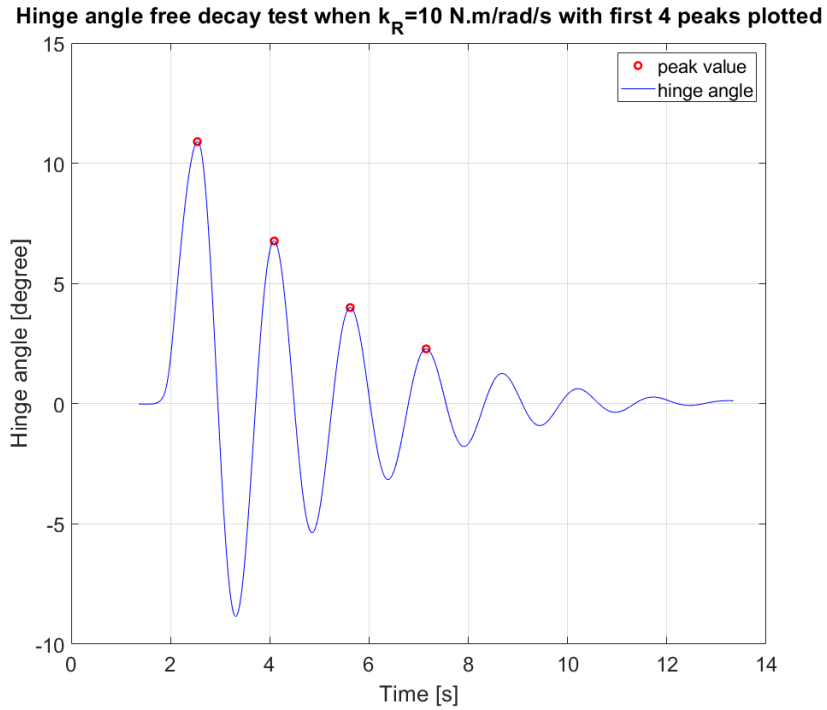

Figure 9.1: Free decay test with k_R = 10 N.m/rad/s.

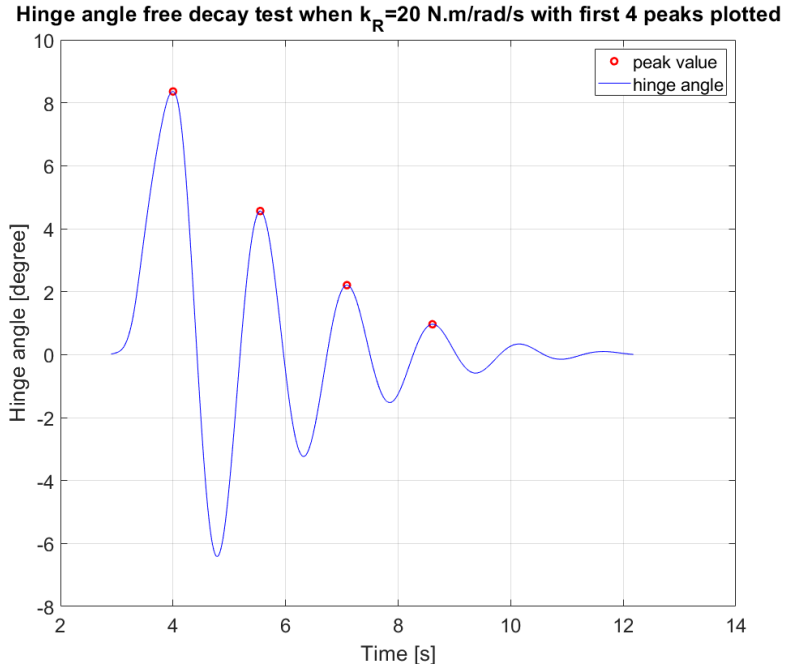

Figure 9.2: Free decay test with k_R = 20 N.m/rad/s.

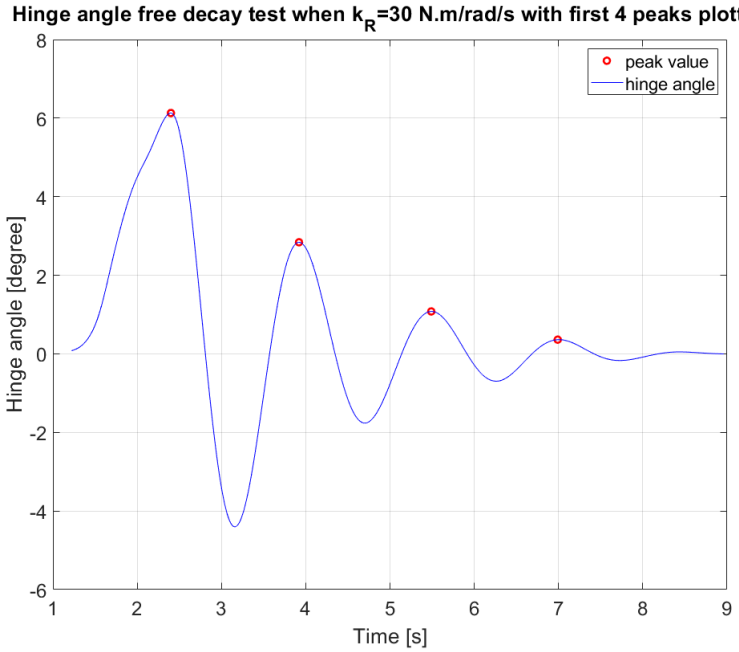

Figure 9.3: Free decay test with k_R = 30 N.m/rad/s.

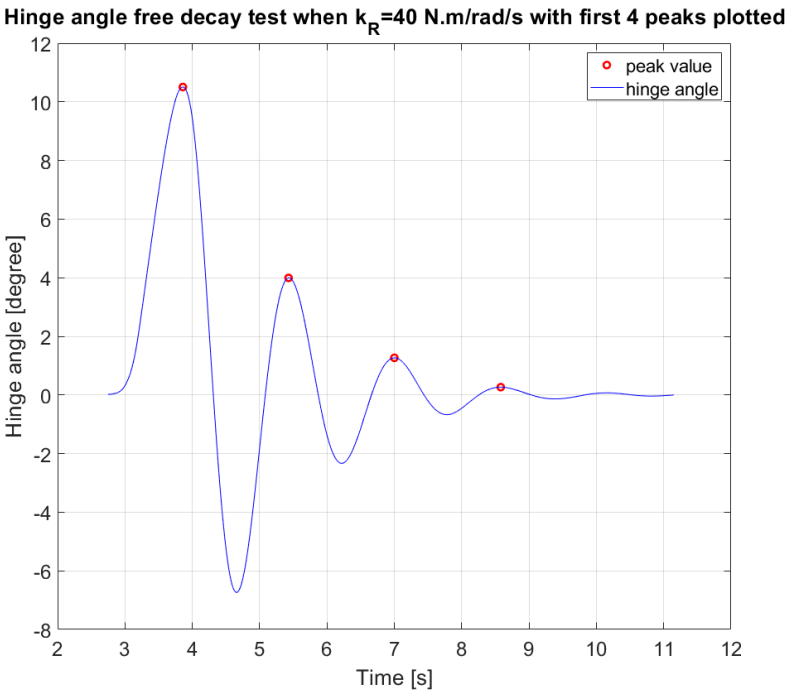

Figure 9.4: Free decay test with k_R= 40 N.m/rad/s.

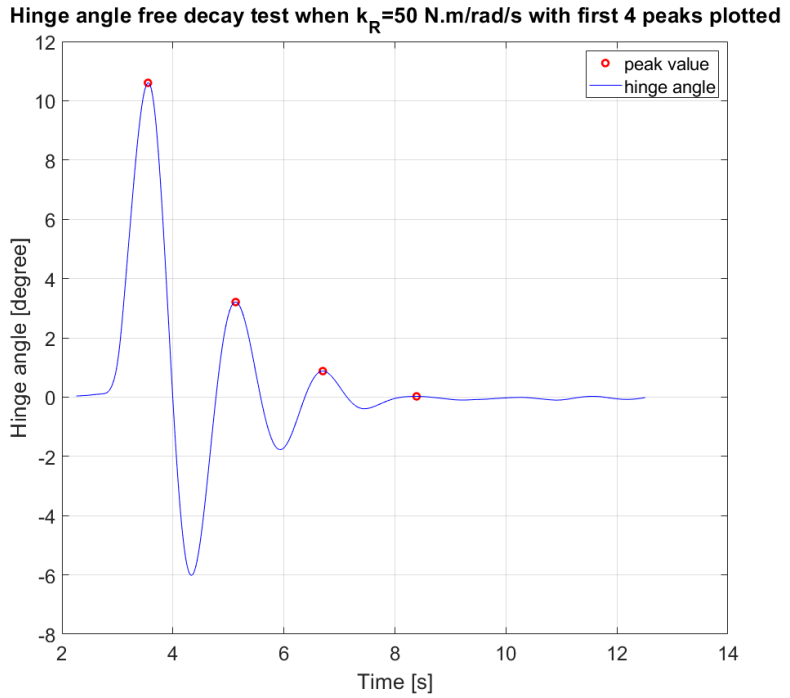

Figure 9.5: Free decay test with k_R = 50 N.m/rad/s.